Ultrasonic measurement system for gas.

Experimental and theoretical characterization using piezoelectric elements at radial mode vibration in air

Master Thesis in Acoustics

Renate Grindheim

June 2019

Department of Physics and Technology
UNIVERSITY OF BERGEN
NORWAY

"A goal without a plan is just a wish."

Antoine de Saint-Exupéry

Acknowledgements

The current thesis is part of a long-term project by the acoustics group at the University of Bergen, under the supervision of prof. Per Lunde and co-supervisor Magne Vestrheim. The objective of the project is to, with high accuracy, describe transmit-receive ultrasound measurement systems in air using finite element modelling.

I would like to thank my supervisors for guidance and support through weekly meetings, for always having their doors open when extra discussions were needed and for the invaluable assistance and guidance in co-writing a paper for the 42nd Scandinavian Symposium on Physical Acoustic 2019 at Geilo, Norway. The paper and this work would not have been possible without your input and encouraging feedback.

A special thanks goes to Espen Storheim, Andreas Hagen and Magnus Esdal Reicht for helpful advice, tips, tricks and assistance with the simulations, experimental setup and in general when life has seemed hard. Your support has been very much appreciated, both in the exciting moments and the not so exciting part of this journey.

The people at the Acoustics group at the University of Bergen have also been a big support with lunches and discussions, both scientific and social. The help from the in-house workshop is also much appreciated and their quick response to facilitate changes in the experimental setup requested by the current author.

Villy and Elena also deserve thanks for encouragement and numerous laughs in the hallways and for always showing up with a smile. You make the day brighter with your presence.

Finally, I would like to thank my family, for their patience throughout these past few years, and my friends, Tordis and Marta, for invaluable tea breaks and recharging lunches.

Renate Grindheim
Bergen, 2019

Summary

High accuracy modelling of ultrasound transmit-receive measurement systems are useful for many applications and with Finite Element (FE) modelling a 3D representation of the system is possible.

A model for an ultrasound transmit-receive measurement system has been developed by the Acoustics group at the University of Bergen, consisting of several blocks representing different modules in the system. Each block is assumed linear in behaviour and the blocks are connected through nodes.

The transmission line model is used to make equivalent circuits representing the cables and electronics used in the system model, Khimunins baffled piston diffraction correction is used for calculating diffraction effects and Cramers model for speed of sound, along with Howell and Morfeys dispersion correction, is used to estimate the speed of sound used to calculate the slowly varying phase of the system model.

The objective of this thesis is to investigate the effect of some of the parameters included in the system model, perform measurements and simulations of the transfer function for the transmitted signal for different separation distances of the transmitter and receiver and compare results with prior work done using the same system model and experimental setup.

Discussion and experimental plots are made, with respect to the use of different parameters, such as input voltage, accuracy in alignment of the transmit-receiver pair and measured and separation distances for simulated transfer functions. Measurements and simulated data were also compared to prior work.

Contents

Chapter 1

Introduction

1.1 Background and motivation

The use of ultrasound measurement systems are numerous in both science and industry, ranging from marine, medical and gas measurement applications. In many of these applications, such as fiscal flow measurement for custody transfer (e.g. sales and allocation) of natural gas [1–3], energy and quality measurement of gas [2, 4, 5] and sound velocity and absorption measurements [6–9], an ultrasonic transmit-receive system is used. Ultrasonic acoustic measurements can be accurate down to micrometer level [10] and this high accuracy combined with price and the convenience of non-invasive clamp-on installation makes it a compelling alternative to other measurement flow meters, such as the turbine, orifice plate and gamma densitometer [11, 12]. There are several different methods used for different ultrasonic gas flow meters, including transit time method, Doppler method, correlation method, noise method and the beam deflection method [13]. The transit time method, which measures the difference in time of flight caused by the fluid velocity in the medium between the transmit-receive pair, is most widely used in the industry and offers high accuracy [14].

An ultrasound measurement system often consists of signal generation, transmitting electronics, transmitting transducer, the propagation medium, receiving transducer, receiving electronics and termination [15–22], which can be referred to as different modules [41]. A theoretical model of such an ultrasound measurement system, which describes the measurement system, is desirable for numerous reasons. It can give a better understanding and analysis of the measured data and it allows each parameter in the system to be investigated in a controlled manner. Accurate simulations are of great value for design and optimization of measurement systems for use in industry. Theoretical research is also cost and time efficient, compared to experimental work. Such a theoretical model, describing a ultrasonic measurement system, will be referred to as a system model. For a linear system each module included in the system model can be modelled separately or combined to make a full system model [15]. This allows for investigation of the signal propagation though the full system model or only through parts of the system. In particular the transmitting and receiving transducers including the propagation medium between them are of interest. The transmitting and receiving transducers will be referred to as the transmit-receive pair in this work.

A frequency range of up to 300 kHz may be of interest in many ultrasonic measurement systems due to absorption increasing with increasing frequency [41]. In order to compare the simulated system model to experimental measurements of the transmit-receive system high accuracy is required of the measured quantities. These quantities include temperature, humidity, pressure, separation distance and the alignment of the transmitter and receiver pair, as well as accurate knowledge of the instruments used in the system, experimentally.

1.2 Previous work

A high precision method for modelling the transmit-receive ultrasonic measurement system consisting of a transmitting transducer and a receiving transducer, as well as the transmitting and receiving electronics and cables, is sought after and various methods and approaches have been used. This includes theoretical representation of the system models using one-dimensional (1-D), two-dimensional (2-D) and three-dimensional (3-D) modelling tools to describe piezoelectric transducers vibrating in thickness extension (TE) mode and/or radial (R) mode vibration.

A model using transmission line theory and Thevenin equivalent circuits to model the different modules in the transmit-receive system was presented by Papadakis in 1977 [23]. In 1984 Hayward et al. presented a 1-D model based on plane wave in TE mode using z-transform [24, 25]. The modelling software tool FLOSIM, a 1-D Mason model for single acoustic beam and uniform flow, was presented by Lygre et al. [17] in 1987. Later, FLOSIM and TRANSCAD was used as a 1-D Mason type transmission line model [18, 19].

In 1989 an analysis of ultrasound NDT probes using Mason 1-D model was presented, which included effects of both the electrical load and diffraction was developed to predict probe performance [26]. This is just one of numerous articles on this subject. An electromechanical modelling using Mason 1-D model and reciprocity formulation was incorporated into an ultrasonic transducer measurement model [27]. In this paper it was shown that the electrical components could be examined in the same manner as the mechanical components and the output impedance of the receiver in the system was shown to have a significant effect on the measured output.

In 1999 a model for lossless 1-D multilayer ultrasound transducers were presented [30], and many other publications have been made on this topic. This model was designed for time-domain analysis. A reciprocal ultrasound multi-layer transducer 1-D modelling was presented for transducers operating in TE mode vibration two years later [29]. An electro acoustic measurement (EAM) model for ultrasonic non-destructive evaluation (NDE) measurements was developed in 2002, which measures all the components of an ultrasonic measurements system and then by combining them allows for measurements of the full system [20, 21].

A 1-D multilayer transducer modelling principle combined with FIELD II software was presented in 2010 [31]. In this paper a FIELD II simulation software, which predicts the pressure in front of transducers of any given geometry, is used to predict the impulse response of ultrasound transducers. In the paper the results show an error of 11.2% to 36.2% with a 2 dB decrease in amplitude.

Then, in 2018, Sanabria et al. presented a paper on the calculation of air-coupled ultrasound (ACU) transducers based on single-plane measurements [28]. In the paper it is stated that the reradiation model used "clearly outperforms the baffles piston models." and its can be applicable for calibration and manufacturing of ultrasound transducers and accurate source functions for NDE inverse problems. The model holds for 2-D (rectangular) and 3-D (circular and square) planar transducers in the frequency range 50-230 kHz.

1.2.1 Previous work at UiB

There has been several works done at UiB on piezoelectric elements vibration in air including six master theses [32–37] and a phd thesis [38]. The work on ultrasound transmit-receive pair vibrating in gas was initiated by [38] and [32].

In [32] determination of material constants for piezoelectric materials were investigated and in [38] the diffraction effects of non-uniformly vibrating sources were investigated through FE simulations, which allows for a 3-D representation of the trancdusers. The FE simulations were done using a finite element tool for modelling piezoelectric transducers (FEMP), developed by Jan Kocbach at the University of Bergen (UiB) during his masters and phd theses in association with the Christian Michelsen Research (CMR), cf. [39, 40].

A modified three-transducer reciprocity calibration method was developed in [33] and implemented for an ultrasound transmit-receive system in gas, which included correction factors for absorption in air, diffraction effects and transmitting and receiving electronics. In collaboration with this, [35] developed and implemented a FE based linear system model for the same system. The system model included different modules describing signal generation, transmitting electronics, transmitting transducer, medium, receiving transducer, receiving electronics and termination, allowing for analysis of single modules or combinations of several modules. Transmission line modelling was introduced to model the cables and connected hardware. Comparisons were made for the magnitude of the experimental measurements and simulations of the system model.

The work was further improved by [34] to include phase response of the transmit-receive system and diffraction effects caused by having a non-uniformly vibrating transducer. However, measurement uncertainties were not included for the phase. Uncertainty in the measurement of the separation distance between the transmitter and receiver caused deviations between the simulated and measured slowly varying phase and investigation of the noise showed significant levels of electrical crosstalk, which was reduced by the use of Faraday shields around the transmitting and receiving transducer.

In [36] a three transducer reciprocity calibration method was used to calibrate two piezoelectric disks for both magnitude and phase for the piezoelectric disks. The experimental results for both magnitude and phase were compared to FE simulations using FEMP. Lasers were installed to achieve high accuracy in the measurements of the separation distance between the disks and measurement uncertainties were developed for the system model. The two distances investigated were 0.5 m and 0.85 m.

The measurement scripts were rewritten in [37] to improve the runtime of experimental measurements and to facilitate measurements at shorter separation distances between the transmitter and the receiver. A method to reduce crosstalk was presented and the experimental results were compared to FE simulations using both (FEMP) and (COMSOL) for magnitude and phase. The distances investigated were 0.5 m, 0.4 m, 0.3 m and 0.2 m.

1.3 Objectives

The first objective of the present work is to measure the transfer function of the transmit-receive system at hand and compare with prior work, cf. [36, 37]. One motivation for this is to ensure that the renovation of the lab in 2017 did not change the experimental setup inherited by [37]. Another motivation for this is to compare

[36] and [37], since the latter introduced new methods for experimental measurement acquisition utilizing PYTHON scripts instead of the previously used MATLAB scripts developed by [33–36, 38] and it yields information as to the repeatability of the experimental results obtained over several years.

An in depth documentation of the measurement and post processing scripts is done in order to fully understand the measurements and measurement procedure done by [37]. This documentation enables comparison with current and prior work and leads to easy use and understanding for the current author and future works.

The use of different input voltage and different degrees of accuracy in alignment of the transmitting and receiving disk is investigated due to differences seen in prior work. The influence of these parameters are measured and discussed.

Different parameters were also observed in prior simulations [36, 37], both concerning material data and the dimensions of the piezoelectric disk being simulated. These are simulated for the different material data sets and for the different dimensions in order to quantify the effect the different parameters have on the simulation.

Lastly the transfer function of the transmit-receive pair is investigated for different separation distance. The distances used in the current work are 50 cm, 30 cm, 20 cm and 15 cm.

1.4 Thesis outline

A description of the system model and the theory used in the current thesis is given in **Chapter 2**. This includes the system model utilized, changes in the system model from previous work, transfer functions used in the thesis and the finite element theory used for simulations of the acoustical measurement presented in **Chapter 3**. The acoustical measurement system is presented in **Chapter 3**. Methods for measurements are also presented along with an overview of the scripts used for acoustic and electrical measurements. A theoretical overview of the simulation tool FEMP (Finite Element Modelling of Piezoelectric transducers) is briefly presented in **Chapter 4**. Results from experimental measurements and theoretical calculations are presented in **Chapter 5** for the electrical measurements and the measured transfer functions. Discussion of the results from **Chapter 5** are presented in **Chapter 6**. Conclusion and suggestions for further work are presented in **Chapter 7**. The PYTHON source codes used for data acquisition are included in **Appendix A**. The MATLAB source code used for post-processing the acquired data are included in **Appendix B**. Files used for simulation and post-processing the simulations are included in **Appendix C**. Plots of sent and received waveforms for four different separation distances given at five frequencies are included in **Appendix D**. The paper submitted for the proceedings of the 41st Scandinavian Symposium on Physical Acoustics is included in **Appendix E**.

Chapter 2

Theory

In the current chapter the theory used in the current work is presented. An overview of the transmit-receive pair and the system model is first presented in Section 2.1. In Section 2.2 the system model describing the transmit-receive system is presented and in Section 2.3 the Fourier transform used to transform the recorded time-domain voltages to the frequency domain is presented. As the simulation used is based on spherical reciprocity the transmitting and receiving properties of piezoelectric transducers are presented in Section 2.4. The transmission line model used to calculate the effect of the transmitting and receiving cables and electronics is presented in Section 2.5. This includes the transmitting electronics transfer function H_{0m1}^{VV}, the open-circuit transfer function transfer function $H_{5open5'}^{VV}$ and the receiving electronics transfer function $H_{5'6}^{VV}$. The equations for electrical impedance is presented in Section 3.1.1. In Section 2.7 the sound speed model used in the current work is presented and in Section 2.9.1 the diffraction correction used in the present work is presented. In Section 2.10 and Section 2.11 the theory for the measured and the simulated transfer function $H_{15open}VV$ is presented. Lastly, in Section 2.12 the finite element model equations used to simulate the admittance and far-field pressure used to calculate $H_{15open}VV$ is presented.

2.1 Transmit-receive pair

The transmit-receive pair are mounted in air, parallel to one another with the distance, d defined as the distance between the two facing surfaces of the transmitter, T_x, and receiver, R_x, cf. Fig. 2.1. The polarization, P, of the disks are marked on the front surface of each disk, with the polarization direction going from the front to the back of the disk. The disks used are two cylindrical Pz27 piezoelectric ceramic disks with a nominal diameter D of 20.0 mm and thickness T = 2.0 mm, yielding a diameter to thickness ratio D/T = 10.

2.2 System model

The system model consists of two cylindrical piezoelectric ceramic disks in radial mode vibration in air, where the transmitting disk, T_x, is coupled to the transmitting electronics (signal generator, oscilloscope and cables), and the receiving disk, R_x, is coupled to the receiving electronics (amplifier, filter, cables and oscilloscope). The two disks are mounted parallel (with respect to the xy-plane at a separation distance d along the z-axis, cf. Fig. 2.1. The system model illustrated in Fig. 2.2 shows the different components included in the measurement setup as linear blocks where transfer functions relate the signal going from one block to another in the frequency domain.

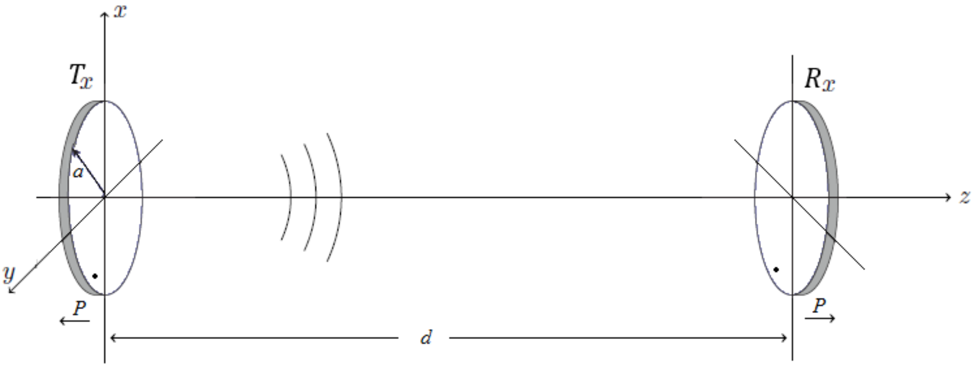

FIGURE 2.1: Illustration of the transmitting and receiving disk with coordinate system, separation distance, d, and polarization, P, indicated.

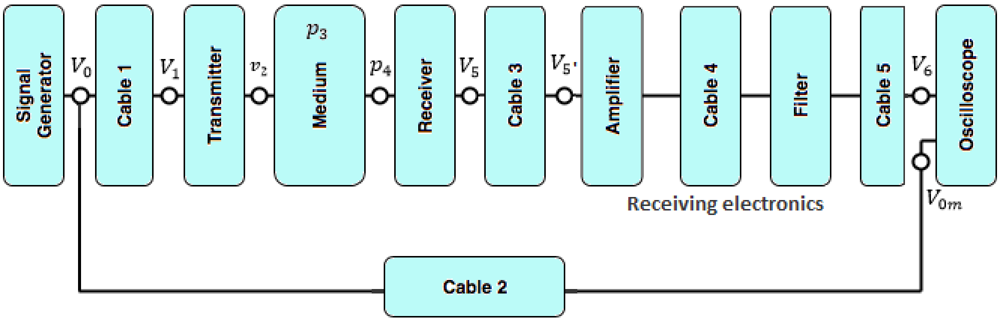

FIGURE 2.2: Block diagram representation of system model used in the current work.

The voltage signals $V_6(t)$ and $V_{0m}(t)$ measured at the oscilloscope are Fourier transformed as described in [37], giving the respective spectral components $V_6(f)$ and $V_{om}(f)$, where t is the time and f is the frequency. For these spectral components a monochromatic time dependency $e^{i\omega t}$ is assumed and suppressed. At angular frequency $\omega = 2\pi f$, $V_0(f)$ is the output voltage spectral component generated by the signal generator and $V_{0m}(f)$ is the output voltage spectral component measured in Channel 1 on the oscilloscope.

Each circle in Figure 2.2 represents a node, and the variables presented are as follows:

- $V_0(f)$ is the output voltage spectral component at node 0, generated by the signal generator.
- $V_{0m}(f)$ is the output voltage spectral component at node 0m, measured at Channel 1 on the oscilloscope.
- $V_1(f)$ is the input voltage spectral component at the terminals of T_x at node 1.
- $v_2(f)$ is the spectral component of the particle velocity vector at the center of the front surface of T_x at node 2.
- p_3 is the on-axis free-field pressure in the medium at node 3, defined in [33].

- p_4 is the on-axis spectral component of the free-field pressure at the front surface of R_x, at node 4.
- $V_5(f)$ is the output voltage spectral component from R_x at node 5.
- $V_{5'}(f)$ is the output voltage spectral component at node 5′.
- $V_6(f)$ is the input voltage spectral component measured and terminated in Channel 2 on the oscilloscope at node 6.

2.2.1 Changes from previous works

The system model presented in this chapter is inherited from [33–37] but with some changes to how the receiving electronics is represented and experimentally measured. In [37] a method for measuring the transfer function of the receiving electronics was introduced, whereas the previous had included transmission line model for a mathematical description of all the receiving cables. In the current work the method for handling the receiving electronics has been adopted and modified slightly from [37] by increasing the frequency resolution of the measurement and adopting the experimental values of the amplifiers impedance as found by [34]. The system model numeration has been kept as used by [33–36] for continuity and to facilitate comparison between different works.

2.2.2 Transfer function representation

The transmit-receive measurement setup used in the present work consists of two piezoelectric disks in radial mode vibration in air, where the transmitting disk, T_x, is coupled to transmitting electronics (signal generator, oscilloscope and cables) and the receiving disk, R_x is coupled to receiving electronics (amplifier, filter, cables and oscilloscope). A system model based on this setup was first introduced by [33, 35] cf. [41] and further developed by [34, 36, 37] and this is a continuation of their work. A brief overview of the system model and theory used in the current work will be given in the following.

A transfer function relates the different blocks in a system model through their respective input and output signal, under the assumption that each block in the system displays linear behaviour, cf. Section 2.3 in [15]. It is assumed that each of the blocks in Fig. 2.2 display linear behaviour and thus the effect of moving from one block to another can be expressed through transfer functions. These are multiplied in order to move between one or several blocks. The transfer function representation for the system model is then given as Eq. (2.1) in [34]:

$$H_{06}^{VV} \equiv \frac{V_6}{V_0} = \frac{V_1}{V_0} \cdot \frac{v_2}{V_1} \cdot \frac{p_3}{v_2} \cdot \frac{< p_4 >}{p_3} \cdot \frac{V_5}{< p_4 >} \cdot \frac{V_6}{V_5}. \tag{2.1}$$

This can be written as a voltage-to-voltage transfer function of the complete signal chain as defined in Eq. (2.1) in [34] with the receiving electronics treated as in Eq. (2.64) in [37], i.e.

$$H_{0m6}^{VV}(f) \equiv \frac{V_6(f)}{V_{0m}(f)} = \frac{V_1(f)}{V_{0m}(f)} \cdot \frac{V_{5open}(f)}{V_1(f)} \cdot \frac{V_{5'}(f)}{V_{5open}(f)} \cdot \frac{V_6(f)}{V_{5'}(f)}. \tag{2.2}$$

The various transfer functions used in Eq. (2.1) are described in the following. The open-circuit voltage-to-voltage transfer function describing the sound propagation from T_x to R_x at lossless conditions in the air medium is defined as Eq. (2.20) in [35]

$$H^{VV}_{15open}(f) \equiv \frac{V_{5open}(f)}{V_1(f)}, \tag{2.3}$$

where V_{5open} is the open-circuit voltage at R_x.

The transfer function relating the measured voltage at Channel 1 on the oscilloscope to the voltage at the terminals of T_x, H^{VV}_{0m1}, is defined as Eq. (2.5) in [36] :

$$H^{VV}_{0m1}(f) \equiv \frac{V_1(f)}{V_{0m}(f)}. \tag{2.4}$$

The transfer functions $H^{VV}_{5open5'}$, describing the influence of the electrical load from cable 3 and the receiving electronics on the output voltage from R_x, and $H^{VV}_{5'6}$, describing the receiving electronics including cables 4 and 5, are defined as [37]:

$$H^{VV}_{5open5'}(f) \equiv \frac{V_{5'}(f)}{V_{5open}(f)} \tag{2.5}$$

and $H^{VV}_{5'6}$ is the transfer function relating the input voltage at the receiving electronics to the recorded voltage at the oscilloscope, V_6,

$$H^{VV}_{5'6}(f) \equiv \frac{V_6(f)}{V_{5'}(f)}. \tag{2.6}$$

H^{VV}_{0m1} and $H^{VV}_{5open5'}$ are estimated using transmission line models as proposed by [34], and $H^{VV}_{5'6}$ is found by measuring the transfer function of only the receiving electronics including cables 4 and 5, by coupling the signal generator to an attenuator and then directly into the receiving electronics, bypassing the transmitting and receiving transducer completely as in [37].

2.3 Fourier transform

When a signal is transformed from the time domain to the frequency domain a Fourier transform is used. Fourier transform (FT), and inverse Fourier transform (IFT) is used when going from frequency domain to time domain. For an arbitrary signal in the time domain, V(t), the equivalent frequency domain signal is given by FT as

$$V(f) = FT\{V(t)\} = \int_{-\infty}^{\infty} V(t)e^{-i2\pi ft}dt \tag{2.7}$$

$$V(t) = IFT\{V(f)\} = \int_{-\infty}^{\infty} V(f)e^{i2\pi ft}df \tag{2.8}$$

The result of classical Fourier transform is a list of both positive and negative frequencies where the negative values of frequency are the conjugates of the corresponding positive frequency value. The negative values are discarded for real applications and in order to avoid computing the negative values all together the Goertzel algorithm, which computes single frequency DFT (Discrete Fourier Transform), was chosen by [37] in Appendix B.3.3 for the Fourier transformation of the measurement done at the laboratory, excluding the noise measurement. For accurate noise measurement the full FT is computed in Appendix B.3.4.

2.4 Transmitting and receiving properties of piezoelectric transducers

2.4.1 Transmitting voltage response

The transmitting voltage response is defined in Section 5.4 in [15] as

$$S_V(f, d_0) = \frac{p_3(d_0)}{V_1(f)}, \tag{2.9}$$

where $p_3(d_0)$ is the far-field pressure extrapolated to the distance d_0.

For the case of a lossless medium the extrapolated far-field spherical pressure at d_0 is

$$p(d_0) = \frac{z}{p_4(d_0)} p(z) e^{-ik(d-d_0)}. \tag{2.10}$$

For a given input voltage at the receiver, the far-field axial pressure at a given distance, d, can be calculated as

$$p_{ax}(d) = p(d_0) \frac{d_0}{d} p(z) e^{-ik(d-d_0)}. \tag{2.11}$$

2.4.2 Receiving voltage sensitivity

The free-field open-circuit receiving voltage sensitivity, M_V, is defined in Eq. (6.44) in [15] as

$$M_V \equiv \frac{V}{p} = \frac{V_{5open}}{p_4(0, d)} = |M_V| e^{i\theta_{M_V}}, \tag{2.12}$$

where $|M_V|$ and θ_{M_V} are the magnitude and phase of the receiving voltage sensitivity, respectively.

2.4.3 Spherical reciprocity factor

The lossless complex spherical reciprocity factor, J, is defined by Eq. 51 in [42] or Eq. 1 in [43] as

$$J(\rho, f, c) \equiv \frac{M_V}{S_I} = \frac{M_V}{S_V Z_T} = \frac{2 d_0 \lambda}{i \rho c} e^{ikd_0}. \tag{2.13}$$

When spherical reciprocity is assumed the transmitting voltage sensitivity, S_V^{Tx}, is equal to the receiving voltage sensitivity, S_V^{Rx}, and Eq. 2.3 can be written as

$$H_{15}^{VV} = J_{sph}^{Rx} Z_T (S_V)^2 V_1 \frac{d_0}{d} e^{-ik(d-d_0)}. \tag{2.14}$$

2.5 Transmission line model

In the lossless transfer function H^{VV}_{15open} the effect of transmitting and receiving cables and electronics is corrected for. It has been shown that the transmitting, and especially the receiving electronics, affect the measured transfer function [33–37].

In order to account for cables in the system model the transmission line model, defined in [44, 45], is used by [34–37] to represent the effect of the coaxial cables and electronic equipment in the experimental setup. The method uses distributed elements to model the coaxial cables as ideal and uniform transmission lines. The method will be briefly repeated for continuity.

A coaxial cable number i is modelled as a voltage divider with impedances Z_{ai} and Z_{bi} that terminates in an impedance, Z_L, cf. Fig. 2.3.

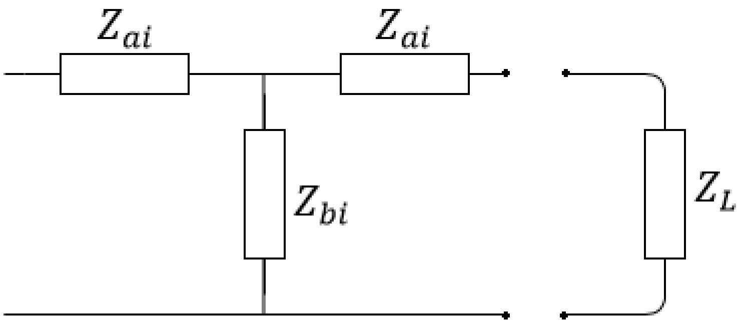

FIGURE 2.3: Equivalent circuit for a cable represented as a lossless transmission line, terminated in the load, Z_L.

As in Eq. (5.66) in [45] the transmission line impedances, Z_{ai} and Z_{bi}, are given as

$$Z_{ai} = iZ_0 \tan\left(k_{em}\frac{l_i}{2}\right) \tag{2.15}$$

and

$$Z_{bi} = \frac{Z_{0i}}{i\sin(k_{em,i}l_i)}, \tag{2.16}$$

where Z_0 is the characteristic impedance of cable number i, $k_{em,i}$ is the electromagnetic wave number and l_i is the length of the cable number i. The electromagnetic wave number is given as

$$k_{em,i} = \frac{\omega}{c_{em,i}} = \omega\sqrt{L_iC_i}, \tag{2.17}$$

where $c_{em,i}$ is the electrical propagation speed in cable number i. For a lossless transmission line the characteristic impedance of the cable is given as

$$Z_0 = \sqrt{\frac{L_i}{C_i}}, \tag{2.18}$$

where L_i is the inductance and C_i is the capacitance of cable number i per meter.

2.5.1 Transmitting electronics and cables

Fig. 2.4 shows the transmitting electronics, cable 1 and cable 2 expressed using the transmission line model. The transfer function H_{0m1}^{VV} describing the effect of the transmitting electronics on the transmitting transducer is given as Eq. (2.4), and can be further expanded to

$$H_{0m1}^{VV} = \frac{V_1/V_0}{V_{0m}/V_0}. \tag{2.19}$$

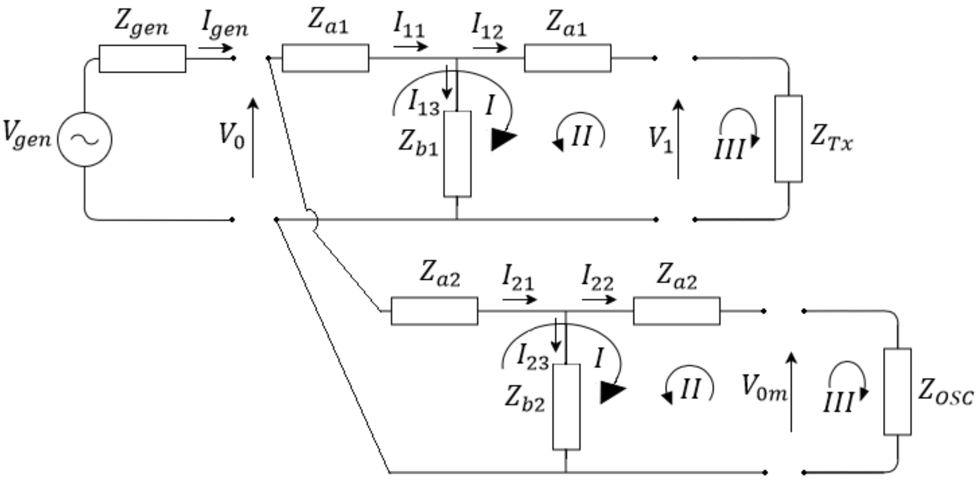

FIGURE 2.4: Equivalent circuit for the transmitting electronics and cable 1 and cable 2 represented as a lossless transmission line.

The nominator and denominator of Eq. (2.19) can then be calculated separately by dividing the circuit in Fig. 2.4 into two separate circuits. Fig. 2.5 represents the cable 1 from the signal generator terminating at the transmitting disk, T_x and Fig. 2.6, represents the signal generator and cable 2 into the oscilloscope.

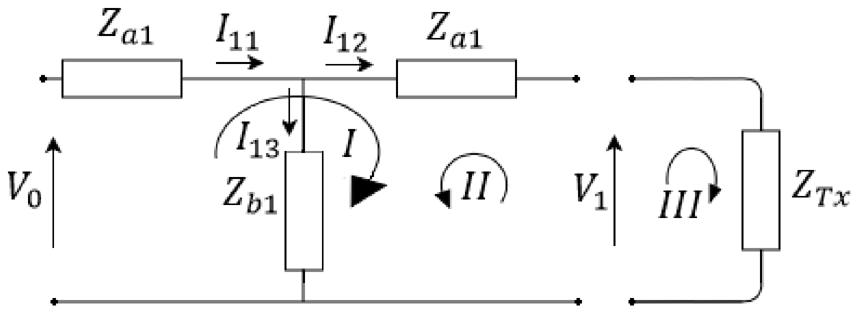

FIGURE 2.5: Equivalent circuit for cable 1 represented as a lossless transmission line, terminated in T_x.

Kirchoff's first rule gives the relation of the three currents as

$$I_{11} = I_{12} + I_{13}. \tag{2.20}$$

Using Kirchoff's second rule, as indicated by the three arrows in Fig. 2.5, gives three equations,

$$V_0 - I_{11}Z_{a1} - I_{13}Z_{a1} - V_1 = 0, \tag{2.21}$$

$$V_1 + I_{13}Z_{a1} - I_{12}Z_{b1} = 0 \tag{2.22}$$

and

$$V_1 - I_{13}Z_{Tx} = 0. \tag{2.23}$$

By substitution and algebra Eq. (2.20)-(2.23) gives, as in [34–37]

$$\frac{V_1}{V_0} = \frac{Z_{b1}Z_{Tx}}{Z_{a1}^2 + Z_{a1}Z_{Tx} + 2Z_{a1}Z_{b1} + Z_{b1}Z_{Tx}}. \tag{2.24}$$

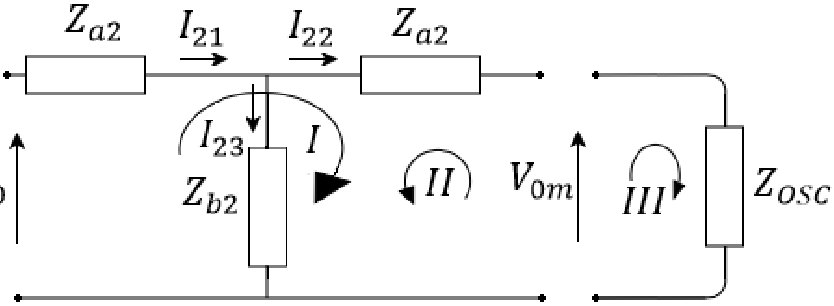

FIGURE 2.6: Equivalen circuit for cable 2 represented as a lossless transmission line, terminated in the oscilloscope.

As the circuit in Fig. 2.6 is equivalent to the circuit in Fig. 2.5 the same approach has been performed, using Kirchoff's first and second rule, as in [34–37], giving

$$\frac{V_{0m}}{V_0} = \frac{Z_{b2}Z_{osc}}{Z_{a2}Z_{b2} + (Z_{a2} + Z_{osc})(Z_{a2} + Z_{b2})}. \tag{2.25}$$

2.5.2 Receiving electronics and cables

The transfer function $H^{VV}_{5open5'}$ describing the influence of the electrical load from cable 3 and the receiving electronics on the output open-circuit voltage from R_x can be expressed by the transmission line model, cf. Fig. 2.7. The definition of $H^{VV}_{5open5'}$ is given as Eq. (2.5).

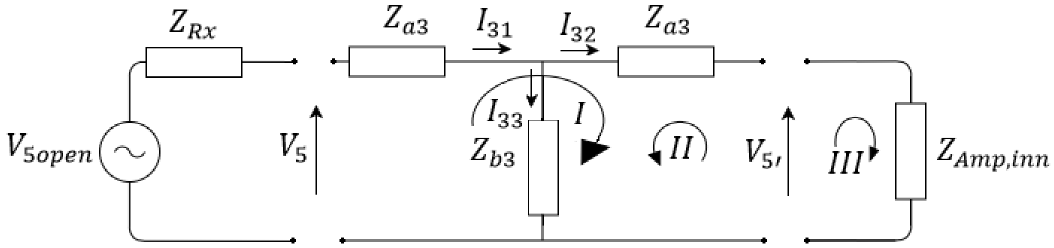

FIGURE 2.7: Equivalen circuit for cable 3 represented as a lossless transmission line, terminated in the amplifier.

Kirchoff's first rule gives the relation of the three currents as

$$I_{31} = I_{32} + I_{33} \tag{2.26}$$

Using Kirchoff's second rule, as indicated by the three arrows in Fig. 2.7, gives three equations,

$$V_{5open} - I_{31}Z_{Tx} - I_{31}Z_{a3} - I_{33}Z_{a3} - V_{5'} = 0, \tag{2.27}$$

$$V_{5'} + I_{33}Z_{a3} - I_{32}Z_{b3} = 0 \tag{2.28}$$

and

$$V_{5'} - I_{33}Z_{Amp,inn} = 0. \tag{2.29}$$

By substitution and algebra Eq. (2.26)-(2.29) gives

$$H^{VV}_{5open5'} \equiv \frac{V_{5'}}{V_{5open}} = \frac{Z_{Amp,inn}Z_{b3}}{Z_{Rx}(Z_{Amp,inn} + Z_{a3} + Z_{b3}) + Z_{a3}(Z_{Amp,inn} + Z_{a3} + 2Z_{b3}) + Z_{Amp,inn}Z_{b3}} \tag{2.30}$$

The transmission line model has previously been used to determine the transfer function $H^{VV}_{5'6open}$ and $H^{VV}_{5'6open}$ [34–36]. However, in [37] measurements were done directly on the receiving electronics to obtain a full experimental transfer function of the receiving electronics, H^{VV}_{56}. This method of experimentally measure the effect of the amplifier and filter is used in the current work, but the equations for calculating the effect of the amplifier and filter with cables is presented here for continuity, as this method was used in [36] and comparisons will be made with both [36] and [37].

The transfer function $H^{VV}_{5'6}$ describing the influence of the electrical load from cable 4 and the amplifier and filter terminated in the oscilloscope, as used in [36], can be expressed by the transmission line model, cf. Fig. 2.8.

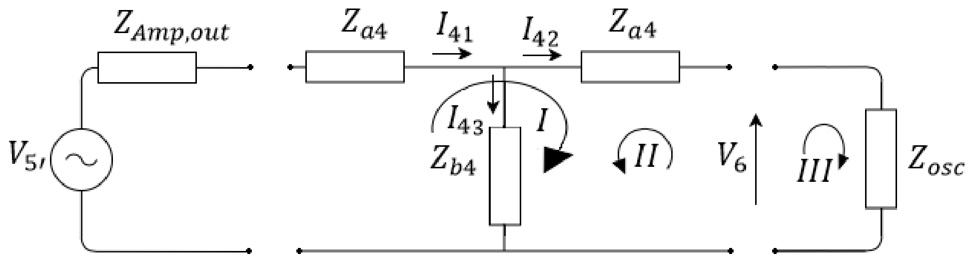

FIGURE 2.8: Equivalen circuit for the electrical load from cable 4 and the amplifier and filter represented as a lossless transmission line, terminated in the oscilloscope.

As the circuit in Fig. 2.5 is equivalent to the circuit in Fig. 2.8 the same approach has been performed, giving

$$H_{5'6}^{VV} \equiv \frac{V_6}{V_{5'}} = \frac{Z_{Amp,out} Z_{b4}}{Z_{Amp,out}(Z_{Osc} + Z_{a4} + Z_{b4}) + Z_{a4}(Z_{Osc} + Z_{a4} + 2Z_{b4}) + Z_{Osc} Z_{b4}}. \tag{2.31}$$

2.6 Electrical impedance

The electrical impedance of a component is defined as the effective resistance of that component to alternating current, due to the combined effects of resistance and reactance in the component. This is defined above Eq. (1.12.4) in [46] as

$$Z = |Z| e^{i\phi_Z} = \frac{V}{I} \tag{2.32}$$

The impedance, Z, can be expressed by a real part; the resistance, R, and an imaginary part; the reactance, X, as defined in Eq. (1.12.4) in [46] as

$$Z = R + iX \tag{2.33}$$

The admittance, Y, is inversely related to the impedance and can be expressed by a real part; the conductance, G, and an imaginary part; the susceptance, B.

$$Y = \frac{1}{Z} = G + iB. \tag{2.34}$$

2.7 Sound speed model

When calculating the slowly varying phase the plane wave component, $kd = \omega d/c$, is calculated and as this is dependent on the speed of sound an accurate model for speed of sound is needed.

A model for sound speed was presented by Wong [47], with the maximum uncertainty estimated to be 200 ppm and the predictions are presented to be applicable for temperatures ranging from $0° - 30°$ Celcius. However, unexplained discrepancies were found at relative humidity below approximately 20%. The model has been criticised for the assumptions of ideal gas being used, as it builds on work by Wong and Embleton [48], and the way the model calculates the plane-wave speed of sound [49].

The sound speed model presented by Wong and Embleton was extended by Cramer, who removed the assumption of ideal gas and calculates the speed of sound as a function of temperature given in Kelvin, T_K, atmospheric pressure, p, humidity and CO_2 concentration, presented in Eq. 8 in [50] as

$$c_0^2 = \gamma \frac{RT_K}{M}\left(1 + \frac{2pB}{RT_K}\right), \tag{2.35}$$

where c_0 is the speed of sound value at zero frequency, $\gamma = \frac{C_p}{C_v}$ is the specific heat ratio and C_p and C_v are the specific heat at constant pressure and constant volume, respectively. The uncertainty in this calculation of the sound speed is estimated to be in the region of 300 ppm and does not take into calculation any corrections for dispersion due to vibrational relaxation effects of nitrogen, N_2, or oxygen, O_2, which are frequency dependant.

An approximate formula for calculating the sound speed, c_0, for any combination of the environmental parameters is given in Eq. (15) in [50] and is presented here on matrix form:

$$c_0 = \begin{bmatrix} 1 & x_\omega & p & x_c \end{bmatrix} \begin{bmatrix} a_0 & a_1 & a_2 \\ a_3 & a_4 & a_5 \\ a_6 & a_7 & a_8 \\ a_9 & a_{10} & a_{11} \end{bmatrix} \begin{bmatrix} 1 \\ t \\ t^2 \end{bmatrix} + \begin{bmatrix} x_\omega^2 & p^2 & x_c^2 & x_\omega p x_c \end{bmatrix} \begin{bmatrix} a_{12} \\ a_{13} \\ a_{14} \\ a_{15} \end{bmatrix}, \tag{2.36}$$

where t is the temperature in Celcius, p is the ambient pressure in Pascals, x_ω is the water vapour mole fraction, x_c is the carbon dioxide mole fraction and the accompanying coefficients are presented in Table 2.1.

TABLE 2.1: Coefficients of Eq. (2.36).

Coefficient	**Value**	**Unit**
a_0	331.5024	ms^{-1}
a_1	0.603 055	$ms^{-1}\,{}^\circ C^{-1}$
a_2	-0.000 528	$ms^{-1}\,{}^\circ C^{-2}$
a_3	51.471 935	ms^{-1}
a_4	0.149 587 4	$ms^{-1}\,{}^\circ C^{-1}$
a_5	-0.000 782	$ms^{-1}\,{}^\circ C^{-2}$
a_6	$-1.82 \cdot 10^{-7}$	$ms^{-1}Pa^{-1}$
a_7	$3.73 \cdot 10^{-8}$	$ms^{-1}\,{}^\circ C^{-1}Pa^{-1}$
a_8	$-2.93 \cdot 10^{-10}$	$ms^{-1}\,{}^\circ C^{-2}Pa^{-1}$
a_9	-85.209 31	ms^{-1}
a_{10}	-0.228 525	$ms^{-1}\,{}^\circ C^{-1}$
a_{11}	$5.91 \cdot 10^{-5}$	$ms^{-1}\,{}^\circ C^{-2}$
a_{12}	-2.835 149	ms^{-1}
a_{13}	$-2.15 \cdot 10^{-13}$	$ms^{-1}Pa^{-2}$
a_{14}	29.179 762	ms^{-1}
a_{15}	0.000 486	$ms^{-1}Pa^{-1}$

O'Donnell et al. showed that a system which satisfies conditions of linearity and causality and exhibits attenuation must also exhibit dispersion [51, 52]. For linear acoustical systems relations for linking the attenuation and dispersion are e.g. the

Kramer-Kronig relations, cf. Eq. (1)-(4) in [52]. An approximation to this relation, commonly used for acoustical systems was presented by Morfey and Howell as Eq. (2) in [53]. Cramer therefore applied a correction for dispersion as proposed by Morfey and Howell in Eq. (14) in [50] on the form

$$\frac{1}{c_0} - \frac{1}{c} = \frac{\alpha_{vN}}{2\pi f_{rN}} + \frac{\alpha_{vO}}{2\pi f_{rO}}, \tag{2.37}$$

where $c = c(f)$ is the estimated sound speed at any given frequency and α_{vN} and α_{vO} are the plane-wave attenuation coefficient due to vibrational relaxation of nitrogen and oxygen, respectively, and f_{rN} and f_{rO} are the relaxation frequencies for nitrogen and oxygen, respectively. The attenuation coefficients and relaxation coefficients are calculated according to ANSI S1.26 [54], as proposed by Cramer [50]. Thus, including dispersion in Cramer's sound speed model.

2.8 Attenuation in air

For a pure-tone sound propagating through the atmosphere the pressure amplitude decreases exponentially as [54]

$$p_t = p_i e^{-0.1151\alpha d}, \tag{2.38}$$

where d is the propagation distance measured in meters, p_t is the sound pressure amplitude that decreases exponentially and p_i is sound pressure amplitude that decreases with the decay formula for plain sound waves in free space and α is the pure-tone sound attenuation coefficient measured in decibels per meter. Both the sound pressure amplitudes, p_t and p_i are measured in pascals. The effect of the attenuation in air, C_α, is found by dividing the two, giving

$$C_\alpha = \frac{p_i}{p_t} = e^{0.1151\alpha d}, \tag{2.39}$$

The correction for the attenuation in air, C_α, accounts for attenuation due to classical absorption of sound in air, α_{cl}, rotational motion of the air molecules, α_{cl}, vibrations of oxygen moleculer, $\alpha_{vib,O}$ and vibration of nitrogen molecules, $\alpha_{vib,N}$. These are calculated according to [54] and the total attenuation correction in dB can be expressed as

$$C_\alpha = e^{0.1151d\alpha} = e^{0.1151d(\alpha_{cl}+\alpha_{rot}+\alpha_{vib,O}+\alpha_{vib,N})} \tag{2.40}$$

Figure 8.6.2 in [46] shows the contributions of the different absorption coefficients included in α.

2.9 Diffraction correction

Diffraction effects due to the finite size of the transmitter and receiver are important to account for in ultrasound transmit-receive systems as this affects both the magnitude and the phase of the signal being transmitted and received. A transmitter of a finite extent will produce a spherical wave front which differs from that of a plane wave, and this is called the diffraction effect and is defined in Sec. 1 in [55] as

$$H_{dif} \equiv \frac{p}{p^{plane}}. \tag{2.41}$$

2.9.1 Baffled Piston Diffraction Correction

The Baffled Piston Diffraction Correction, C_{diff} is given by

$$C_{dif} = \frac{d_{z_{ff}}}{d} \frac{H_{dif}(z_{ff})}{H_{dif}(z)} \tag{2.42}$$

where the deviation of the average pressure of a baffled piston source from a plane wave pressure as defined by Khimunin [56, 57] is used to define the baffled piston diffraction correction, H^{BPDC}_{dif}, as Eq. (2.43) and z_{ff} is in the far-field so no near-field effects are present.

$$H^{BPDC}_{dif} = \frac{\langle p_4 \rangle}{p_4^{plane}} = 1 - \frac{4}{\pi} \int_0^{\frac{\pi}{2}} e^{-ik(\sqrt{z^2+(2a\cos(\theta))^2}-z)} \sin^2(\theta) d\theta \tag{2.43}$$

2.10 Measured lossless transfer function, H^{VV}_{15open}

By multiplying the transfer function for the transmit-receive pair with the correction for attenuation in air, C_α, from Section 2.8 and correction for diffraction effects, C_{dif}, from Section 2.9.1 the transfer function is made loss-less and the finite extent of the transmitter is accounted for. Thereby the loss-free voltage-to-voltage transfer function describing the sound propagation from the transmitting disk to the receiving disk is defined by Eq. (2.44).

From Eq. (2.2)-(2.6) in Section 2.2.2 and by using the corrections for attenuation, C_α, and diffraction, C_{dif}, the measured lossless open-circuit transfer function $H^{VV}_{15open}(f)$ is obtained as

$$H^{VV}_{15open} = \frac{H^{VV}_{0m6}}{H^{VV}_{0m1} H^{VV}_{5open5'} H^{VV}_{5'6}} C_\alpha C_{dif}. \tag{2.44}$$

2.10.1 Slowly varying phase of H^{VV}_{15open}

A transfer function can be expressed as consisting of a magnitude and an accompanying phase. For the lossless open-circuit transfer function H^{VV}_{15open} this is expressed as

$$H^{VV}_{15open}(f) = |H^{VV}_{15open}(f)| e^{i\theta_{15open}}, \tag{2.45}$$

where $|H^{VV}_{15open}(f)|$ is the magnitude and θ_{15open} the phase of this transfer function. In order to observe the small changes in the phase over a large frequency range, the plane wave component is removed from the total phase. This is done by dividing the transfer function with the equivalent plane wave pressure. The plane wave phase component is given as e^{-ikd}, when a time dependency $e^{i\omega t}$ is assumed, cf. Eq. (5.13) in [15], yielding

$$e^{i\theta^{slow}_{15open}} = \frac{e^{i\theta_{15open}}}{e^{-ikd}}. \tag{2.46}$$

The slowly varying phase is then given by

$$\theta^{slow}_{15open} = \theta_{15open} + kd, \tag{2.47}$$

where $k = \omega/c$ is the wave number and c is the speed of sound in air calculated according to Section 2.7.

2.11 Simulated transfer function H_{15open}^{VV}

The simulated lossless open-circuit transfer function H_{15open}^{VV} is calculated by assuming spherical reciprocity and using the simulated far-field axial pressure $p_{ff} = p_4(z_{ff})$, where $z_{ff} = 1000$ m is used, extrapolating it to the desired distance, d. Identical transducers are assumed for the simulations and losses in the medium are not included nor diffraction effects caused by the distance, d, being in the near-field of the transducers. The simulated lossless open-circuit transfer function is then given as Eq. (2.52) in [36]

$$H_{15open}^{VV}(f) = \frac{Z_T p_4^2(z_{ff}) 2 z_{ff}^2}{i\rho d f} e^{ik(2z_{ff}-d)}. \tag{2.48}$$

2.12 Finite Element Modelling

A finite element (FE) software, FEMP5.1, for modelling piezoelectric transducers, sound field and electronics developed by Jan Kochbach [40] at UiB in association with Christian Michelsen Research (CMR) and is used to simulate the transmit-receive pair radiating into a fluid/vacuum medium. A full description of the software can be found in [40]. Only brief overview of the method is presented here.

For a piezoceramic disk in an infinite fluid medium the FE equations given as Eq. (3.215) in [40] rewritten to H-form are

$$-\omega^2 \begin{bmatrix} M_{uu} & 0 & 0 \\ 0 & 0 & 0 \\ 0 & 0 & -M_{\psi\psi} \end{bmatrix} \begin{Bmatrix} \hat{u} \\ \hat{V} \\ \hat{\psi} \end{Bmatrix} + i\omega \begin{bmatrix} 0 & 0 & C_{u\psi} \\ 0 & 0 & 0 \\ C_{\psi u} & 0 & 0 \end{bmatrix} \begin{Bmatrix} \hat{u} \\ \hat{V} \\ \hat{\psi} \end{Bmatrix} + \begin{bmatrix} H_{uu} & H_{u\phi} & 0 \\ H_{\phi u} & H_{\phi\phi} & 0 \\ 0 & 0 & -K_{\psi\psi} \end{bmatrix} \begin{Bmatrix} \hat{u} \\ \hat{V} \\ \hat{\psi} \end{Bmatrix} = \begin{Bmatrix} 0 \\ -I/i\omega \\ 0 \end{Bmatrix}, \tag{2.49}$$

where the variables are defined in Table 2.2, as done in [33].
The global fluid velocity potential vector $\{\hat{\psi}\}$ is then expressed from Eq. 2.49 as Eq. (3.217) in [40] as

$$\{\hat{\psi}\} = i\omega(-[K_{\psi\psi}] + \omega^2[M_{\psi\psi}])^{-1}[C_{\psi u}]\hat{u}. \tag{2.50}$$

The relationship between the velocity potential ψ and the acoustic pressure in the fluid, when a time dependency of $e^{i\omega t}$ is assumed, is given as Eq. (3.220) in [40] as

$$p = -i\omega\rho_f\psi. \tag{2.51}$$

For a piezoelectric disk the electrical admittance is given as Eq. (3.214) in [40]

$$Y = i\omega[\{H_{u\phi}\}^T][D]^{-1})^{-1}\{H_{u\phi}\} - H_{\phi\phi}, \tag{2.52}$$

where [D] is expressed as Eq. (3.219) in [40]

$$[D] = i\omega[H_{uu}] - \omega^2[M_{uu}] + \omega^2[C_{u\psi}](-[K_{\psi\psi}] + \omega^2[M_{\psi\psi}])^{-1}[C_{\psi u}]. \tag{2.53}$$

TABLE 2.2: Definition of variables presented in Eq. 2.49 and reference to the equation number they are defined at in [40].

Variable	**Definition**	**Eq. number in [40]**
ω	Angular frequency	-
$[M_{uu}]$	Global mass matrix	(3.51)
$[M_{\psi\psi}]$	Global fluid mass matrix	(3.129)
$[C_{u\psi}]$	Global fluid/structure coupling matrix	(3.139)
$[C_{\psi u}]$	Global fluid/structure coupling matrix	(3.139)
$[H_{uu}]$	Global stiffness matrix[1]	(3.189)
$[H_{u\phi}]$	Global piezoelectric stiffness matrix	(3.191)
$[H_{\phi u}]$	Global piezoelectric stiffness matrix	(3.191)
$[H_{\phi\phi}]$	Global dielectric stiffness matrix	(3.192)
$[K_{\psi\psi}]$	Global fluid stiffness matrix	(3.132)
$\{\hat{Q}\}$	Global charge vector	(3.76)
$\{\hat{u}\}$	Global displacement vector	(3.47)
$\{\hat{V}\}$	Electric potential between the electrodes of the disk	(3.189)
$\{\hat{\psi}\}$	Global fluid velocity potential vector	(3.119)

The electrical admittance, Y, is used through the use of Eq. 2.34 to compare the measured impedance of the piezoelectric disks to simulation and the acoustic pressure in the fluid, p, is used in Eq. (2.48) to simulate the far-field pressure $p_4(z_{ff})$, as in [36].

Chapter 3

Experimental setup and method

In this chapter the experimental setup used for experimental measurements and the method used to obtain the experimentalism measurement results are presented. In Section 3.1 the electrical measurement setup used for acquiring the electrical impedance and the transfer function of the receiving electronics is presented and in Section 3.2 the acoustic measurement setup is presented. In Section 3.3 the equipment and cables used in both the electrical and acoustical setups are presented. The method for aligning the disks and determining the separation distance between them is presented in Section 3.4. An overview of the methods used to minimize and calculate noise in the measurement system is presented in Section 3.5. In Section 3.6 an overview of the flow charts for the measurement scripts used in data acquisition is presented. Lastly, a description of the post-process routine used for the acquired data is given in Section 3.7.

The experimental setup has been largely kept as used by [34, 36, 37] with only minor changes such as the lengths of cables 4 and 5, and the different instruments having been moved due to a renovation at the laboratory in 2017. Also, a metal rod has been installed at the roof of the acoustic cage a few cm in front of the receiving disk, cf. Fig. 3.9.

3.1 Electrical measurement setup

In this section the electrical setups used in the present work will be presented. In Section 3.1.1 the electrical setup for measuring the impedance of the piezoelectric disk, used to calculate H_{0m1}^{VV} and $H_{5open5'}^{VV}$, is presented and in Section 3.1.2 the electrical setup for measuring the receiving electronics, $H_{5'6}^{VV}$, is presented.

3.1.1 Electrical impedance measurement setup

The impedance analyser HP 4192A [67] is used for impedance measurement, cf. Fig. 3.1. As the terminals of the cables in the system model are connected to the disks through a lightly twisted pair cable the impedance is measured from the point where the cables in the system model connect with the cables soldered onto the piezoelectric disks, cf. Fig. 3.2. The impedance analyzer is calibrated for the doc connected to the input channels as instructed in [67].

3.1.2 Receiving electronics measurement setup

In order to measure the effect on the transfer function caused by the receiving electronics the acoustic part of the setup in Fig. 3.6 and Fig. 3.7 is bypassed by coupling the oscilloscope directly to the receiving electronics i.e. the amplifier and filter. The filter has a maximum input voltage of 4.4 V peak and in order to stay well within

FIGURE 3.1: Impedance analyzer measuring the impedance of a piezoelectric disk connected at the terminals of the lightly twisted pair cable.

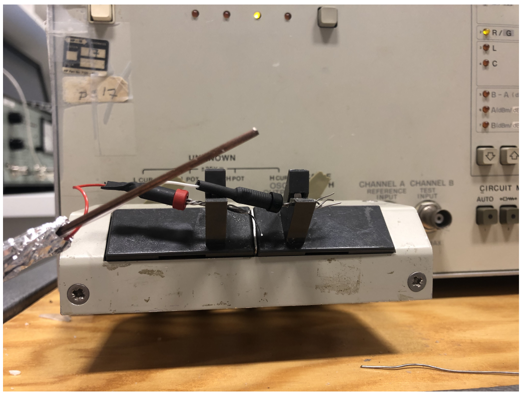

FIGURE 3.2: Close up of impedance analyzer measuring the impedance of a piezoelectric disk connected at the terminals of the lightly twisted pair cable.

this range no higher voltage than 1 V peak-to-peak was inserted to the receiver in this work.

When the signal moves through the medium between the transmitter and receiver it experiences an attenuation of about 60 dB. Since this attenuation is not present when the acoustic part of the setup is bypassed and because the signal generator has a minimum limit of 10 mV, an attenuator is introduced between the signal generator and the oscilloscope. Since the input voltage, V_{0m} is measured at the oscilloscope the effect of the attenuator is accounted for automatically when measuring the transfer function as according to Section 2.2.2. The settings of the signal generator, amplifier and filter are thus kept identical as for an acoustic measurement and the effect of them can be measured without overpowering the filter.

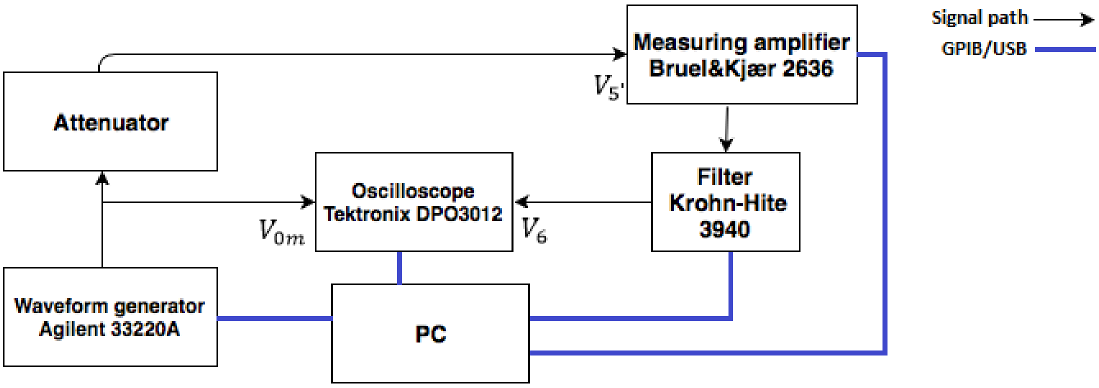

FIGURE 3.3: Illustration of the electrical setup in the laboratory.

A decade resistor is used as a voltage divider, cf. Fig. 3.4, coupled with 4.91 kΩ in parallel with 50 Ω. For an input voltage of 10 mV peak-to-peak the output voltage after the voltage divider, called an attenuator in this work, is 0.1 mV peak-to-peak. This attenuates the signal by 60 dB.

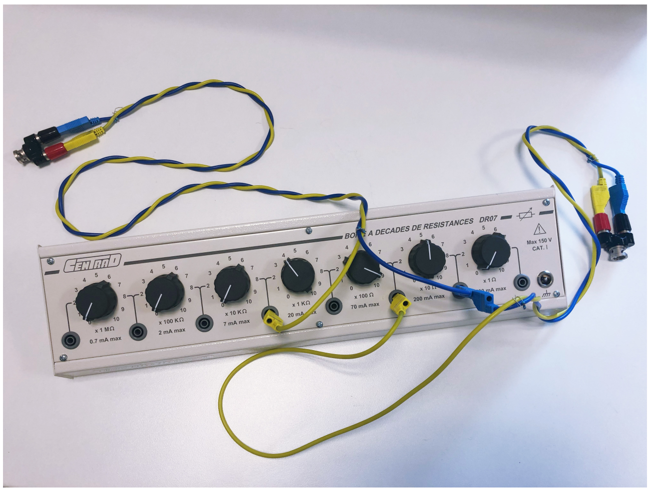

FIGURE 3.4: Attenuator/voltage divider borrowed fron another laboratory.

3.2 Acoustic measurement setup

The experimental setup consists of two piezoelectric elements mounted opposite each other in a large cage. The transmitting element, T_x, is connected to a signal generator and an oscilloscope. The receiving element, R_x, is connected to an amplifier, a filter and the terminated in the oscilloscope, see Fig. 3.5.

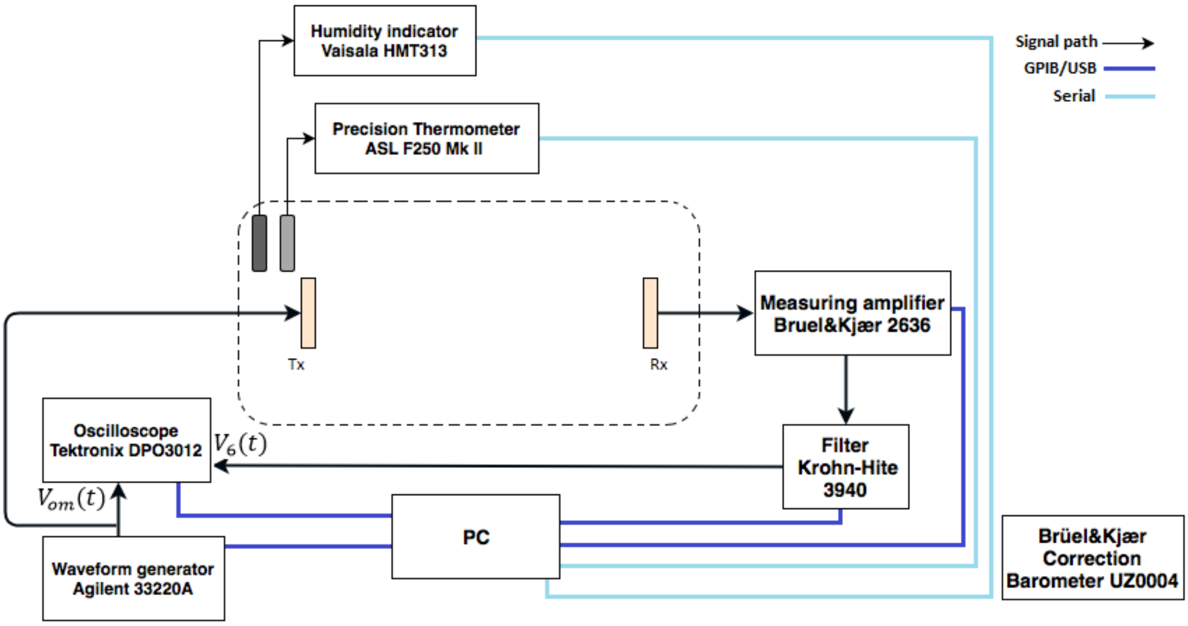

FIGURE 3.5: Illustration of the acoustical setup in the laboratory, inspired by [34].

Due to possible interference between the electronics and the high accuracy measurements the electronics were later moved into the acoustic cage for convenience and to shorten cables. These two stups are referred to as Setup I and Setup II and will be explained in detail.

The two piezoelectric disks are mounted in air on positioning stages (PI M-531.DG [58] and PI M-535.22 [59], Physik Instrumente GmbH&Co., Germany) and the transmitting disk is also connected to a rotation stage (PI M-037.PD [60], Physik Instrumente GmbH&Co., Germany). A laser is mounted on a rod allowing it to e suspended up between the two disks in order to measure aligning and accurately determine the distance, d, between the disks. The stages are then used to position the disks at a desired distance, d.
An Agilent 33220A function generator is used to generate the input signal at desired voltage over the frequency range 30-300 kHz. The signal is then monitored through a Tektronix DPO3012 digital oscilloscope before it is sent to T_x. R_x is connected to a Brüel & Kjær 2636 amplifier and a Krohn-Hite 3940A digital filter before the signal terminates in the Tektronix DPO3012 digital oscilloscope.

3.2.1 Measurement Setup I

The setup inherited by [37] was moved due to a renovation of the laboratory facilities. The setup could no longer stay as it had before the renovation moved the acoustic cage and the desk, where the electronics had previously been placed. Due to this the electronics was placed on aluminium shelves in the acoustic cage, cf. Fig. 3.6.

For Setup I the filter was set to a high pass filter with a cut-off frequency of 2 kHz and the signal generator had an input voltage of 0.1 V peak-to-peak for the frequency ranges 80-120 kHz and 240-260 kHz, respectively. For all other frequencies in the measurement range the input voltage was 10 V peak-to-peak.

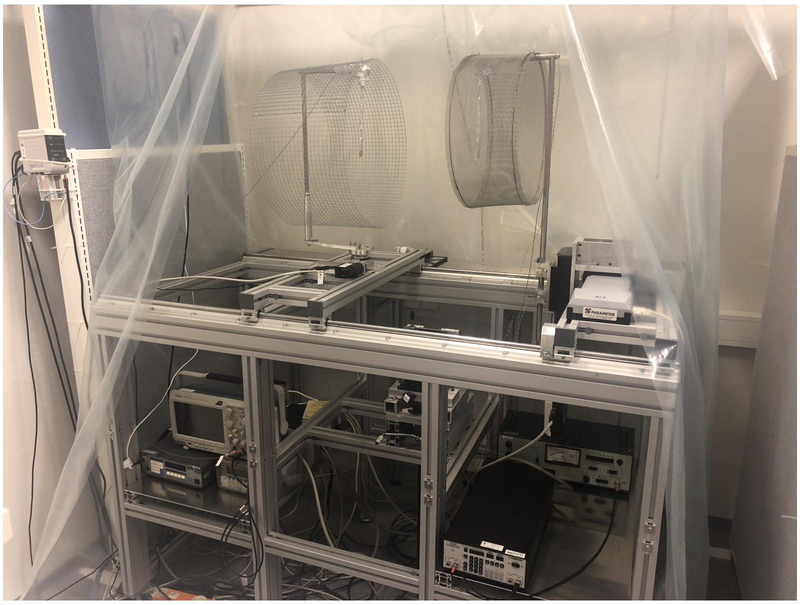

FIGURE 3.6: Experimental setup I at the acoustics laboratory, with equipment inside the cage.

3.2.2 Measurement Setup II

The equipment was in early 2019 moved away from the cage in order to reduce the impact from the equipment on the experimental measurements in form of noise, vibrations in the cage and a rise in temperature caused by the electrical equipment generating heat. The rise in temperature was especially a problem when the plastic covering the frame was left down during measurements. Therefore measurements done before the equipment was moved were conducted with the plastic not fully covering the cage, thus airflow may not have been as constant as for the later measurements done in Setup II.

After the electronics was moved from the acoustic cage, going from Setup I to Setup II, changes were also done to the filter in order to minimize the signal to noise ratio (SNR), by increasing the high pass filter setting from 2 kHz to 4 kHz. The signal generator settings were altered to an input voltage of 1 V peak-to-peak for the frequency range 90-117 kHz and 0.1 V peak-to-peak for the frequency range 240-260 kHz. For all other frequencies in the measurement range the input voltage was 10 V peak-to-peak.

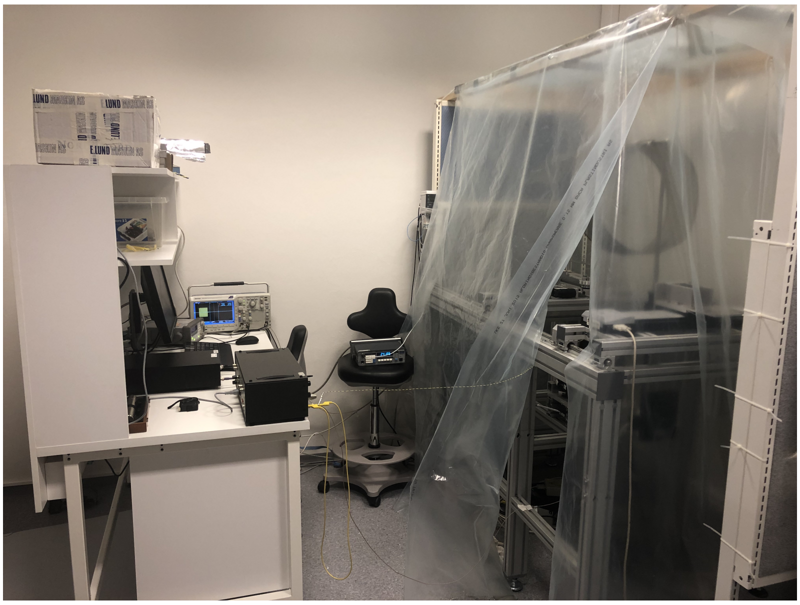

FIGURE 3.7: Experimental setup II at the acoustics laboratory, with equipment outside the cage and plastic fully covering the acoustic setup.

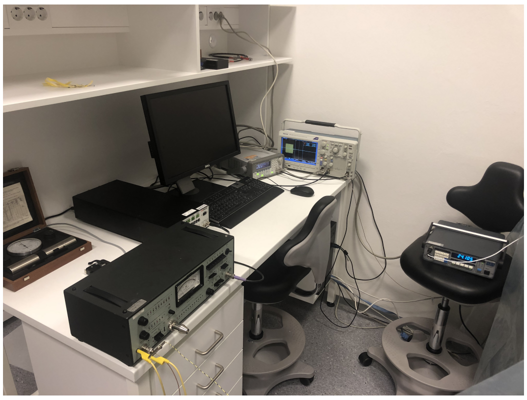

FIGURE 3.8: The electrical part of the experimental setup II.

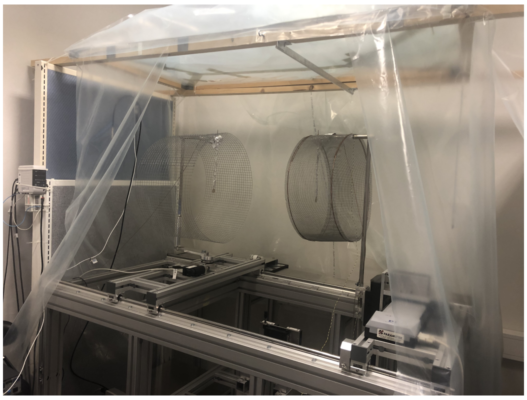

FIGURE 3.9: The acoustical part of the experimental setup II.

3.3 Equipment and cables

In this section a description of the equipment and cables used in the electrical and acoustic setup will be given. A list of all the different equipment and the cables used to connect them in the electrical and acoustical setups is presented in Table 3.1 and Table 3.3, respectively, and the piezoelectric disks used, along with their dimensions, is listed in Table 3.2.

Equipment	Spesification	GPIB adress	Serial number
Signal generator	Agilent 33220A [61]	10	MY44023589
Oscilloscope	Tektronix DPO3012 [62]	USBO	195539
Amplifier	Brüel & Kjær 2636 [63]		1615638
Filter	Krohn-Hite 3940 [64]	21	AM2626
Thermometer	ASL-F250 [65]	3	1365026993
Hygdrometer	Vaisala HMT313 [66]	4	F4850018
Barometer	Brüel & Kjær UZ0004	–	1918465
Impedance Analyzer	HP 4192A [67]	17	23423

TABLE 3.1: List of equipment used in the electrical and acoustical experimental setup and their corresponding GPIB address.

3.3.1 Signal generator

A signal generator, of type Agilent 33220A [61], is used to generate a sinusoidal electric burst of a predetermined voltage. In the current work the voltages used are 10 V, 1 V, 0.1 V and 0.01 V peak-to-peak and it is stated in the results when which voltage is used.

The generated signal is transmitted to T_x and to an oscilloscope using coaxial cables, of type RG-178 B/U and RG-58, with a characteristic impedance of 50 Ω. The output channel of the signal generator has an output impedance of ? Ω, but the parallel capacitance is not given by manufacturer.

Burst length is determined by 0.8 * propagation time, where propagation time is given as d/c. The distances used in the current work are d = 50 cm, d = 30 cm, d = 20 cm and d = 15 cm and the sound speed, c, is found using Cramers method, described in Chapter 2.

3.3.2 Oscilloscope

An oscilloscope, of type Tektronix DPO3012 [62], is used to measure the generated signal from the signal generator that is being sent to T_x, and the received signal from the filter. The acquisition is triggered by the trigger on the waveform generator and the oscilloscope works as a digitizer for the analogue signals V_{om}, generated by the signal generator, and V_6, received from the filter.

The oscilloscope has an input impedance of 1 M Ω in parallel with 11.5 pF. The signal bursts that are recorded are averaged over 128 bursts in order to reduce random noise in the system.

3.3.3 Amplifier

A voltage amplifier, of type Brüel & Kjær 2636 [63], is used to amplify the received signal from R_x by 60 dB. R_x is connected to the amplifier through a RG-178 B/U coaxial cable with a characteristic impedance of 50 Ω and is connected to the input of the amplifier, which has an input impedance of 1 MΩ parallel with 90 pF.

Experimental values for the input impedance of the amplifier were found in [34] and [36] and are used in the present work. The values found in [34] and [36] for the input of the amplifier is within the uncertainties given by manufacturer for the amplifier. The values are presented in Table 3.2.

TABLE 3.2: List of input impedance of the amplifier, both experimental values and data sheet values given by manufacturer.

Variable	**Manufacture value**	**Experimental value [34] and [36]**
Amplifier input resistance, R	1 MΩ	0.95 MΩ
Amplifier input capacitance, C	90 pF	96 pF

The amplifier has a maximum amplification of 100 dB in 10 dB ± 0.05 dB steps. In the current work an amplification of 40 dB is used on the input and another 20 dB on the output, resulting in a total amplification of 60 dB.

Between the input and output of the amplifier there are connections for an external filter. In the current work this is not used, since it is deemed beneficial to amplify the signal before filtering, so as to best filer out more noise. However this method is more likely to clip the signal since all the amplification is performed before filtering. The noise is also amplified along with the signal before filtering so a high enough high pass filter setting in desired, and this has been monitored in the current work in order to avoid filtering that filters away the signal along with the noise.

3.3.4 Filter

The filter used in the current set-up is a Krohn-Hite 3940 filter which is connected from the front output of the amplifier to the front input CH1 on the filter. The output from CH2 on the filter is terminated in CH2 on the oscilloscope. In [37] and the present work the filter was used as a static high pass filter of type Butterworth with a cut-off frequency $f_c = 4\ kHz$.

It is important to notice that the filter has a max input voltage of 4.4 V peak. In the current work a voltage of no higher than 1 V peak-to-peak, corresponding to 0.5 V peak, has been used in the present work.

3.3.5 Impedance analyzer

An impedance analyzer, HP 4192A [67], is used to measure the impedance of the piezoelectric disks used in the experimental setup. The impedance analyser is turned on for 1 hour before any measurements are performed in order for the instrument to warm up and a zero offset adjustment is performed to account for the effect of the docking station used to connect the terminals of the piezoelectric disk to the impedance analyzer. The measurements are done using 1 V RMS.

The impedance analyzer is connected to the PC via a GPIB-to-USB adaptor and the script used for acquiring data from the impedance analyzer is rechecks the settings before every data acquisition, as a safety assurance for errors or malfunctions in the analyzer. This increases the total runtime of the program, but since the total runtime is less than half an hour this is kept as programmed by [37].

3.3.6 Piezoelectric elements

The piezoelectric disks used in the current work are disks number 7 and 13, cf. [36]. In order to not disturb the soldering on the disk or the disk themselves as little as possible, the measurements of the thickness and diameter of the disks performed in [36] is used in the current work and are listen in Table 3.3. The disks are handled with care and only touched very gently with clean hands when necessary for alignment correction. Since it is indicated that reciprocity holds only for identical transducers [68], and the simulations which the measurements are compared to assumes spherical reciprocity, it is important that the disks are as equal and uniform as possible. They are therefore from the same batch purchased from Meggit Ferroperm [69] and only the disks that were the most similar were chosen by Andersen [36].

TABLE 3.3: List of piezoelectric disks used in the experimental set-up and their dimensions.

Disk number	**Diameter, D, [mm]**	**Thickness, T, [mm]**
7	20.20±0.05	2.0410±0.0010 [36]
13	20.24±0.04	2.0288±0.0008 [36]

3.3.7 Cables

There are five cables used in the experimental setup listed in Table 3.4. The last two are included in the measurement of the transfer function $H_{5'6}^{VV}$ and they are measured experimentally. The effect from cables 1, 2 and 3 are calculated using the transmission line model from Section 2.5. The specifications for the cables are listed in Table 3.5.

3.3.8 Motorized stages

Three motorized stages from Physik Instrumente are included in the experimental set-up in order to place the discs at desired distance and with desired accuracy of

TABLE 3.4: List of cables used in the experimental setup and their specifications.

Cable	From/To	Length [m]	Cable type
1	Waveform generator/transmitting disk	2.970	RG-178 B/U
2	Waveform generator/oscilloscope	0.304	RG-58
3	Receiving disk/amplifier	2.975	RG-178 B/U
4	Amplifier/filter	0.475	RG-58
5	Filter/oscilloscope	1.470	RG-58

TABLE 3.5: Spesifications for coaxial cables.

Cable type	Impedance, Z	Inductance, L	Capacitance, C
RG-58	50 Ω	250 [nH/m]	100 [pF/m]
RG-178 B/U	$50 \pm 2\ \Omega$	–	93 [pF/m] (at 1 kHz)

alignment. Two of the stages are connected to the transmitting disk, T_x. One rotational stage to move the disk in y-direction and one translational stage to move the disk in z-direction. The last stage is connected to the receiving disk, R_x, and allows it to be moved in x-direction. These are high accuracy stages and they have an 0.1μm incremental motion and a 1μm full-travel accuracy. So the uncertainty related to the stages will be no more than 1μm. There is also an uncertainty caused by the laser, which can be from -6 to +10 μm.

TABLE 3.6: List of equipment used in the experimental setup and their corresponding GPIB adress.

Positioning stage	Spesification	Serial number
Linear position stage (x-axis)	PI M-535.22 [59]	109040312
Linear position stage (y-axis)	PI M-531.DG [58]	–
Linear position stage (z-axis)	PI miCos LS270 [70]	414000926
Rotation stage	PI M-037.PD [60]	109040312
2 axea Motion Controller	SMC Hydra TT [70]	1404-0153
Motion Controller Card	PI MS77E-C-84341 [71]	0095103296

The software PIMicroMove is used to control the stages from the PC. When a connection is made in the software with the stages they need to be adjusted to a reference distance for the program to know their position to a high accuracy. Since the stages may have different target references for this position calibration, each stage with its respective target reference is listed in Table 3.7. When moving the stages in PIMicroMove a left and right option is available for each stage and the direction this represents for each stage is also listed in Table 3.7.

TABLE 3.7: List of motorized stages in the experimental setup, their respective target reference and movement direction.

Stage name in PI MicroMove	Target reference	Left/right
1 Hydra/Pullox [70]	pos.limit	forwards/backwards
1 PDM-037 [60]	on target	angle, clockwise/counter clockwise
2 DG.M-531 [58]	ref.switch	right/left
3 M-535.22 [59]	pos.limit	up/down

3.3.9 Laser

In order to accurately determine the separation distance between the transmitter and receive pair in the experimental setup a pair of lasers were installed by [36]. The lasers are mounted on a rod which allows them to be lowered down during measurements. A controller with display is connected to the lasers and a computer software, LK-Navigator, is installed in order to acquire distance values from the lasers. The equipment is listed in Table 3.8 and a schematic of how the lasers are mounted, by [36], is presented in Fig. 3.10. The transmitting and receiving disks are moved into the measuring range of the lasers, alignment is adjusted for and then the lasers are placed in the center of both disks so that the relative distance the transmitter needs to be moved can be calculated from the current position of the disks.

TABLE 3.8: List of equipment used in the experimental setup and their corresponding GPIB adress.

Laser sensor	Spesification	Serial number
Sensor head	KEYENCE LK-G32 [72]	2041141
Sensor head	KEYENCE LK-G32 [72]	2041143
Controller with display	KEYENCE LK-G3001PV [72]	1741187
Computer Software LK-Navigator	KEYENCE LK-H1W [72]	–

FIGURE 3.10: Laser schematics, cf. [36].

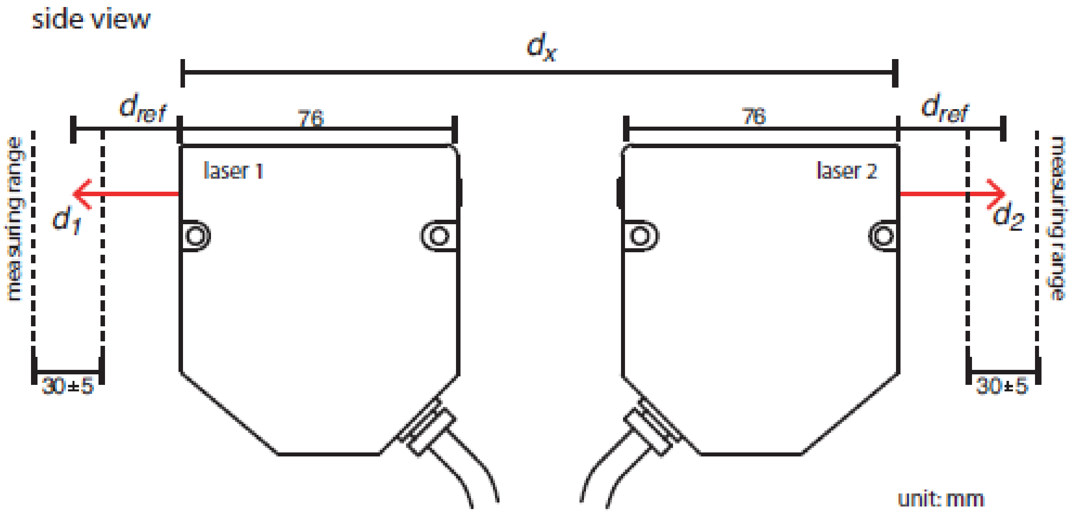

3.4 Positioning of the discs

In order to get a good transmit-receiver measurement it is necessary for the disks to be aligned with each other and that the separation distance between them is highly accurate. The disks are aligned when the transmitter and the receiver are mounted flush in the xy-plane, as shown in Figure 3.11. This is done using a high precision Keyence laser, installed by [36] and high precision translation stages from Physik Instrumente, cf. [73]. The separation distance between the disks is measured from the center of the front of one disk to the center of the front of the other disk, cf. Fig. 2.1.

The disks are polarized and the polarization direction is marked by a small dot on the positive side, called the front of the disk, so that the polarization direction goes from the front of the disk to the back of the disk. When the disks were soldered onto the partially twisted pair cables in the laboratory, precautions were made to not change the polarization or the material characteristics of the disk. However, some altercations are observed in the material constants of the disks. This is explained in depth in [36].

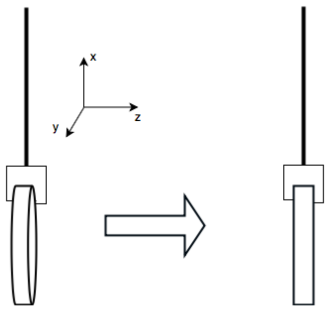

FIGURE 3.11: Aligning of a piezoelectric disc.

3.4.1 Horizontal and lateral alignment

Firstly the disks are placed facing each other, the dots marking the polarization are placed towards the other disk, to avoid a 180° shift in phase and an x marking the center of each disk is used to place the disks in lateral and horizontal alignment with each other. The laser is then used to check alignment at the edges of the disks in x- and y-direction by moving the laser to the farthest positive and farthest negative value of both x and y, checking that the disks "disappear from the laser sensor at the same location. This process is repeated after rotational alignment is achieved to avoid error caused by rotational misalignment.

3.4.2 Rotational alignment

When the disks are both centred on the z-axis and aligned vertically and horizontally, the rotational alignment is investigated. For rotation about the y-axis this is done by moving the laser to the top and the bottom of T_x, noting the distance from the laser to the disk in both positions and subtracting them to find the difference. This is referred to as uncertainty in the alignment caused by rotation about the y-axis. If alignment is not satisfactory the disk is moved by a light touch at the bottom of the disk, continuously monitoring the position on the laser display until the desired deviation about the y-axis is acquired. This procedure is then repeated for R_x.

For rotation about the x-axis the laser is placed on one of the furthest horizontal sides of the disk. The uncertainty in alignment is found by measuring at the two horizontal sides of the disk and subtracting the two distances to find the difference. For T_x corrections are now made by using the rotation stage mentioned in Section 3.1.5. For R_x a light touch or a screw at the top of the mounting rod allows for the rod and the disk to be rotated and is used to correct its positioning.

The process is repeated several times, to check that corrections in one direction did not affect the deviation or uncertainty in alignment in another direction, until satisfactory alignment is achieved.

3.4.3 Separation distance

The separation distance, d, measured from the center of the front of T_x to the center of the front of R_x is presented by [36] as

$$d = d_{rel} + d_{xe} + d_1 + d_2, \tag{3.1}$$

with an associated combined standard uncertainty given as

$$uc(d) = \sqrt{u^2(d_{rel}) + u^2(d_{xe}) + u^2(d_1) + u^2(d_2)}. \tag{3.2}$$

The distance d_{rel} is the relative distance the translation stage needs to move in order to position the disks at a separation distance d form each other, given as

$$d_{rel} = d - d_{xe} - d_1 - d_2, \tag{3.3}$$

All the distances in Eq. (3.1), (3.2) and (3.3) are listed in Table 3.4 and illustrated in Fig. 3.10.

TABLE 3.9: List of values used for calculating separation distance d.

	Value	Description
d_{ref} [cm]	30	
d_1 [cm]	acquired from laser after alignment	Distance from front of laser to front of T_x disk.
d_2 [cm]	acquired from laser after alignment	Distance from front of laser to front of R_x disk.
d_x [cm]	182.5692	Distance between the two laser fronts
α_{Al}	22.5·10−6	Thermal expansion coefficient for aluminium
T_{cal} [°C]	≈ 24	Calibrated temperature measurement
T_{lab} [°C]	acquired from thermometer	Measured temperature in the lab at start of measurement

A positioning stage in z-direction is used to position the front of the transmitting disk at the separation distance $z = d$ and the front face of the receiver is placed at $z = 0$.

3.4.4 Uncertainty in transducer separation distance

The combined standard uncertainty for the separation distance, d, as claimed in Section 7.1.1 in [36], is 10 μm at a coverage factor k = 1.

(50.0000 ± 0.0040) cm This is then the uncertainty at the center of the disks. It is also nessecary to keep in mind the uncertainty in alignment. The uncertainty in the separation distance of an arbitrary point on the disks will then be the total uncertainty of the separation distance d, combined with the alignment uncertainty.

3.5 Noise

In previous work the white noise has been reduced by averaging the measured signals over 128 bursts [33–37]. The coherent electrical noise caused by the transducers in the experimental setup being unshielded piezoelectric disks has been reduced by the use of Faraday cages [34, 36, 37] and the grounding of them [34, 36]. Shielding of the cables soldered onto the disks and leading up to the coaxial cables was introduced in [37] to further reduce the coherent electrical noise. Since the recorded signal contains both the acoustic and the electrical signal a method was developed in [37] to record the coherent electrical noise in order to later subtract it from the recorded signal without affecting the acoustic signal.

3.5.1 Ground

In an experimental measurement setup there can be noise present due to the system having multiple grounds or earths. The electrical instruments in the setup are grounded to earth through earth in the power cable. However, the transmitter and receiver works as antennas for electrical current, since they are unshielded, and subsequently has a different ground from the sending and receiving electronics, which are all connected to the same ground; earth. To remedy this the Faraday cage of the receiving disk is grounded to the input of the amplifier rendering the entire setup to have the same electrical voltage potential for the entire measurement system. The receiving disk is in contact with the Faraday cage at the banana plug connection through a small metal piece touching both the cable from the transmitting disk and the shielding around the cable which is in firm contact with the Faraday cage.

3.5.2 Coherent noise

Coherent electrical noise can be removed by measuring the coherent noise when there is no acoustic signal present and subtracting the recorded coherent noise from the total acoustic measurement where both the acoustic signal and the coherent electrical noise is present. This method was done by [36] [p.88 section 6.3.2] using an acrylic plate of approximately 2-5 mm thickness and by [37] using a POM plate. The method used by the latter has been used and improved upon in the current work. In order to isolate the coherent electrical noise the plate is mounted between the transmitter and the receiver during an acoustic measurement. Thereby no acoustic signal should be recorded and the resulted measured signal is only the coherent electrical signal.

An approximately 86 x 90 cm Polyoksymethylen (POM) plate is paced between the two piezoelectric discs during the noise measurement to block out the acoustic signal and thereby recording the electromagnetic signal which we can then subtract from the acoustic measurements done directly before or after the noise measurement. This method was developed by [37], but a similar approach was used by [36] utilizing a 2-5 mm plexyglass plate, and has been documented and further developed by the current author. The plate was purchased by the in house work shop from Astrup.

The POM plate has a high density compared to air it works as a wall for the acoustic signal, but the thickness of it makes in ivisible to the electrical signal, which has a much higher wavelength. By placing the screen between T_x and R_x during an acoustic measurement only the coherent electrical noise, created by the transmitter, is recorded and can later be subtracted from an acoustical measurement.

Since this noise measurement is highly dependent on the environmental parameters, such as temperature, pressure and humidity, a noise measurement is done as close to an acoustic measurement as possible. It is also highly dependent on the separation distance, d, between the disks, so if the disks are moved closer or further apart a new noise measurement is needed for the corresponding acoustic measurement.

3.5.3 Signal to noise ratio, SNR

The signal to noise ratio (SNR) is defined as the ratio between the measured signal and the measured noise, and is defined in Eq. (6.36) [74] as

$$SNR = 20\log_{10}\left(\frac{V_{rms}^{rec}}{V_{rms}^{noise}}\right), \tag{3.4}$$

where

$$V_{rms}^{noise} = \sqrt{\frac{1}{N}\sum_{i=1}^{N}(V_i - \bar{V})^2} \tag{3.5}$$

is RMS value of the recorded noise signal and

$$V_{rms}^{rec} = \frac{V_{rec}^{pp}}{2\sqrt{2}} \tag{3.6}$$

is the RMS value of the recorded signal. The SNR is important as it speaks to the strength of the signal compared to the noise present in the measurement system.

3.6 Data acquisition, pylabctrl

All the scripts for data acquisition were written in Python by [37] and has been modified by current author, cf. Appendix A. They consist of a script for each instrument used at the lab, four scripts for the different type of measurements you want to perform and spec scripts that communicate between these. See figure 3.12. There is also a pycache folder created by Python in each of the folders in pylabctrl and these are generated by Python and should be left as they are. Changes are to be done in the scripts directly.

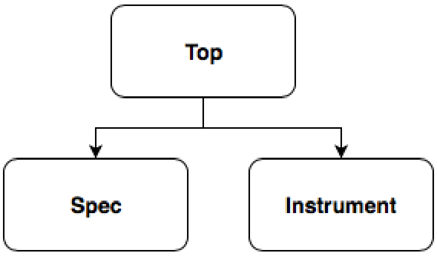

FIGURE 3.12: The general flow chart of a pylabctrl measurement program.

Each of the scripts are run directly from the terminal by changing the directory to the folder where the scripts are stored using the cd-command and then run directly in the terminal using python. The command "python acoustic.py" is written directly in the terminal when the acoustic measurement is run and equivalently for the noise, impedance or receiver measurements.

3.6.1 Acoustic measurements

The script acoustic.py measures the output voltage from the signal generator as it is recorded by the oscilloscope at Channel 1, and the received voltage coming from the filter as it is terminated in the oscilloscope at Channel 2. In order to minimize the time an acoustic measurement takes the temperature acquisition is reduced to every 5 seconds in stead of one acquisition for every frequency measurement. The temperature measurements therefore need to be interpolated in the post-processing routine.

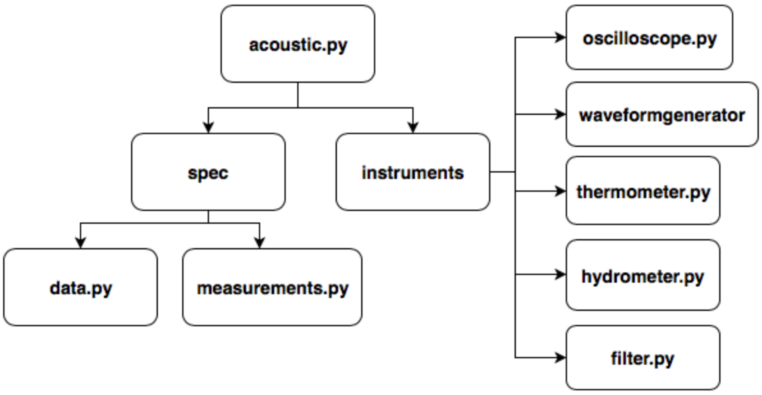

FIGURE 3.13: The general flow chart of an acoustic measurement.

The script acoustic.py has been modified from [37] to include the option of a gliding band pass filter, but it was not deemed necessary as the settings described in 3.3.4 yielded good result. It is however kept in for possible future use and as an example of how to implement equipment to the Python measurement scripts.

Parameters needed for an acoustic measurement are the separation distance, d, and the current humidity at the lab, acquired manually by a barometer. These should always be checked before an acoustic measurement is done.

3.6.2 Noise measurements

The script noise.py measures the coherent electrical noise when the POM screen is placed between T_x and R_x, in order to block any acoustical signal. As stated in [37] electrical signal has a much faster propagation time compared to acoustic signals, so propagation time is not applied and reflections are not compensated for because any reflections would also be present in the full acoustic measurement, so the removal of them by recording them in the noise measurement will only improve the final post-processed signal. Acoustic measurements should always have an accompanying noise measurement performed on the same day and at the same separation distance since both the environment and the separation distance influence the recorded electrical noise and therefore should be as identical as for the acoustic measurement as possible.

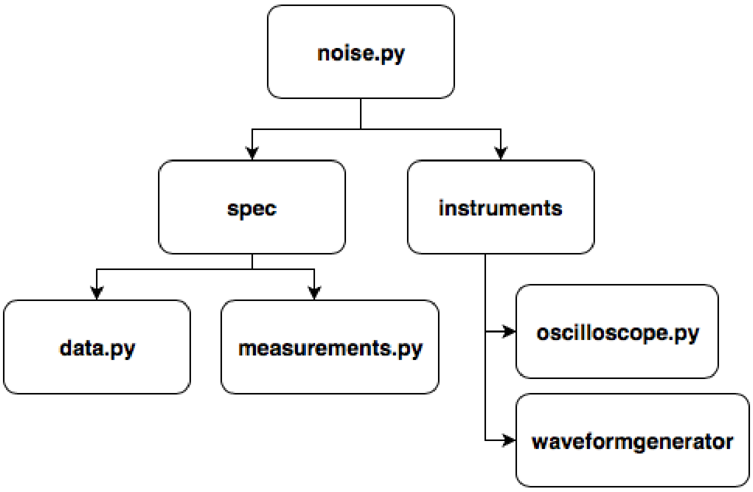

FIGURE 3.14: The general flow chart of a noise measurement.

3.6.3 Admittance measurements

The script admittance.py measures the impedance measured by the impedance analyser over a given frequency specified and easily changeable in the script. The impedance analyser is calibrated according to Figure 3-30 in [67] and connected to the PC using a GPIB connection.

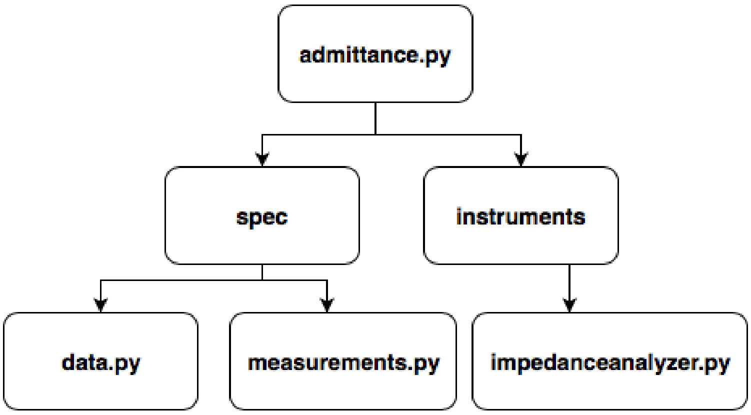

FIGURE 3.15: The general flow chart of an admittance measurement.

3.6.4 Receiver measurements

The script receiver.py measures effect of the receiving electrical signal in the measurement setup. Because the filter has a maximum input voltage of 4.4 V peak an attenuator with an attenuation factor of 60 dB is introduced when measuring the receiving electronics, as explained in Section 3.1.2.

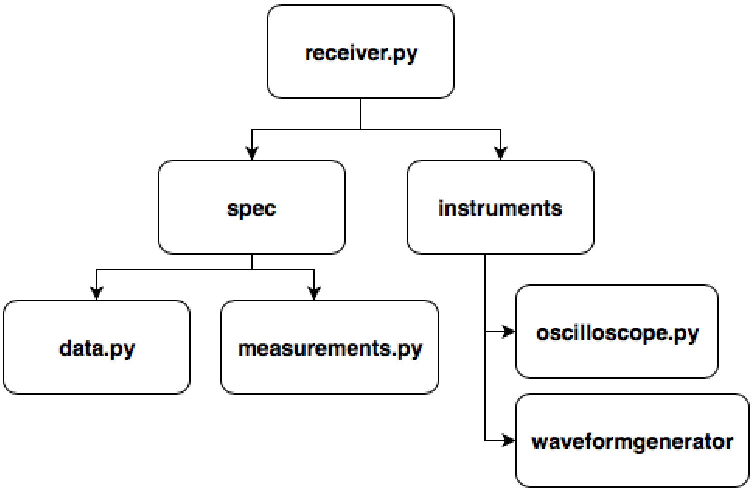

FIGURE 3.16: The general flow chart of a receiver measurement.

3.7 Post-processing

The signal waveforms, $V_{0m}(t)$ and $V_6(t)$, recorded at the oscilloscope are presented in Appendix D for various frequencies at different distances. When post-processing the measured data the waveforms are first applied a Fast Fourier Transform-window (FFT-window) and then a Discrete Fourier Transform (DFT) is performed before they are divided to obtain the measured voltage-to-voltage transfer function, $H_{0m6}VV$, cf. Section 2.2.2. In order to avoid spectral leakage and apply the window at the desired steady-state part of the signal several steps are required.

3.7.1 FFT-window

In order to obtain a steady-state part of the signal the upper and lower bounds of the FFT-window have to be carefully chosen. The lower bound of the FFT-window is placed at the estimated time-of-arrival for the plane wave component of the propagating wave yielding a propagation time given as

$$p_t = d/c, \tag{3.7}$$

where d is the separation distance between the center of the two disks and c is the speed of sound calculated according to Section 2.7. By placing the windows lower bound here the phase of the plane wave is not included in the FFT-window and only the slowly varying phase remains, cf. Fig. 3.17.

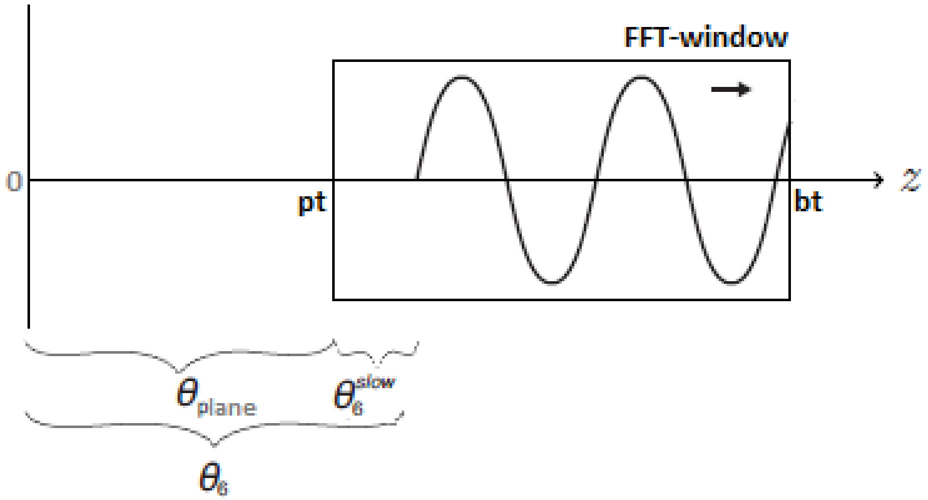

FIGURE 3.17: Illustration of a received waveform signal travelling from left to right in a FFT-window with the total phase, θ_6, plane wave phase, $/theta_{plane}$, and the slowly varying phase, $/theta_6^{slow}$ indicated.

The upper bound of the FFT-window is given as the burst length of the signal. The burst length is chosen so that it does not include unwanted signals, such as ringing or delays from the prior burst, but still contain as large amount of the given signal as possible. The burst length is chosen as

$$b_t = 0.8 \cdot p_t = 0.8 \cdot d/c. \tag{3.8}$$

3.7.2 Discrete Fourier transform

When adding a window to a signal spectral leakage can be caused by the signal not being cut at a zero value may occur. In order to avoid this the window needs to contain a whole number of periods of the signal [75]. This is done by cutting the signal to an integer number of periods and reduces spectral leakage at the cost of some frequency resolution. Firstly, in order to obtain an integer number of periods, an integer number of periods is transmitted. Secondly, the received signal is cut in both ends so that it starts and ends in points crossing zero, cf. Appendix B.3.5.

For the DFT a MATLAB [76] Goertzel algorithm is used, which has default Fourier "bins" or frequency intervals with a center frequency given as

$$f_c = k\frac{f_s}{N}, \tag{3.9}$$

where k is the bin number, f_s is the signal sampling frequency and N is the signal sampling length.

As adding zeroes to the end of a signal does not affect the DFT, zeroes are added to change the center frequency of the bin to the frequency of the signal, cf. Appendix B.3.6, before the signal is Fourier transformed.

Lastly the transfer function of the measured system is found by dividing the two Fourier transformed waveforms.

Chapter 4

FE simulation

Simulations are an important part in the present work and finite element simulations are used to model the transmit-receive pair. A brief overview of the software tool will be presented in Section 4.1. In Section 4.2 the two sets of material parameters investigated in the current work are presented. In Section 4.3 the simulation parameters of three different simulations performed in the current work are presented.

4.1 FEMP 5.3

A finite element software tool for piezoelectric transducers (FEMP) was developed by [40] in cooperation with UiB and CMR and has since been further developed by researchers and students at CMR and UiB. In the current work FEMP 5.3 written for MATLAB [76] is used to simulate the transmit-receive pair without the transmitting or receiving electronics.

Three different files are needed to run a simulations; an input file, a structure file and a material data file. The input file definers the simulation parameters for the simulation and ends with a **.inn** extension. The structure files defines the input parameters, areas, points and boundary conditions for a transducer structure being simulated and can be modified in **read_inn_project.m** and **init_const project.m**. Lastly, the material parameter file defines the material parameters of the piezoceramic disks, the medium and any front or backing layer used in the simulation and ends in an **.mat** extension.

The simulation problems in FEMP are defined in the *rz*-plane, where *r* is in the direction of the radius of the piezoelectric disk and *z* is along the acoustic axis. As computational time is dependent on the size and complexity of the problem symmetry along the acoustic axis is assumed along with spherical reciprocity for the transmitting and receiving disk, allowing for only the transmitter to be simulated. This reduces the 3-D solution to a 2-D problem with only one transducer needing to be simulated.

As finite element methods depend on dividing the problem into finite elements the simulation problem is divided into two domains. The first domain is a region of finite elements consisting of the piezoelectric disk and the fluid loading, which is solved using 8 node isoparametric elements. The second domain is a region of infinite elements, which are solved using $12th$ order conjugate Astley-Leis infinite elements.

4.2 Material parameters

For the simulations to be comparable to measurements it is important that the material data which are used in simulations are accurate to the material constants that are measured in the experimental measurements. For a piezoelectric element the mechanical terms of the material constants are denoted c^E and make up the elasticity matrix, Fig. 4.1, the coupling terms, e, are collected in the coupling matrix, Fig. 4.2 and lastly the dielectric terms are collected in the relative permittivity matrix, Fig. 4.3.

$$\begin{pmatrix} c_{11}^E & c_{12}^E & c_{13}^E & 0 & 0 & 0 \\ c_{12}^E & c_{11}^E & c_{13}^E & 0 & 0 & 0 \\ c_{13}^E & c_{13}^E & c_{33}^E & 0 & 0 & 0 \\ 0 & 0 & 0 & c_{44}^E & 0 & 0 \\ 0 & 0 & 0 & 0 & c_{44}^E & 0 \\ 0 & 0 & 0 & 0 & 0 & c_{66}^E \end{pmatrix}$$

FIGURE 4.1: Elasticity matrix.

$$\begin{pmatrix} 0 & 0 & e_{31} \\ 0 & 0 & e_{31} \\ 0 & 0 & e_{33} \\ 0 & e_{15} & 0 \\ e_{15} & 0 & 0 \\ 0 & 0 & 0 \end{pmatrix}$$

FIGURE 4.2: Coupling matrix.

$$\begin{pmatrix} \epsilon_{11}^S/\epsilon_0 & 0 & 0 \\ 0 & \epsilon_{11}^S/\epsilon_0 & 0 \\ 0 & 0 & \epsilon_{33}^S/\epsilon_0 \end{pmatrix}$$

FIGURE 4.3: Relative permittivity matrix.

The disks used in the current work were purchased from Meggit Ferroperm A/S and a list of material characteristics were provided. It was found that the provided material constants were not sufficiently accurate and adjustments were needed. This is described in [77], page 78, but will be briefly repeated for contiunity. A new set of material constants was calculated for a circular Pz27 disk with D/T (20 x 1 mm) = 20 by Lohne [78] in 2005 and later modified by Knappskog for disks with D/T (20 x 2) = 10. They both used methods described by Sherrit [79, 80] and the sensitivity analysis provided in [81] to adjust the electrical measurements of the disks in air. The material data was further adjusted by Aanes in 2014 for the specific disks used in [77]. All three sets of material data are presented in Table 4.1.

4.3 Simulation parameters

The simulation parameters used in the FE simulation are of high interest. The number of elements, N_λ, and the total number of finite and infinite elements in the simulation, f_{mesh}, will increase the accuracy, in terms of resolution, of the simulation if one or both is increased. However, this can greatly affect the computation time of the problem. The accuracy of the simulation can also be improved by increasing the domain of the infinite elements, R_{inf}, but this will not influence the resolution of the simulation since the number of infinite elements will increase correspondingly.

TABLE 4.1: List of material data used in the simulations.

Material constant	**Ferroperm**	**Lohne/ Knappskog**	**Lohne/ Knappskog/Aanes**
c_{11}^E $[10^{10}N/m^2]$	14.7	11.875(1+i/95.75)	12.025(1+i/96)
c_{12}^E $[10^{10}N/m^2]$	140.5	7.430(1+i/71.24)	7.62(1+i/70)
c_{13}^E $[10^{10}N/m^2]$	9.37	7.425(1+i/120.19)	7.42(1+i/120)
c_{33}^E $[10^{10}N/m^2]$	11.3	11.205(1+i/177.99)	11.005(1+i/190)
c_{44}^E $[10^{10}N/m^2]$	2.3	2.110(1+i/75)	2.11(1+i/75)
c_{66}^E $[10^{10}N/m^2]$	—	2.22250(1+i/225.342)	2.16(1+i/315)
e_{31} $[C/m^2]$	-3.09	-5.4(1-i/166)	-5.4(1-i/166)
e_{33} $[C/m^2]$	16.0	16.0389(1-i/323.77)	17.0(1-i/324)
e_{15} $[C/m^2]$	11.64	11.20(1-i/200)	11.20(1-i/200)
ϵ_{11}^S $[C/m^2]$	10.005	8.110436208(1-i/50)	8.11044(1-i/50)
ϵ_{33}^S $[C/m^2]$	8.0927	8.14585296(1-i/86.28)	8.14585(1-i/130)
ρ $[kg/m^3]$	7700	7700	7700

In previous work there has been different simulation parameters used and in order to compare prior simulations to the simulations in the present work, an investigation into the effect of these parameters is done. The parameters investigated are in particular two different sets of material data and the effect of small changes in the radius and thickness of the piezoelectric disks. Three different simulations are performed in order to investigate these effect of different parameters on the simulated transfer function, cf. Table 4.2.

In the present work the simulated far-field axial pressure, $p_{ff} = p_4(z_{ff})$ is calculated at a distance z_{ff} = 1000m. This particular distance has been used in [2], and results in [38] showed that this was sufficiently in the far-field and does not introduce significant numerical errors due to the large distance. It was shown that there is a $1/z$ behaviour for the magnitude, and that the slowly varying phase tends to a constant value.

TABLE 4.2: List of parameters used in the different simulations.

Parameter	**Simulation I**	**Simulation II**	**Simulation III**
Material data	Lohne/ Knappskog	Lohne/ Knappskog/Aanes	Lohne/ Knappskog/Aanes
Disk radius, r [mm]	10.10	10.01	10
Disk thickness, T [mm]	2.041	2.041	2
Far-field distance $z_{ff}[m]$	1000	1000	1000
Frequency range [Hz]	$1\text{-}300{\cdot}10^3$	$0\text{-}300{\cdot}10^3$	$(1\text{-}300){\cdot}10^3$
Medium density (air), ρ $[kg/m^3]$	1.205	1.205	1.18817
No. of elements per wavelength, N_λ	7	7	10
R_{inf}	$30{\cdot}10^{-3}$	$30{\cdot}10^{-3}$	$30{\cdot}10^{-3}$
Order of infinite elements	12	12	12

Apart from Section 5.7, where the three simulations are compared, only Simulation I is used. This means that for all comparisons between measurements and simulations in the current work it is Simulation I that is used.

Chapter 5

Results

In this chapter results obtained from measurements and simulations are presented. In Section 5.1 the measured electrical impedance of the disks are presented and compared to simulation. In Section 5.3 the corrections performed on the experimental measurements in order to compare them to simulations are presented. This includes the transmitting electronics transfer function, H_{0m1}^{VV}, the open circuit transfer function, H_{5open5}^{VV}, the measured receiving electronics transfer function, H_{56}^{VV}, attenuation and diffraction effects as well as corrections done to the temperature measurements acquired during an acoustic measurement. In Section 5.4 the effect of different input voltage in the acoustical measurements is investigated. In Section 5.5 the effect of accuracy in the alignment of the piezoelectric disks is investigated. In Section 5.6 results from the present work is compared to prior work. In Section 5.7 the effect of different parameters in the simulations are investigated. In Section 5.8 measurements compared with simulations are presented for four different distances; $d = 50$ cm, $d = 30$ cm, $d = 20$ cm and $d = 15$ cm. In Section 5.9 plots devoted to the investigation of the dip found at R_1 are presented. Lastly, in Section 5.10 the uncertainties in the measurements are presented.

5.1 Electrical impedance measurements and simulations

In this section the results of the electrical impedance measurements are presented. The measured impedance for the disks used in the present work are presented and compared to simulations. The experimental impedance measurements are used for calculating the transmitting electronics transfer function, H_{0m1}^{VV} and the open circuit transfer function, H_{5open5}^{VV}, as described in Section 2.5.1. The simulated impedance is used for calculating the simulated transfer function H_{15open}^{VV}, as described in Section 2.11.

In Fig. 5.1 the measured impedances of the disks used in the present work are presented for 0-300 kHz and compared to FE-simulation. The simulated disk has the same dimensions as disk 7. The measurements have been performed as given in Section 3.1.1, with an 1 V RMS used for the impedance measurements in order to avoid non-linear behaviour in the disks. Both a) the magnitude, $|Z|$, and b) the phase, ϕ_Z, are presented.

In the impedance plot of the disks, cf. Fig. 5.1, it is seen that the disks used in the current work have the first radial mode, R_1, at 90-120 kHz and the second radial mode, R_2, at 240-260 kHz.

There is a good agreement between the measured and the simulated disk impedances with the largest deviation found at the peaks associated with R_1 and R_2, when comparing disk 7 to the simulation. For the first dip there is a upwards frequency shift

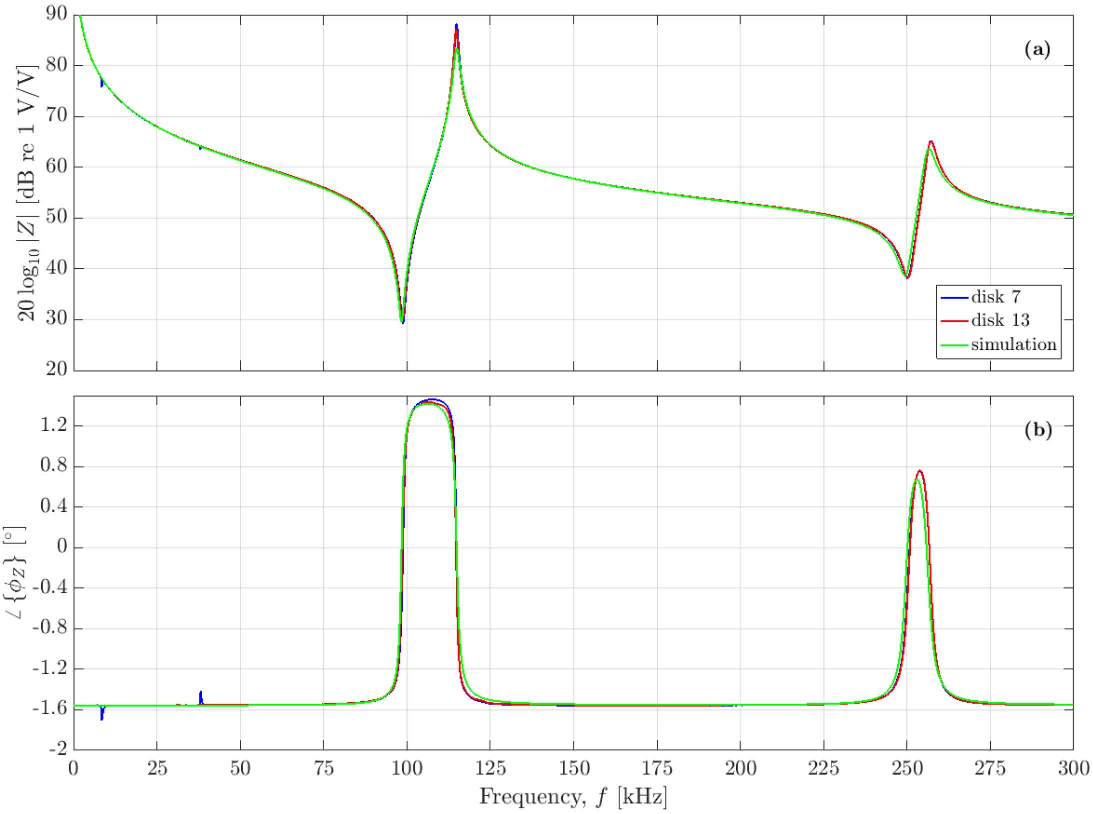

FIGURE 5.1: Impedance measurements with a) the magnitude and b) the phase measured for disk 7 and 13 compared to simulated impedance.

of 0.32 kHz for disk 7 compared to the simulated disk and a decrease in magnitude of 0.23 dB.

For the first peak the difference in magnitude between the two disks is 0.85 dB and the largest difference is again between disk 7 and the simulation, with a 4.68 dB increase is observed for disk 7 compared to simulation. The frequency is identical for the two measured disks and higher by 0.2 kHz for the simulation.

The second dip, associated with R_2, shows a lower magnitude of 0.39 dB for disk 7 compared to simulation and a higher frequency of 0.9 kHz for disk 13 compared to simulation.

For the second peak, associated with R_2, disk 7 has a higher magnitude of 1.59 dB compared to simulations and a higher frequency of 0.6 kHz.

The conductance and susceptance for disk 7, disk 13 and simulations is presented in Fig. 5.2 and Fig. 5.3, respectively. The spikes seen in the impedance of disk 7 in Fig. 5.1 are more prominent in the conductance in Fig. 5.2. However, these spikes in T_x do not noticeably affect the measured output of the system at hand. This was investigated by using the impedance measured for disk 13 in place of disk 7 when measuring the effedt of the transmitting electronics and no visible changes were observed in the magnitude or slowly varying phase of the transfer function $H_{0m1}VV$.

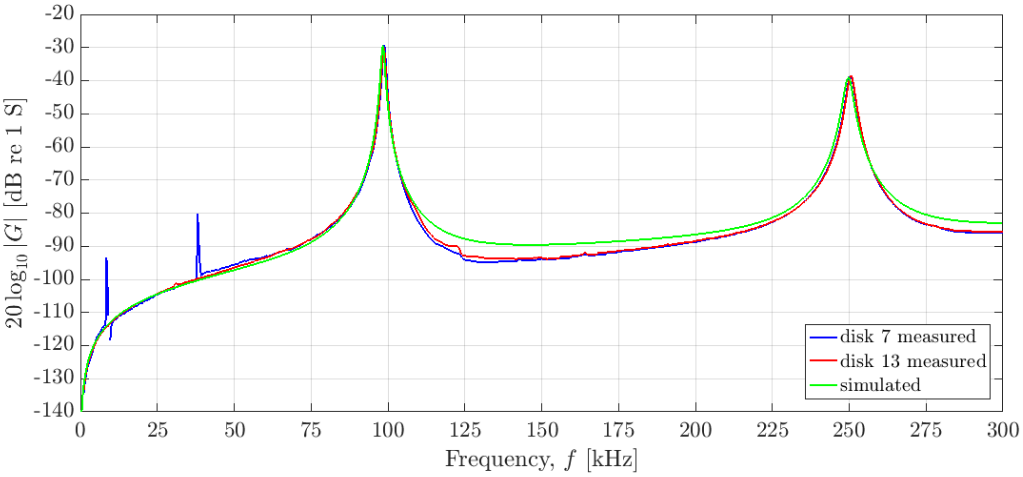

FIGURE 5.2: Conductance measured for disk 7 and 13 compared to simulated impedance.

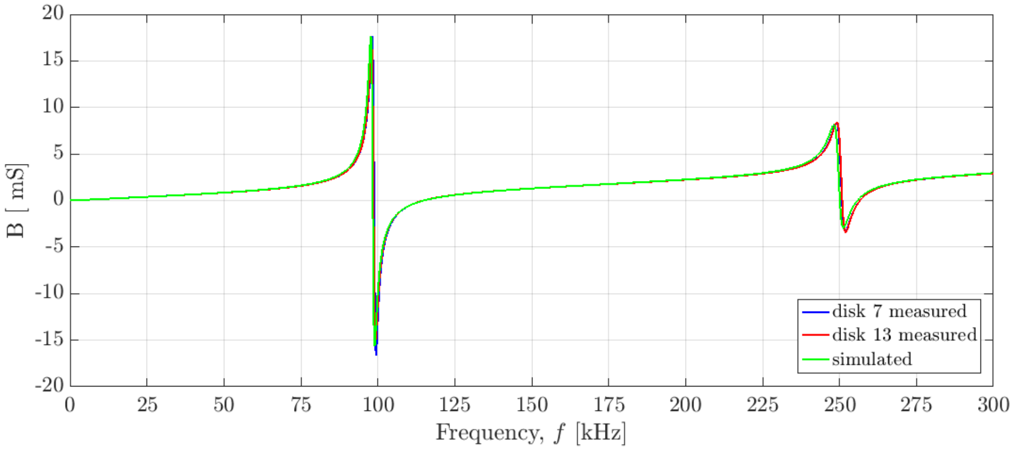

FIGURE 5.3: Susceptance measured for disk 7 and 13 compared to simulated impedance.

5.2 Measured noise

Investigations has been made into the noise recorded along with the acoustic measurements, cf. Section 3.5. The white noise is reduced by averaging over 128 bursts, as seen in Fig. 5.4 compared to Fig. 5.5.

The electrical coherent noise is reduced by the use of Faraday cage, shielding of the cables with aluminium foil, twisting the cables and by utilizing a noise reduction method (NRM) introduced in [37]. To see the effect of the NRM the envelope of the transfer function in question is calculated, as this allows for the amplitude of the signal to be more clearly seen. The envelope of the transfer function H_{0m6}^{VV} is calculated using the envelope function in MATLAB, which utilizes a Hilbert transformation for calculating the amplitude of the signal, given as

$$env(H_{0m6}^{VV}) = |H_{0m6}^{VV} + iH(H_{0m6}^{VV})|, \tag{5.1}$$

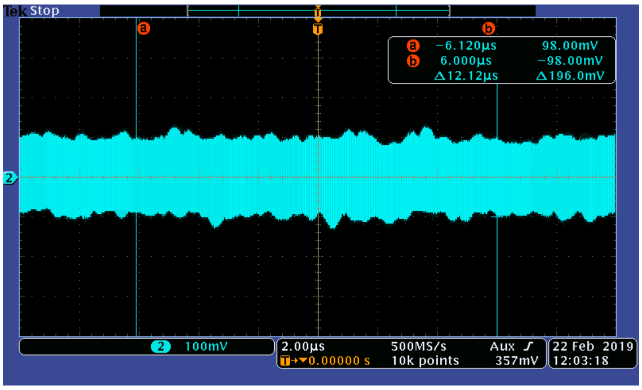

FIGURE 5.4: Recorded noise at the oscilloscope from the acoustic measruement Setup I without averaging.

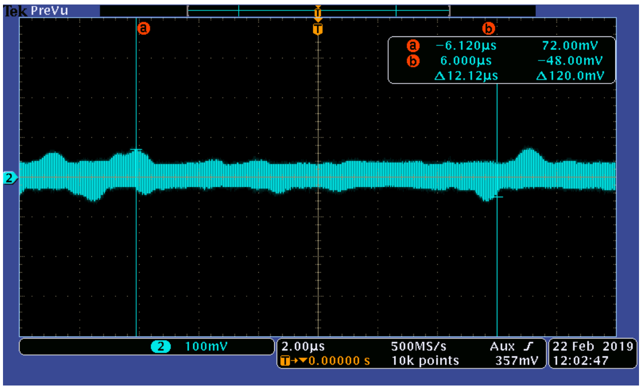

FIGURE 5.5: Recorded noise at the oscilloscope from the acoustic measruement Setup I with averaging over 128 bursts.

where H() is the Hilbert transform. The calculated envelopes of H_{0m6}^{VV} with and without noise reduction is presented in Fig. 5.6 for measurements performed at $d = 50$ cm and in Fig. 5.7 for measurements performed at $d = 15$ cm.

From Fig. 5.6 it is seen that the NRM method is most effective for the frequency range above 240 kHz. This includes the R_2 mode. For measurements performed at a shorter distance, cf. Fig. 5.7 the method appears to be less effective, however some coherent noise appears to be removed from the H_{0m6}^{VV} with the NRM.

5.3 Corrections performed on measurements

In this section the corrections performed on the experimental measurements, in order to be able to compare them to simulations, are presented. Since none of the transmitting or receiving electronics or cables are simulated the effect of these will have to be removed before comparisons between simulations and measurements can be made. In Section 5.3.1 the transmitting electronics transfer function, H_{0m1}^{VV}, calculated using the measured impedance of the transmitting disk is presented. In Section 5.3.2 the open circuit transfer function, H_{5open5}^{VV}, calculated using the measured impedance of the receiving disk is presented. In Section 5.3.3 the measured receiving electronics transfer function, H_{56}^{VV}, is presented. There is also no attenuation or diffraction effect calculated in the simulations, so the effect of these are found and presented in Section 5.3.4 and Section 5.3.5, respectively. Lastly, some corrections have been made to

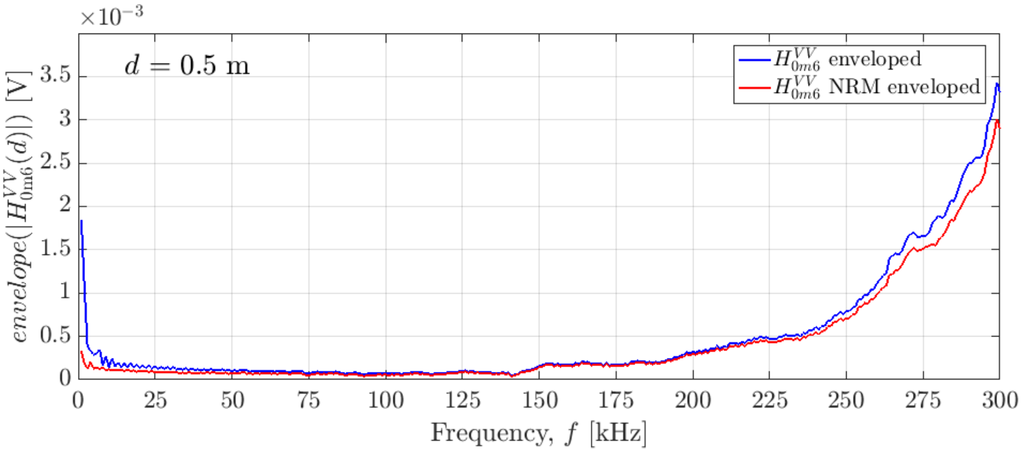

FIGURE 5.6: Envelope of H_{0m6}^{VV} with and without noise reduction for measurements performed at $d = 50$ cm.

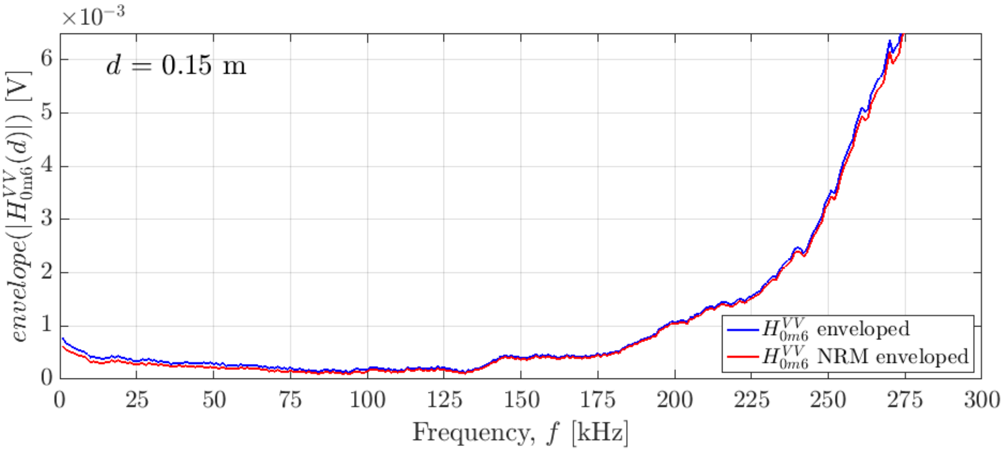

FIGURE 5.7: Envelope of H_{0m6}^{VV} with and without noise reduction for measurements performed at $d = 15$ cm.

the temperature measurements acquired during the acoustic measurements. These are explained and presented in Section 5.3.6.

5.3.1 Transmitting electronics transfer function, H_{0m1}^{VV}

The transfer function for the transmitting electronics, H_{0m1}^{VV}, is presented in Fig. 5.8 for both magnitude and the slowly varying phase. Since the length of the cable has been measured differently in previous work H_{0m1}^{VV} is calculated for three different cable lengths. The first measurement is using the cable length measured from the start of the plugs on each end of the cable, yielding a length of 2.970 m. The second measurement is using the cable length measured from the end of the plugs on each end of the cable, yielding a length of 3.044 m.The third measurement is using the cable length measured from the start of the plugs on each end on the cable and including the t-plug used to connect the cable to the oscilloscope, yielding a length of 3.072 m.

For both the magnitude, in Fig. 5.8a), and the slowly varying phase, in Fig. 5.8b), no change is observed for the differences in cable lengths. This is expected, since the effect of the cable on the transfer function is negligible on cm level. The largest influence on H_{0m1}^{VV} is the impedance of the transmitting disk.

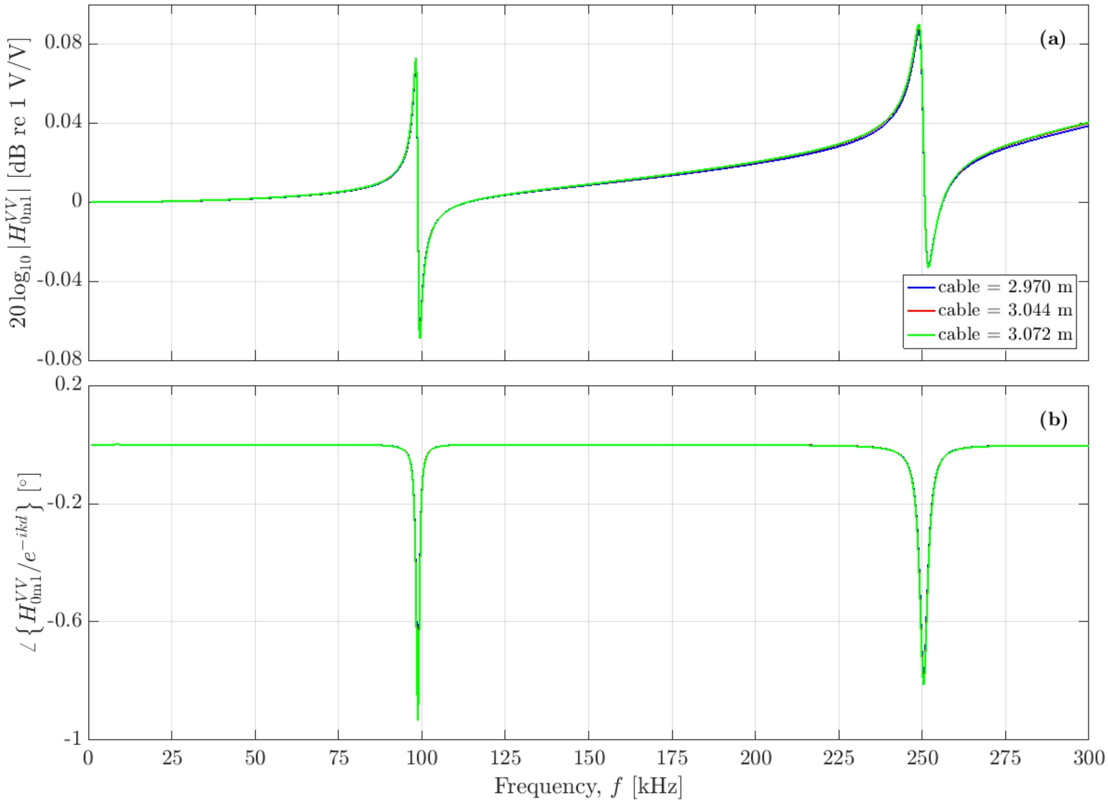

FIGURE 5.8: Transmitting electronics transfer function H_{0m1}^{VV} for a) the magnitude and b) the slowly varying phase, for different cable lenths calculated using transmission line model.

The magnitude of $H_{5open5'}^{VV}$ in Fig. 5.9a) has a peak of 0.0732 dB at 98.27 kHz and a dip of -0.06912 dB at 99.47 kHz. Another peak of 0.08979 dB is found at 248.8 kHz and a dip of -0.03242 dB at 252.1 kHz.

For the slowly varying phase of $H_{5open5'}^{VV}$ in Fig. 5.9b) a dip is found of -0.9332° at 98.87 kHz and a last dip of -0.806° is found at 250.6 kHz.

5.3.2 Open circuit transfer function, $H_{5open5'}^{VV}$

The open circuit transfer function, $H_{5open5'}^{VV}$, is presented in Fig. 5.9 for a separation distance d = 0.5 m, for both magnitude and the slowly varying phase. As in the case of H_{0m1}^{VV} the length of the cable has been measured differently in previous work. Therefore, $H_{5open5'}^{VV}$ is calculated for three different cable lengths. The first measurement is using the cable length measured from the start of the plugs on each end of the cable, yielding a length of 2.974 m. The second measurement is using the cable length measured from the end of the plugs on each end of the cable, yielding a length of 3.048 m.

For both the magnitude, in Fig. 5.9a), and the slowly varying phase, in Fig. 5.9b), no change is observed for the differences in cable lengths. This is expected, since the effect of the cable on the transfer function is negligible on cm level. The largest influence on $H_{5open5'}^{VV}$ is the impedance of the receiving disk.

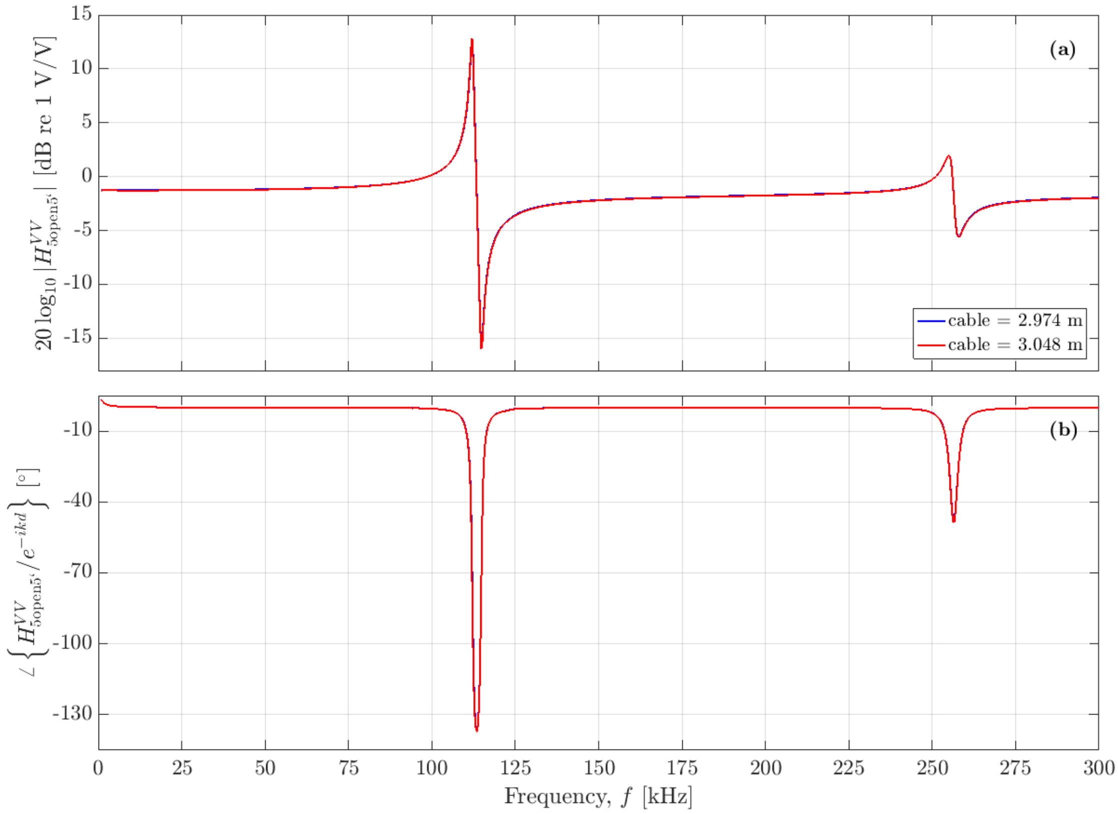

FIGURE 5.9: Open circuit transfer function $H^{VV}_{5open5'}$ for a) the magnitude and b) the slowly varying phase, for different cable lenths calculated using transmission line model.

The magnitude of $H^{VV}_{5open5'}$ in Fig. 5.9a) has a peak of 12.8 dB at 112 kHz and a dip of -15.77 dB at 115 kHz. Another peak of 1.961 dB is found at 255.1 kHz and a dip of -5.609 dB at 258.1 kHz.

For the slowly varying phase of $H^{VV}_{5open5'}$ in Fig. 5.9b) a dip is found of -137.1° at 113.5 kHz and a last dip of -48.65° is found at 256.3 kHz.

5.3.3 Receiving electronics transfer function, $H^{VV}_{5'6}$

The transfer function for the receiving electronics, $H^{VV}_{5'6}$, is presented in Fig. 5.8 for both magnitude and the slowly varying phase.

The magnitude of $H^{VV}_{5'6}$ in Fig. 5.10a) has a value of -6.99 dB at 1 kHz and a peak of 61.03 dB at 7.585 kHz. For the rest of the frequency range, up to 300 kHz, there are small fluctuations going from 60.9 dB to 60.4 dB. This is presented separately in Fig. 5.11.

For the slowly varying phase of $H^{VV}_{5'6}$ in Fig. 5.10b) a dip is found of -165.6° at 3.694 kHz and a peak of 178.4° is found at 3.993 kHz. The phase continues to decrease after this peak and has a value of -212.6° at 300 kHz.

The magnitude of $H^{VV}_{5'6}$ plotted from 30 kHz in Fig. 5.11a) shows a variation that varies from 60.82 dB at the maximum for 219.8 kHz and a minimum of 60.45 dB for 300 kHz.

The slowly varying phase of $H^{VV}_{5'6}$ plotted from 30 kHz in Fig. 5.11b) shows a decrease in phase from -0.1218° at 30 kHz to -212.6° at 300 kHz.

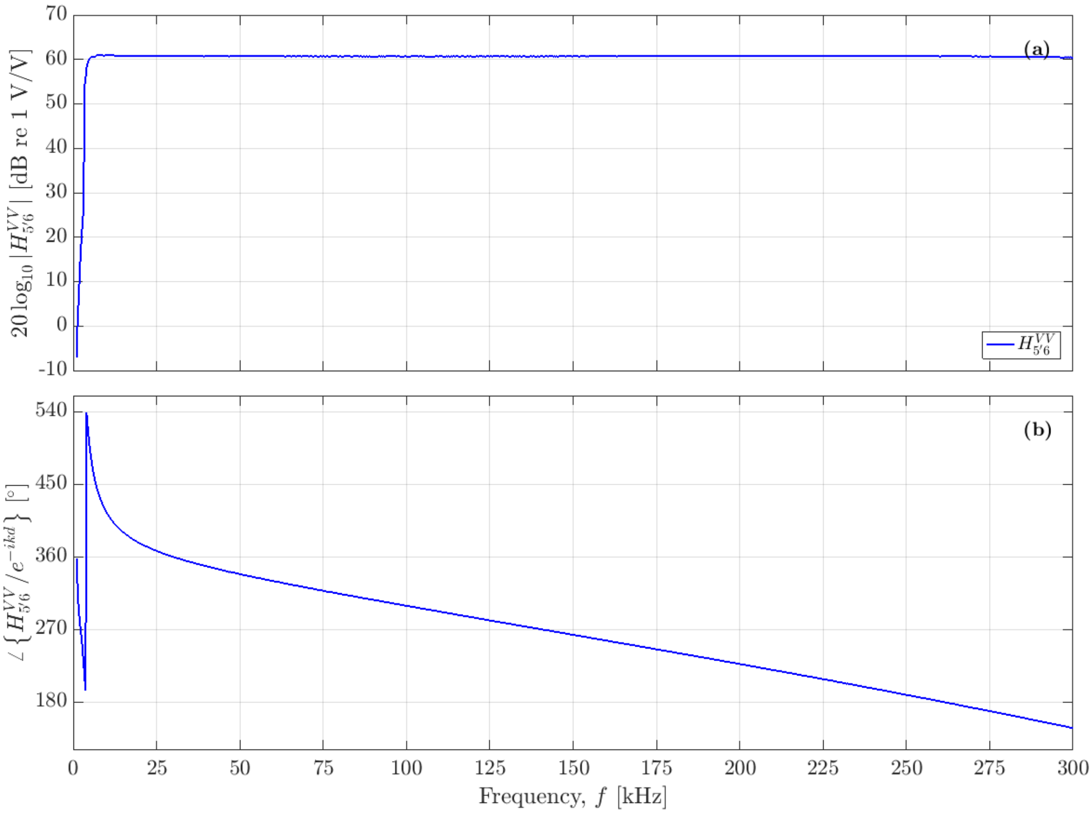

FIGURE 5.10: Receiving electronics transfer function $H_{5'6}^{VV}$ for a) the magnitude and b) the slowly varying phase measured with attenuator 4.

5.3.4 Correction for attenuation in air

Fig. 5.12 shows the correction for attenuation, C_α for separation distances $d = 50$ cm, $d = 30$ cm, $d = 20$ cm and $d = 15$ cm.

In Fig. 5.12 C_α increases with increasing separation distance, as is expected since larger separation distance increases the distance the sound propagates through the medium and therefore increases the attenuation caused by the medium. No abnormalities or discrepancies are observed in the behaviour of the attenuation for the different separation distances and apart from the expected increase in attenuation, no difference is observed at the 112 kHz area.

For the measurement performed at $d = 50$ cm in Fig. 5.12 the attenuation correction C_α is increasing with increasing frequency, from 0.0003146 dB at 1 kHz to 0.8923 dB at 300 kHz. For the measurement performed at $d = 30$ cm C_α is increasing with increasing frequency, from 0.0003984 dB at 1.599 kHz to 0.5266 dB at 300 kHz. For the measurement performed at $d = 20$ cm C_α is increasing with increasing frequency, from 0.00004819 dB at 2.197 kHz to 0.35 dB at 300 kHz. For the measurement performed at $d = 15$ cm C_α is increasing with increasing frequency, from 0.0006618 dB at 3.095 kHz to 0.263 dB at 300 kHz.

The maximum value for C_α for a measurement performed at $d = 15$ cm is found to be 0.263 dB at 300 kHz. This is considerably lower than for a measurement performed at $d = 50$ cm, which is expected when the propagation distance is shorter. No phase is calculated in the model used for attenuation correction in this work, and

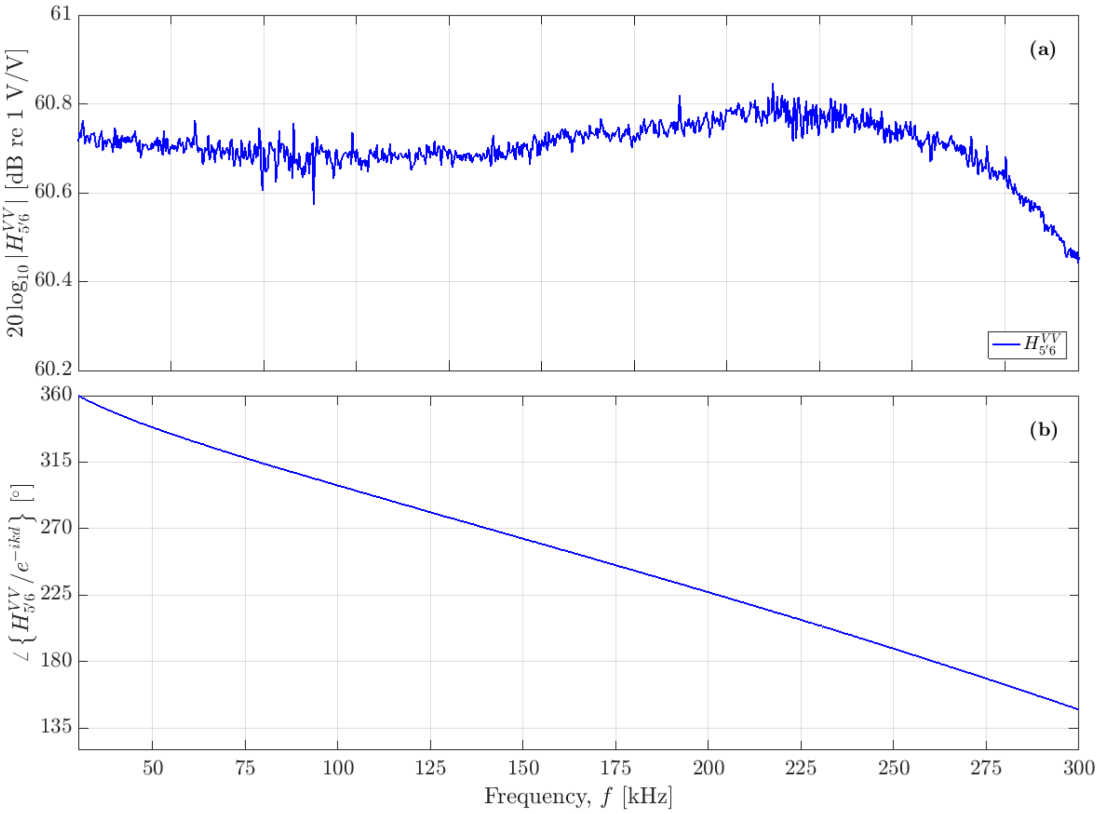

FIGURE 5.11: Transfer function $H_{5'6}^{VV}$ for a) the magnitude and b) the slowly varying phase measured with attenuator plotted from 30 kHz.

the plot of the phase is only kept in to illustrate that the phase of C_α in no way affects the slowly varying phase of H_{15open}^{VV}.

5.3.5 Correction for diffraction effects

Fig. 5.13 shows the baffled piston diffraction correction, C_{dif}^{BPDC} for separation distances $d = 50$ cm, $d = 30$ cm, $d = 20$ cm and $d = 15$ cm.

In Fig. 5.13 the diffraction correction, C_{dif}, is seen to increase in both magnitude and phase for increasing frequency. For the measurement performed at $d = 50$ the magnitude increases from 0.001746 dB at 1 kHz to 0.8563 dB at 300 kHz. The phase for the measurement performed at $d = 50$ increases from 0.001815° at 1 kHz to 0.5304° at 300 kHz. For the measurement performed at $d = 30$ the magnitude increases from 0.004888 dB at 1.599 kHz to 2.346 dB at 300 kHz. The phase for the measurement performed at $d = 30$ increases from 0.004829° at 1.599 kHz to 0.8389° at 300 kHz. For the measurement performed at $d = 20$ the magnitude increases from 0.01112 dB at 2.197 kHz to 5.026 dB at 300 kHz. The phase for the measurement performed at $d = 20$ increases from 0.009943° at 2.197 kHz to 1.114° at 300 kHz. For the measurement performed at $d = 15$ the magnitude increases from 0.02022 dB at 3 kHz to 7.804 dB at 300 kHz. The phase for the measurement performed at $d = 15$ increases from 1.068° at 3.095 kHz to 1.214° at 300 kHz.

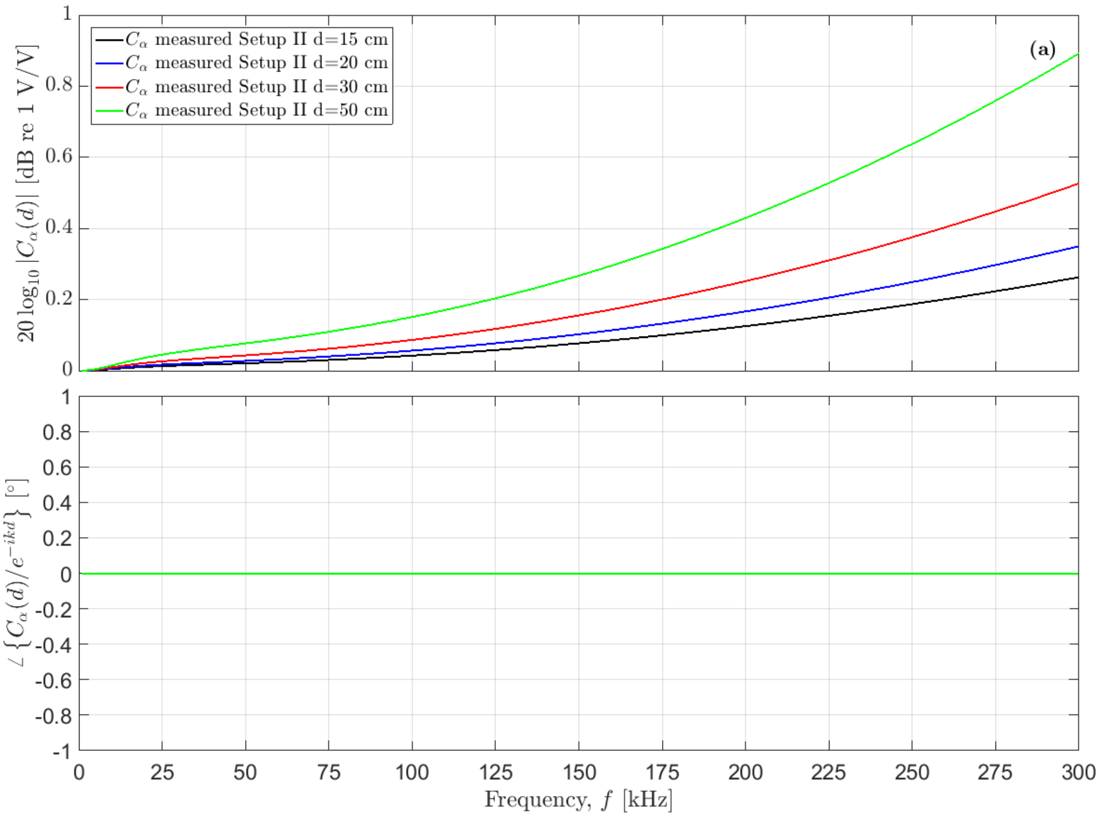

FIGURE 5.12: Measured transfer function correction C_{alpha} for a) the magnitude and b) the phase, θ_{alpha}, using Setup II for separation distances $d = 50$ cm, $d = 30$ cm, $d = 20$ cm and $d = 15$ cm.

5.3.6 Corrections made to temperature measurements

The temperature measurement is only done every 5 seconds in order to greatly reduce the time of a measurement series, cf. Fig. 5.14. This results in fewer temperature measurements than the rest of the variables measured so an interpolation of the temperature is done to remedy this, cf. Fig. 5.15.

Error in temperature measurements

When measuring at the lab after setup II had been introduced the thermometer started showing error message E-1 before resuming normal measurements again. This indicated a bad connection causing an open circuit, but no such problem was discovered and the measurement software was reprogrammed to ignore error messages from the thermometer. Subsequently each temperature measurement recorded after this code was implemented has been checked to make sure no bad temperature measurements are used. An example showing the worst case, Fig. 5.15, of the temperature measurements recorded after the thermometer started producing the error E-1 shows that the effect is negligible and the measurements are used for calculating the sound speed.

The plateaus in Fig. 5.16 are believed to be where the thermometer displayed the error message and the software was programmed to return no value, thus letting the

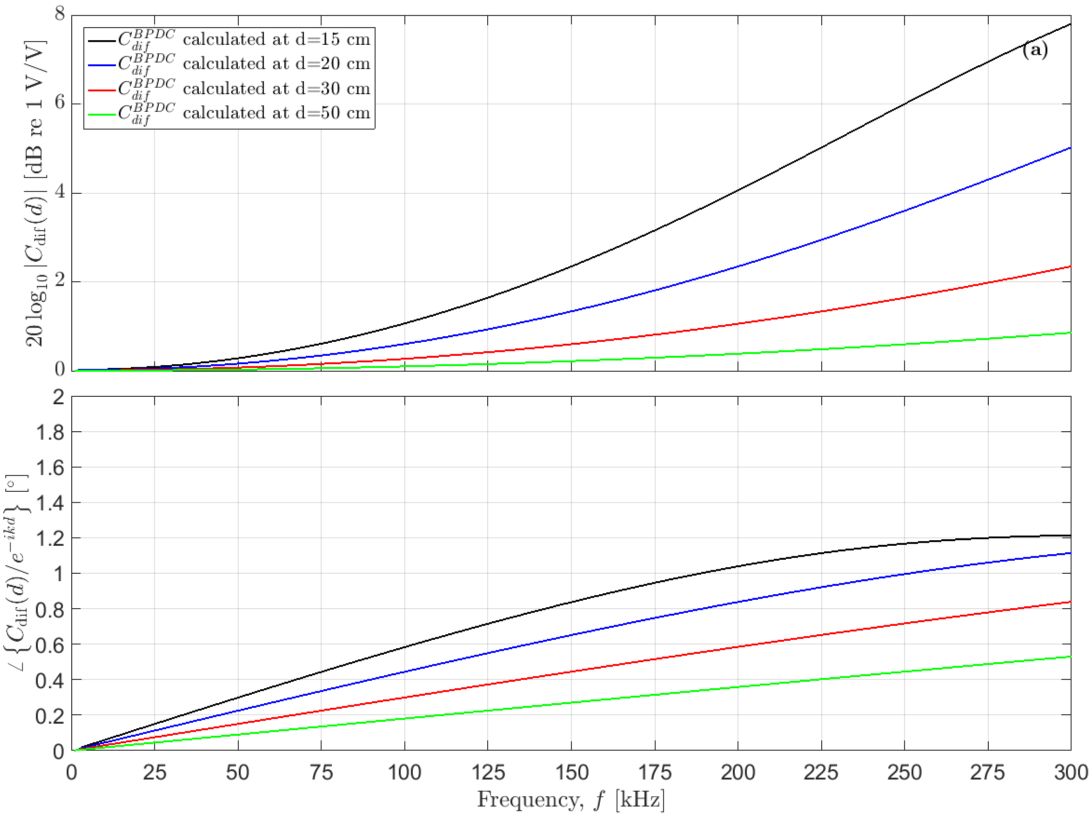

FIGURE 5.13: Measured transfer function correction C_{dif}^{BPDC} for a) the magnitude and b) the phase, θ_{dif}, using Setup II for separation distances $d = 50$ cm, $d = 30$ cm, $d = 20$ cm and $d = 15$ cm.

interpolation step cover over the missing measurement. This is deemed an acceptable solution and the results look similar to results obtained before the thermometer started showing the error message, Fig. 5.15.

5.4 The influence of input voltage

In order to achieve a good signal to noise ration (SNR) it is of interest to have a high input voltage. However, too high input voltage causes non linear behaviour in the disk at R_1 and R_2, cf. [36], and the system model is based on linear components. On the other hand too low input voltage may lead to the signal being drowned in noise. Therefore measurements are done with different input voltages and are presented in Figure 5.17.

It is clear from Fig. 5.17 that an input voltage of 0.01 V makes it impossible to distinguish the signal from the noise, so this is removed from the plot, cf. Fig. 5.18.

For the R_1 peak in Fig. 5.18a) an increase of 5.98 dB is seen in the first peak for the measurements with 0.1 V and 1 V, compared to the measurement with 10 V. At the second peak associated with R_1 the three measurements are inseparable. The 0.1 V measurement is heavily fluctuating below 93.48 kHz and above 117.1 kHz.

For the R_2 peak an increase of 1.1 dB is seen in the first peak for the measurement with 0.1 V compared to the measurement with 1 V and 5.87 dB compared to the measurement with 10 V. At the second peak associated with R_2 increase of 1.22 dB is seen for the measurement with 0.1 V compared to the measurement with 1 V and

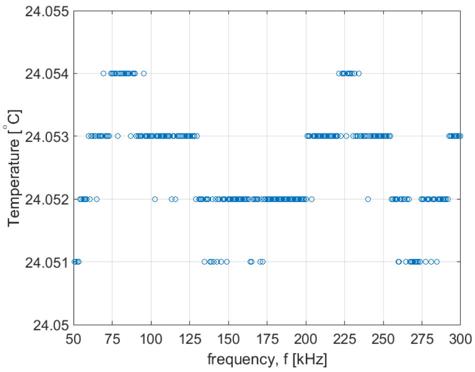

FIGURE 5.14: Temperature measurement at 5 second intervals for one acoustic measurement.

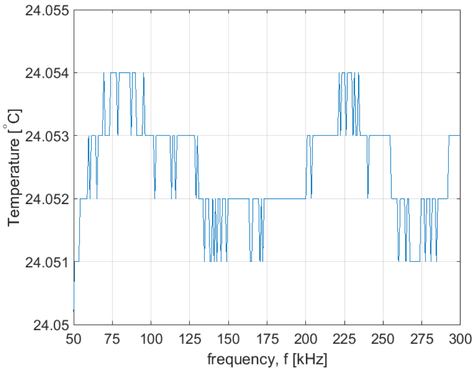

FIGURE 5.15: Interpolated temperature measurement for one acoustic measurement.

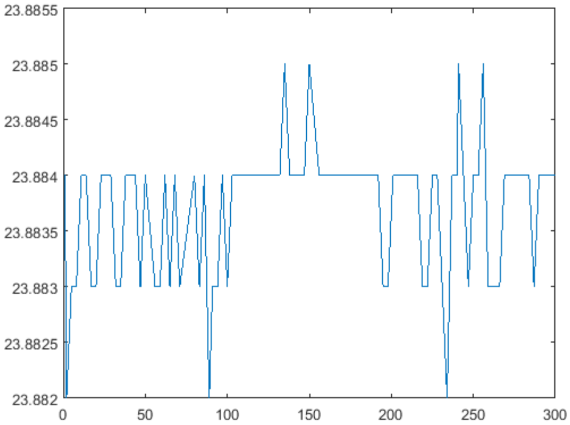

FIGURE 5.16: Temperature measurement recorded with lab setup II after the thermometer startd displaying error message E-1.

3.08 dB compared to the measurement with 10 V. The measurement with 0.1 V is fluctuation for the entire peak of R_2, likely due to too low input voltage, causing a too low SNR.

For the slowly varying phase in Fig. 5.18b) the difference in input voltage greatly affects the ranges of the phase. The measurements using 1 V and 10 V are fairly agreeing up to 129 kHz.

5.5 The influence of accuracy in alignment

In [36] the tolerated uncertainty in alignment of the disks in the xy-plane was given as 10 μm or less, whereas [37] allowed for uncertainties up to 100 μm. Therefore the effect of different alignment uncertainty is investigated by aligning the disks to different degrees of accuracy and observing how this affects the transfer function, H_{0m6}^{VV}. The accuracies chosen were 500 μm, 50 μm and 10 μm. The results are shown in Fig. 5.19.

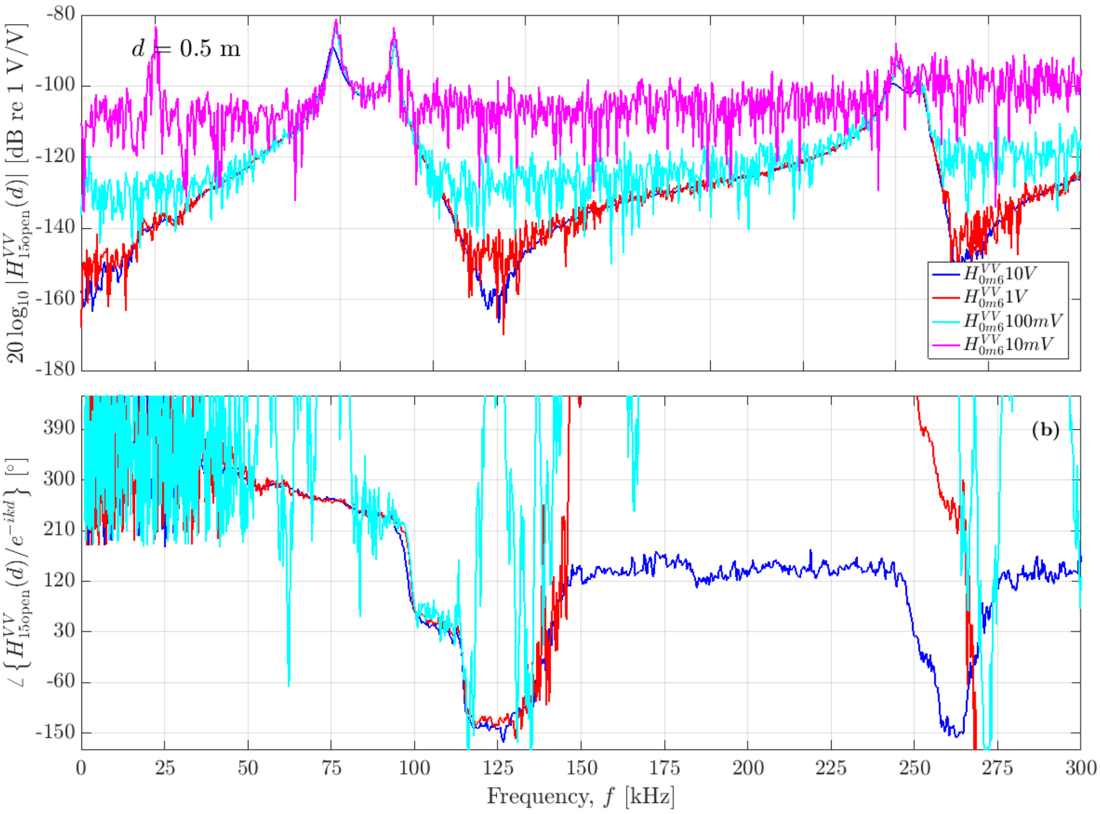

FIGURE 5.17: Measuremed transfer function H^{VV}_{15open} for a) the magnitude and b) the slowly varying phase, θ^{slow}_{15open}, for different input voltages.

For the first two peaks, associated with the fundamental radial mode R_1, there is little to no change in the magnitude of the transfer function H^{VV}_{0m6}, for all three accuracies. At the second pair of peaks, associated with the second radial mode R_2, there is no noticeable change in the magnitude for alignment to the degree of 50 μm and 10 μm. However, the measurement with 500 μm uncertainty in the alignment shows a decrease in magnitude of almost 5 dB compared to the measurements with 50 μm and 10 μm misalignment.

5.6 Comparing transfer function with prior work

In the present section comparisons are made between the measurements and simulation of the present work and prior work. In Section 5.6.1 the measured open-circuit transfer function H^{VV}_{15open} compared to prior work is presented and in Section 5.6.2 the simulated open-circuit transfer function H^{VV}_{15open} compared to prior work is presented.

5.6.1 Comparing experimental measurements with prior work

Measurements of the open-circuit transfer function H^{VV}_{15open} as compared to prior work [36, 37] is shown in Fig. 5.20 for both the magnitude and the slowly varying phase.

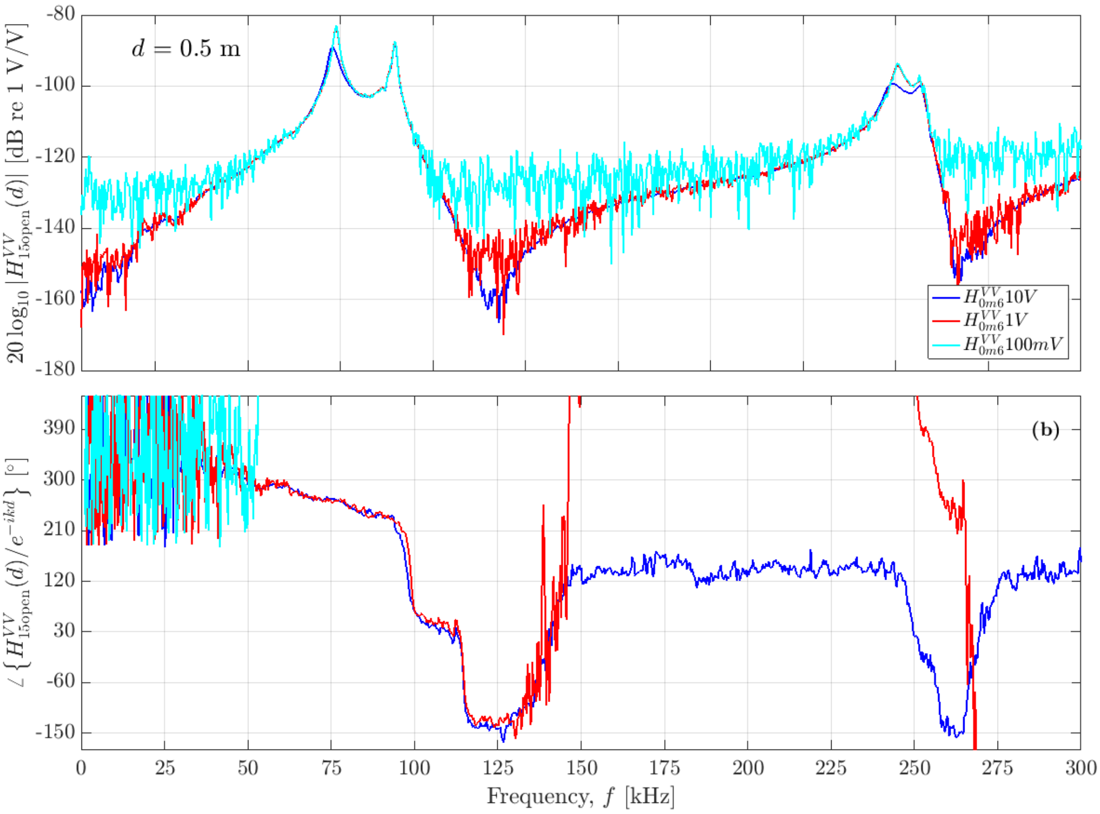

FIGURE 5.18: Measuremed transfer function H^{VV}_{15open} for a) the magnitude and b) the slowly varying phase, θ^{slow}_{15open}, for different input voltages.

It should be noted that the receiving disk used by Hagen [37] and in the present work are not the same as used by Andersen [36], and the calculation of the receiving electronics transfer function, $H^{VV}_{5'6}$, differ slightly as the filter is coupled in series after the amplifier in the present work and [37], whereas [36] coupled the filter between the input and output sections of the amplifier. The signal generator voltage settings used for measurements vary for the different frequencies, cf. [41]. At R_1 the voltage settings used are 0.1 V for the present work and 1 V for [36] and [37]. For R_2 the voltage settings used are 1 V in the present work and [36] and 0.1 V in [37]. For all other frequencies the voltage setting is 10 V in the current work, [36] and [37]. The frequency steps used in the present work, [36] and [37], are 300 Hz, 500 Hz and 1 kHz, respectively.

In the frequency range 30 - 80 kHz the measurements in the present work reveal a clear undulation pattern, which is also present in the measurements presented in [33, 35–37, 41]. In [38] these are shown to be due to side radiation from T_x.

For the magnitude of H^{VV}_{15open} in Fig. 5.20 a) at the first peak associated with R_1, the deviations of the present work are about 3.18 dB and 6.85 dB relative to [36] and [37], respectively. For the second peak associated with R_1 the deviations of the present work are 2.6 dB and 2.13 dB, relative to [36] and [37].

With respect to the frequencies for the first peak associated with R_1, the corresponding deviations of the present work relative to [36] and [37] are about 1 kHz and 1.27 kHz, respectively. For the second peak associated with R_1, the corresponding deviations of the present work relative to [36] and [37] are about 0.7 kHz and 0.1

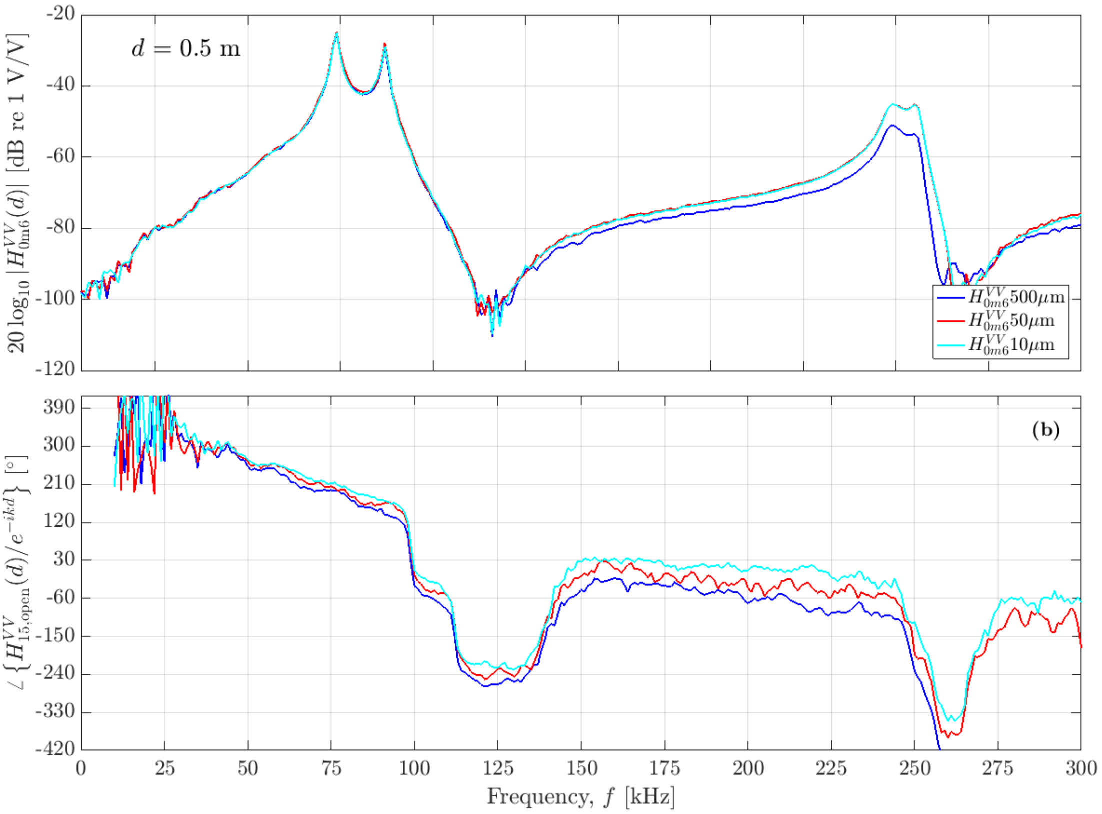

FIGURE 5.19: Measuremed transfer function H^{VV}_{15open} for a) the magnitude and b) the slowly varying phase, θ^{slow}_{15open}, for different accuracies in alignment.

kHz, respectively.

Similarly, for R_2, the corresponding deviations of the present work at the first peak are 6 dB and 0.6 dB, relative to [36] and [37]. At the second peak associated with R_2, the deviations of the present work relative to [36] and [37] are 3.81 dB and 0.3 dB, respectively. Small oscillations are observed in the measurement from [36] in the frequency range of R_2, i.e. 248-257 kHz.

In the frequency range 175-235 kHz deviations of the present work relative to [36] and [37] are about 1.3 kHz and 0.5 kHz, respectively.

The oscillations in the magnitude of [37] around 240 kHz is likely due to the switch from 10 V input voltage to 0.1 V input voltage for the R_2 frequency range. This effect is investigated further in Section 5.8 for the plots of Setup I compared to Setup II.

For the slowly varying phase in Fig. 5.20 b) undulations are observed in the present work and measurements from [36] for the frequency range 50-95 kHz. In this frequency range [36] is up to 13.4° higher and [37] is up to 19.8° lower than the present work.

Both the present work and [36] show a small, sharp dip at 111.6 kHz. A similar effect is observed at 112 kHz for [37].

The present work has a peak at 119.8 kHz. [36] has a dip at 129 kHz which is 110.7° lower and [37] has a peak at 129 kHz which is 12.1° higher than the present work.

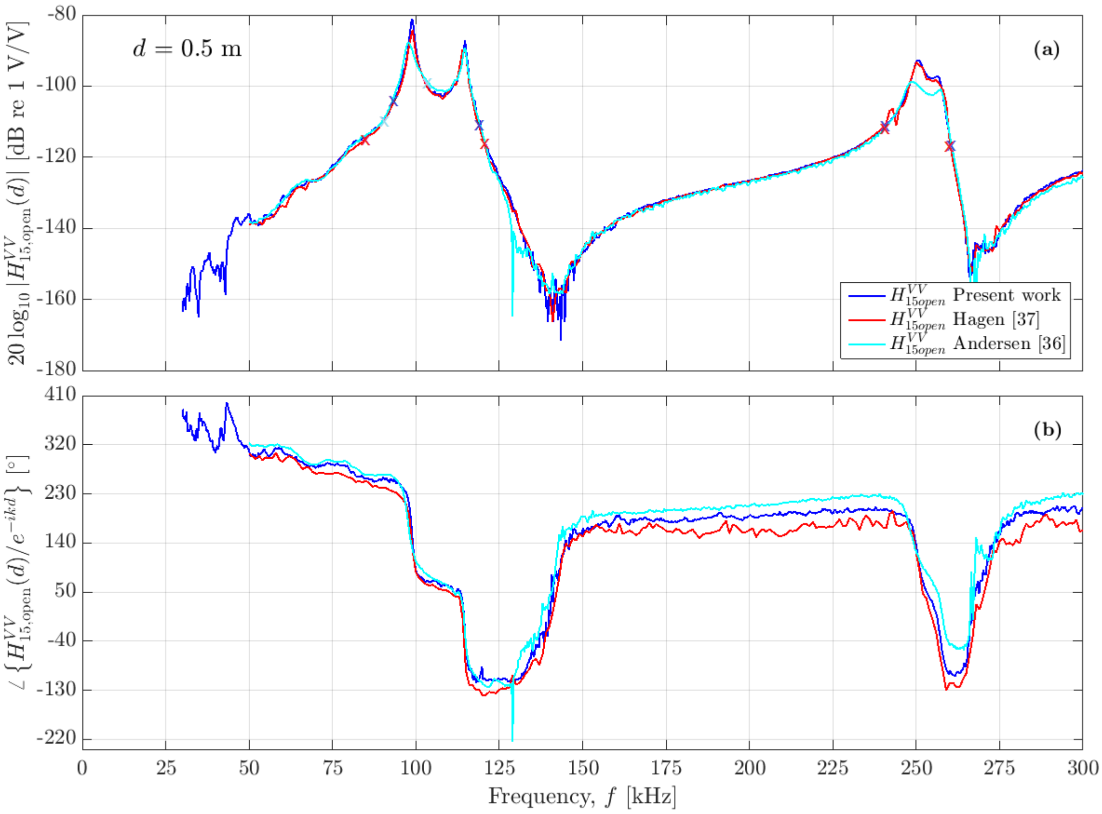

FIGURE 5.20: Measurements of transferfunction H^{VV}_{15open} for a) magnitude and b) slowly varying phase compared with previous work.

For the frequency range 150-240 kHz [36] is up to 25° higher and [37] is up to 35.9° lower than the present work.

In the dip at the frequency range 250-275 kHz [36] is 51.95° higher and [37] is 19.5° lower than the present work.

5.6.2 Comparing simulations with prior work

Fig. 5.21 shows simulations of the magnitude and the slowly varying phase of the transfer function H^{VV}_{15open}, as compared to prior work [36, 37], calculated using two different finite element software tools: FEMP [40] and COMSOL [82].

The same material parameters, piezoelectric disk dimensions, software (FEMP) and finite element mesh, are used for simulations in the current work and by Andersen [36]. Therefore these curves are identical, cf. Fig. 5.21. The simulations done in COMSOL and FEMP by Hagen [37] differ from the current work and Andersen [36]. There is a lower magnitude found in the present work and [36] compared to [37] for the first and second peak associated with R_1, of about 0.3 dB and 0.7 dB, respectively. For the two peaks associated with R_2 the deviations are about 0.6 dB and 1 dB, respectively. There is a lower frequency for the two peaks associated with R_1 for the present work and [36] as compared to [37], and the differences are about 2 and 3 kHz, respectively. For the two peaks associated with R_2, the differences are about 3 and 5 kHz, respectively.

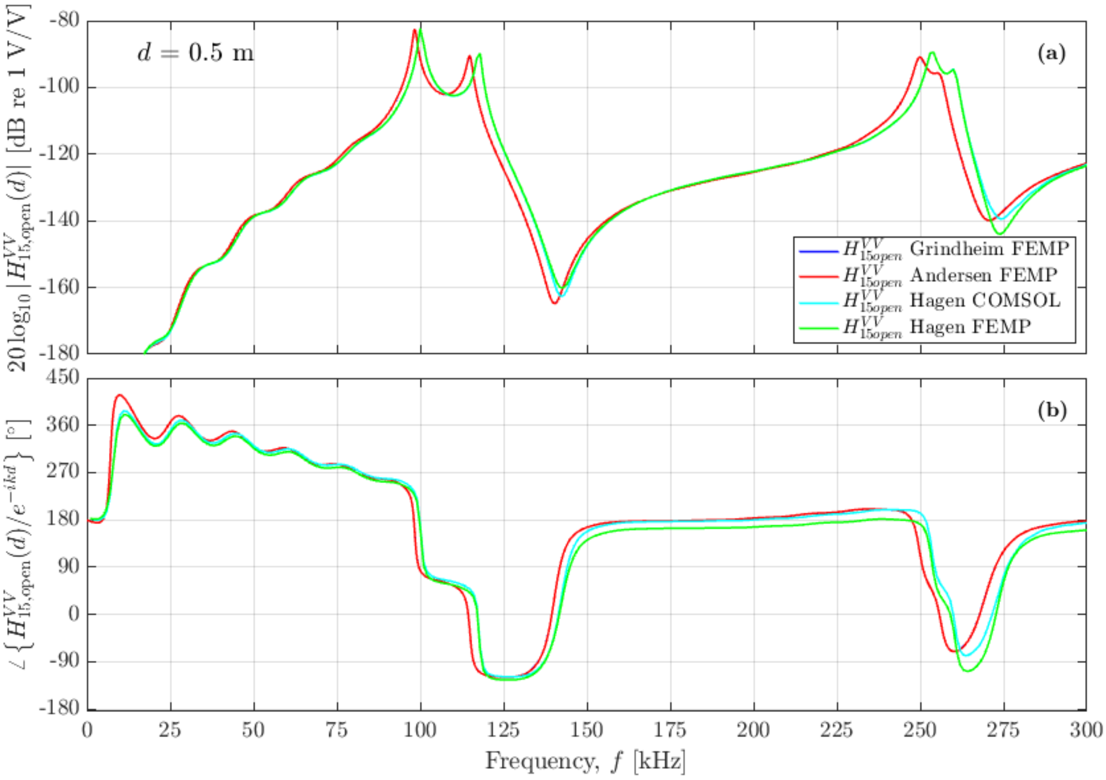

FIGURE 5.21: Simulated transferfunction H^{VV}_{15open} for a) magnitude and b) slowly varying phase compared with previous work. The x denotes change in input voltage.

5.7 Simulation with different parameters

In order to further investigate the deviations observed in the simulations in Fig. 5.21 three different simulations are performed. The first simulation, Simulation I, is identical to Andersen [36], for the second simulation, Simulation II, only the material parameters are changed to match the set used by Hagen [37] and for the third simulation, Simulation III, the dimensions of the simulated disk were changed. All parameters for the three simulations are listed in Section 4.1.

For the magnitude in Fig. 5.22 a) compared to Simulation I at the two peaks associated with R_1, Simulation II is 0.7 kHz and 1.7 kHz higher in frequency and 0.54 dB and 2.03 dB higher in magnitude, respectively. Simulation III is 1.7 kHz and 2.8 kHz higher in frequency and 0.49 dB and 1.92 dB higher in magnitude, for the two peaks respectively.

In the dip after R_1 Simulation II is 0.1 dB lower than Simulation I and 0.3 kHz higher in frequency. Simulation III is 1 dB lower than Simulation I and 1.3 kHz higher in frequency for the dip.

In the range 150-225 kHz Simulation I is lowest in magnitude with Simulation II 0.5 dB higher and Simulation III 0.9 dB higher.

For the two peaks associated with R_1, Simulation II compared to Simulation I is 1.1 kHz and 1.8 kHz higher in frequency and 2.6 dB and 1.78 dB higher in magnitude, respectively. Simulation III is 3.2 kHz and 3.7 kHz higher in frequency and 2.87 dB and 2.08 dB higher in magnitude, for the two peaks respectively.

In the dip after R_2 Simulation II is 0.5 dB lower than Simulation I and 0.6 kHz higher in frequency. Simulation III is 0.9 dB lower than Simulation I and 3.2 kHz

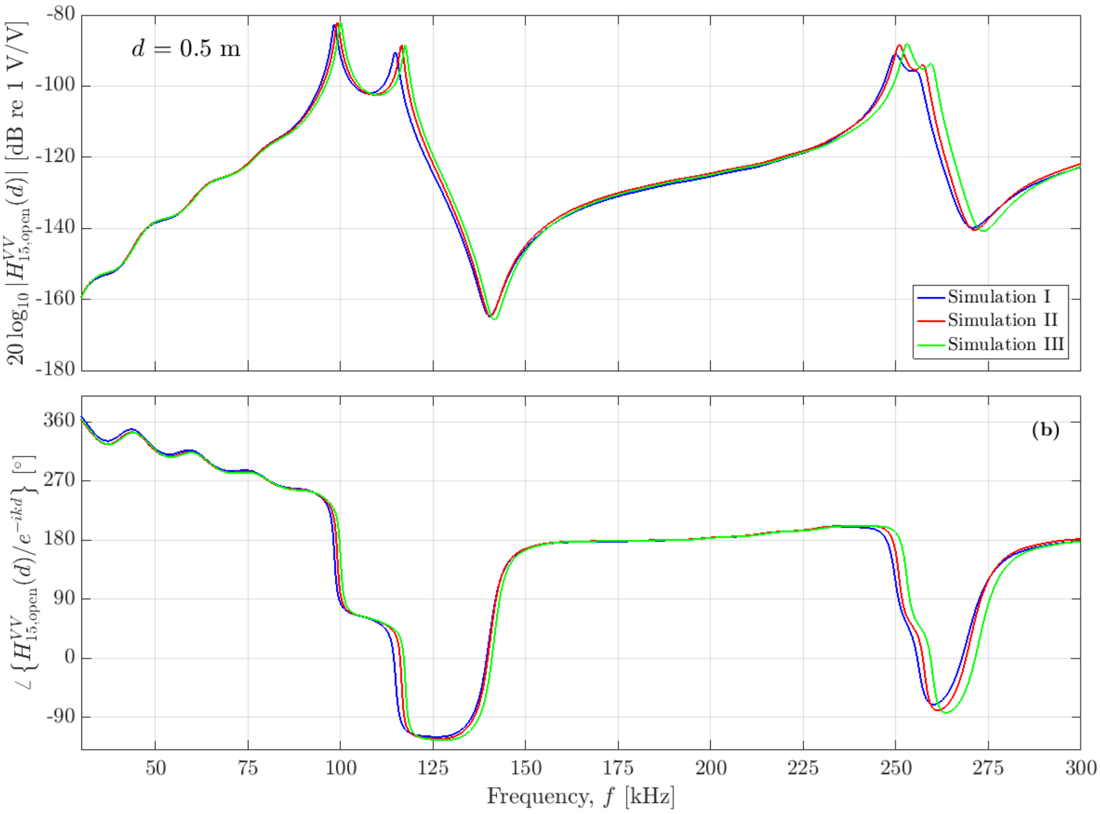

FIGURE 5.22: Simulated transferfunction H^{VV}_{15open} for magnitude a) and slowly varying phase b) for three different simulationd using different material data and disk dimentions.

higher in frequency for the dip.

For the slowly varying phase in Fig. 5.22 b) an increase 360° is observed in Simulation III compared to Simulation I and II. The only change from Simulation II to Simulation III is a slight alteration in the dimensions of the simulated disk, from 10.01 x 2.041 mm^2 to 10.00 x 2.00 mm^2 and a slight change in the density of the air medium, from 12.05 to 1.18818 kg/m^3.

Simulation I is 0.9 kHz lower and 30.3° higher for the first undulation below 50 kHz, compared to Simulation II and III. For the area 95-150 kHz Simulation II is 8.0 kHz higher and Simulation III is 1.8 kHz higher than Simulation I. A larger shift in frequency is seen at 240-280 kHz, where the largest deviation is between Simulation I and II of 3.7 kHz. For the last dip in the slowly varying phase compared with Simulation I, Simulation II is 1.6 kHz higher and 9.22° lower and Simulation III is 3.6 kHz higher and 12.41° lower.

5.8 Comparing simulations with measurements

In this section the measured transfer functions H^{VV}_{0m6} and H^{VV}_{15open} measured using Setup I and Setup II are presented for four different separation distances; $d = 50$ cm, $d = 30$ cm, $d = 20$ cm and $d = 15$ cm. The measured transfer function H^{VV}_{15open} from Setup II, with and without diffraction correction, will also be presented and compared to the simulated transfer function for the different separation distances.

The recorded pulse form for different distances are presented in Appendix D and shows the pulses before any post-processing is performed.

5.8.1 Transfer function at 50 cm

The measured transfer function H_{0m6}^{VV} at separation distance $d = 50$ cm is presented in Fig. 5.23 for measurements preformed using Setup I and Setup II.

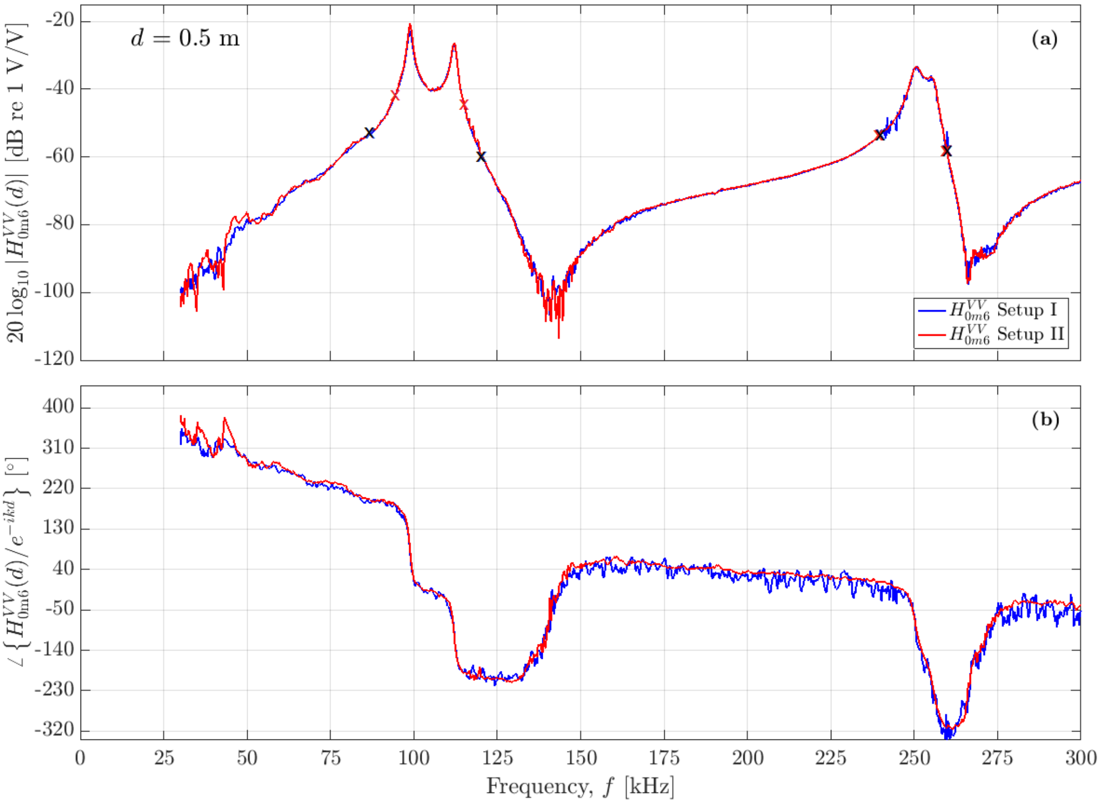

FIGURE 5.23: Measured transfer function H_{0m6}^{VV} for a) the magnitude and b) the slowly varying phase, θ_{0m6}^{slow}, for separation distance 50 cm using Setup I and Setup II.

The measurements presented in Fig. 5.23 were performed 6 months apart and as the equipment was moved during that time the plot speaks to the reproducibility of the measurements.

For the magnitude in Fig. 5.23 a) the undulations, at 30-85 kHz, are more clearly in the measurement done using Setup II. There is also a slight increase in magnitude by 1.8 dB for the first peak associated with R_1 and 0.75 for the second peak associated with R_1. At R_2 there is no difference observed between the magnitude of the two measurements.

In the range of 130-150 kHz noise is seen on the plot. A similarity is observed in this area for both measurements, but a shift of up to 2.3 kHz in frequency and a decrease in magnitude of up to 7 dB is observed in Setup II compared to Setup I. The same effect is observed in the noisy signal in the 260-280 kHz area, where a shift of up to 0.3 kHz in frequency and a decrease in magnitude of up to 0.5 dB is observed in Setup II compared to Setup I. This may point to this being coherent noise or a part of the signal, as it is relatively consistent in the two measurements.

For the slowly varying phase there are clear oscillations in the measurement using Setup II. It is believed that this is caused by the equipment being placed in the acoustic cage which the disks are mounted on, causing vibrations throughout the entire measurement.

The undulations observed in the range 30-85 kHz are more distinct for the measurement done using Setup II.

In the range of 150-240 kHz, where the phase is more stable, an increase of up to 10° is observed in the measurement done using Setup II compared to that of Setup I. This effect of lower value in the slowly varying phase in this area was postulated in [37] to be due to inaccuracy in alignment of the transmit-receiver pair, Fig. 5.19 support this and Setup I was performed with an inaccuracy of about 40 μm whereas for Setup II only inaccuracies below 10 μm were permitted. This all supports the claim that the difference in the slowly varying phace, apart from the oscillations in Setup I, are due to different degree of accuracy in alignment.

For the dip in the slowly varying phase in Fig. 5.23 b) around 260 kHz an increase of about 30° is observed in Setup II compared to Setup I and after the dip an increase of 20°- 30° is observed.

Comparison of transfer function H^{VV}_{15open}

The measurements presented in Fig. 5.23 are now used to find the transfer function H^{VV}_{15open} at separation distance $d = 50$ cm for measurements preformed using Setup I and Setup II, using Eq. 2.44. They are presented in Fig. 5.24.

The undulations observed in Fig. 5.23 a) are still clear in Fig. 5.24 a). The overall magnitude has decreased by about 60 dB and the difference in magnitude of the two measurements for the two peaks associated with R_1 are now lower. For the first peak the increase of magnitude in the measurement performed using Setup II compared to that of Setup I is 2 dB, and for the second peak no difference is observed.

At 112 kHz a small but noticeable dip in the magnitude occurs, which is not seen in H^{VV}_{0m6}.

For the slowly varying phase an increase of 10°- 20° is observed in Setup II compared to Setup I in the range 150-240 kHz. This is again believed to be due to higher accuracy in alignment in Setup II compared to Setup I, as discussed for Fig. 5.23 b).

Due to the quick oscillations in the Setup I measurements accurate comparisons are difficult. With this in mind, an increase of about 25°- 40° is observed for the second dip around 250-260 kHz and an increase of 10°- 30° is observed in the frequency range 260-300 kHz, for Setup II compared to Setup I.

Comparison with simulation

In Fig. 5.25 the measured transfer function H^{VV}_{15open} from Setup II is presented, with and without diffraction correction, C_{dif}, and compared to a simulated transfer function, for the distance $d = 50$ cm.

In Fig. 5.25 the transfer function H^{VV}_{15open} with and without diffraction correction are indistinguishable from one another in magnitude for frequencies below 150 kHz. For the first and second peak associated with R_1 they are higher in magnitude compared to the simulation with 1.7 dB and 3 dB, for the the first and second peak respectively.

For the range 150-225 the simulation is higher than H^{VV}_{15open} without diffraction correction by about 1 dB, for H^{VV}_{15open} with correction closer to the simulation.

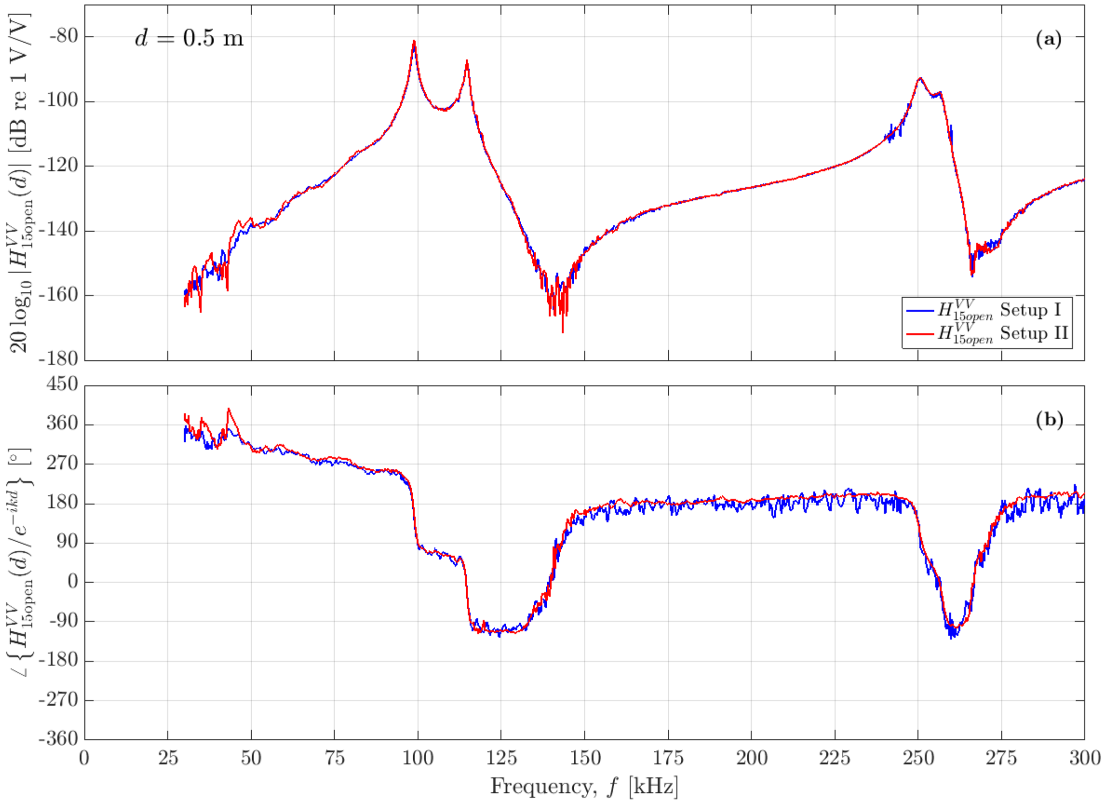

FIGURE 5.24: Measured transfer function H^{VV}_{15open} for a) the magnitude and b) the slowly varying phase, θ^{slow}_{15open}, for separation distance 50 cm using Setup I and Setup II.

For the first and second peak associated with R_2 H^{VV}_{15open} without diffraction correction is 1.7 dB and 1.38 dB lower that the simulation, respectively, and H^{VV}_{15open} with diffraction correction is 0.7 dB higher than that without.

For the dip after R_2 a decrease of 13.3 dB is observed for H^{VV}_{15open} without diffraction correction compared to simulation.

For the slowly varying phase undulations are observed in both simulated and measured H^{VV}_{15open} for the frequency range 50-90 kHz. For the frequency range 100-150 kHz H^{VV}_{15open} with diffraction correction is 25° higher than the simulation, and H^{VV}_{15open} without diffraction correction is closer to the simulation.

In the frequency range 150-240 kHz H^{VV}_{15open} with diffraction correction is 30° higher than the simulation, and H^{VV}_{15open} without diffraction correction is closer to the simulation.

In the dip at the frequency range 260-275 kHz H^{VV}_{15open} with diffraction correction is 10° lower than the simulation, and H^{VV}_{15open} without diffraction correction is 40° lower than the simulation.

For the frequency range above 275 kHz H^{VV}_{15open} with diffraction correction is 45° lower than the simulation, and H^{VV}_{15open} without diffraction correction is 25° lower than the simulation.

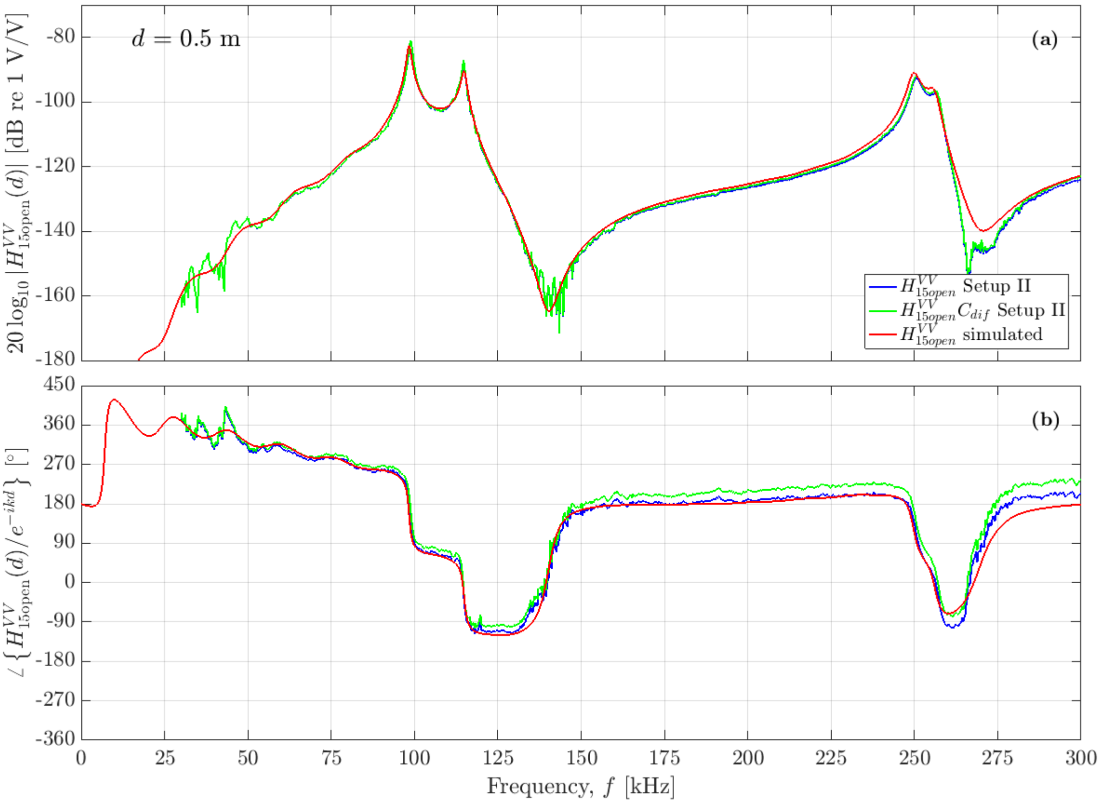

FIGURE 5.25: Measured transfer function H^{VV}_{15open} for a) the magnitude and b) the slowly varying phase, θ^{slow}_{15open}, for separation distance 50 cm using Setup II with and without diffraction correction, compared to simulation.

5.8.2 Transfer function at 30 cm

The measured transfer function H^{VV}_{0m6} at separation distance $d = 30$ cm is presented in Fig. 5.26 for measurements preformed using Setup I and Setup II.

As in the previous section, the measurements in Fig. 5.26 were performed 6 months apart and the equipment was moved between the measurements.

For the magnitude in Fig. 5.26 a) the undulations, at 30-85 kHz, are more clearly in the measurement done using Setup II, as for the case of $d = 50$. There is a slight increase in magnitude by 0.97 dB for the first peak associated with R_1 and 0.98 for the second peak associated with R_1. At R_2 oscillations in Setup I makes comparison difficult but an estimate of no more than 0.5 dB increase in magnitude of Setup II compared to that of Setup I is found.

A dip is observed in the Setup II measurement at 198.8 kHz of about 8 dB. A similar, but smaller effect is observed in Setup I at 224.9 kHz.

For the slowly varying phase in Fig. 5.26 b) the range in degrees is much larger than that of $d = 50$ cm, cf. Fig. 5.23 b). There are clear oscillations in the measurement using Setup II. As mentioned before, it is believed that this is caused by the equipment being placed in the acoustic cage which the disks are mounted on, causing vibrations throughout the entire measurement.

An overall larger discrepancy is observed in the comparison with the slowly varying phase from Setup I and that of Setup II. This may point to an increased need for accuracy in alignment for smaller separation distances. For the frequency

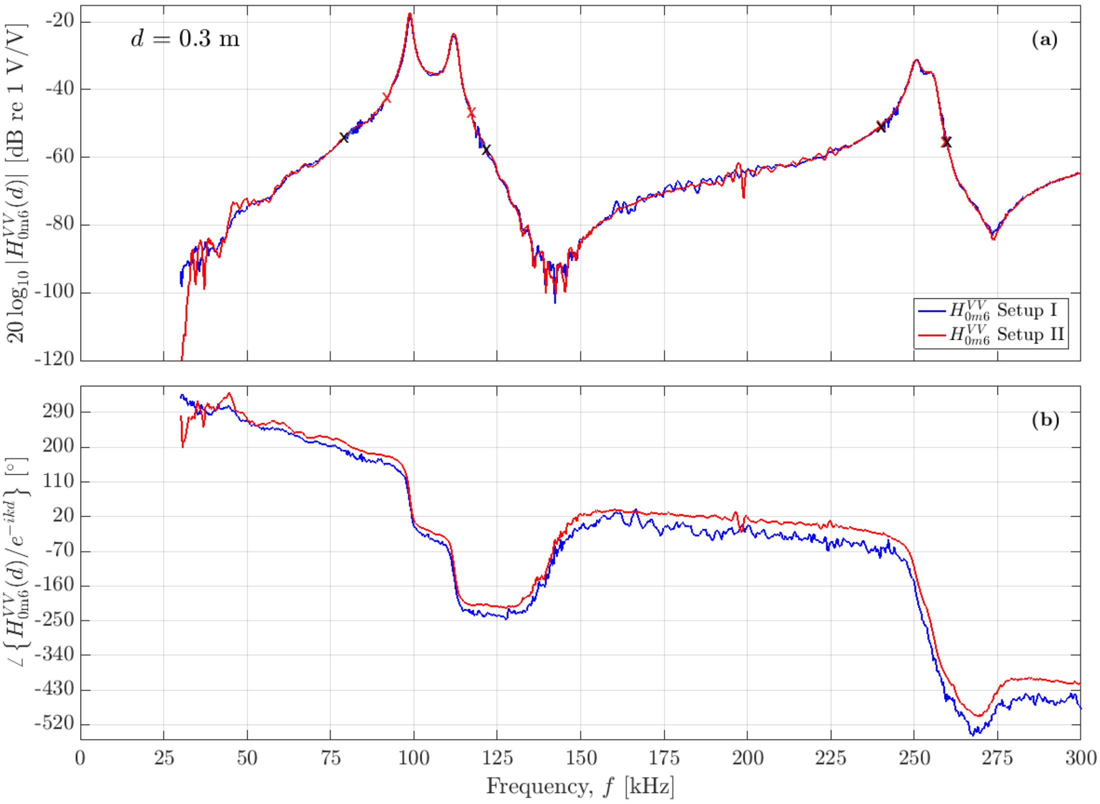

FIGURE 5.26: Measured transfer function H_{0m6}^{VV} for a) the magnitude and b) the slowly varying phase, θ_{0m6}^{slow}, for separation distance 30 cm using Setup I and Setup II.

range 50-95 kHz an increase of about 20° in Setup II compared to Setup I is observed. The same difference is for the frequency range 100-110 kHz and for the dip around 125 kHz.

In the range of 150-240 kHz, where the phase is more stable, an increase of 20°-40° is observed in the measurement done using Setup II compared to that of Setup I. This effect of lower value in the slowly varying phase in this area is as discussed in the previous section most likely due to the different degree of accuracy in alignment in Setup I and Setup II.

For the dip in the slowly varying phase at 268-269 kHz an upwards shift in frequency of 0.9 kHz and an increase of about 55° is observed in Setup II compared to Setup I.

Comparison of transfer function H_{15open}^{VV}

The measurements presented in Fig. 5.26 are now used to find the transfer function H_{15open}^{VV} at separation distance $d = 30$ cm for measurements preformed using Setup I and Setup II, using Eq. 2.44, and they are presented in Fig. 5.27.

The undulations observed in the magnitude in Fig. 5.26 a) are still clear in Fig. 5.27 a). The overall magnitude has decreased by about 60 dB and the difference in magnitude for the two peaks associated with R_1 are now lower. For the first peak the increase of magnitude in the measurement performed using Setup II compared to that of Setup I is 0.97 dB, and for the second peak no difference is observed.

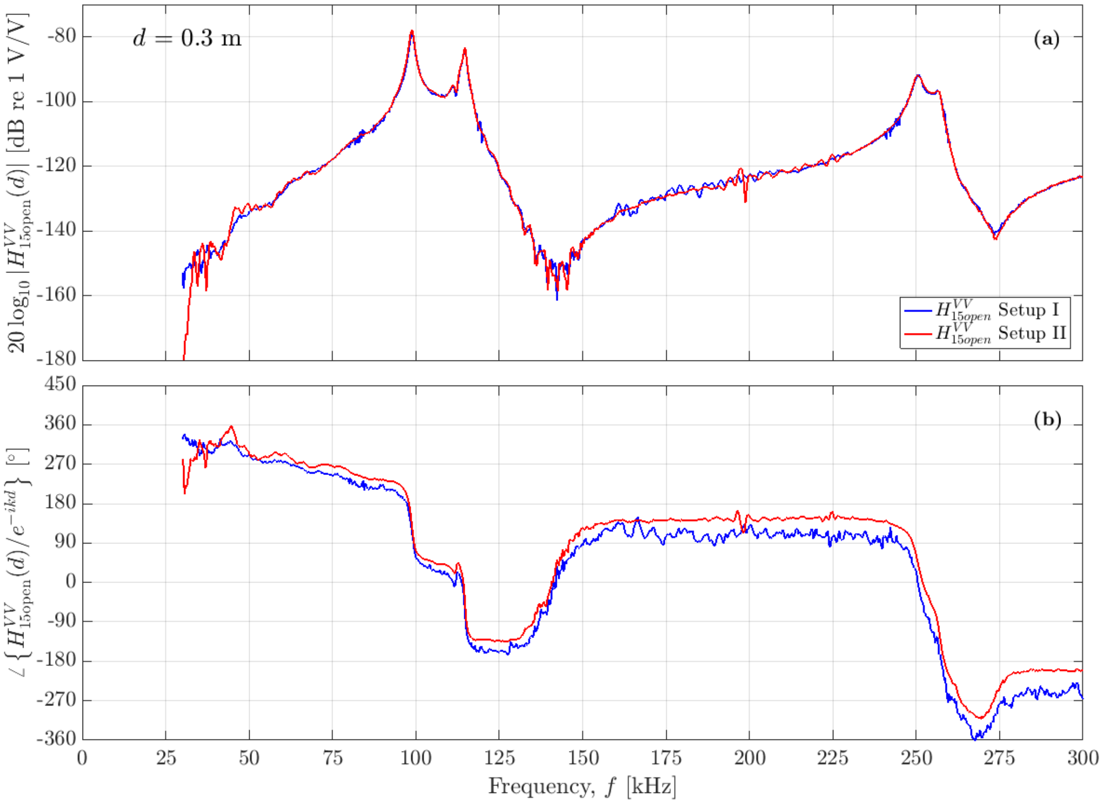

FIGURE 5.27: Measured transfer function H^{VV}_{15open} for a) the magnitude and b) the slowly varying phase, θ^{slow}_{15open}, for separation distance 30 cm using Setup I and Setup II.

At 112 kHz a dip in the magnitude occurs, which is not seen in H^{VV}_{0m6}. This is the same effect seen in Fig. 5.23 a) for a separation distance of 50 cm, but the dip is now larger and more visible.

For the first peak associated with R_2 an increase of magnitude in the measurement performed using Setup II compared to that of Setup I of 0.4 dB is observed, and for the second peak no difference is observed.

The dip after R_2 has an upward shift in frequency of 0.6 kHz and an decrease in magnitude of 1.4 dB for Setup II compared to Setup I.

For the slowly varying phase an increase of 20°- 80° is observed in Setup II compared to Setup I in the range 150-240 kHz. This is again believed to be due to higher accuracy in alignment in Setup II compared to Setup I, as discussed in the previous section.

A slight shift in frequency is observed for the last peak, with a higher frequency of 0.6 kHz for Setup II compared to Setup I and an increase in magnitude of 44.4 dB. After the peak the slowly varying phase of Setup II is approximately 50°- 70° higher than that of Setup I.

Comparison with simulation

In Fig. 5.28 the measured transfer function H^{VV}_{15open} from Setup II is presented, with and without diffraction correction, C_{dif}, and compared to a simulated transfer function, for the distance $d = 30$ cm.

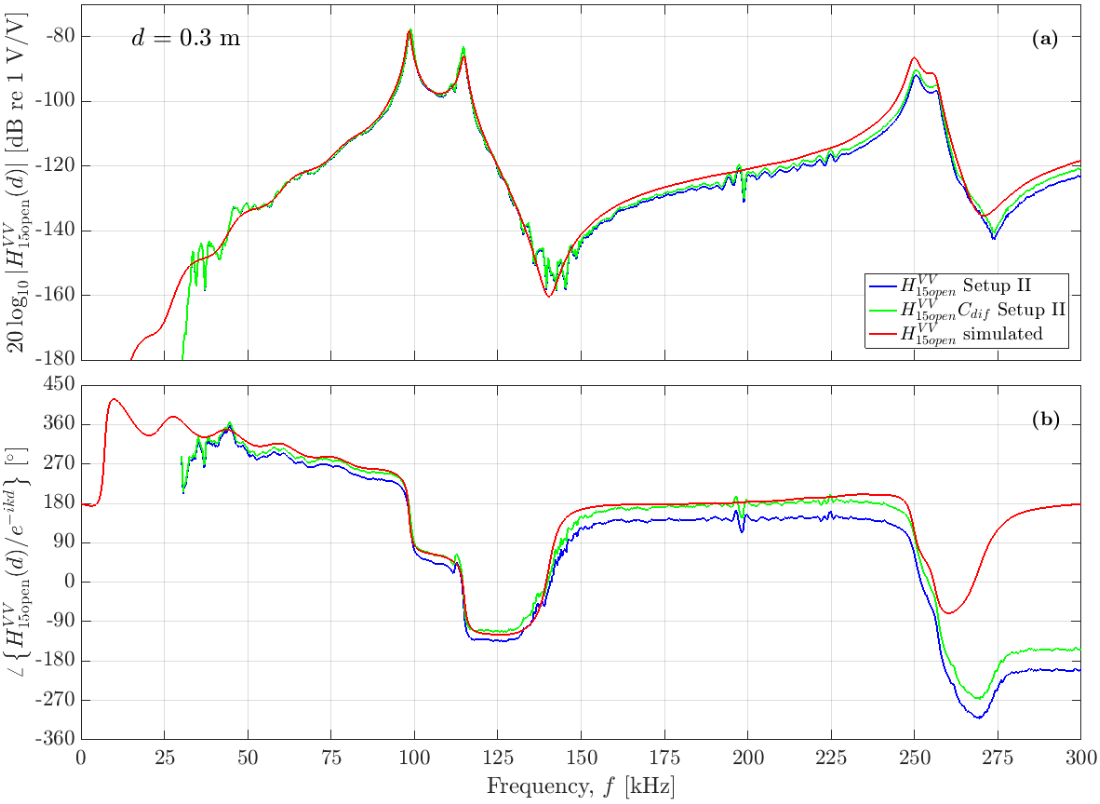

FIGURE 5.28: Measured transfer function H^{VV}_{15open} for a) the magnitude and b) the slowly varying phase, θ^{slow}_{15open}, for separation distance 30 cm using Setup II with and without diffraction correction, compared to simulation.

In Fig. 5.28 the transfer function H^{VV}_{15open} with and without diffraction correction are indistinguishable from one another in magnitude for frequencies below 150 kHz. For the first and second peak associated with R_1 they are higher in magnitude compared to the simulation with 0.61 dB and 3.13 dB, for the the first and second peak respectively.

For the range 150-225 the simulation is higher in magnitude than H^{VV}_{15open} without diffraction correction by about 2 dB, with H^{VV}_{15open} with correction closer to the simulation.

For the first and second peak associated with R_2, H^{VV}_{15open} without diffraction correction is 5.45 dB and 5.22 dB lower that the simulation, respectively, and H^{VV}_{15open} with diffraction correction is 2 dB higher than that without.

For the dip after R_2 an upward shift in frequency of 4.1 kHz and a decrease of 3.5 dB is observed for H^{VV}_{15open} without diffraction correction compared to simulation. H^{VV}_{15open} with diffraction correction is 2 dB above that without.

For the slowly varying phase in Fig. 5.28 b) H^{VV}_{15open} without diffraction correction is now closest to the simulation, unlike for the case with $d = 50$ cm where H^{VV}_{15open} without diffraction correction was closest. In Fig. 5.28 undulations are observed in both simulated and measured H^{VV}_{15open} for the frequency range 50-90 kHz.

For the frequency range 150-240 kHz H^{VV}_{15open} without diffraction correction is about 40° lower than the simulation, and H^{VV}_{15open} without diffraction correction is about 10° lower than the simulation.

A clear peak is observed at 224.9 kHz, and this matches a peak in the magnitude. The cause of this is unclear, but as the effect is present in both measurements in Fig. 5.27 it may be reasonable to think that it is caused by a resonance or a reflection in the acoustic setup that is present at a separation distance of 30 cm.

In the dip at the frequency range 250-275 kHz H^{VV}_{15open} with diffraction correction is 10 kHz higher and 197° lower than the simulation, and H^{VV}_{15open} without diffraction correction is 9.8 kHz higher and 239.52° lower than the simulation.

For the frequency range above 275 kHz H^{VV}_{15open} with diffraction correction is about 150° lower than the simulation, and H^{VV}_{15open} without diffraction correction is 160°- 170° lower than the simulation.

5.8.3 Transfer function at 20 cm

The measured transfer function H^{VV}_{0m6} at separation distance $d = 20$ cm is presented in Fig. 5.29 for measurements preformed using Setup I and Setup II.

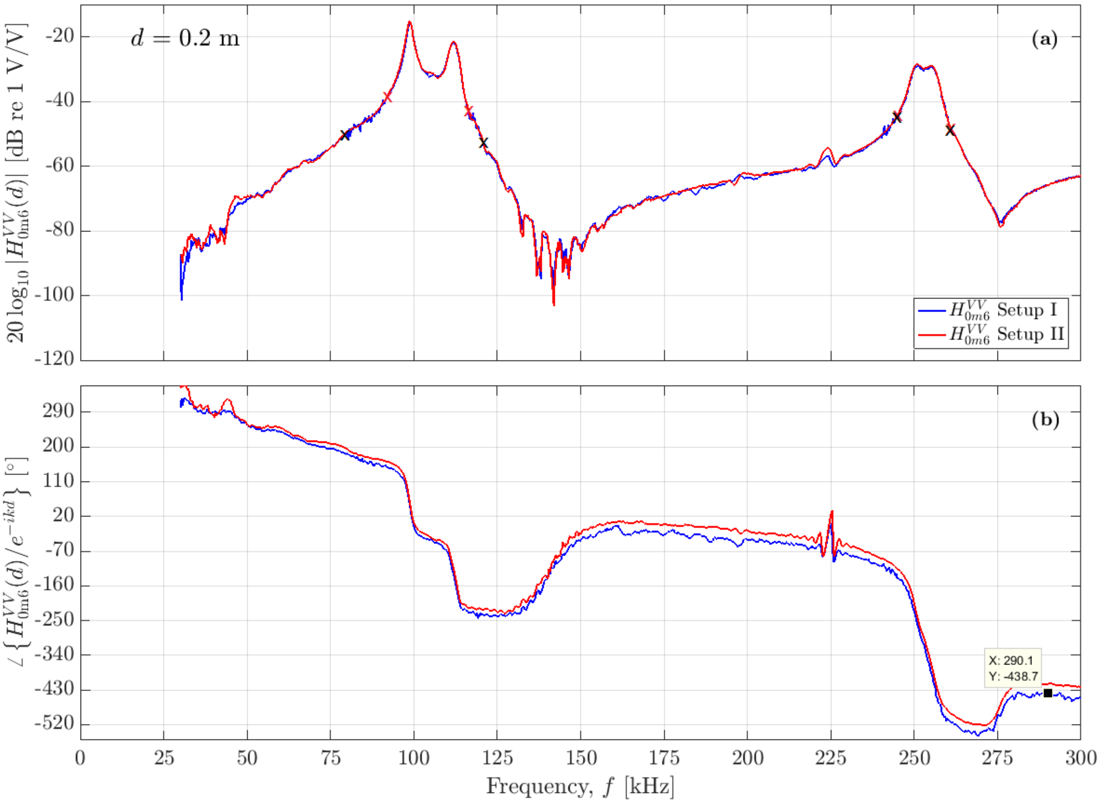

FIGURE 5.29: Measured transfer function H^{VV}_{0m6} for a) the magnitude and b) the slowly varying phase, θ^{slow}_{0m6}, for separation distance 20 cm using Setup I and Setup II.

As in the two previous section, the measurements in Fig. 5.29 were performed 6 months apart and the equipment was moved between the measurements.

For the magnitude in Fig. 5.29 a) the undulations, at 30-85 kHz, are more clearly in the measurement done using Setup II, as for the case of $d = 50$ and $d = 30$.

There is a slight increase in magnitude of 0.4 dB for the first peak associated with R_1 and 0.5 for the second peak associated with R_1. At R_2 oscillations in Setup I makes comparison difficult but an estimate of no more than 1 dB increase in magnitude of Setup II compared to that of Setup I is found.

The noisy area around 130-150 kHz line up very good for the frequencies with the highest difference at 0.3 kHz and a dip in the magnitude of 2 dB lower for Setup II compared to Setup I. This may indicate that the noise is coherent noise or not noise at all, but part of the signal measured at $d = 20$ cm. Since the time between the two measurements is as long as it it and the setups are not identical, this is a very interesting find and should be investigated further.

A peak is observed at 224 kHz for both measurements, with a 2 dB lager peak for Setup II compared to Setup I. The cause of this peak is unclear and may be due to reflections or resonances present at the separation distance $d = 20$ cm.

For the last dip in the magnitude a decrease of about 1.3 dB and an upward shift in frequency of 1 kHz is observed in Setup II compared to Setup I.

For the slowly varying phase in Fig. 5.29 b) the range in degrees is much larger than that of $d = 50$ cm, cf. Fig. 5.23 b), as for the case of $d = 30$ cm. There are clear oscillations in the measurement using Setup I, probably caused by the equipment being placed in the measurement cage.

An overall larger discrepancy is observed in the comparison with the slowly varying phase from Setup I and that of Setup II. This may point to an increased need for accuracy in alignment for smaller separation distances, as for the case of $d = 30$ cm. For the frequency range 50-95 kHz an increase of about 15° in Setup II compared to Setup I is observed. The same difference is for the frequency range 100-110 kHz and for the dip around 125 kHz.

In the range of 150-220 kHz, where the phase is more stable, an increase of 20°-40° is observed in the measurement done using Setup II compared to that of Setup I. This effect of lower value in the slowly varying phase in this area is as discussed in the previous section most likely due to the different degree of accuracy in alignment in Setup I and Setup II.

For the peak in the slowly varying phase at 225.2 kHz for Setup I an upwards shift in frequency of 0.3 kHz and an increase of about 35° is observed in Setup II compared to Setup I.

At the last dip in the slowly varying phase in the frequency range 260-280 kHz an increase of about 15° in Setup II compared to Setup I is observed and an increase of about 35° is observed after the dip.

Comparison of transfer function H^{VV}_{15open}

The measurements presented in Fig. 5.29 are now used to find the transfer function H^{VV}_{15open} at separation distance $d = 20$ cm for measurements preformed using Setup I and Setup II, using Eq. 2.44. They are presented in Fig. 5.30.

The undulations in the magnitude observed in Fig. 5.29 a) are still clear in Fig. 5.30 a). The overall magnitude has decreased by about 60 dB and the difference in magnitude for the two peaks associated with R_1 are now lower. For the first peak the increase of magnitude in the measurement performed using Setup II compared to that of Setup I is 0.5 dB, and for the second peak 0.3 dB.

At 112 kHz a dip in the magnitude occurs, which is not seen in H^{VV}_{0m6}. This is the same effect seen in Fig. 5.23 and 5.26 for a separation distance of 50 cm and 30 cm, but the dip is now larger and more visible.

For the two peaks associated with R_2 an increase of magnitude in the measurement performed using Setup II compared to that of Setup I of 1 dB is observed.

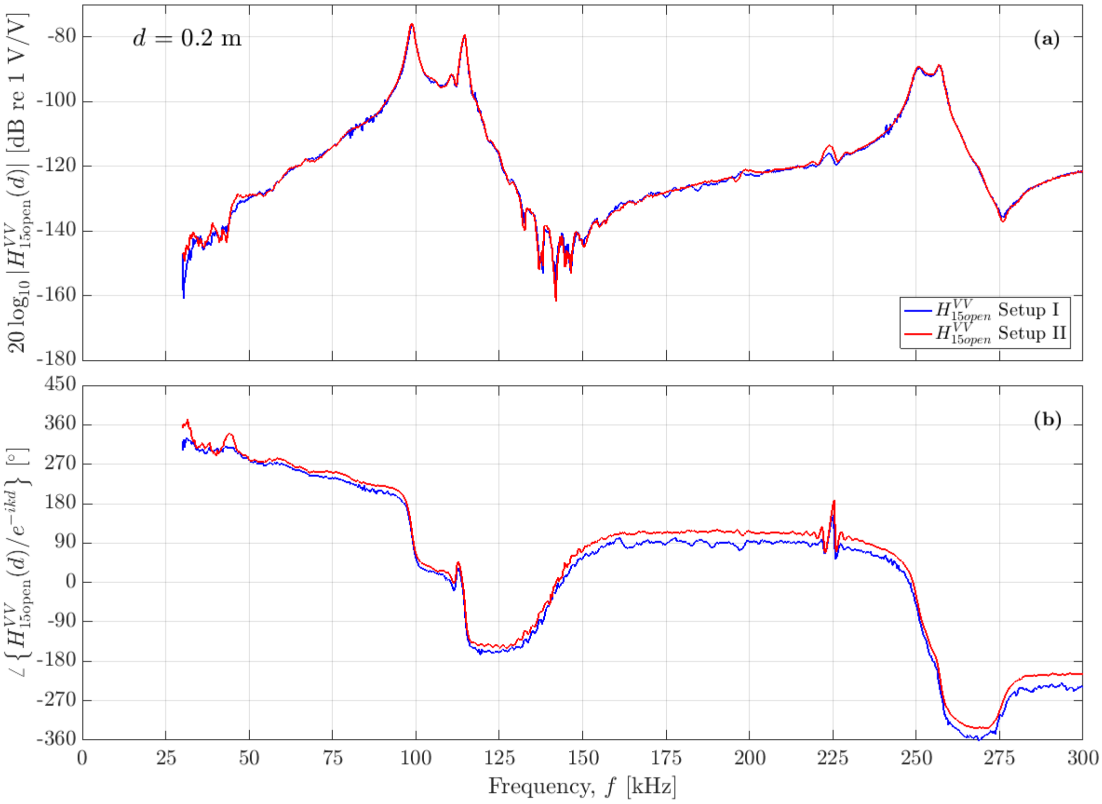

FIGURE 5.30: Measured transfer function H^{VV}_{15open} for a) the magnitude and b) the slowly varying phase, θ^{slow}_{15open}, for separation distance 20 cm using Setup I and Setup II.

The dip after R_2 has an upward shift in frequency of 1 kHz and an decrease in magnitude of 1.3 dB for Setup II compared to Setup I.

For the slowly varying phase in Fig. 5.30 b) an increase of 20°- 50° is observed in Setup II compared to Setup I in the range 150-220 kHz. This is again believed to be due to higher accuracy in alignment in Setup II compared to Setup I, as discussed in the previous section.

A slight shift in frequency is observed for the last dip around 270 kHz, with an increase of 20° for Setup II compared to Setup I. After the peak the slowly varying phase of Setup II is approximately 20°- 30° higher than that of Setup I.

Comparison with simulation

In Fig. 5.31 the measured transfer function H^{VV}_{15open} from Setup II is presented, with and without diffraction correction, C_{dif}, and compared to a simulated transfer function, for the distance $d = 20$ cm.

For the magnitude in Fig. 5.31 a) for the first and second peak associated with R_1 an increase in the magnitude og H^{VV}_{15open} without diffraction correction compared to the simulation of 0.91 dB and 2.19 dB, for the the first and second peak respectively. H^{VV}_{15open} with diffraction correction is 1.2 dB and 0.5 dB above H^{VV}_{15open} without diffraction correction for the two peaks, respectively.

In the frequency range of 130-150 kHz the dip in the measured signal is 2 kHz higher than the simulation and 5 dB lower in magnitude.

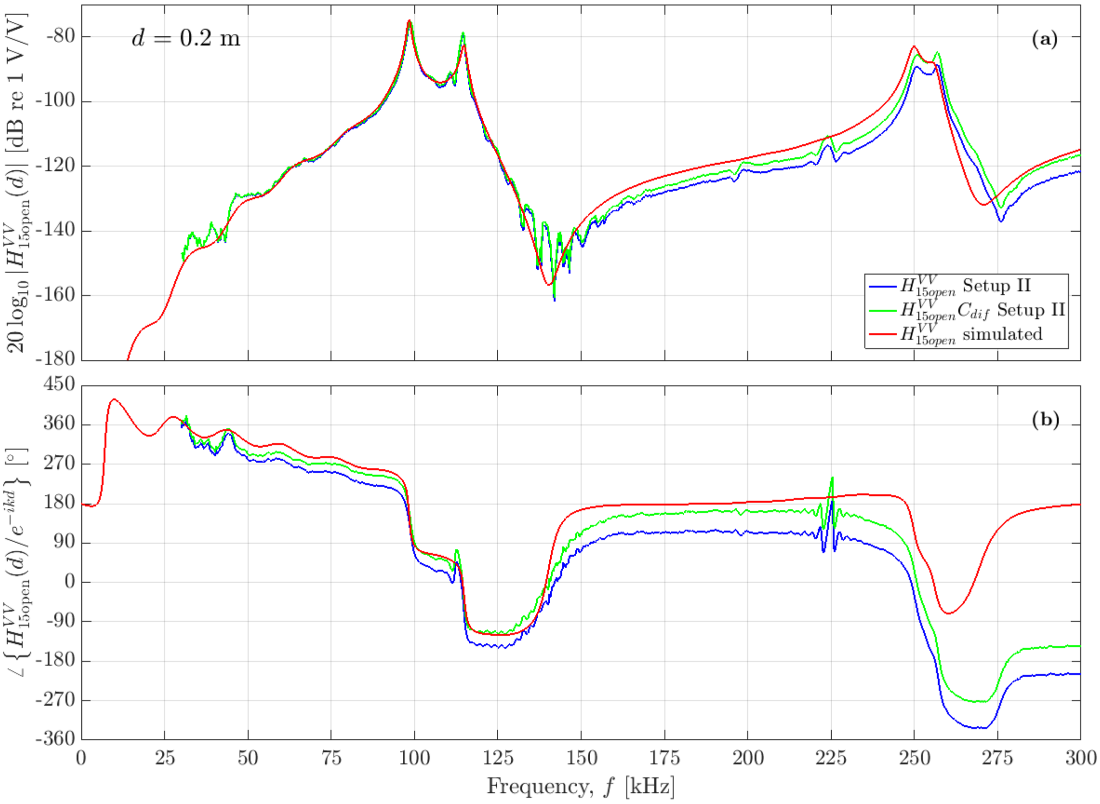

FIGURE 5.31: Measured transfer function H^{VV}_{15open} for a) the magnitude and b) the slowly varying phase, θ^{slow}_{15open}, for separation distance 20 cm using Setup II with and without diffraction correction, compared to simulation.

For the frequency range 150-220 the simulation is higher than H^{VV}_{15open} without diffraction correction by about 6 dB, with H^{VV}_{15open} with correction 4 dB below the simulation.

For the first and second peak associated with R_2, H^{VV}_{15open} without diffraction correction is 6.22 dB and 0.75 dB lower that the simulation, respectively. H^{VV}_{15open} with diffraction correction is 4.3 dB and 4 dB higher than that without for the two peaks, respectively.

For the dip after R_2 an upward shift in frequency of 6.1 kHz and a decrease of 5.4 dB is observed for H^{VV}_{15open} without diffraction correction compared to simulation. H^{VV}_{15open} with diffraction correction is 4 dB above that without.

For the slowly varying phase in Fig. 5.31 b) H^{VV}_{15open} without diffraction correction is now closest to the simulation, unlike for the case with $d = 50$ cm where H^{VV}_{15open} without diffraction correction was closest. Undulations are observed in both simulated and measured H^{VV}_{15open} for the frequency range 50-90 kHz.

For the frequency range 150-220 kHz H^{VV}_{15open} without diffraction correction is about 65° lower than the simulation, and H^{VV}_{15open} without diffraction correction is about 20° lower than the simulation.

A clear peak is observed at 225.2 kHz in the measured signals, and this matches a peak in the magnitude. The cause of this is unclear, but as the effect is present in both measurements in Fig. 5.30 it may be reasonable to think that it is caused by a resonance or a reflection in the acoustic setup that is present at a separation distance of $d = 20$ cm. A similar effect is observed for the separation distance of 30 cm in Fig. 5.27 b) and 5.28 b) but at 224.9 kHz.

In the dip at the frequency range 250-270 kHz H_{15open}^{VV} with diffraction correction is 6.9 kHz higher and 260.84° lower than the simulation, and H_{15open}^{VV} without diffraction correction is 200.24° lower than the simulation.

5.8.4 Transfer function at 15 cm

The measured transfer function H_{0m6}^{VV} at separation distance $d = 15$ cm is presented in Fig. 5.32 for measurements preformed using Setup I and Setup II.

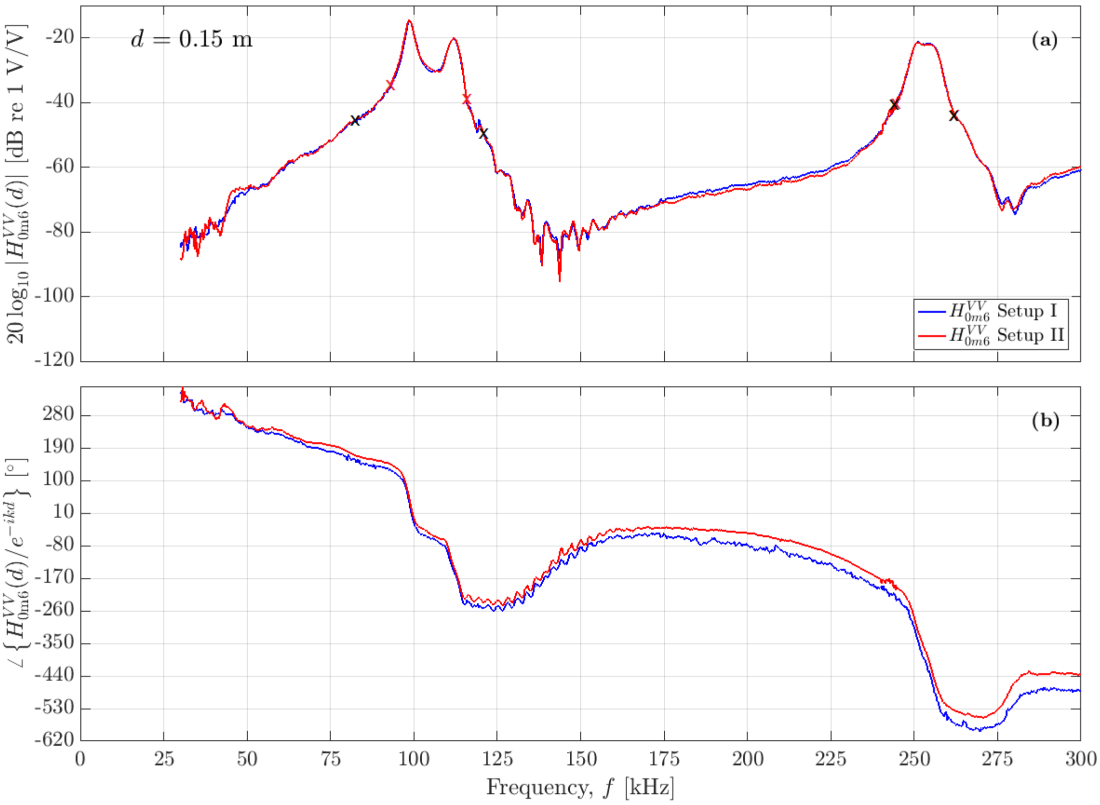

FIGURE 5.32: Measured transfer function H_{0m6}^{VV} for a) the magnitude and b) the slowly varying phase, θ_{0m6}^{slow}, for separation distance 15 cm using Setup I and Setup II.

As in the three previous section, the measurements in Fig. 5.32 were performed 6 months apart and the equipment was moved between the measurements.

For the magnitude in Fig. 5.32 a) the undulations, at 30-85 kHz, are more clearly in the measurement done using Setup II, as for the case of $d = 50$ cm, $d = 30$ cm and $d = 20$ cm. There is a slight increase in magnitude of 0.2 dB for the first peak associated with R_1 and 0.15 for the second peak associated with R_1. At R_2 oscillations in Setup I makes comparison difficult but an estimate of no more than 1 dB increase in magnitude of Setup II compared to that of Setup I is found.

The noisy area around 130-150 kHz line up very good for the frequencies. A dip in the magnitude of 7 dB lower for Setup II compared to Setup I is observed. This may indicate, as in the previous section, that this is coherent noise or not noise at all, but part of the signal measured at $d = 15$ cm, as for the case of $d = 20$ cm and tendencies observed in the cases of $d = 30$ cm and $d = 50$ cm.

At the two peaks associated with R_2 no more than 0.5 dB difference is found between the two measurements, with the measurement performed using Setup II as the highest of the two in magnitude.

For the last dip in the magnitude a decrease of about 2 dB is observed in Setup II compared to Setup I and after the dip a difference of 2 dB is observed.

For the slowly varying phase in Fig. 5.32 b) the range in degrees is much larger than that of $d = 50$ cm, cf. Fig. 5.23, as for the case of $d = 30$ cm and $d = 20$ cm. There are again clear oscillations in the measurement using Setup I, probably caused by the equipment being placed in the measurement cage.

An overall discrepancy is observed in the comparison with the slowly varying phase from Setup I and that of Setup II. This may point to an increased need for accuracy in alignment for smaller separation distances, as for the case of $d = 30$ cm and $d = 20$ cm. For the frequency range 50-95 kHz an increase of about 10°- 30° in Setup II compared to Setup I is observed. The same difference is for the frequency range 100-110 kHz and for the dip around 125 kHz.

In the range of 150-250 kHz, where the phase is more stable, an increase of 20°- 50° is observed in the measurement done using Setup II compared to that of Setup I. This effect of lower value in the slowly varying phase in this area is as discussed in the previous sections most likely due to the different degree of accuracy in alignment in Setup I and Setup II.

At the last dip in the slowly varying phase in the frequency range 260-280 kHz an increase of about 40° in Setup II compared to Setup I is observed and an increase of about 40° is observed after the dip.

Comparison of transfer function H^{VV}_{15open}

The measurements presented in Fig. 5.32 are now used to find the transfer function H^{VV}_{15open} at separation distance $d = 15$ cm for measurements preformed using Setup I and Setup II, using Eq. 2.44, and they are presented in Fig. 5.33.

The undulations observed in the magnitude in Fig. 5.32 a) are still clear in Fig. 5.33 a). The overall magnitude has decreased by about 60 dB and the difference in magnitude for the two peaks associated with R_1 are now lower. For the first peak the increase of magnitude in the measurement performed using Setup II compared to that of Setup I is 0.3 dB for both peaks.

At 112 kHz a dip in the magnitude occurs, which is not seen in H^{VV}_{0m6}. This is the same effect seen in Fig. 5.23 a), 5.26 a) and 5.29 a) for a separation distance of 50 cm, 30 cm and 20 cm, but the dip is now even larger and more visible.

For the two peaks associated with R_2 an increase of magnitude in the measurement performed using Setup II compared to that of Setup I are indistinguishable.

The dip after R_2 has an upward shift of a decrease in magnitude of 2 dB for Setup II compared to Setup I and a difference of 1 dB is observed after the dip.

For the slowly varying phase an increase of 50°- 90° is observed in Setup II compared to Setup I in the range 150-220 kHz. This is again believed to be due to higher accuracy in alignment in Setup II compared to Setup I, as discussed in the previous sections.

A peak is observed for the slowly varying phase at 112.9 kHz. Quick oscillations follow after this peak for the frequency range 117-157 kHz, which vary with approximately 15°- 20°.

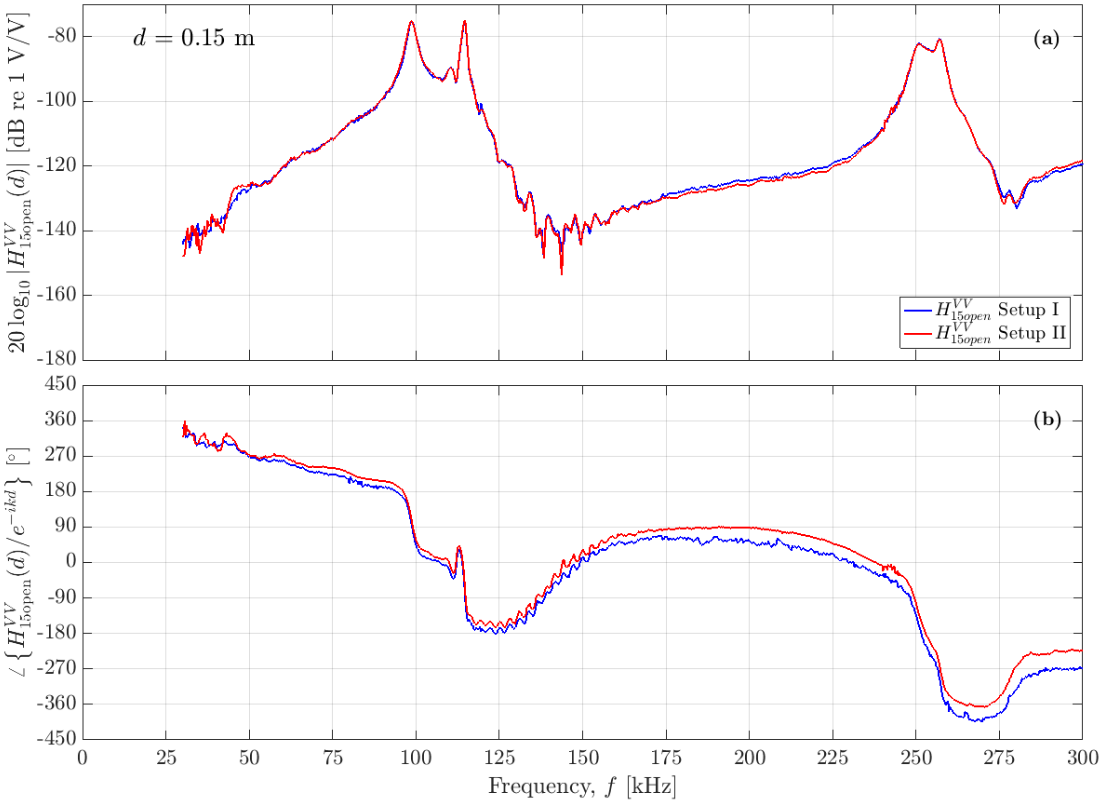

FIGURE 5.33: Measured transfer function H^{VV}_{15open} for a) the magnitude and b) the slowly varying phase, θ^{slow}_{15open}, for separation distance 15 cm using Setup I and Setup II.

A slight shift in frequency is observed for the last dip around 270 kHz, with an increase of 30° for Setup II compared to Setup I. After the peak the slowly varying phase of Setup II is approximately 45° higher than that of Setup I.

Comparison with simulation

In Fig. 5.34 the measured transfer function H^{VV}_{15open} from Setup II is presented, with and without diffraction correction, C_{dif}, and compared to a simulated transfer function, for the distance $d = 15$ cm.

For the magnitude in Fig. 5.34 a) for the first and second peak associated with R_1 an increase in the magnitude og H^{VV}_{15open} without diffraction correction compared to the simulation of 3.08 dB and a decrease of 5.11 dB, for the the first and second peak respectively. H^{VV}_{15open} with diffraction correction is 1 dB and 1.5 dB above H^{VV}_{15open} without diffraction correction for the two peaks, respectively.

In the frequency range of 130-150 kHz the dip in the measured signal is 3.5 kHz higher than the simulation and 0.6 dB higher in magnitude.

For the frequency range 170-225 the simulation is higher than H^{VV}_{15open} without diffraction correction by about 10 dB, with H^{VV}_{15open} with correction 7 dB below the simulation.

For the first and second peak associated with R_2, H^{VV}_{15open} without diffraction correction is 1.77 dB lower and 4.78 dB higher that the simulation, respectively, and

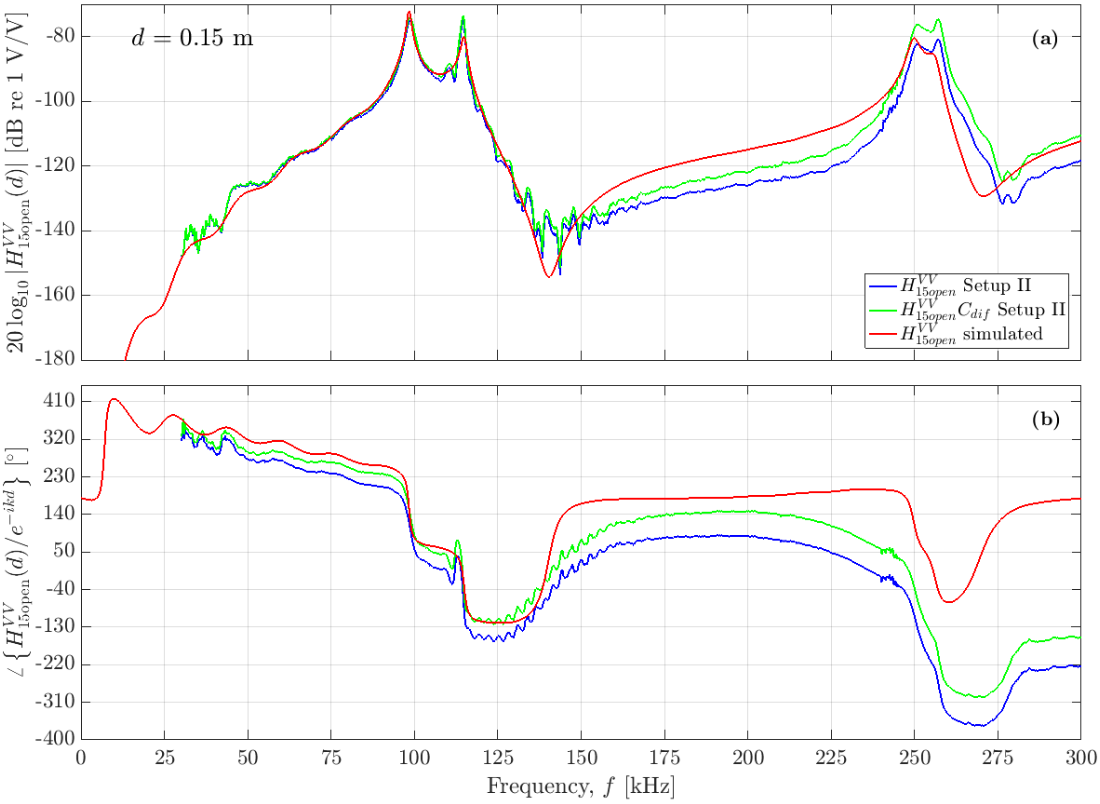

FIGURE 5.34: Measured transfer function H^{VV}_{15open} for a) the magnitude and b) the slowly varying phase, θ^{slow}_{15open}, for separation distance 15 cm using Setup II with and without diffraction correction, compared to simulation.

H^{VV}_{15open} with diffraction correction is 4.5 dB higher than that without for the both peaks.

For the dip after R_2 a upward shift in frequency of 6.1 kHz and a decrease of 2.7 dB is observed for H^{VV}_{15open} without diffraction correction compared to simulation. H^{VV}_{15open} with diffraction correction is 15 dB above that without. After the last dip R_2 H^{VV}_{15open} without diffraction correction is about 5 dB lower than the simulation and R_2 H^{VV}_{15open} with diffraction correction is about 2 dB higher than the simulation.

For the slowly varying phase in Fig. 5.34 b) H^{VV}_{15open} without diffraction correction is now closest to the simulation, only 20°- 30° below the simulation, unlike for the case with $d = 50$ cm where H^{VV}_{15open} without diffraction correction was closest. Undulations are observed in both simulated and measured H^{VV}_{15open} for the frequency range 50-90 kHz.

For the frequency range 150-210 kHz H^{VV}_{15open} without diffraction correction is about 90° lower than the simulation, and H^{VV}_{15open} without diffraction correction is about 40° lower than the simulation.

A small peak is observed at 242.5 kHz in the measured signals the effect is not present in both measurements in Fig. 5.33.

In the dip at the frequency range 250-275 kHz H^{VV}_{15open} with diffraction correction is 7.5 kHz higher and 224.48° lower than the simulation, and H^{VV}_{15open} without diffraction correction is 294.18° lower than the simulation. After 285 kHz H^{VV}_{15open}

with diffraction correction is about 330.3° lower than the simulation, and H_{15open}^{VV} without diffraction correction is 398.6° lower than the simulation

5.8.5 Repeatability

In Fig. 5.35 four measurements performed consecutively are presented as the transfer function H_{0m6}^{VV}, with a) the magnitude, $|H_{0m6}^{VV}|$, and b) the phase, $\angle H_{0m6}^{VV}$, of the transfer function, describing the full acoustic setup. The measurements are done using Setup II and all use the same noise measurement, as the electrical noise is assumed to be constant within the day the measurements were performed.

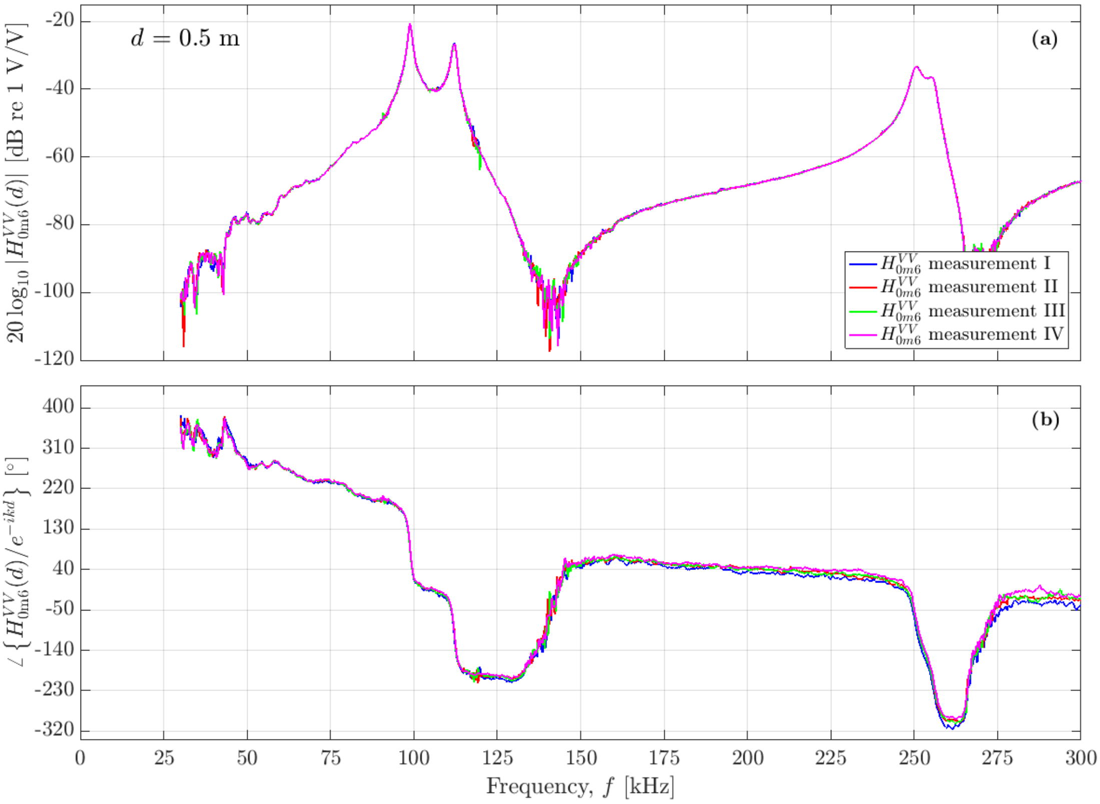

FIGURE 5.35: Transfer function H_{0m6}^{VV} for a) the magnitude and b) the slowly varying phase, for four different measurements in Setup II.

From Fig. 5.35 a good agreement between the different measurements is seen. For the first two peaks, associated with R_1, no distinction can be made between the magnitude or the frequency for the four measurements.

For the two peaks associated with R_2 measurements II, III and IV are inseparable in magnitude and frequency. The first measurement however, differs from the other in magnitude only by an increase of 0.3 dB and 0.88 dB for the two peaks respectively.

In the frequency domain 150-240 kHz measurement I is higher than the other measurements by approximately 0.8 dB.

For the phase a deviation is found at 191 kHz where there is a decrease of 21.3 deg in measurement II compared to measurement I. Another deviation in the phase is observed between measurement I and measurement III at the dip associated with R_2, where measurement III has a decrease of 23.95 deg compared to measurement I. Lastly the largest deviation is found in the frequency range 280-300 kHz where deviations up to 30 deg can be seen, due to oscillations. In general measurement I and IV are higher than measurement II and III.

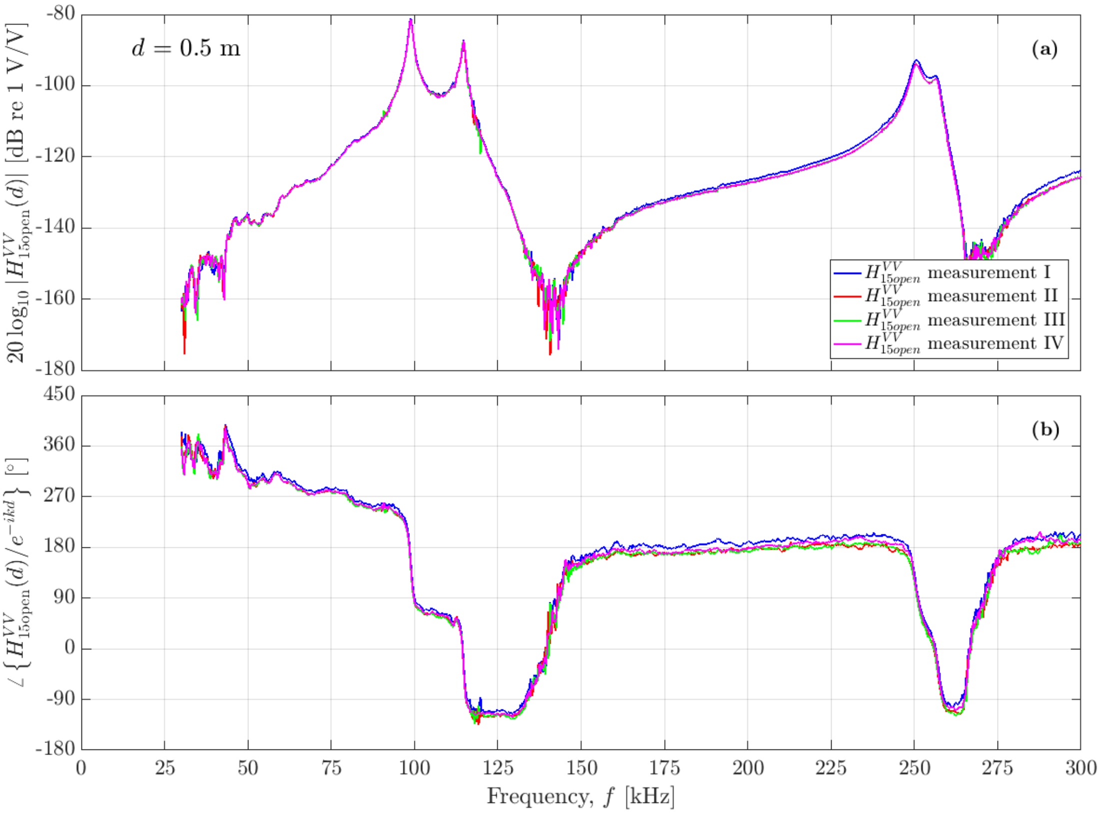

FIGURE 5.36: Transfer function H^{VV}_{15open} for a) the magnitude and b) the slowly varying phase, for four different measurements in Setup II.

From Fig. 5.36 a good agreement between the different measurements is seen, as in the case of H^{VV}_{0m6} in Fig. 5.35. For the first two peaks, associated with R_1, no distinction can be made between the magnitude or the frequency for the four measurements.

For the two peaks associated with R_2 measurements II, III and IV are inseparable in magnitude and frequency. The first measurement however, differs from the other in magnitude only by an increase of 1.3 dB for the first peak and 0.88 for the second peak.

In the frequency domain 150-240 kHz measurement I is higher than the other measurements by approximately 1.0 dB.

For the slowly varying phase a deviation is found at 191.4 kHz where there is a decrease of 19.8 deg in measurement II compared to measurement I. Another deviation in the phase is observed between measurement I and measurement III at the dip at 250-275 kHz, where measurement III has a decrease of 22.1 deg compared to measurement I. Lastly the largest deviation in phase is found in the frequency range 280-300 kHz where deviations up to 33 deg can be seen, due to oscillations. In general measurement I and IV are higher than measurement II and III.

5.9 Investigation of dip at R_1 in H^{VV}_{15open}

A small dip is observed at 112 kHz for the magnitude of the transfer function H^{VV}_{15open} measured at a separation distance of $d = 50$ cm. The same dip is seen at the same frequency, but with a larger effect, for $d = 30$ cm, $d = 20$ cm and $d = 15$ cm. This increase in the dip for shorter separation distances and the presence of a dip at all leads to further investigation. The effect was noticed in [37], but no explanation as to the cause or the physical effect of the dip has been found as of yet.

In order to investigate this dip at R_1 Eq. 2.44 is divided into parts and presented for the different separation distances, $d = 50$ cm, $d = 30$ cm, $d = 20$ cm and $d = 15$ cm.

Eq. 2.44 is divided into five parts; H^{VV}_{0m6}, H^{VV}_{15open}, C_{alpha}, C^{BPDC}_{dif} and the denominator that H^{VV}_{0m6} is divided by, here called H_{div}, where $H_{div} = H^{VV}_{0m1} \cdot H^{VV}_{5open5'} \cdot H^{VV}_{5'6} \cdot$.

Fig. 5.37 shows the magnitude and slowly varying phase of H^{VV}_{0m6} for all the four separation distances presented in the previous section.

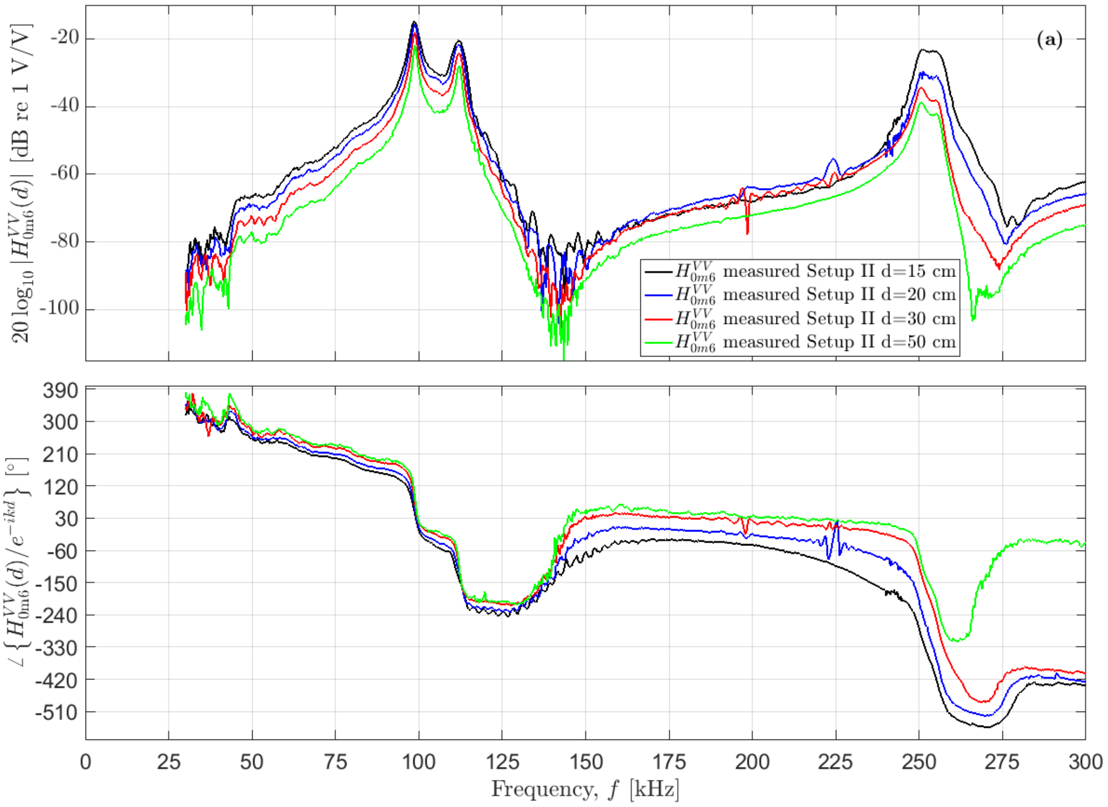

FIGURE 5.37: Measured transfer function H^{VV}_{0m6} for a) the magnitude and b) the slowly varying phase, θ^{slow}_{0m6}, using Setup II for separation distances $d = 50$ cm, $d = 30$ cm, $d = 20$ cm and $d = 15$ cm.

An increase in signal is seen for shorter separation distances, as well as clearer undulations. There is also a change in the shape of R_2, with the two peaks at a more equal magnitude at $d = 15$ cm and $d = 20$ cm than for $d = 30$ cm and $d = 50$ cm. In the two latter the first peak associated with R_2 is larger than the first.

Fig. 5.38 shows the magnitude and slowly varying phase of H^{VV}_{0m6} for all the four separation distances presented in the previous section.

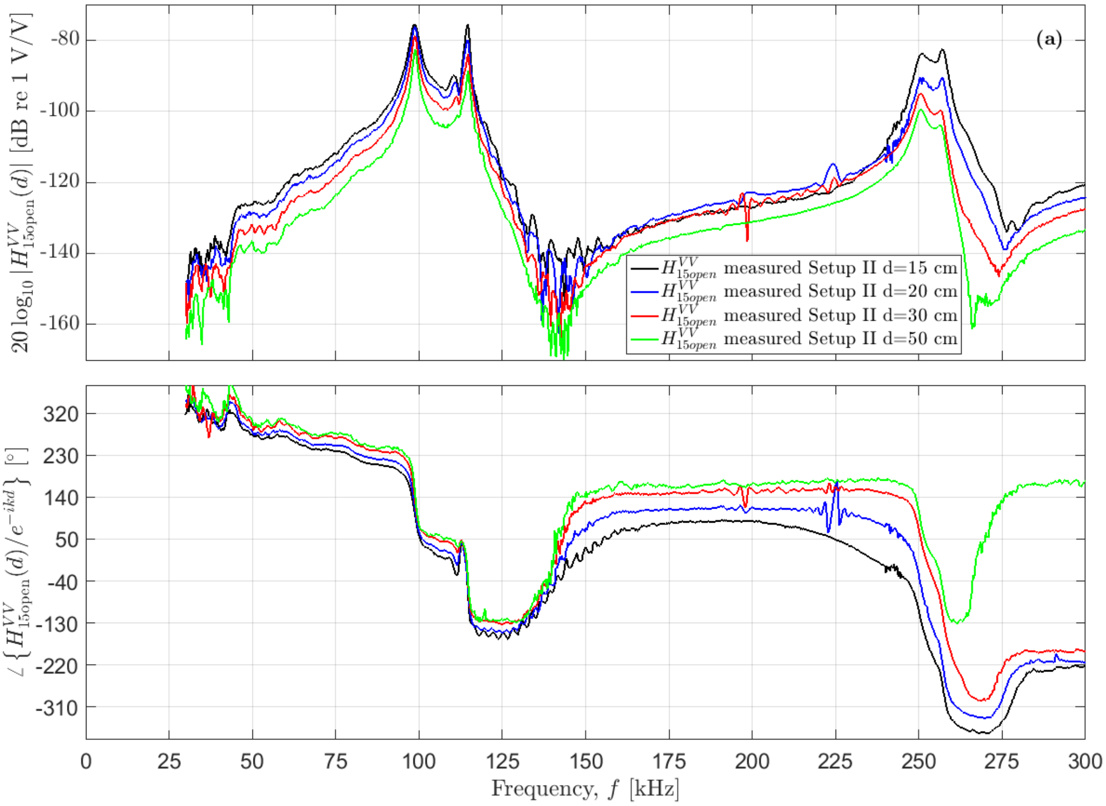

FIGURE 5.38: Measured transfer function H^{VV}_{15open} for a) the magnitude and b) the slowly varying phase, θ^{slow}_{15open}, using Setup II for separation distances $d = 50$ cm, $d = 30$ cm, $d = 20$ cm and $d = 15$ cm.

In Fig. 5.38 the dip in magnitude at R_1, at 112 kHz, is clearly seen increasing with decreasing separation distance. The same effect in magnitude of the two peaks associated with R_2 is seen as for H^{VV}_{0m6}, but they are more distinct and easier to separate as two peaks. The four remaining parts of Eq. 2.44 are now presented to investigate the increase in the dip in the magnitude at 112 kHz.

In Fig. 5.12 C_α increases with increasing separation distance, as is expected since larger separation distance increases the distance the sound propagates through the medium and therefore increases the attenuation caused by the medium. No abnormalities or discrepancies are observed in the behaviour of the attenuation for the different separation distances and apart from the expected increase in attenuation, no difference is observed at the 112 kHz area.

In Fig. 5.13 C^{BPDC}_{dif} the baffled piston diffraction correction, C^{BPDC}_{dif} for separation distances $d = 50$ cm, $d = 30$ cm, $d = 20$ cm and $d = 15$ cm is showed to decreases with increasing separation distance. This is expected since the deviation of a plane wave from will be larger at shorter distances. As in the case of the attenuation correction, no differences are observed apart from the expected increase due to the shorter distances.

Fig. 5.39 shows the magnitude and slowly varying phase of H^{VV}_{div} for all the four separation distances presented in the previous section.

In Fig. 5.39 both the magnitude and the phase of H^{VV}_{div} are identical for all separation distances, as expected. Therefore only one line is visible in the plot.

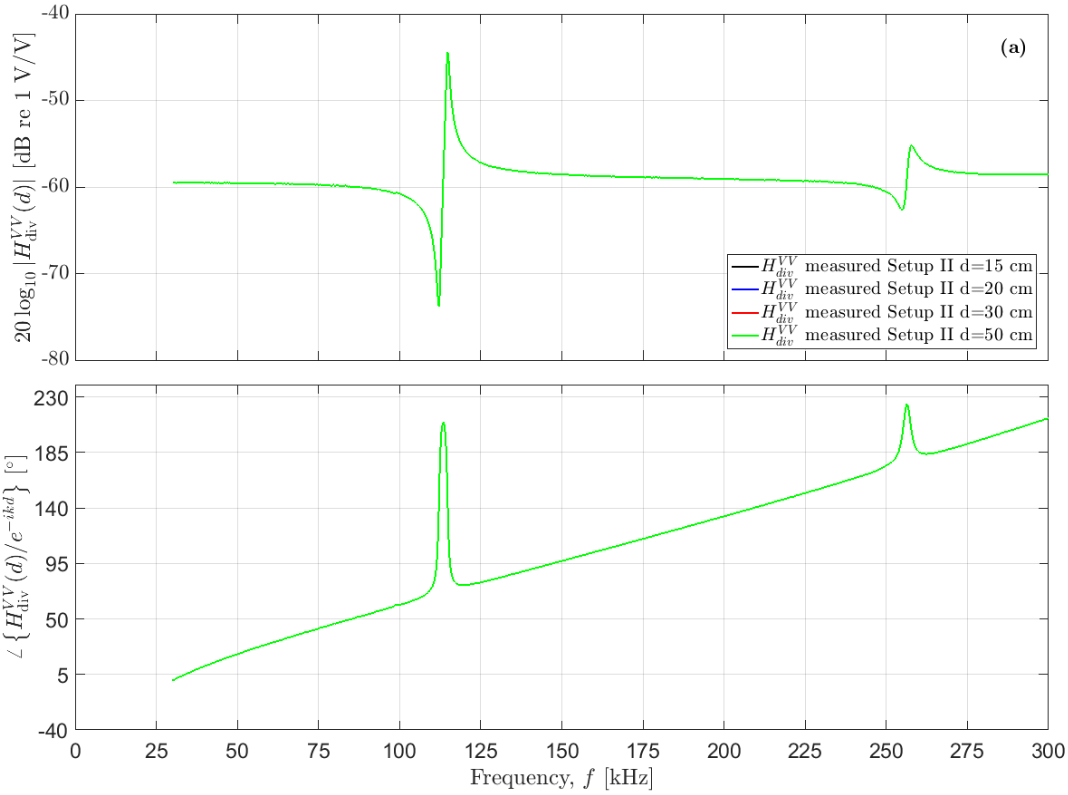

FIGURE 5.39: Measured transfer function H_{div}^{VV} for a) the magnitude and b) the slowly varying phase, θ_{div}^{slow}, using Setup II for separation distances $d = 50$ cm, $d = 30$ cm, $d = 20$ cm and $d = 15$ cm.

5.10 Measurement uncertanties

In this section the uncertainties relating to the measured quantities in the present work will be presented. This is based on the work in [36] which builds on the Guide to the expression of Uncertainty in Measurement (GUM), but is not fully completed in the present work and will be discussed in Chapter 6.

5.10.1 Uncertainty in measured electrical impedance

The uncertainty of the measured electrical impedance of a piezoelectric disk as a B type uncertainty, i.e. evaluated after manufacturer's specification, is given by [67] to be 0.1%. The type B standard uncertainty of the magnitude and phase of the electrical impedance measurements of the disks is then given by

$$u(|Z|) = \frac{|Z| \cdot 0.001}{2\sqrt{3}} \tag{5.2}$$

and

$$u(\angle Z) = \frac{\angle Z \cdot 0.001}{2\sqrt{3}}, \tag{5.3}$$

where dividing by $\sqrt{3}$ is done to obtain rectangular distribution and the half-width of the distribution is obtained by dividing by 2. The measurement uncertainty of disk 7 and disk 13 is presented in Fig. 5.40.

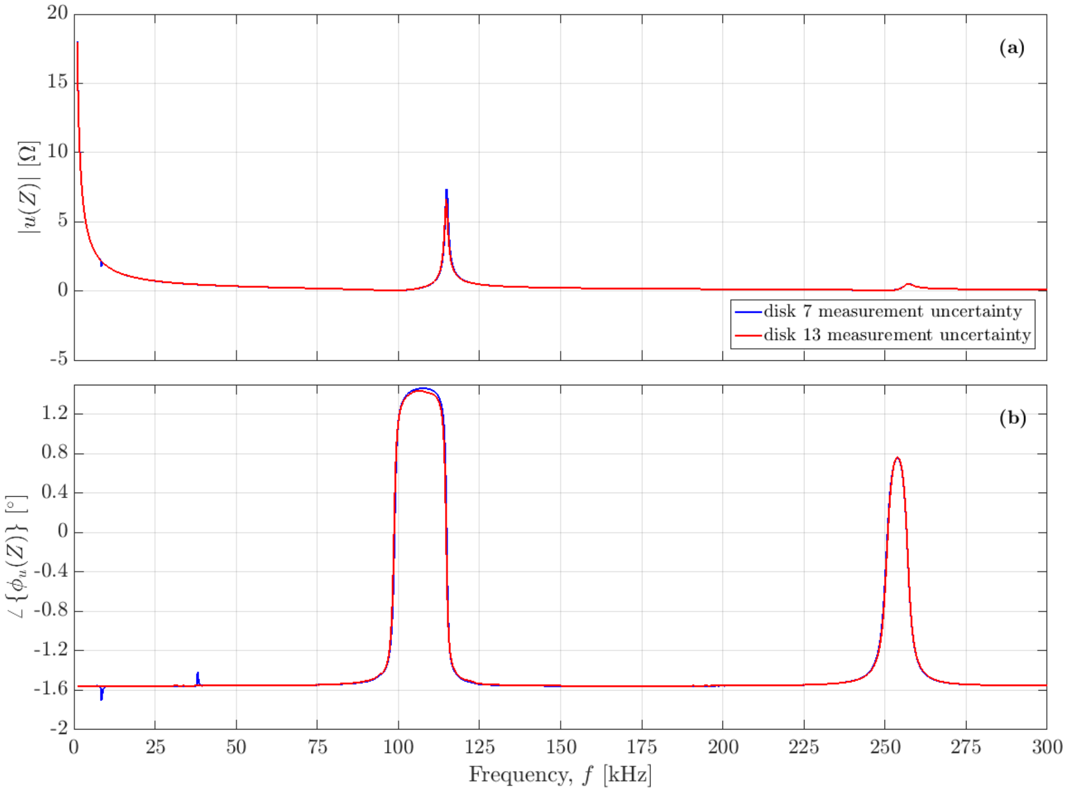

FIGURE 5.40: Uncertainty of measured electrical impedance of piezoelectric disk 7 and 13 for a) the magnitude and b) the phase, θ_{div}^{slow}.

In Fig. 5.40 a maximum measurement uncertainty is observed for both disks at 1 kHz of 17.95 Ω. At 114.7 kHz the measurement uncertainty of disk 7 is 7.366 Ω where that of disk 13 is 6.663 Ω. Another peak in the uncertainty of 0.5212 Ω is found at 257 kHz.

For the measurement uncertainty of the phase a maximum is found at 107 kHz where it is 1.436° for disk 13 and 1.460° for disk 7. For both disks another peak is found at 253.6 kHz of 0.7607°.

5.10.2 Uncertainty in the correction for attenuation in air

Since the correction for attenuation in air, C_α, given by Eq. 2.39 is dependent on both the attenuation coefficient α and the separation distance, d, the uncertainty in C_α is given as

$$u(C_\alpha) = 0.1151 C_\alpha \sqrt{d^2 u^2(\alpha + \alpha^2 u^2(d)}. \tag{5.4}$$

From Eq. 5.7 and Fig. 5.12 it is seen that the uncertainty will increase for higher frequencies and decrease for shorter separation distances. For a measurement performed at a separation distance of 50 cm at 300 kHz the uncertainty of C_α is 0.009. For 1 kHz at the same separation distance it is only 0.0006. In comparison, for a measurement performed at a separation distance of 15 cm at 300 kHz the uncertainty of C_α is 0.000002, due to the low amount of attenuation at such a short separation distance. The measured humidity for this measurement was 19.6%, which may have contributed to such a low value in the attenuation and the attenuation uncertainty.

5.10.3 Combined standard uncertainty for $|H^{VV}_{15open}|$

The combined standard uncertainty for the open-curcuit transfer function $|H^{VV}_{15open}|$, defined in Eq. 2.44, is given as

$$u_c(|H^{VV}_{15open}|) = \beta[\frac{1}{|H^{VV}_{0m6}|^2} \cdot u^2(|H^{VV}_{0m6}|) + \frac{1}{|H^{VV}_{0m1}|^2} \cdot u^2(|H^{VV}_{0m1}|) + ...$$
$$\frac{1}{|H^{VV}_{5open5'|^2}} \cdot u^2(|H^{VV}_{5open5'}|) + \frac{1}{|H^{VV}_{5open5'|^2}} \cdot u^2(|H^{VV}_{5open5'}|) + \frac{1}{|H^{VV}_{5'6|^2}} \cdot u^2(|H^{VV}_{5'6}|)]^{1/2}, \tag{5.5}$$

where β is defined as the combined uncertainty of all the transfer functions and corrections included in the calculation of $|H^{VV}_{15open}|$, yielding

$$\frac{H^{VV}_{0m6}}{H^{VV}_{0m1}H^{VV}_{5open5'}H^{VV}_{5'6}} C_\alpha C_{dif}. \tag{5.6}$$

The relative uncertainty for $|H^{VV}_{15open}|$ can then be found by

$$u_r(|H^{VV}_{15open}|) = \frac{u_c(|H^{VV}_{15open}|)}{|H^{VV}_{15open}|}. \tag{5.7}$$

Chapter 6

Discussion

In this chapter a discussion of the experimental measurements and simulations are presented.

6.1 Measurement setup

There are several parameters that influence the acoustical and electrical measurements of the transmit-receive pair. In this work a focus has been on the separation distance and alignment of the disks.

The separation distance, z, greatly impact the slowly varying phase, more so than the magnitude. Small changes, on μm level can lead to an error in phase in the 10^2 range. Therefore accurate positioning of the center of the disks on the acoustic axis and careful measurements of the position of each disk using laser is paramount for good measurements. Since there are no measurement uncertainty calculated for the slowly varying phase the accuracy or uncertainty of the method is not cleas. In addition the measurement uncertainty of the sound speed model used to calculate the slowly varying phase by [50] does not give an overlap with the sound speed model calculated by [53], which does raise some questions as to the validity of the model. This will be further discussed in Section 6.5.

An attempt at finding an acceptable degree of accuracy in alignment of the transmit-receive pair has been done in the current work. A noticeable difference in the slowly varying phase was found for accuracy below 10 μm when compared to accuracies of 50 μm. It is intuitive that higher accuracy would yield even better results, but higher accuracy than 10 μm has not been achieved for all axis in the current work, although not for the lack of trying.

Influence of the receiving electronic and the impedance of the receiving disk was discussed in [27], as mentioned in Chapter 1. In that paper it was shown that the electrical components could be examined in the same way as the mechanical components and that the output impedance of the receiver in the system had a significant effect on the measured output. The same is found in the current work, as the effect of the open-circuit receiving cable connected to the receiving disk, $H^{VV}_{5open5'}$, is much greater than effect of the transmitting electronics and cables, H^{VV}_{H0m1}, with a maximum of 12.8 dB compared to a maximum of 0.0732 dB. Not to mention that the effect of the receiving $H^{VV}_{5'6}$ is even greater, with a maximum value of 60.82 dB and a value of about 60 dB for the frequency range 30-300 kHz, which is investigated in the present work. This effect was also seen in the results found in [33–37].

6.2 Non-linearity in piezoelectric disks

The system model described in Chapter 2 is assumed to be linear in behaviour. For physical systems this is normally not the case, as most are non-linear in nature. Therefore, investigation into the non-linear behaviour of the piezoelectric disks at hand have been done. It is seen in Fig. 5.18 that for the first peak associated with R_1 and the first peak associated with R_2 the transmitting disk displays non-linear behaviour for the case of an input voltage of 10 V peak-to-peak. Since the propagation of the sound in air causes an attenuation of the signal this is not as prominent in the case for the second peaks associated with R_1 and R_2, but an input voltage of 1 V and 0.1 V is used for R_1 and R_2, respectively, in order to avoid non-linear behaviour in the disks. However, as high voltage as possible is desired to get a good SRN. This method could be optimized by looking at input voltages between 1 V and 0.1 V peak-to-peak.

6.3 Noise

It is seen from Fig. 5.4 and Fig. 5.5 that averaging the signal over 128 bursts greatly improves the noise floor in the recorded signal. This corresponds to results found in [33**?** –35] and has therefore not been allocated much study in the present work.

The use of shielding in form of Faraday cages and aluminium foil has been utilized but not been investigated separately. Grounding the receiving disk at the input of the amplifier showed a decrease in the coherent electrical noise, when investigated in the acoustic Setup I, but a plot for this has not been presented in the present work.

From Fig. 5.6 the NRM method is seen to be most effective for the frequency range above 240 kHz, which includes the R_2 mode. This could explain the oscillations observed in R_2 for the measurement by [36] in Fig. 5.20. The oscillations observed there could be due to high coherent noise, which speaks to the efficiency of the NRM introduced in [37]. For measurements performed at a shorter distance, cf. Fig. 5.7 the method appears to be less effective, however some coherent noise appears to be removed from the H_{0m6}^{VV} with the NRM.

6.4 Material parameters

Previously the parameters given by Ferroperm have been tested against the experimental values found by Lohne/Knappskog, cf. [36]. However, in [37] the material set adjusted by Aanes [77] was used. In the current thesis it is shown that these small changes in the material data caused noticeable effects in the magnitude and phase of the simulated transfer function. Previous work [35, 36] have mentioned alternative methods to soldering the piezoelectric disks onto the cables, such as using epoxy or silver lacquer. This could lead to better correlation between measured and simulated transfer function.

In the simulation of different material parameters, Simulation I vs. Simulation II in Fig. 5.22, a higher value is seen both for frequency and magnitude in the second peak associated with R_1 and the two peaks associated with R_2. When the measurements are compared to simulations in Section 5.8 they are compared to Simulation I. For all the four separation distances investigated in this work a lower value is found at the peaks associated with R_2, but not for the peaks associated with R_1. In the case of the second peak associated with R_1 the magnitude is lower than the simulation for all distances. This may suggest that neither the material data set used in Simulation

I (adjusted by Lohne/Knappskog) or the material data set used in Simulation II (adjusted by Lohne/Knappskog/Aanes) are an accurate representation for the physical material couplings found in the piezoelectric elements used in the current work. The most likely reason for this discrepancy in the material data is that the soldering of the piezoelectric disks onto the cables connecting them to the measurement setup have changed the material constants in the disks. This could be solved by using an alternative way of connecting the piezoelectric disks to the measurement setup. This could be done through using glue, epoxy or silver laquer.

6.5 Limitations regarding the sound speed model

Cramer mentions an unexplained discrepancies in the sound speed for low humidities, when compared to Harris [83], which is an effect discussed in Morfey and Howell [53] arising in the humidity range of $10\% - 20\%$ humidity. There it is postulated that the discrepancy at low humidity could be caused by the vibrational relaxation of CO_2 not being included in the model. Cramer also mentions that while there is a better agreement at levels of humidity over 30% there is still an unexplained shift of the curves for higher values of humidity.

For the work in the current thesis this includes the measurements done using Setup II as this was performed in the early spring of 2019 when humidity was not as high as in the fall and winter, when the measurements using Setup I was conducted.

The humidity recorded during acoustic measurements at the lab in the current work has varied from $19\% - 43\%$, so both the discrepancies mentioned by Cramer can be present in the calculation of the speed of sound used to estimate the slowly varying phase.

When calculating the slowly varying phase the sound speed plays an integral part and accurate calculations or measurements of the sound speed is therefore paramount for an accurate calculation of the slowly varying phase. Therefore, an alternative way could be to measure the diffraction effect and by that finding the phase.

6.6 Transmit-receive measurements

For the separation distances $d = 30$ cm, $d = 20$ cm and $d = 15$ cm only two measurements are presented in the current thesis, one using SetupI and one using SetupII, as repeatability is presented for the case of $d = 50$ cm. The results for repeatability were good for $d = 50$ cm with maximum deviations less than 1 dB for the magnitude and less than 24° for the slowly varying phase for H_{0m6}^{VV}.

The comparison of Simulation I compared to Simulation II show a good degree of reproduceability for all distances, although only two measurements are presented for each separation distance. Even for the noise in the frequency range 130-150 kHz, a good agreement is seen between the measurements. As the measurements for each separation distance were taken 6 months apart this agreement in the noisy section is not expected and may pint to the noise being coherent.

The dip observed at 112 kHz for a separation distance d=50 cm is also observed in [36] and [37] in Figure 5.20. In [36] Andersen proposes that it may stem from the electrical corrections. However, in the present work an experimental approach is used for measuring the effect of the receiving electronics. That is not to say that any such electrical effect could lie in the calculation of the receiving cable with output and input impedance of Rx and the amplifier. Since 112 kHz is in the peak of the receiving sensitivity this seems plausible that the receiving disk or the receiving electronics and cables could cause the deviation. This effect is not seen in [**?**] or [34] and in the current work the deviation effect is more prominent for shorter separation distances. An attempt to isolate the factors contributing to this deviation effect has been made by plotting the different transfer functions included in the calculation of H^{VV}_{15open}, cf. Fig. 5.37-Fig.5.39.

In Andersen it was suggested that the experimental values obtained for the amplifier could cause the effect seen at 112 kHz. In the present work these values have only been used to calculate $H^{VV}_{5open5'}$, which is of much less importance to the calculation of H^{VV}_{15open} compared to $H^{VV}_{5'6}$.

6.7 Measurement uncertainties

The measurement uncertainty of the measured electrical impedance is quite high in the present work and can be reduced by introducing a type A uncertainty, i.e. an uncertainty obtained by statistical methods. Repeated measurements of the impedance of the receiving disk have been made and show little to no deviation in the measurements and would decrease the combined uncertainty considerably.

In the present work the measurement uncertainty for $|H^{VV}_{15open}|$ is not fully calculated, but an equation is presented for the combined uncertainty of $|H^{VV}_{15open}|$ including all the transfer functions and corrections included when calculating H^{VV}_{15open}. It can however be argued that for shorter separation distances the uncertainty in the correction factor C_α can be assumed to be zero as it is small enough to be negligible, cf. Section 5.10.2. The opposite is true for the uncertainty of the diffraction correction, $u(C_dif)$, which can be assumed negligible for longer distances, cf. Section 5.3.5, but should be accounted for in distances such as $d = 15$ cm.

Although full uncertainty measurements for $|H^{VV}_{15open}|$ has not been calculated for the present work great caution and accuracy has been taken during measurements and the values achieved in [36] should be comparable with the uncertainties for the present work, had they been completed. It is expected that the calculated uncertainty for $|H^{VV}_{15open}|$ is largest in the noisy area in the frequency range 130-155 kHz and lowest in the frequency ranges 30-90 kHz and 160-225 kHz. For reference the values of $u_r(|H^{VV}_{15open}|)$ in these frequency ranges are 1 dB, -21 to -29 dB and -25 dB, respectively. A peak in the uncertainty around 114 kHz is expected due to the uncertainty in the impedance of the transmitting disk causing a large uncertainty in $|H^{VV}_{5open5'}|$ in that area, cf. Fig. 5.40.

Chapter 7

Conclusions and further work

7.1 Conclusions

In this study the transfer function of an ultrasonic transmit-receive measurement system has been found experimentally and through FE simulations. Comparison have been made with prior measurements and shows deviations with Andersen [36] and Hagen [37], but an overall agreement is found. The largest deviations are found in the second peak associated with R_1. Comparisons with simulations of prior work show deviations from the present work and [36] compared to [37]. Since the two former had used a different set of material data compared to the former and slightly different dimensions for the simulated disk, the effect of material data and disk dimension on the simulations was investigated through three simulations and showed deviations like the ones observed in Fig. 5.20.

Comparison with prior simulation show deviation from the current work and Andersen [36] and Hagen [37]. The simulations by [37] using FEMP [40] and COMSOL [82] show little deviation, especially at R_1 and R_2. A higher shift in frequency is observed in [37] compared to the current work and [36]. Both a higher shift in frequency and an increase in magnitude is found in [37] compared to the current work and [36]. Differences in material data show similar effect and causes much of the differences observed.

The source code has been documented and is presented in Appendix A and Appendix B, for data acquisition and post-processing, respectively.

The sensitivity of the rotary alignment about the y- and y-axis is investigated. It is found that a rotary misalignment less than 50 μm does not significantly influence the magnitude of H^{VV}_{15open}. A rotary misalignment of approximately 500 μm significantly reduces the magnitude of H^{VV}_{15open}, especially for R_2. A limit of maximum 10 μm is found to give a better agreement with simulations and is the smallest uncertainty in rotary misalignment achieved in the current work.

When decreasing the separation distance, d, a larger deviation is seen between the measured and simulated transfer function. For the magnitude of H^{VV}_{15open} this is largely seen in the area above 150 kHz. For the slowly varying phase of H^{VV}_{15open} the deviations are larger, as expected, since the slowly varying phase is highly dependent on both the accuracy of the separation distance, d, the calculated sound speed and the alignment of the transmit-receiver pair. For the magnitude a dip is found at 112 kHz, which is more distinct for shorter separation distances. This effect is investigated but no conclusion is drawn as to the cause of the effect. It is also observed in the prior work by [36] and [37] and needs further investigation.

7.2 Suggestions for further work

Investigation of alternative methods of measuring the sound speed are suggested for further work. Alternatively, measurement of the diffraction correction experimentally and calculation of the sound speed from measurements. If there is a good control on distance measurements and alignment uncertainties this could yield usable results that may be compared to the current calculated sound speed and calculated slowly varying phase.

It has previously been suggested to find alternative ways of connecting the disks to the cables in the experimental setup, as soldering changes the material constants of the disks. The difference caused in simulation by using the material data supplied by manufacturer, Ferroperm, has been investigated in [36] and in the current work the effect of two different adjusted data sets have been investigated. Both results show that the material data, and small changes in these, have a noticeable change in the simulated transfer function. So, to achieve a better agreement between simulation and measurements alternative methods, such as epoxy or silver laquer as suggested by [34] and [36], could be attempted.

Measurements with microphone along the acoustic axis and in the plane of the receiver would be of great interest. Near field effects observed in simulations in [38] can be investigated experimentally and effects, such as the peaks found at the 225 kHz area for $d = 20$ cm could be investigated for in the sound pressure to see if it is due to a reflection in the cage.

Uncertainty measurements should also be calculated for smaller distances than what is presented in [36], i.e. 85 cm and 50 cm, as well as uncertainty measurements for the slowly varying phase.

Bibliography

[1] ISO 17089-1:2010, “Measurement of fluid flow in closed conduits. ultrasonic meters for gas. part 1: Meters for custody transfer and allocation measurement,” *International Organization for Standardization, Geneva, Switzerland*, 2010.

[2] P. Lunde, K.-E. Frøysa, R. A. Kippersund, and M. Vestrheim, “Transient diffraction effects in ultrasonic meters for volumetric, mass and energy flow measurement of natural gas.” 21st International North Sea Flow Measurement Workshop, Tønsberg, Norway, 28-31 Oct., 2003.

[3] P. Lunde, K.-E. Frøysa, V. Martinez, and Ø. Torvanger, “Pressure and temperatur effecs for ormen lange ultrasonic gas flow meters, - results from a follow-up study.” 26th International North Sea Flow Measurement Workshop, Tønsberg, Norway, 21-24 Oct., 2008.

[4] K.-E. Frøysa, P. Lunde, A. Paulsen, and E. Jacobsen, “Density and calorific value measurement of natural gas using ultrasonic flow meters. Results from testing on various north sea gas field data.” 24th International North Sea Flow Measurement Workshop, St. Andrews, Scotland, 24-27 Oct., 2006.

[5] M. Farzaneh-Gord, A. Arabkoohsar, and R. N. N. Koury, “Novel natural gas molecular weight calculator equation as a function of only temperature, pressure and sound speed,” *Journal of Natural Gas Science and Engineering*, vol. 30, pp. 195–204, 2016.

[6] P. Norli, P. Lunde, and M. Vestrheim, “Investigation of precision sound velocity measurement methods as reference for ultrasonic gas flow meters,” *IEEE Ultrason. Symp.*, vol. 3, pp. 1443–1447, 2005.

[7] P. Norli and P. Lunde, “A three-way pulsed method for a precision sound velocity measurement cell,” *IEEE Ultrason. Symp.*, pp. 884–893, 2006.

[8] P. Norli, *"Sound velocity cell for gas characterizsation"*. PhD thesis, University of Bergen, Department of Physics and Technology, Bergen, Norway, 2007.

[9] P. Lunde, P. Norli, M. Vestrheim, and R. Kippersund, “Precision sound velocity cell as reference for gas quality measurement in ultrasonic flow meters. preliminary results using two candidate methods with argon at low pressure.” Proc. 30th Scand. Symp. Phys. Acoust., Geilo, Norway, Jan. 28-31, 2007.

[10] P. F. Smith, M. A. Player, and D. A. L. Collie, “The determination of surface topology by the signal processing of ultrasonic pulses,” *J. Phys. E: Sci. Instrum*, vol. 21, pp. 397–402, 1988.

[11] L. C. Lynnworth and Y. Liu, “Ultrasonic flowmeters: Half-century progress report, 1955-2005,” *Ultrasonics*, vol. 44, pp. 1371–1378, 2006.

[12] M. Fang, K. Xu, W. Zhu, and Z. Shen, “Energy transfer model and its applications of ultrasonic flow-meter under static and dynamic flow rates,” *Rec. Sci. Instrum.*, vol. 87, p. 015107, 2016.

[13] P. Hauptmann, N. Hoppe, and A. Püttmer, “Application of ultrasonic sensors in the process industry,” *Meas. Sci. Technol.*, vol. 13(8), pp. 73–83, 2002.

[14] P. Brassier, B. Hosten, and F. Vulovic, “High-frequency transducers and correlation method to enhance ultrasonic gas flow metering,” *Flow Meas. Instrum.*, vol. 12(3), pp. 201–211, 2001.

[15] M. Vestrheim, “PHYS373 - Akustiske målesystemer,” University of Bergen, Department of Physics and Technology, Bergen, Norway, March 2003, (in Norwegian).

[16] L. W. Schmerr and S. Song, “Ultrasonic nondestructive evaluation systems: Models and measurements.” Springer, London, UK, 2007.

[17] A. Lygre, M. Vestrheim, P. Lunde, and V. Berge, “Numerical simulation of ultrasonic flowmeters,” *Proc. 1987 Ultrasonics International, Butterworth Scientific Ltd., Guildford, UK*, pp. 196–201, 1981.

[18] S. Vervik, “Transitt-tidsbestemmelse for ultralyd strømingsmetre. Nullstrømningsforhold [Transit time detection for ultrasonic flow meters at zero flow conditions],” Master’s thesis, Dept. of Physics, Univ. of Bergen, Norway, 1995. (In Norwegian).

[19] S. Vervik, *"Methods for characterization of gas-coupled ultrasonic sender-receiver measurement systems"*. PhD thesis, University of Bergen, Department of Physics, Bergen, Norway, 2000.

[20] C. Dang, L. W. Schmerr, and A. Sedov, “Modeling and measuring all the elements of an ultrasonic nondestructive evaluation system I: Modeling foundations,” *Res. Nondestr. Eval.*, vol. 14(3), pp. 141–176, 2002.

[21] C. Dang, L. W. Schmerr, and A. Sedov, “Modeling and measuring all the elements of an ultrasonic nondestructive evaluation system II: Model-based measurements,” *Res. Nondestr. Eval.*, vol. 14(4), pp. 177–201, 2002.

[22] P. Lunde, R. A. Kippersund, and M. Vestrheim, “Signal modeling using the flosim system model in ultrasonic instrumentation for industrial applications.” Proc. Norw. Symp. Signal Proc. (NORSIG 2003), Bergen, Norway, Oct. 6, 2003.

[23] E. Papadakis, “Ultrasonic transducer evaluation in five "domains": time, space, frequency, surface motion, and theory,” *IEEE Trans. Ultrason. Symp., Phoenix, Arizona, USA, Oct. 26-28*, pp. 104–112, 1977.

[24] G. Hayward and M. Jackson, “Discrete-time modeling of the thickness mode piezoelectric transducer,” *IEEE Trans. Son. Ultras.*, vol. 31(3), pp. 137–150, 1984.

[25] G. Hayward, M. Jackson, and T. Durrani, “A systems model of the thickness mode piezoelectric transducer,” *J. Acoust. Soc. Am.*, vol. 76(2), pp. 369–382, 1984.

[26] D. A. L. Collie and M. A. Player, “Extended computer method for predicting the transient response of ultrasound NDT probes,” *Ultrasonics*, vol. 27, pp. 141–149, 1989.

[27] C. Dang, L. W. Schmerr, and A. Sedov, "Electromechanical modeling of ultrasonic transducers," *Res. Nondestr. Eval.*, vol. 17, pp. 891–898, 1998.

[28] S. J. Sanabria, T. Marhenke, R. Furrer, and J. Neuenschwander, "Calculation of volumetric sound field of pulsed air-coupled ultrasound transducer based on single-plane measurements," *IEEE Transactions on Ultrasonics, Ferroelectrics, and Frequency Control*, vol. 65, pp. 72 – 84, 2018.

[29] M. Willatzen, "Ultrasound transducer modeling - General theory and applications to ultrasound reciprocal systems," *IEEE Trans. Ultrason. Ferroelectr. Freq. Control*, vol. 48(1), pp. 100–112, 2001.

[30] M. Willatzen, "Ultrasound transducer modeling - Receieved voltage signals and the use of half-wavelength window layers with acoustic coupling layers," *IEEE Trans. Ultrason. Ferroelectr. Freq. Control*, vol. 46(5), pp. 1164–1174, 1999.

[31] D. B. k, J. A. Jensen, and M. Willatzen, "Modeling transducer impulse responses for predicting calibrated pressure pulses with the ultrasound simulation program field II," *J. Acoust. Soc. Am.*, vol. 127(5), pp. 2825– 2835, 2010.

[32] "Ørnulf S. Amundsen, "Material constants determination for piezoelectric disks, and influence on source sensitivity. Measurements and simulations," Master's thesis, University of Bergen, Department of Physics and Technology, Bergen, Norway, 2011.

[33] E. Mosland, "Reciprocity calibration method for ultrasonic piezoelectric transducers in air," Master's thesis, University of Bergen, Department of Physics and Technology, Bergen, Norway, 2013.

[34] A. A. Søvik, "Ultrasonic measurements systems for gas. Finite element modeling compared with measurements in air," Master's thesis, University of Bergen, Department of Physics and Technology, Bergen, Norway, 2015.

[35] R. Hauge, "Finite element modeling of ultrasound measurements for gas. Comparison with experiments in air," Master's thesis, University of Bergen, Department of Physics and Technology, Bergen, Norway, 2013.

[36] K. K. Andersen, "Reciprocity calibration of ultrasonic piezoelectric disks in air," Master's thesis, University of Bergen, Department of Physics and Technology, Bergen, Norway, 2015.

[37] A. Hagen, "Ultrasonic measurement system with diffraction correction for gas," Master's thesis, University of Bergen, Department of Physics and Technology, Bergen, Norway, 2017.

[38] E. Storheim, *"Diffraction effects in the ultrasonic field of transmitting and receiving circular piezoceramic disks in radial mode vibration. FE modelling and comparison with measurements in air"*. PhD thesis, University of Bergen, Department of Physics and Technology, Bergen, Norway, 2015.

[39] J. M. Kocbach, "Endelig element mo dellering av piezo elektriske skiver," Master's thesis, Dept. of Physics, Univ. of Bergen, Norway, 1996. (In Norwegian).

[40] J. M. Kocbach, *"Finite element modeling of ultrasonic piezoelectric transducers"*. PhD thesis, University of Bergen, Department of Physics and Technology, Bergen, Norway, 2000.

[41] R. Øyerhamn, E. N. Mosland, E. Storheim, P. Lunde, and M. Vestrheim, "Finite element modeling of ultrasound measurement systems for gas. Comparison with experiments in air," *J. Acoust. Soc. Am.*, vol. 144(4), pp. 2613–2625, 2018.

[42] L. L. Foldy and H. Primakoff, "A general theory of passive linear electroacoustic transducers and the electroacoustic reciprocity theorem. I," *J. Acoust. Soc. Am.*, vol. 17(2), pp. 109–120, 1945.

[43] H. Primakoff and L. L. Foldy, "A general theory of passive linear electroacoustic transducers and the electroacoustic reciprocity theorem. II," *J. Acoust. Soc. Am.*, vol. 19(1), pp. 50–58, 1947.

[44] P. R. Clayton, *Transmission Lines in Digital and Analog Electronic Systems : Signal Integrity and Crosstalk.* John Wiley & Sons Inc., 1st ed., New York, 2010.

[45] M. Vestrheim, "PHYS272 - Akustiske transdusere," University of Bergen, Department of Physics and Technology, Bergen, Norway March 2005, (in Norwegian).

[46] L. E. Kinsler, A. R. Frey, A. B. Coppers, and J. V. Sanders, *Fundamentals of Acoustics.* John Wiley & Sons Inc., 4th ed., New York, 2000.

[47] G. S. K. Wong, "Speed of sound in standard air," *J. Acoust. Soc. Am.*, vol. 79(5), pp. 1359–1366, 1986.

[48] G. S. K. Wong and T. F. W. Embleton, "Variation of the speed of sound in air with humidity and temperature," *J. Acoust. Soc. Am.*, vol. 77(5), pp. 1710– 1712, 1985.

[49] M. Greenspan, "Comments on "speed of sound in standard air"[j. acoust. soc. am. 79, 1359-1366 (1986)]," *J. Acoust. Soc. Am.*, vol. 82(1), pp. 370–372, 1987.

[50] O. Cramer, "The variation of the spesific heat ratio and the speed of sound in air with temperature, pressure, humidity and CO2 concentration," *J. Acoust. Soc. Am.*, vol. 93(5), pp. 2510– 2516, 1993.

[51] M. O'Donnell, E. T. Jaynes, and J. G. Miller, "General relationships between ultrasonic attenuation and dispersion," *J. Acoust. Soc. Am.*, vol. 63(6), p. 1935–1937, 1978.

[52] M. O'Donnell, E. T. Jaynes, and J. G. Miller, "Kramers–kronig relationship between ul- trasonic attenuation and phase velocity," *J. Acoust. Soc. Am.*, vol. 69(3), p. 696– 701, 1981.

[53] C. L. Morfey and G. P. Howell, "Speed of sound in air as a function of frequency and humidity," *J. Acoust. Soc. Am.*, vol. 68(5), pp. 1525– 1527, 1980.

[54] ANSI S1.26 , "Method for calculation of the absorption of sound by the atmosphere," *American National Standards Institute, New York*, vol. (R2009), pp. 2613–2625, 1995.

[55] P. Lunde, "PHYS374 - Utvalgte emner i teoretisk akustikk," University of Bergen, Department of Physics and Technology, Bergen, Norway 2006, (in Norwegian).

[56] S. Khimunin, “Numerical calculation of the diffraction correction for the precise measurement of ultrasound absorption,” *Acta Acustica united with Acustica*, vol. 27(4), pp. 173–181, 1972.

[57] S. Khimunin, “Numerical calculation of the diffraction corrections for the precise measurement of ultrasound phase velocity,” *Acta Acustica united with Acustica*, vol. 32, pp. 192–200, 1975.

[58] Physik Instrumente (PI) GmbH & Co. KG, *Datasheet M-511, M-521, M-531, High-Precision Linear Stage*. Germany, January 15 2018.

[59] Physik Instrumente (PI) GmbH & Co. KG, *MP 33E User Manual, M-5x1 Series Linear Positioning Stages*. Germany, September 20 2004.

[60] Physik Instrumente (PI) GmbH & Co. KG, *User Manual MP 34E Rotation Stages M-038, M-035 Series*, Germany, August 28 2002.

[61] Agilent technologies Inc., *User's guide - Agilent 33220A 20 MHz Waveform generator*. 5301 Stevens Creek Blvd, Santa Clara, CA 95051, US, 2007.

[62] Vaisala, *DPO3000 Series Datasheet*. Oyj, Finland, 2010.

[63] Brüel & Kjær Sound & Vibration Measurement A/S, *Product Data - Wide Range Measuring Amplifiers - Types 2610 and 2636*. Nærum, Denmark, 1996.

[64] Krohn-Hite Corporation, *Product data - Krohn-Hite Model 3940*. 15 Jonathan Drive, Unit 4, Brockton, MA 02301, 2014.

[65] Automatic Systems Laboratories Ltd., *Operator's Handbook - F250 Mk II Precision Thermometer*. Isotech North America, 158 Brentwood Drive, Unit 4, Colchester, VT 05404, 1997.

[66] Tektronix Inc., *User's guide - Vaisala HUMICAP Humidity and Temperature Transmitter HMT310*. 14150 SW Karl Braun Drive, Beaverton, OR 97077, United States, 2013.

[67] Yokogawa-Hewelett-Packard, Ltd, *Operation and Service Manual - Model 4192A LF Impedance Analyzer*. Tokyo, Japan, March 1982.

[68] J. van Deventer and J. Delsing, “Apparent transducer non-reciprocity in an ultrasonic flow meter,” *Ultrasonics*, vol. 40, pp. 403–405, 2002.

[69] Meggit A/S, *Meggit Sensing Systems*. Porthusvej 4, 3490 Kvistgaård, Denmark, 2013.

[70] Physik Instrumente (PI) GmbH & Co. KG, *Datasheet SMC Hydra Motion Controller*. Germany, March 1 2018.

[71] Physik Instrumente (PI) L.P., *MS77E User manual, C-843 DC-Servo-Motor Controller card*. Germany, October 8 2018.

[72] Keyence Corporation, *LK-G Series User's Manual*. 1100 North Arlington Heights Road, Suite210, Itasca, IL 60143, United States, 2010, www.keyence.com.

[73] R. Grindheim, P. Lunde, and M. Vestrheim, “Characterization of ultrasound transmit-receive measurement systems in air. comparison with prior work on piezoelectric elements in radial mode vibration.” Proceedings of the 42nd Scandinavian Symposium on Physical Acoustics, Geilo, Norway, Jan. 27-30, 2019.

[74] J. P. Bentley, *Principles of measurement systems*. Pearson Education Limited, England, 4th ed., 2005.

[75] K. Kido, *Digital Fourier Analysis: Fundamentals*. Springer, New York, NY, 2015.

[76] MATLAB, *version 9.4.0 (R2018a)*. Natick, Massachusetts: The MathWorks Inc., 2018.

[77] M. Aanes, *Interaction of piezoelectric transducer excited ultrasonic pulsed beams with a fluid-embedded viscoelastic plate. Finite element modeling, angular spectrum modeling and measurements*. PhD thesis, University of Bergen, Department of Physics and Thechnology, 2014.

[78] K. D. Lohne, "Undersøkelse og utnyttelse av svingemoder i ultralyd transduserkonstruksjoner," Master's thesis, University of Bergen, Department of Physics and Thechnology, Norway, 20005.

[79] S. Sherrit, N. Gauthier, H. D. Wiederick, and B. K. Mukherjee, "Accurate evaluation of the real and imaginary material constants for a piezoelectric resonator in the radial mode," *Ferroelectrics*, vol. 119(1), p. 17, 1991.

[80] S. Sherrit, H. D. Wiederick, and B. K. Mukherjee, "A polynomial fit for calculating the electromechanical coupling constants of piezoelectric materials using the method described by onoe et al.," *J. Acoust. Soc. Am.*, vol. 91(3), pp. 1770–1771, 1992.

[81] R. Fardal, "Endeligelementanalyse av elektriske egenskaper til piezoelektriske skiver," Master's thesis, University of Bergen, Department of Physics and Thechnology, Norway, 20002.

[82] COMSOL AB, *COMSOL Multiphysics version 4.2a Manual*.

[83] C. M. Harris, "Effects of humidity in the velocity of sound in air," *J. Acoust. Soc. Am.*, vol. 49(3), pp. 890–893, 1971.

Appendix A

Data acquisition, pylabctrl

The scripts used for data acquisition at are written in Python code and collected in a folder named pylabctrl. This folder consists of four main scripts for various measurements, one folder called instruments, containing scripts for all instruments called on in the main measurement scripts, and lastly a folder called spec, containing all the specifications for the different instruments.

A.1 Measurement scripts

In the present section the main measurement scripts used for data acquisition are presented.

A.1.1 admittance.py

```python
# admittance.py
# Performes admittance measurements.
#
# Variables to check before each run
# measurement count : should be the same as for the acoustic measurement in
#                     for matrix dimensions to agree during post-process
# frequencies : should be the same as for the acoustic measurement in
#                     for matrix dimensions to agree during post-process
#
# Output variables stored to h5-file
# Y : impedance structure containing two vectors; r and i for the real and
#     imaginary impedance values, respectively.
# f : frequency vector
#
# A. Hagen 2017, modified by R. Grindheim 2019

from contextlib import closing
from datetime import datetime
from numpy import linspace
from tables import open_file
from progressbar import ProgressBar # progressbar in terminal window
pbar = ProgressBar()

# Import instruments and their specifications
from instruments.impedanceanalyzer import ImpedanceAnalyzer
from spec.data import frequency_variable, admittance_variable
from spec.measurements import measure_admittance

# Connect to instruments
impedance_analyzer = ImpedanceAnalyzer('GPIB0::17::INSTR')
print("connected to instruments!")
```

```python

# Measurement parameters
measurement_count = 1000
frequencies = linspace(start=1e3, stop=3e5, num=measurement_count)


with closing(open_file('D:\\Renate\\datanew\\admittance'
                       f'{datetime.strftime(datetime.now(), "%d%m%y_%H%M%S")}.h5', mode='w')) as file:
    # Setup output
    f = frequency_variable(file, expected_rows=measurement_count)
    Y = admittance_variable(file, expected_rows=measurement_count)

    for frequency in pbar(frequencies):
        f.append((frequency,))
        Y.append((measure_admittance(frequency, impedance_analyzer),))
```

A.1.2 acoustic.py

```python
# acoustic.py
# Performes an acoustic measurement from a transmitter, Tx, to a receiver, Rx,
# over the frequency range specified in the script, as start and stop frequencies.
#
# Variables to check before each run
# distance : set equal to the distance between Tx and Rx.
# p.append : update the current atmospheric pressure at the lab using a barrometer.
#
# Output variables stored to h5-file
# d : distance between Tx and Rx
# f : frequency vector
# h : relative humidity vector
# l : burst length
# p : atmospheric pressure vector
# htx : amplitude vector for transmitted signal
# ttx : time vector for transmitted signal
# hrx : amplitude vector for received signal
# trx : time vector for received signal
#
# A. Hagen 2017, modified by R. Grindheim 2019
#
# Note: implemetnation of the filter is kept in but commented out in order to easily
# change the script to include a moving bandpass filter if desireable in the future.

from contextlib import closing
from datetime import datetime
from numpy import linspace, newaxis
from tables import open_file
from progressbar import ProgressBar # progressbar in terminal window
pbar = ProgressBar()

# Import instruments and their specifications
from instruments import Oscilloscope, WaveformGenerator, Thermometer, Hygrometer#, Filter
from spec.data import setup_variables, frequency_variable, environment_variables, waveform_variables
from spec.measurements import measure_waveforms
```

```

# Connect to instruments
oscilloscope = Oscilloscope('USB0::0x699::0x0410::C010246::INSTR')
waveform_generator = WaveformGenerator('GPIB0::10::INSTR')
thermometer = Thermometer('GPIB0::3::INSTR')
hygrometer = Hygrometer('ASRL4::INSTR')
#filter = Filter('GPIB0::21::INSTR')
print("connected to instruments!")

# Measurement parameters
distance = .15
propagation_time = distance / 347  # Underestimate
burst_length = .8 * propagation_time
measurement_count = 1000 # Determines the frequency resolution of the measurement
sample_count = 10000
frequencies = linspace(start=1e3, stop=3e5, num=measurement_count)

with closing(open_file('D:\\Renate\\datanew\\acoustic'
                       f'{datetime.strftime(datetime.now(), "%d%m%y_%H%M%S")}.h5', mode='w')) as file:
    # Setup output
    setup_variables(file, distance=distance, burst_length=burst_length)
    f = frequency_variable(file, expected_rows=measurement_count)
    t, p, h, = environment_variables(file, expected_rows=measurement_count)
    ttx, htx, trx, hrx = waveform_variables(file, sample_count=sample_count, expected_rows=measurement_count)

    for frequency in pbar(frequencies):
        #filter.config(lowpass=frequency/2, highpass=frequency*2, kind='butterworth')
        try:
            timestamp, amplitude = measure_waveforms(
                frequency=frequency,
                burst_length=burst_length,
                propagation_time=propagation_time,
                voltage=1 if 90e3 < frequency < 117e3 else .1 if 240e3 < frequency < 260e3 else 10,
                oscilloscope=oscilloscope,
                waveform_generator=waveform_generator
            )
        except ValueError:
            continue

        # Frequency
        f.append((frequency,))

        # Waveforms
        ttx.append(timestamp['tx'][newaxis])
        htx.append(amplitude['tx'][newaxis])
        trx.append(timestamp['rx'][newaxis])
        hrx.append(amplitude['rx'][newaxis])

        # Environmental parameters
        t.append((thermometer.temperature,))
        p.append((102500.,))
        h.append((hygrometer.relative_humidity / 100,))
```

A.1.3 noise.py

```python
# noise.py
# Performes a noise measurement of the coherent electrical signal, which is to
# accompany an acoustic measurement from a transmitter, Tx, to a receiver, Rx.
#
# Variables to check before each run
# distance : set equal to the distance between Tx and Rx
#
# Output variables stored to h5-file
# d : distance between Tx and Rx
# f : frequency vector
# l : burst length
# htx : amplitude vector for transmitted signal
# ttx : time vector for transmitted signal
# hrx : amplitude vector for received signal
# trx : time vector for received signal
#
# A. Hagen 2017, modified by R. Grindheim 2019
#
# Note: implemetnation of the filter is kept in but commented out in order to easily
# change the script to include a moving bandpass filter if desireable in the future.

from contextlib import closing
from datetime import datetime
from numpy import linspace, newaxis
from tables import open_file
from progressbar import ProgressBar # progressbar in terminal window
pbar = ProgressBar()

# Import instruments and their specifications
from instruments import Oscilloscope, WaveformGenerator#, Filter
from spec.data import setup_variables, frequency_variable, waveform_variables
from spec.measurements import measure_waveforms

# Connect to instruments
oscilloscope = Oscilloscope('USB0::0x699::0x0410::C010246::INSTR')
waveform_generator = WaveformGenerator('GPIB0::10::INSTR')
#filter = Filter('GPIB0::21::INSTR')

# Measurement parameters
distance = .15
burst_length = 3.2e-3
measurement_count = 5001
sample_count = 10000
frequencies = linspace(start=0, stop=1.25e6, num=measurement_count)

with closing(open_file('D:\\Renate\\datanew\\noise'
                       f'{datetime.strftime(datetime.now(), "%d%m%y_%H%M%S")}.h5', mode='w')) as file:
    # Setup output
    setup_variables(file, distance=distance, burst_length=burst_length)
    f = frequency_variable(file, expected_rows=measurement_count)
    ttx, htx, trx, hrx = waveform_variables(file, sample_count=sample_count, expected_rows=measurement_count)

    for frequency in pbar(frequencies):
        #filter.config(lowpass=frequency/2, highpass=frequency*2, kind='butterworth')
```

```
        try:
            timestamp, amplitude = measure_waveforms(
                frequency=frequency,
                burst_length=burst_length,
                propagation_time=0,
                voltage=1 if 90e3 < frequency < 117e3 else 1 if 240e3 < frequency < 260e3 else 10,
                oscilloscope=oscilloscope,
                waveform_generator=waveform_generator
            )
        except ValueError:
            continue

        # Frequency
        f.append((frequency,))

        # Waveforms
        ttx.append(timestamp['tx'][newaxis])
        htx.append(amplitude['tx'][newaxis])
        trx.append(timestamp['rx'][newaxis])
        hrx.append(amplitude['rx'][newaxis])
```

A.1.4 receiver.py

```
# receiver.py
# Performes an electrical measurement of the receiving electronics; the amplifier
# and filter, with an attenuator coupled before the oscilloscope to avoid
# overpowering the filter.
#
# Variables to check before each run
# voltage : make sure the input voltage at the filter does not exceed 4.4 V
#
# Output variables stored to h5-file
# f : frequency vector
# l : burst length
# htx : amplitude vector for transmitted signal
# ttx : time vector for transmitted signal
# hrx : amplitude vector for received signal
# trx : time vector for received signal
#
# A. Hagen 2017, modified by R. Grindheim 2019
#
# Note: implemetnation of the filter is kept in but commented out in order to easily
# change the script to include a moving bandpass filter if desireable in the future.

from contextlib import closing
from datetime import datetime
from numpy import linspace, newaxis
from tables import open_file
from progressbar import ProgressBar # progressbar2
pbar = ProgressBar()

# Import instruments and their specifications
from instruments import Oscilloscope, WaveformGenerator#, Filter
from spec.data import setup_variables, frequency_variable, waveform_variables
from spec.measurements import measure_waveforms
```

```python

# Connect to instruments
oscilloscope = Oscilloscope('USB0::0x699::0x0410::C010246::INSTR')
waveform_generator = WaveformGenerator('GPIB0::10::INSTR')
#filter = Filter('GPIB0::21::INSTR')
print("connected to instruments!")

# Measurement parameters
burst_length = 2*1.6e-3
measurement_count = 1000
sample_count = 10000
frequencies = linspace(start=1e3, stop=3e5, num=measurement_count)

with closing(open_file('D:\\Renate\\datanew\\receiver'
                       f'{datetime.strftime(datetime.now(), "%d%m%y_%H%M%S")}.h5', mode='w')) as file:
    # Setup output
    setup_variables(file, burst_length=burst_length)
    f = frequency_variable(file, expected_rows=measurement_count)
    ttx, htx, trx, hrx = waveform_variables(file, sample_count=sample_count, expected_rows=measurement_count)

    for frequency in pbar(frequencies):
        #filter.config(lowpass=frequency/2, highpass=frequency*2, kind='butterworth')
        try:
            timestamp, amplitude = measure_waveforms(
                frequency=frequency,
                burst_length=burst_length,
                propagation_time=0,
                voltage=150e-3,
                oscilloscope=oscilloscope,
                waveform_generator=waveform_generator
            )
        except ValueError:
            continue

        # Frequency
        f.append((frequency,))

        # Waveforms
        ttx.append(timestamp['tx'][newaxis])
        htx.append(amplitude['tx'][newaxis])
        trx.append(timestamp['rx'][newaxis])
        hrx.append(amplitude['rx'][newaxis])
```

A.2 Instrument scripts

In the present section the instrument scripts used in the main measurements scripts are presented.

A.2.1 _init_.py

```python
# _init_.py
# This script defines how to import the instruments to another script
# and imports the syntax for the instrument from base.py.
#
# A. Hagen 2017, comments added by R. Grindheim 2019

```

```python
from .base import Instrument, Property, SCPIInstrument

from .oscilloscope import Oscilloscope
from .waveformgenerator import WaveformGenerator
from .thermometer import Thermometer
from .hygrometer import Hygrometer
from .filter import Filter
```

A.2.2 base.py

```python
# base.py
# This script defines how a generic instruments functions and allows for easier
# syntax in measurement scripts.
#
# A. Hagen 2017, comments added by R. Grindheim 2019

from functools import lru_cache, partialmethod, partial
from pyvisa import ResourceManager


@lru_cache()  # Lazy load
def _rm():
    return ResourceManager()


class Instrument:
    def __init__(self, resource, set_message='{} {}', query_message='{}?'):
        if isinstance(resource, str):
            resource = _rm().open_resource(resource)

        self.resource = resource
        self.set_message = set_message
        self.query_message = query_message

    def __repr__(self):
        return f'{self.__class__.__name__}({self.resource!r})'

    def _io(self, func, *args, **kwargs):
        return getattr(self.resource, func)(*args, **kwargs)

    read = partialmethod(_io, 'read')
    read_raw = partialmethod(_io, 'read_raw')
    write = partialmethod(_io, 'write')
    query = partialmethod(_io, 'query')
    query_values = partialmethod(_io, 'query_values')
    query_ascii_values = partialmethod(_io, 'query_ascii_values')
    query_binary_values = partialmethod(_io, 'query_binary_values')

    def __getattribute__(self, item):
        attr = super().__getattribute__(item)

        if isinstance(attr, Property):
            message = self.query_message.format(self.attribute_to_property(item))
            query_function = getattr(self, attr.query_function)
            return attr.parse(query_function(message))
        else:
            return attr

```

```python
    def __setattr__(self, item, value):
        try:
            attr = super().__getattribute__(item)

            if isinstance(attr, Property):
                message = self.set_message.format(self.attribute_to_property(item), attr.format(value))
                self.write(message)
                return
        except AttributeError:
            pass

        return super().__setattr__(item, value)

    def attribute_to_property(self, attr):
        return attr


class Property:
    _formaters = {}

    def __init__(self, type_=str, query_function='query', formater=str, **kwargs):
        self.type = type_
        self.formater = formater
        self.query_function = query_function

        if (1 if formater is not str else 0) + len(kwargs) > 1:
            raise ValueError('Incorrect number of formaters specified.')

        for formater, param in kwargs.items():
            if formater in self._formaters:
                setattr(self, formater, param)
                self.formater = partial(self._formaters[formater], param)
            else:
                raise ValueError(f'Unknown formater {formater}.')

    def format(self, value):
        return self.formater(self.type(value))

    def parse(self, value):
        return self.type(value)

    @classmethod
    def add_formater(cls, caster, method):
        cls._formaters[caster] = method


def propertyformater(caster):
    return lambda method: Property.add_formater(caster, method)


@propertyformater('choices')
def choice_formater(choices, choice):
    if choice not in choices:
        raise ValueError(f'Invalid option {choice}..')

    return choice


@propertyformater('quotes')
def quoted_formater(quotes, string):
    return f'{quotes}{string}{quotes}'
```

```python


@propertyformater('prefix')
def prefix_formater(prefix, string):
    return f'{prefix}{string}'


@propertyformater('postfix')
def postfix_formater(postfix, string):
    return f'{string}{postfix}'


class SCPIInstrument(Instrument):
    namespace_separator = ':'

    def attribute_to_property(self, attr):
        return f':{attr.replace("_", self.namespace_separator)}'
```

A.2.3 impedanceanalyzer.py

```python
# impedanceanalyzer.py
# This script is imported to measurement scripts from instruments.
# It sets the settings for the impedance analyzer to be used in the measurement.
#
# A. Hagen 2017, comments added by R. Grindheim 2019

import re
from instruments import Instrument, Property


class HP4192A(Instrument):
    A = Property(int)
    C = Property(int)
    F = Property(int)
    V = Property(int)
    OL = Property(float, postfix='EN')
    FR = Property(float, postfix='EN')

    def __init__(self, resource):
        super().__init__(resource, set_message='{}{}')
        self.resource.read_termination = '\r\n'


class ImpedanceAnalyzer(HP4192A):
    def measure(self, frequency, voltage):
        self.V = 1  # Enable averaging
        self.A = 2  # Set a + ib output
        self.C = 3  # Select admittance (parallel circuit)
        self.F = 0  # Output from display A and B
        self.OL = voltage  # Set voltage
        self.FR = frequency / 1e3  # Set frequency
        value = self.query('EX')

        number = '[+\-]?[\d.]+E[+\-]?[\d]+'
        match = re.match(f'NGFN({number}),NBFN({number})', value)

        if match:
            return float(match.group(1)) + float(match.group(2))*1j
        else:
```

```
            raise ValueError(f'Impedance analyzer returned unreadable value {value!r}.')
```

A.2.4 waveformgenerator.py

```
# waveformgenerator.py
# This script is imported to measurement scripts from instruments.
# It sets the settings for the waveform generator Agilent33220A to be used in the
# measurement.
#
# A. Hagen 2017, comments added by R. Grindheim 2019

from instruments import SCPIInstrument, Property


class Agilent33220A(SCPIInstrument):
    BURST_INTERNAL_PERIOD = Property(float)
    BURST_MODE = Property(choices=('TRIGGERED', 'GATED'))
    BURST_NCYCLES = Property(int)
    BURST_STATE = Property(choices=('OFF', 'ON'))

    FREQUENCY = Property(int)
    FUNCTION = Property(choices=('SINUSOID', 'SQUARE', 'RAMP', 'PULSE', 'NOISE', 'DC', 'USER'))
    OUTPUT = Property(choices=('OFF', 'ON'))
    VOLTAGE = Property(float)


class WaveformGenerator(Agilent33220A):
    def __init__(self, *args, **kwargs):
        super().__init__(*args, **kwargs)

        self.write('*RST')
        self.FUNCTION = 'SINUSOID'

    def signal(self, frequency, cycles, voltage, period):
        self.FREQUENCY = frequency
        self.VOLTAGE = voltage

        self.BURST_STATE = 'ON'
        self.BURST_MODE = 'TRIGGERED'
        self.BURST_NCYCLES = cycles
        self.BURST_INTERNAL_PERIOD = period

        self.OUTPUT = 'ON'
```

A.2.5 oscilloscope.py

```
# oscilloscope.py
# This script is imported to measurement scripts from instruments.
# It sets the settings for the oscilloscope TektronixDPO3000 to be used in the
# measurement.
#
# A. Hagen 2017, comments added by R. Grindheim 2019

from collections import namedtuple, OrderedDict
from time import strftime
```

```python

from numpy import array, arange, logspace, newaxis, absolute, int16

from . import SCPIInstrument, Property


_channels = ('CH1', 'CH2', 'CH3', 'CH4',
             'MATH', 'REF1', 'REF2', 'REF3', 'REF4',
             'D0', 'D1', 'D2', 'D3', 'D4', 'D5', 'D6', 'D7', 'D8', 'D9', 'D10', 'D11', 'D12', 'D13', 'D14', 'D15',
             'DIGITAL', 'AUX')
_scales = namedtuple('Scales', ('horizontal', 'ch1', 'ch2'))


class TektronixDPO3000(SCPIInstrument):
    ACQUIRE_MODE = Property(choices=('SAMPLE', 'PEAKDETECT', 'HIRES', 'AVERAGE', 'ENVELOPE'))
    ACQUIRE_NUMAVG = Property(int)
    ACQUIRE_STATE = Property(choices=('OFF', 'ON', 'RUN', 'STOP'))
    ACQUIRE_STOPAFTER = Property(choices=('RUNSTOP', 'SEQUENCE'))

    CH1_COUPLING = Property(choices=('AC', 'DC', 'GND'))
    CH1_LABEL = Property(quotes='"')
    CH1_POSITION = Property(int)
    CH1_SCALE = Property(float)
    CH2_COUPLING = Property(choices=('AC', 'DC', 'GND'))
    CH2_LABEL = Property(quotes='"')
    CH2_POSITION = Property(int)
    CH2_SCALE = Property(float)

    CURVE = Property(array, query_function='query_values')

    DATA_SOURCE = Property(choices=_channels)
    DATA_ENCDG = Property(choices=('ASCII', 'FASTEST', 'RIBINARY', 'RPBINARY', 'SRIBINARY', 'SRPBINARY'))
    DATA_WIDTH = Property(int)

    CURSOR_FUNCTION = Property(choices=('OFF', 'SCREEN', 'WAVEFORM'))
    CURSOR_VBARS_POSITION1 = Property(float)
    CURSOR_VBARS_POSITION2 = Property(float)
    CURSOR_VBARS_UNITS = Property(choices=('SECONDS', 'HERTZ', 'DEGREES', 'PERCENT'))

    HORIZONTAL_DELAY_MODE = Property(choices=('OFF', 'ON'))
    HORIZONTAL_POSITION = Property(float)
    HORIZONTAL_RECORDLENGTH = Property(int)
    HORIZONTAL_SCALE = Property(float)

    HEADER = Property(choices=('OFF', 'ON'))
    DATE = Property(quotes='"')
    TIME = Property(quotes='"')

    SELECT_CH1 = Property(choices=('OFF', 'ON'))
    SELECT_CH2 = Property(choices=('OFF', 'ON'))
    SELECT_CONTROL = Property(int)

    TRIGGER_A = Property(choices=('SETLEVEL',))
    TRIGGER_A_EDGE_SOURCE = Property(choices=_channels)
    TRIGGER_A_MODE = Property(choices=('AUTO', 'NORMAL'))

    WFMOUTPRE_XINCR = Property(float)
    WFMOUTPRE_XZERO = Property(float)
    WFMOUTPRE_YMULT = Property(float)
```

```python
    WFMOUTPRE_YOFF = Property(float)
    WFMOUTPRE_YZERO = Property(float)

    def __init__(self, *args, **kwargs):
        super().__init__(*args, **kwargs)

        self.resource.read_termination = '\n'
        self.resource.write_termination = '\n'


Channel = namedtuple('Channel', ['number', 'label', 'propagates'])


class Oscilloscope(TektronixDPO3000):
    hdivs = 10
    _hscales = logspace(-9, 3, 13)[newaxis].T * array((1, 2, 4))
    _hscales[3, 0] = 8e-7
    _hscales = _hscales.flatten()[:-2]

    vdivs = 10
    _vscales = logspace(-3, 1, 5)[newaxis].T * array((1, 2, 5))
    _vscales =_vscales.flatten()[:-2]

    def __init__(self, *args, noise_percentage=.1, timeout=300000, **kwargs):
        super().__init__(*args, **kwargs)

        self.resource.timeout = timeout
        self.resource.values_format.is_binary = True
        self.resource.values_format.datatype = 'h'
        self.resource.values_format.is_big_endian = True
        self.resource.values_format.container = int16

        self.write('*RST;*WAI')

        self.TRIGGER_A_EDGE_SOURCE = 'AUX'
        self.TRIGGER_A_MODE = 'NORMAL'
        self.TRIGGER_A = 'SETLEVEL'

        self.SELECT_CH1 = self.SELECT_CH2 = 'ON'
        self.CH1_COUPLING = self.CH2_COUPLING = 'AC'

        self.HORIZONTAL_DELAY_MODE = 'OFF'
        self.HORIZONTAL_RECORDLENGTH = 1e4
        self.HORIZONTAL_POSITION = noise_percentage * 100

        self.DATE = strftime('%Y-%m-%d')
        self.TIME = strftime('%H:%M:%S')

        self.HEADER = 'OFF'
        self.DATA_WIDTH = 2
        self.DATA_ENCDG = 'RIBINARY'

    def acquire(self, time_scale=None, ch1_scale=None, ch2_scale=None, length=None, average=None, position=None):
        if average:
            self.ACQUIRE_MODE = 'AVERAGE'
            self.ACQUIRE_NUMAVG = average

        if time_scale:
            self.HORIZONTAL_SCALE = time_scale

        if length:
```

```
            self.HORIZONTAL_RECORDLENGTH = length

        if position:
            self.HORIZONTAL_POSITION = position

        self.CH1_POSITION = 0
        if ch1_scale:
            self.CH1_SCALE = ch1_scale

        self.CH2_POSITION = 0
        if ch2_scale:
            self.CH2_SCALE = ch2_scale

        self.ACQUIRE_STOPAFTER = 'SEQUENCE'
        self.ACQUIRE_STATE = 'RUN'
        self.write('*WAI')

    def record(self, channel):
        self.DATA_SOURCE = f'CH{channel}'
        data = self.CURVE

        x_zero = self.WFMOUTPRE_XZERO
        x_increment = self.WFMOUTPRE_XINCR
        y_zero = self.WFMOUTPRE_YZERO
        y_multiplier = self.WFMOUTPRE_YMULT
        y_offset = self.WFMOUTPRE_YOFF

        timestamps = x_zero + arange(0, len(data)) * x_increment
        amplitudes = (data - y_offset) * y_multiplier + y_zero

        return timestamps, amplitudes

    def cursors(self, cursor1=None, cursor2=None):
        self.CURSOR_FUNCTION = 'WAVEFORM'
        self.CURSOR_VBARS_UNITS = 'SECONDS'

        if cursor1 is not None:
            self.CURSOR_VBARS_POSITION1 = cursor1

        if cursor2 is not None:
            self.CURSOR_VBARS_POSITION2 = cursor2

    @property
    def channel(self):
        return self.SELECT_CONTROL

    def scale(self, channel=None):
        return getattr(self, (f'CH{channel}' if channel else 'HORIZONTAL') + '_SCALE')

    def get_scales(self, direction, minimum_scale=0, maximum_scale=float('inf')):
        if direction == 'vertical':
            return self._vscales[(minimum_scale <= self._vscales) & (self._vscales <= maximum_scale)]
        elif direction == 'horizontal':
            return self._hscales[(minimum_scale <= self._hscales) & (self._hscales <= maximum_scale)]
        else:
            raise ValueError(f'Unknown direction {direction}.')

    def step_scale(self, current_scale, delta=0, direction='vertical', **kwargs):
```

```python
        scales = self.get_scales(direction, **kwargs)
        current_idx = absolute(scales - current_scale).argmin()
        next_idx = current_idx + delta

        if next_idx < 0:
            next_idx = 0
        elif next_idx >= len(scales):
            next_idx = len(scales) - 1

        return scales[next_idx]

    def scale_delta(self, scale1, scale2, direction='vertical'):
        scales = self.get_scales(direction)
        idx1 = absolute(scales - scale1).argmin()
        idx2 = absolute(scales - scale2).argmin()
        return idx2 - idx1
```

A.2.6 hygrometer.py

```python
# hygrometer.py
# This script is imported to measurement scripts from instruments.
# It sets the settings for the hygrometer VaisalaHMT313 to be used in the
# measurement.
#
# A. Hagen 2017, comments added by R. Grindheim 2019

from instruments import Instrument, Property


class VaisalaHMT313(Instrument):
    FORM = Property()
    SEND = Property()

    def __init__(self, *args, **kwargs):
        super().__init__(*args, query_message='{}', **kwargs)

        self.resource.read_termination = None
        self.resource.write_termination = '\r'


class Hygrometer(VaisalaHMT313):
    def __init__(self, *args, **kwargs):
        super().__init__(*args, **kwargs)

        self.FORM = 'RH #n'
        self.resource.read_termination = '\n'

    @property
    def relative_humidity(self):
        return float(self.SEND)
```

A.2.7 thermometer.py

```python
# thermometer.py
# This script is imported to measurement scripts from instruments.
# It sets the settings for the thermometer ASLF250MKII to be used in the measurement.
#
# A. Hagen 2017, comments added by R. Grindheim 2019
```

```python

import re
from datetime import datetime, timedelta

from instruments import Instrument, Property


class ASLF250MKII(Instrument):
    D = Property()

    def __init__(self, *args, **kwargs):
        super().__init__(*args, query_message='{}', **kwargs)

        self.resource.read_termination = '\r\n'
        self.resource.write_termination = '\n'


class Thermometer(ASLF250MKII):
    def __init__(self, *args, skip_time=timedelta(seconds=5), **kwargs):
        super().__init__(*args, **kwargs)

        self.last_query_time = datetime.min
        self.skip_time = skip_time

    @property
    def temperature(self):
        if datetime.now() - self.last_query_time >= self.skip_time:
            value = self.D
            self.last_query_time = datetime.now()
            match = re.match('(\w) ([\d.]+)(\w)', value)

            if match:
                return float(match.group(2))
            else:
                return float('nan')
                #raise ValueError(f'Thermometer returned unreadable value {value!r}.')
        else:
            return float('nan')
```

A.2.8 filter.py

```python
# filter.py
# This script is imported to measurement scripts from instruments.
# It sets the settings for the filter KrohnHite3940 to be used in the
# measurement.
#
# A. Hagen 2017, comments added by R. Grindheim 2019

from instruments import Instrument, Property


class KrohnHite3940(Instrument):
    CH = Property(int, prefix='1.')
    T = Property(int)
    M = Property(int)
    F = Property(float)

    def __init__(self, *args, **kwargs):
        super().__init__(*args, set_message='{}{}', **kwargs)
        self.write('CE')
```

```


class Filter(KrohnHite3940):
    def config(self, lowpass=None, highpass=None, kind='butterworth'):
        if kind == 'butterworth':
            kind = 1
        elif kind == 'bessel':
            kind = 2
        else:
            raise ValueError(f'Unknown kind passed to config: {kind}.')

        if lowpass and highpass:
            self.CH = 1
            self.M, self.T = 3, kind
            self.F = highpass

            self.CH = 2
            self.F = lowpass

        elif lowpass:
            self.CH = 2
            self.M, self.T = 1, kind
            self.F = lowpass

        elif highpass:
            self.CH = 1
            self.M, self.T = 2, kind
            self.F = highpass

        else:  # Bypass
            self.CH, self.M = 1, 5
            self.CH, self.M = 2, 5
```

A.3 Specification scripts

In the present section the scripts containing the specifications for the different instruments used in the main measurements scripts are presented.

A.3.1 data.py

```
# data.py
# This script is called on using the "from" command in measurement scripts.
# It defines and returnes values to be stored in a file after the measurement.
#
# A. Hagen 2017, comments added by R. Grindheim 2019

from tables import FloatAtom, ComplexAtom


def setup_variables(file, distance=None, burst_length=None):
    if distance is not None:
        file.create_array(file.root, 'd', distance, title='Separation distance')
    if burst_length is not None:
        file.create_array(file.root, 'l', burst_length, title='Burst length')

```

```

def frequency_variable(file, expected_rows=None):
    return file.create_earray(file.root, 'f',
                              atom=FloatAtom(8),
                              shape=(0,),
                              title='Frequency',
                              expectedrows=expected_rows)


def environment_variables(file, expected_rows=None):
    return (file.create_earray(file.root, label,
                               atom=FloatAtom(8),
                               shape=(0,),
                               title=description,
                               expectedrows=expected_rows)
            for label, description in (('t', 'Temperature'),
                                       ('p', 'Pressure'),
                                       ('h', 'Relative humidity')))


def waveform_variables(file, sample_count, expected_rows=None):
    return (file.create_earray(file.root, label,
                               atom=FloatAtom(8),
                               shape=(0, sample_count),
                               title=description,
                               expectedrows=expected_rows)
            for label, description in (('ttx', 'Transmitter timestamps'),
                                       ('htx', 'Transmitter amplitudes'),
                                       ('trx', 'Receiver timestamps'),
                                       ('hrx', 'Receiver amplitudes')))


def admittance_variable(file, expected_rows=None):
    return file.create_earray(file.root, 'Y',
                              atom=ComplexAtom(16),
                              shape=(0,),
                              title='Admittance',
                              expectedrows=expected_rows)
```

A.3.2 measurements.py

```
# measurements.py
# This script is called on using the "from" command in measurement scripts.
# It defines functions and returnes values to be stored in a file during the
# measurement.
#
# A. Hagen 2017, comments added by R. Grindheim 2019

from collections import OrderedDict
from numpy import absolute, floor
from instruments.oscilloscope import Channel

# Function which record and returnes amplitude and timestamp recorded from the
# oscilloscope using parameters from measurement script.
def measure_waveforms(frequency, burst_length, propagation_time, voltage,
                      oscilloscope, waveform_generator):
    # Measurement parameters
    noise_percentage = .1
```

```python
    window = (propagation_time + burst_length) / (1 - noise_percentage)
    cycles = floor(burst_length * frequency)  # Number of cycles per burst
    duration = cycles / frequency

    if cycles < 1:
        raise ValueError('Burst length too short to include any cycles.')

    # Set up burst
    waveform_generator.signal(frequency, cycles, voltage=voltage, period=3 * window)

    # Initialize channels and scales
    channels = (Channel(1, label='tx', propagates=False), Channel(2, label='rx', propagates=True))
    time_scale = oscilloscope.get_scales('horizontal', minimum_scale=window / oscilloscope.hdivs)[0]
    amplitude_scales = OrderedDict(((channel, oscilloscope.scale(channel)) for channel, _, _ in channels))

    timestamp, amplitude = {}, {}
    while not all(label in timestamp and label in amplitude for _, label, _ in channels):
        # Prepare capture
        oscilloscope.acquire(time_scale, *amplitude_scales.values(), average=128, position=100 * noise_percentage)
        oscilloscope.cursors(propagation_time, propagation_time + duration)

        for channel, label, propagates in channels:
            # Record trace
            timestamp[label], amplitude[label] = oscilloscope.record(channel)

            # Check for clipping or suboptimal scaling
            start = propagation_time if propagates else 0
            end = start + duration
            burst = (start < timestamp[label]) & (timestamp[label] < end)
            peak = absolute(amplitude[label][burst]).max()
            fill = peak / (amplitude_scales[channel] * oscilloscope.vdivs / 2)
            next_scale = oscilloscope.step_scale(amplitude_scales[channel],
                                                 delta=-1 if fill < .25 else 1 if fill > .75 else 0,
                                                 minimum_scale=10e-3)

            # Delete trace and rescale if the channel needs to be rescaled
            if oscilloscope.scale_delta(next_scale, amplitude_scales[channel]) != 0:
                amplitude_scales[channel] = next_scale
                del timestamp[label], amplitude[label]

    return timestamp, amplitude

# Function which record and returnes the measured admittance from the impedance
# analyzer using parameters from measurement script.
def measure_admittance(frequency, impedance_analyzer):
    return impedance_analyzer.measure(frequency, voltage=1)
```

Appendix B

Post processing, tftools

The scripts used for post-processing of the acquired data are written in MATLAB code and collected in a folder named tftools. They are divided into three sections; one for the post process script, the second for the models used in the post process script and lastly a section of scripts for calculating the transfer functions in the post process script.

B.1 postprocess.m

```
% postprocess.m
% This script reads inn 5 experimental measurements and plots the
% transfer functions used to calculate H15open.
% Paste in the h5-file of the acoustic measurement you want to plot,
% along with its respective noise measurement.
%
% a = acoustic
% n = noise
% e = electrical
% t = transmitter
% r = receiver
%
% Make sure the files are in the MATLAB path.
%
% Created by A. Hagen 2017, modified by R. Grindheim 2019
%% Load data
a = loaddata('acoustic110419_190517.h5');
n = loaddata('noise110419_192645.h5');
e = loaddata('reciever010419_122957.h5');
t = loaddata('admittanceDisk7SampleCount1000.h5');
r = loaddata('admittance030419_094106.h5');

%% Set contants
f = a.f;
d = a.d;

%% Calculate cable transfer functions
[~, idx] = intersect(t.f, f);
t.Z = 1./(t.Y.r(idx) + t.Y.i(idx)*1i).';
H0m1 = H_0m1(t.f(8:end),t.Z);
plottf(f, H0m1, 'H0m1')

[~, idx] = intersect(r.f, f);
r.Z = 1./(r.Y.r(idx) + r.Y.i(idx)*1i).';
H5open5 = H_5open5(r.f(8:end),r.Z);
plottf(f, H5open5, 'H5open5')

%% Calculate noise transfer function
```

```
H06noise = tf(n, 0);
plottf(n.f, H06noise, 'H16noise')

%% Calculate electronics transfer function
[~, idx] = intersect(e.f, f);
H56 = tf(e, 0);
H56 = H56(idx);
plottf(f, H56, 'H56')

%% Calculate full system transfer function
a.t = griddedInterpolant(a.f(~isnan(a.t)), a.t(~isnan(a.t)));
a.t = a.t(f);
c = speedOfSound(f, a.t, a.p, a.h);
alpha = attenuation(f, a.t, a.p, a.h);
a.hrx = a.hrx - (applytf(a.htx, n.f, H06noise) + mean(a.hrx));
k = 2*pi*f./c;
H_BPDC = BPDC(k, 10e-3, d); %H_BPDC = BPDC(k, a, z);
Cdif = 1i.*k.*(10e-3).^2./(2*d)./H_BPDC;
plottf(f, Cdif, 'Cdif')
H0m6 = tf(a, d ./ c) .* exp(0.1151*alpha * d);
plottf(f, H0m6, 'H06')

%% Calculate acoustic transfer function
H15open = H0m6 ./ H0m1 ./ H5open5 ./ H56;
plottf(f, H15open, 'H15open')

%% Loads HDF5 data into struct in the MATLAB workspace
function data = loaddata(file)
data = struct();
info = h5info(file);
for set = info.Datasets'
   data.(set.Name) = h5read(file, ['/' set.Name]);

   if isvector(data.(set.Name))
       data.(set.Name) = data.(set.Name).';
   end
end
end

%% Calculates transfer function
function H = tf(data, pt)
H = waveformtf(data.f, data.ttx, data.htx, data.trx, data.hrx, data.l, pt)
    ;
end

%% Plots transfer function
function plottf(f, H, name)
figure('Name', name)

subplot(2, 1, 1)
plot(f / 1e3, mag2db(abs(H)))
xlabel('Frequency, f [kHz]')
ylabel('Magnitude (dB re 1 V/V)')

subplot(2, 1, 2)
plot(f / 1e3, [angle(H(f < 50e3)) unwrap(angle(H(f >= 50e3)))] * 180/pi)
xlabel('Frequency, f [kHz]')
ylabel('Phase (deg)')
end
```

B.2 Models

The following sections include the scripts for the different models calculated in the post process script.

B.2.1 BPDC.m

```
% BPDC(k, a, z) Calculates the Baffles Piston Diffraction Correction
% according to Khimunin (1972).
%
% Input variables
% k : wavenumber
% a : radius of the piston.
% z : axial distance.
%
% Output variables
% H : complex diffraction correction.
%
%       A. Hagen 2017, comments added by R. Grindheim 2019

function H = BPDC(k, a, z)
H = 1 - (4/pi) * ...
    integral(@(theta) exp(-1i * k .* (sqrt(z.^2 + (2*a*cos(theta)).^2) - z)) .* ...
                     sin(theta).^2, ...
              0, pi/2, 'ArrayValued', true);
end
```

B.2.2 speedofsound.m

```
% c(f, t, p, h) Calculates the speed of sound based on the values
% given for frequency, temperature, pressure and relative humidity.
%
% Input variables
% f : frequency [Hz]
% t : temperature [Celsius]
% p : pressure [Pascal]
% h : relative humidity [percentage in range 0-1]
%
% Output variables
% c : speed of sound
%
%       A. Hagen 2017, modified by R. Grindheim 2019

function c = speedOfSound(f, t, p, h)

f = f(:)';
t = t(:)';
p = p(:)';
h = h(:)';

xc = 4e-4; % Mole fraction of carbondioxide, assumed 400ppm (CITATION NEEDED)
xw = waterVapor(t, p, h); % Mole fraction of water vapor

[alphaO, frO] = attenuationOxygen(f, t, p, h);
[alphaN, frN] = attenuationNitrogen(f, t, p, h);

% Approximate equation after Cramer (1993)
```

```
a = [331.5024 0.603055 -0.000528 51.471935 0.1495874 -0.000782 -1.82e-7 ...
     3.73e-8 -2.93e-10 -85.20931 -0.228525 5.91e-5 -2.835149 -2.15e-13 ...
     29.179762 0.000486];
tp = [ones(size(t)); t; t.^2];
c0 = a*[tp; repmat(xw, 3, 1).*tp; repmat(p, 3, 1).*tp; xc*tp; ...
        xw.^2; p.^2; repmat(xc^2, 1, length(t)); xw.*p.*xc];

% Dispersion correction after Howell and Morfey/1980
c = (c0.^-1 - (alphaO./frO + alphaN./frN)/(2*pi)).^-1;
end
```

B.2.3 attenuation.m

```
% attenuation(f, t, p, h) Calculates the attenuation of sound in air based
% on ANSI/ASA S.126-1995 and the values given for frequency, temperature,
% pressure and relative humidity.
%
% Input variables
% f : frequency [Hz]
% t : temperature [Celsius]
% p : pressure [Pascal]
% h : relative humidity [percentage in range 0-1]
%
% Output variables
% alpha : attenuation coefficient
%
%       A. Hagen 2017, modified by R. Grindheim 2019

function alpha = attenuation(f, t, p, h)
T = 273.15 + t; % Thermodynamic temperature

% Approximate equations after ANSI/ASA S.126-1995
pa = p/1e3; % Kilopascals
pr = 101.325; % NIST STP pressure in kilopascals
Tr = 293.15; % NIST STP temperature

alphaCR = f.^2 .* 1.84e-11 .* (pa/pr).^-1 .* (T/Tr).^(1/2);
alphaO = attenuationOxygen(f, t, p, h);
alphaN = attenuationNitrogen(f, t, p, h);

alpha = alphaCR + alphaO + alphaN;
end
```

B.2.4 attenuationNitrogen.m

```
% attenuationNitrogen(f, t, p, h) Calculates the attenuation of sound in
% air due to nitrogen concentration based on ANSI/ASA S.126-1995 and the
% values given for frequency, temperature, pressure and relative humidity.
%
% Input variables
% f : frequency [Hz]
% t : temperature [Celsius]
% p : pressure [Pascal]
% h : relative humidity [percentage in range 0-1]
%
% Output variables
% alphaN : attenuation coefficient for nitrogen related absorption
% frN = relaxation frequency for nitrogen
```

```matlab
%
%       A. Hagen 2017, comments added by R. Grindheim 2019

function [alphaN, frN] = attenuationNitrogen(f, t, p, h)
T = 273.15 + t; % Thermodynamic temperature

% Approximate equations after ANSI/ASA S.126-1995
pa = p/1e3; % Kilopascals
pr = 101.325; % NIST STP pressure in kilopascals
Tr = 293.15; % NIST STP temperature
xw = waterVapor(t, p, h);
xwp = xw * 100; % Mole fraction of water vapor in percent

frN = pa/pr .* (T/Tr).^(-1/2) .* (9 + 280*xwp.*exp(-4.170*((T/Tr).^(-1/3)
    - 1)));
alphaN = f.^2 .* (T/Tr).^(-5/2) .* 0.1068.*exp(-3352.0./T).*(frN./(frN.^2
    + f.^2));
end
```

B.2.5 attenuationOxygen.m

```matlab
% attenuationOxygen(f, t, p, h) Calculates the attenuation of sound in
% air due to oxygen concentration based on ANSI/ASA S.126-1995 and the
% values given for frequency, temperature, pressure and relative humidity.
%
% Input variables
% f : frequency [Hz]
% t : temperature [Celsius]
% p : pressure [Pascal]
% h : relative humidity [percentage in range 0-1]
%
% Output variables
% alphaO : attenuation coefficient for oxygen related absorption
% frO = relaxation frequency for oxygen
%
%       A. Hagen 2017, comments added by R. Grindheim 2019

function [alphaO, frO] = attenuationOxygen(f, t, p, h)
T = 273.15 + t; % Thermodynamic temperature

% Approximate equations after ANSI/ASA S.126-1995
pa = p/1e3; % Kilopascals
pr = 101.325; % NIST STP pressure in kilopascals
Tr = 293.15; % NIST STP temperature
xw = waterVapor(t, p, h);
xwp = xw * 100; % Mole fraction of water vapor in percent

frO = pa/pr .* (24 + (4.04e4*xwp).*(0.02 + xwp)./(0.391 + xwp));
alphaO = f.^2 .* (T/Tr).^(-5/2) .* 0.01275.*exp(-2239.1./T).*(frO./(frO.^2
     + f.^2));
end
```

B.2.6 waterVapor.m

```matlab
% waterVapor(t, p, h) calculates the mole fraction of water vapor based on
% the values given for temperature, pressure, and
% relative humidity.
%
% Input variables
```

```
% t : temperature [Celsius]
% p : pressure [Pascal]
% h : relative humidity [percentage in range 0-1]
%
% Output variables
% xw : mole fraction of water vapor
%
%       A. Hagen 2017, modified by R. Grindheim 2019

function xw = waterVapor(t, p, h)
T = 273.15 + t; % Thermodynamic temperature

% fW, psv and xw given in Cramer/1993 appendix
f = 1.00062 + 3.14e-8*p + 5.6e-7*t.^2; % Enhancement factor
psv = exp(1.2811805e-5*T.^2 - 1.9509874e-2*T + 34.04926034 - 6.3536311e3./T); % Saturation vapor pressure
xw = h .* f .* psv./p; % Mole fraction of water vapor
end
```

B.3 Transfer functions

The following sections include the scripts for calculating the transfer functions in the post process script.

B.3.1 H_0m1.m

```
% H_0m1(f, Z_Tx) calculates the transfer function HVV_0m1
%       f = frequency [Hz]
%       ZT = impedance of transmitting disk [Omega]
%       function loads and uses values stored in struct "variables.mat"
%       remember to add path to this struct
%
%       K. K. Andersen 2015, modified by R. Grindheim 2019
function H0m1 = H_0m1(f,ZTx)
%% path and load variables stored in struct
PWD = 'D:\Renate\tftools\';
load([PWD, 'variables.mat'])

%% define variables
w = 2*pi.*f;

% Input impedance oscilloscope Z_osc: 1M ohm || 11.5pF
Zc = 1./(1i*(var.Zosc_inC)*w);
Zr = var.Zosc_inR;
Zosc = (Zr.*Zc)./(Zc + Zr);

%% Cable 1
lx1 = var.cable1;
L1 = var.Lx;
C1 = var.Cx;
Z01 = sqrt(L1/C1);
k_em1 = w.*sqrt(L1*C1);
Za1 = 1i*Z01.*tan(k_em1.*(lx1/2));
Zb1 = Z01./(1i.*sin(k_em1.*lx1));

%% Cable 2
lx2 = var.cable2;
L2 = var.Lx;
C2 = var.Cx;
```

```
Z02 = sqrt(L2/C2);
k_em2 = w.*sqrt(L2*C2);
Za2 = 1i*Z02.*tan(k_em2.*(lx2/2));
Zb2 = Z02./(1i.*sin(k_em2.*lx2));

%% expressions for voltages
V0m = (Zosc.*Zb2)./(Za2.*Zb2 + (Zosc + Za2).*(Za2 + Zb2));
V1 = (Zb1.*ZTx)./(Zb1.*(Za1 + ZTx) + Za1.*Zb1 + Za1.*(Za1 + ZTx));

%% transfer function
H0m1 = V1./V0m;

end
```

B.3.2 H_5open5.m

```
% HVV_5open5(f, ZRx) calculates the transfer function HVV_5open5
%        f = frequency [Hz]
%        ZR = complex impedance of receiving disk [Omega]
%        function loads and uses values stored in struct "variables.mat"
%        remember to add path to this struct
%
%        K. K. Andersen 2015, modified by R. Grindheim 2019
function H5open5 = H_5open5(f,ZRx)
%% path and load variables stored in struct
PWD = 'D:\Renate\tftools\';
load([PWD, 'variables.mat'])

%% Input impedance amplifier
% 1 Mohm || 90 pF vs. 0.95 Mohm || 96pF
w = (2*pi).*f;
C_amp = var.Zamp_inC;
R_amp = var.Zamp_inR;
Zc = 1./(1i*C_amp*w);
Zamp = (R_amp.*Zc)./(Zc + R_amp);

%% Cable 2
lx3 = var.cable3;
L3 = var.Lx;
C3 = var.Cx;
Z03 = sqrt(L3/C3);
k_em3 = w.*sqrt(L3*C3);
Za3 = 1i*Z03.*tan(k_em3.*(lx3/2));
Zb3 = Z03./(1i.*sin(k_em3.*lx3));

Za3 = 0;

%% transfer function
H5open5 = (Zamp.*Zb3)./((ZRx + Za3).*Zb3 + (Za3 + Zamp).*(ZRx + Za3 + Zb3)
    );

end
```

B.3.3 waveformtf.m

```
%% waveformtf(f, ttx, htx, trx, hrx, bt, pt) calculates the
%  transfer function H of the measured signal.
%
% Input variables
```

```
% f : frequency vector
% ttx : time vector for transmitted signal
% htx : amplitude vector for transmitted signal
% trx : time vector for received signal
% hrx : amplitude vector for received signal
% bt : burst length
% pt : apropagation time
%
% Output variables
% H : transfer function
%
%       A. Hagen 2017, modified by R. Grindheim 2019

function H = waveformtf(f, ttx, htx, trx, hrx, bt, pt)
if length(pt) == 1
    pt = repmat(pt, size(f));
end

if length(bt) == 1
    bt = repmat(bt, size(f));
end

H = cellfun(@transferfunctionvalue, ...
    num2cell(f, 1), ...
    num2cell(ttx, 1), num2cell(htx, 1), ...
    num2cell(trx, 1), num2cell(hrx, 1), ...
    num2cell(bt, 1), num2cell(pt, 1));
end

function H = transferfunctionvalue(f, ttx, htx, trx, hrx, bt, pt)
for data = [struct('ch', 'tx', 'time', ttx, 'sig', htx, 'propagates', false), ...
            struct('ch', 'rx', 'time', trx, 'sig', hrx, 'propagates', true)]
    % Reassign loop data
        time = data.time;
    sig = data.sig;
    ch = data.ch;
    propagates = data.propagates;

    % Remove bias
    sig = sig - mean(sig);

    % Calculate sample rate
    dt = time(2) - time(1);
    fs = 1/dt;

    for data = [struct('idx', 1, 'discard', .4, 'indexer', crossings(sig)), ...
                struct('idx', 2, 'discard', 0, 'indexer', 1:length(time))] %#ok<FXSET>
        % Reassing loop data
        idx = data.idx;
        discard = data.discard;
        indexer = data.indexer;

        % Estimate start and stop based on characteristic data
        start = pt * propagates;
        stop = start + bt;

        % Discard part of the signal according to the discard variable and
        % readjust to closest estimated period based on characteristic data
```

```
        discard = discard * bt;
        cyclestarts = (0:floor(f * bt)-1) / f;
        [~, ndx] = min(abs(cyclestarts - discard));
        start = start + cyclestarts(ndx);

        % Select closest sample to calculated start and stop according to
        % the indexer variable
        [~, start] = min(abs(time(indexer) - start));
        [~, stop] = min(abs(time(indexer) - stop));
        ndx = indexer(start):indexer(stop);

        % Calculate DFT bin of cut signal
        h = sig(ndx);
        L = length(h);
        [N, n] = fftpad(f, L, fs);
        dft.(ch)(idx) = goertzel([h; zeros(N-L, 1)], n);
    end
end

% Calculate transfer function value
Habs = abs(dft.rx(1)/dft.tx(1));
Hangle = angle(dft.rx(2)/dft.tx(2));
H = Habs * exp(1i * Hangle);
end
```

B.3.4 applytf.m

```
%% applytf(h, f, H) calculates the
%  transfer function H of the measured signal.
%
% Input variables
% h : amplitude vector
% f : frequency vector
% H : transfer function
%
% Output variables
% h : amplitude vector
%
%       A. Hagen 2017, comments added by R. Grindheim 2019

function h = applytf(h, f, H)
H = griddedInterpolant(f, H, 'nearest');
H = H(0:f(2)-f(1):f(end)) / 2;
H = [H fliplr(conj(H(2:end-1)))].';

for idx = 1:size(h, 2)
    h(:,idx) = real(ifft(fft(h(:,idx)) .* H));
end
end
```

B.3.5 crossings.m

```
% crossings(h) Finds all the points at which the signal
% crosses the zero line. When a zero crossing is found the point before
% or after the crossing is returned depending on which is closer to zero.
%
% Input variables
% h : amplitude vector
%
```

```matlab
% Output variables
% crossings : vector of new values for previous zero points
%
%       A. Hagen 2017, comments added by R. Grindheim 2019

function crossings = crossings(h)
h = h(:);

% Find all crossings
crossings = find(h(1:end-1) .* h(2:end) <= 0 & ...
                  (h(1:end-1) ~= 0 | h(2:end) ~= 0)); % First index of crossings
[~, idx] = min(abs(h([crossings crossings + 1])), [], 2); % Is first or second index smaller?
crossings = crossings + idx - 1; % Correct if second is smaller
crossings = unique(crossings); % Remove duplicates
end
```

B.3.6 fftpad.m

```matlab
% fftpad(f, L, fs, range) Optimizes FFT padding to center a
% frequency bin close to the frequency f.
% fftpad(f, L, fs) finds the optimal signal length in the range [L 2L].
% fftpad(___, range) extends the range to the specified range parameter.
%
% Input variables
% f : frequency vector
% L : length of amplidtude vector
% fs : sample rate
% range : range specified from the amplitude vector, default: [L 2L]
%
% Output variables
% N : optimal signal length
% n : best FFT number close to the frequency f
%
%       A. Hagen 2017, comments added by R. Grindheim 2019

function [N, n] = fftpad(f, L, fs, range)
if nargin < 4
    range = [1 2];
end

% Possible values
n = ceil(range(1)*L*f/fs):floor(range(2)*L*f/fs);
N = n*(fs/f);

% Find optimal
[~, idx] = min(N - round(N));

% Extract
n = n(idx) + 1; % Off by one due to MatLab indexing
N = round(N(idx));
end
```

Appendix C

FEMP simulation

C.1 Structure, piezofluid.inn

```
# FEMP V3.0 INPUT-FILE
# Example file for a PZT-5A isk with diameter 10.0 mm and thickness 2.0 mm
# in vacuum. Calculations are made using direct time-harmonic analysis.
# Admittance and source sensitivity response is calculated for
# a limited frequency range.
# Losses are included using complex material constants.
# The results from this file is equivalent with the results from
# the example input file 'disk_vacuum_modal.inn'. However, instead
# of using modal analysis, direct time-harmonic analysis is used.
# Therefore, no resonance frequencies are calculated.

set
r,10.099e-3
t,2.04102e-3
mesh_pz_fl,3
mesh_inf_fl,1
mat,2
matnumfluid,3
fmin,0
fmax,300e3
fstep,0.1e5
fmesh, 100e3
rinf,30e-3
d0, 1000
end

materialfile
2
end

# The number of elements per wavelength is calculated at upper frequency range
meshingtype
elementsperwavelength,fmesh
end

# The order of the finite elements is 2 - i.e. 8 node isoparametric elements are applied
order
2
end

```

```
infiniteorder
12
end

# Model a piezoelectric disk with radius and thickness defined by the
# variable 't' and 'r' from set, n elements per wavelength in both radial and thickness
# direction, and of material given by mat
piezofluid
r,t,mesh_pz_fl,mesh_pz_fl,mat,rinf,mesh_pz_fl,mesh_pz_fl,mesh_inf_fl,mesh_inf_fl,matnumfluid
end

# Perform a direct time-harmonic analysis, in which calculations are made
# for frequencies between fmin and fmax MHz in steps of fstep.
# Complex losses are used.
directharmonicanalysis
fmin,fstep,fmax,complex_loss
end

# Calculate admittance for the frequencies used in the time-harmonic analysis
admittance
0,0,0
end

# Calculate sensitivity
sensitivity
0,0,0,d0
end

# Save admittance and sensitivity to
# matlab-file 'disk_vacuum_direct_result.mat'.
save
admittance,admittance_f,sensitivity,sensitivity_f
end
```

C.2 Post-processing

```
%% Compute open circuit loss-free simulated transfer function
    % subscript _f denotes FEMP, ff denotes far-field
    % using simulation of disk 07 regardless of actual transmitter and receiving disk
    % Author: Kenneth K. Andersen 2015, modified by Renate Grindheim 2019

    d = 0.5;
    d0 = 1;
    load('piezofluid_result.mat', 'result');
    zff = 1000; % far-field distance
    p4_zff = result.sensitivity{:}; % far-field pressure
    ZT_f = 1./result.admittance{:}; % impedance
    f_f = result.sensitivity_f{:}; % frequency vector
    c_f = 342.9999455620972; % hardcoded value for speed of sound
    k_f = 2*pi*f_f./c_f;
    rho_f = 1.205; % hardcoded value for density of air

    % open circuit loss-free simulated transfer function
    Hvv15open_f = ZT_f.*p4_zff.^2.*(2.*zff.^2)./(1i.*rho_f.*d.*f_f).*exp(1i.*k_f.*(2.*zff - d));
```

```
    Hvv15open_f_phi = rad2deg(unwrap(angle(Hvv15open_f)) + k_f.*d);

    % transmitting and receiving sensitivities
    Sv_f_zff = result.sensitivity{:}; % far-field pressure == source sensitivity
    Sv_f_d0 = Sv_f_zff.*zff./d0.*exp(1i.*k_f.*(zff - d0));

    % calculate reciprocity parameter, valid at d0 = 1 m
    J_f_d0 = 2*d0./(1i.*rho_f.*f_f).*exp(1i.*k_f.*d0);
    Mv_f = J_f_d0.*Sv_f_d0.*ZT_f;

%% Plotting, figure 1
figlabfs = 16;
labfs = 17;

figure(1)
clf
ha = tight_subplot(2,1,[.03 .03],[.09 .04],[.12 .04]);
axes(ha(1))

% Magnitude
plot(f_f/1000, mag2db(abs(Hvv15open_f)),'b', 'LineWidth', 1.5);

set(gca, 'YGrid','on', 'XGrid','on','fontsize',labfs,'box', 'on', 'Xtick', 0:25:300);
ylabel('$20\log_{10}|H^{VV}_\mathrm{15,open}(d)|$ [dB re 1 V/V]', 'Interpreter','LaTeX')
xlim([0, 300])
ylim([-180, -80])
ll = legend({'FEM'},'Location','southeast');
ll.Interpreter = 'LaTeX';
xl = xlim;
xls = abs(xl(2) - xl(1));
yl = ylim;
yls = abs(max(yl) - min(yl));
set(gca, 'XTickLabel', '')
text(xl(1) + 0.95*xls, min(yl) + 0.9*yls, '\textbf{(a)}', 'FontWeight', 'Bold', 'FontSize', figlabfs, 'Interpreter', 'LaTeX')
text(xl(1) + 0.05*xls, min(yl) + 0.9*yls, ['$d$ = ', num2str(d), ' m'],'FontSize', figlabfs+4, 'Fontweight', 'Normal', 'Interpreter', 'LaTeX')
set(gca,'TickLabelInterpreter','latex')
% ----------------
axes(ha(2))
 % Phase
plot(f_f/1000, Hvv15open_f_phi, 'b', 'LineWidth', 1.5);

set(gca, 'YGrid','on', 'XGrid','on','fontsize',labfs,'box', 'on', 'Xtick', 0:25:300,'Ytick', -180:90:540);
xlabel('Frequency, $f$ [kHz]', 'Interpreter', 'LaTeX')
ylabel('$\angle \left\{ H^{VV}_\mathrm{15,open}(d) / e^{-ikd} \right\}$ $[^{\circ}]$', 'Interpreter', 'LaTeX')
xlim([0,300])
ylim([-185, 450])

xl = xlim;
xls = abs(xl(2) - xl(1));
yl = ylim;
yls = abs(max(yl) - min(yl));
text(xl(1) + 0.95*xls, min(yl) + 0.9*yls, '\textbf{(b)}', 'FontSize', figlabfs, 'Interpreter', 'LaTeX')

set(gca,'TickLabelInterpreter','latex')
set(gcf, 'Position', [400, 400, 900, 600])
```

```
%print(gcf,'renate_test.png', '-dpng', '-r600')
```

Appendix D

Waveform of different pulses

D.1 Waveform of pulses at $d = 50$ cm

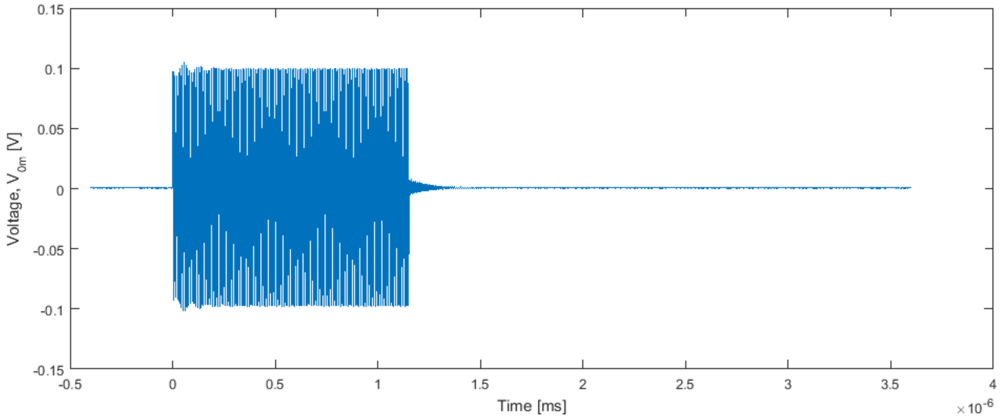

FIGURE D.1: Waveform of sent pulse at 112.04 kHz at a separation distance $d = 50$ cm.

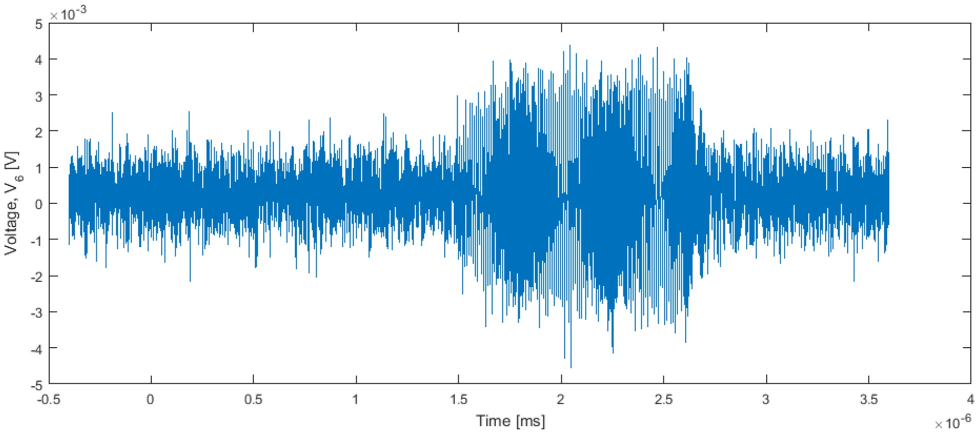

FIGURE D.2: Waveform of received pulse at the first peak associated with R_1 at 98.572 kHz with a separation distance $d = 50$ cm.

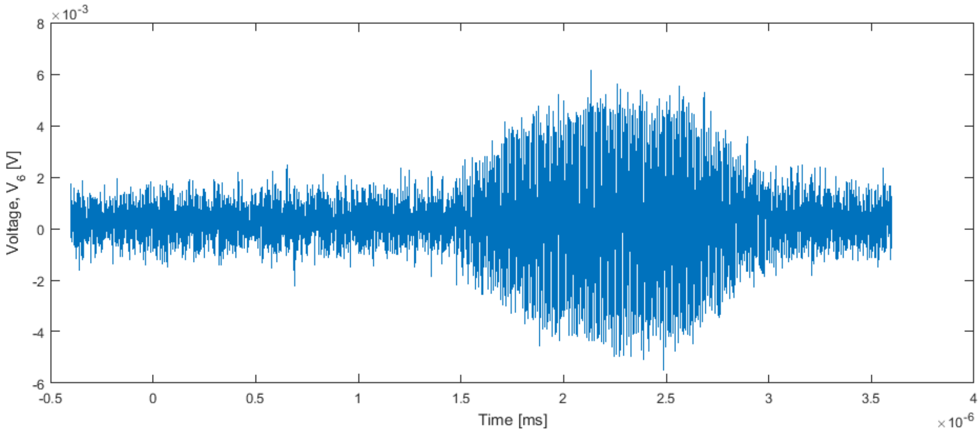

FIGURE D.3: Waveform of received pulse at the second peak associated with R_1 at 112.04 kHz with a separation distance $d = 50$ cm.

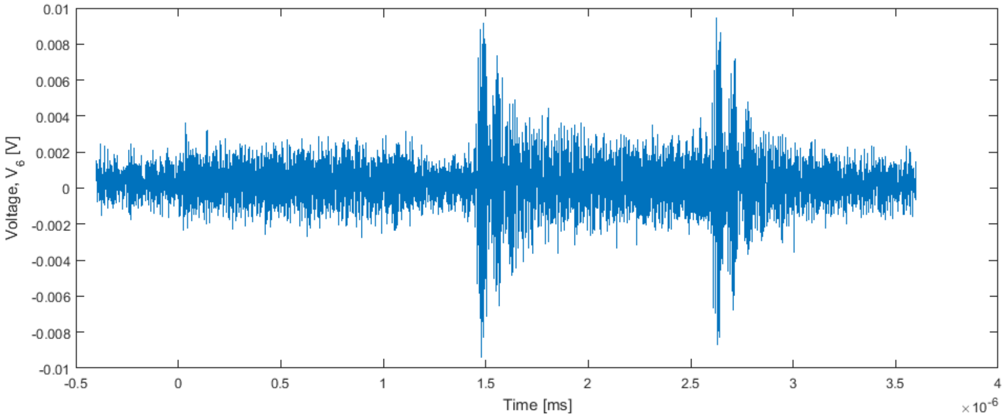

FIGURE D.4: Waveform of received pulse at 175.192 kHz at a separation distance $d = 50$ cm.

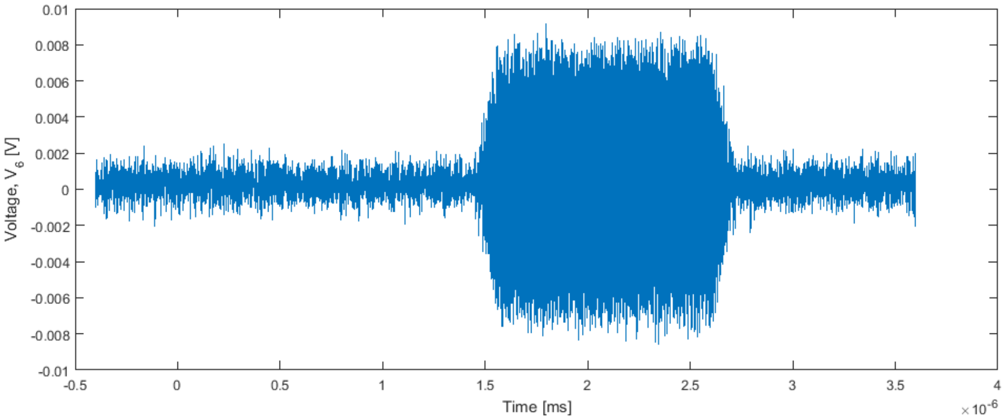

FIGURE D.5: Waveform of received pulse at the first peak associated with R_2 at 251.214 kHz with a separation distance $d = 50$ cm.

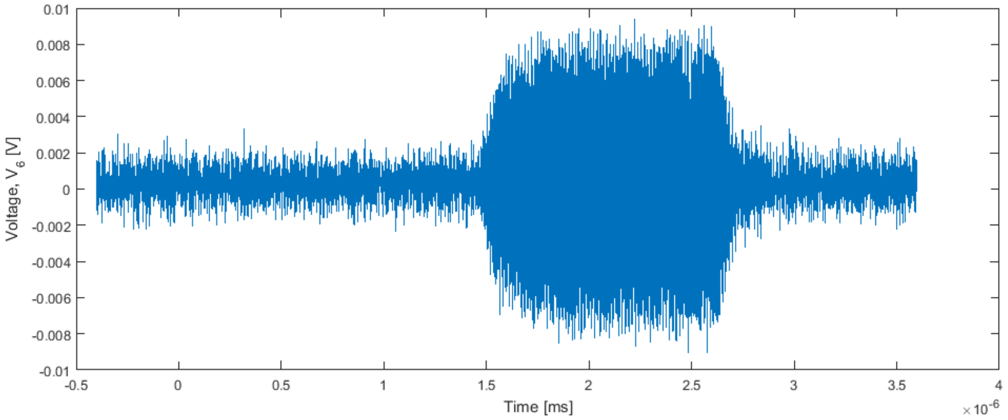

FIGURE D.6: Waveform of received pulse at the second peak associated with R_2 at 255.105 kHz with a separation distance $d = 50$ cm.

D.2 Waveform of pulses at $d = 30$ cm

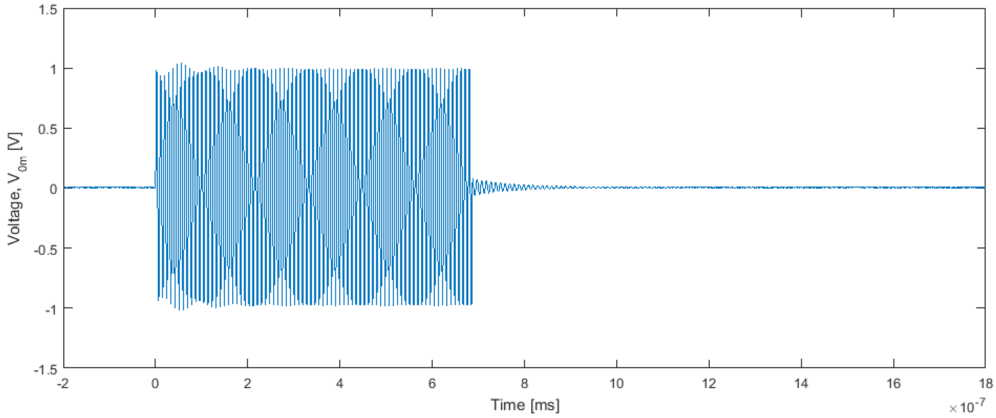

FIGURE D.7: Waveform of sent pulse at 112.04 kHz at a separation distance $d = 30$ cm.

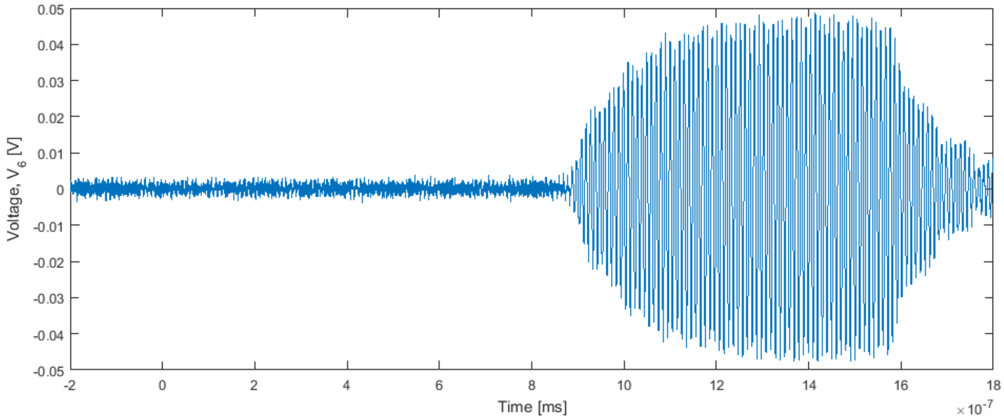

FIGURE D.8: Waveform of received pulse at the first peak associated with R_1 at 98.572 kHz with a separation distance $d = 30$ cm.

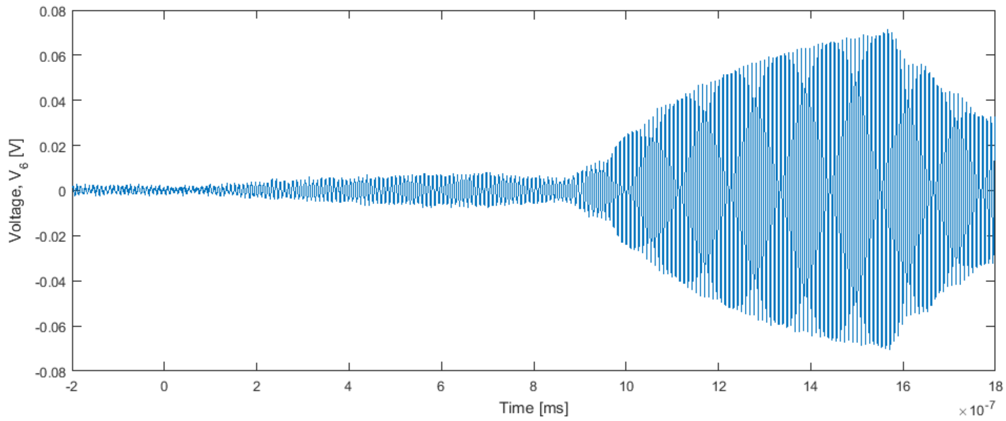

FIGURE D.9: Waveform of received pulse at the second peak associated with R_1 at 112.04 kHz with a separation distance $d = 30$ cm.

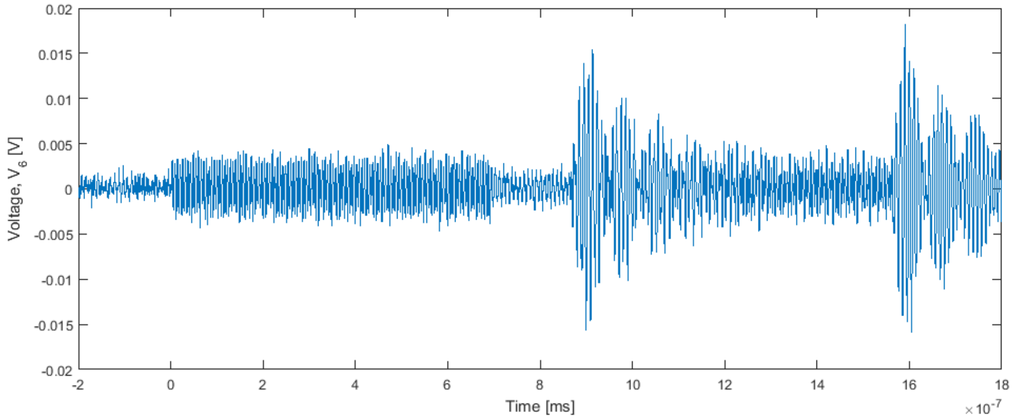

FIGURE D.10: Waveform of received pulse at 175.192 kHz at a separation distance $d = 30$ cm.

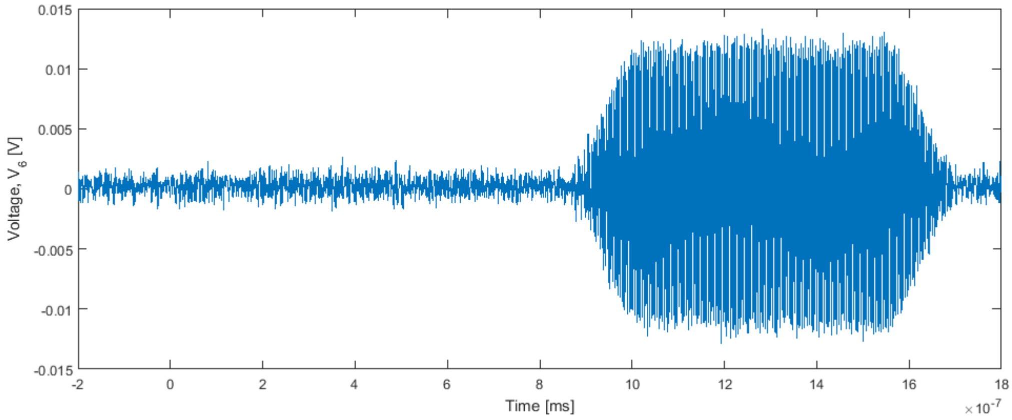

FIGURE D.11: Waveform of received pulse at the first peak associated with R_2 at 251.214 kHz with a separation distance $d = 30$ cm.

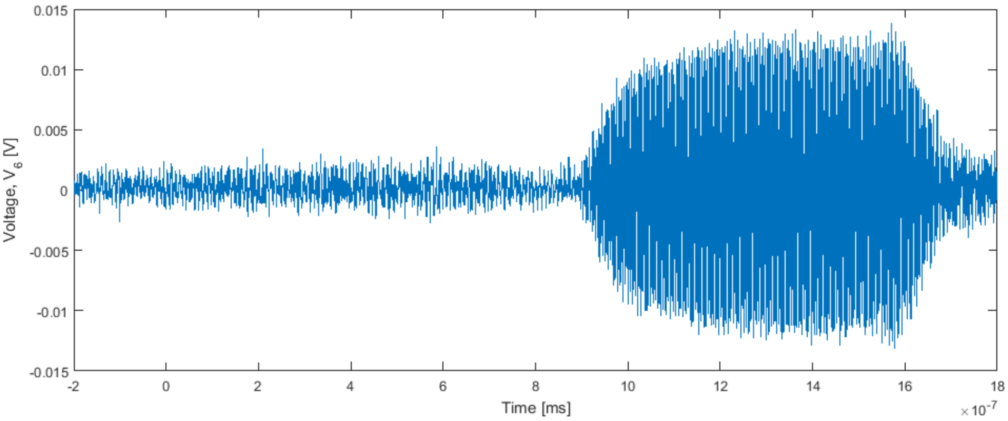

FIGURE D.12: Waveform of received pulse at the second peak associated with R_2 at 255.105 kHz with a separation distance $d = 30$ cm.

D.3 Waveform of pulses at $d = 20$ cm

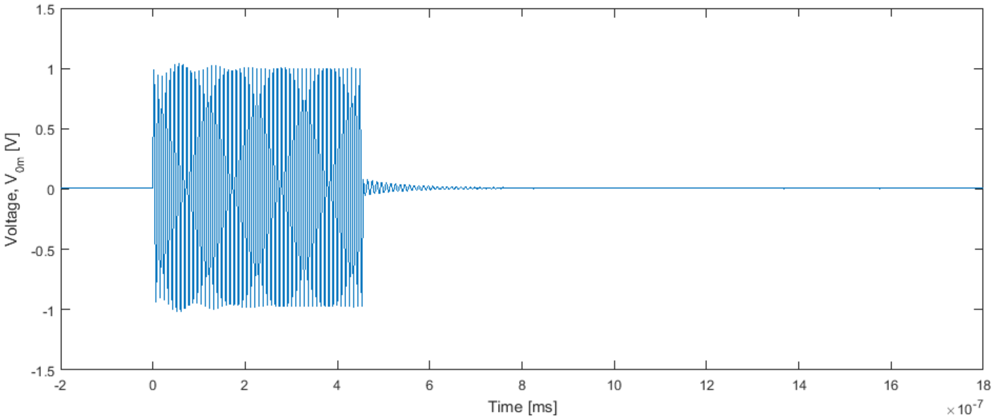

FIGURE D.13: Waveform of sent pulse at 112.04 kHz at a separation distance $d = 20$ cm.

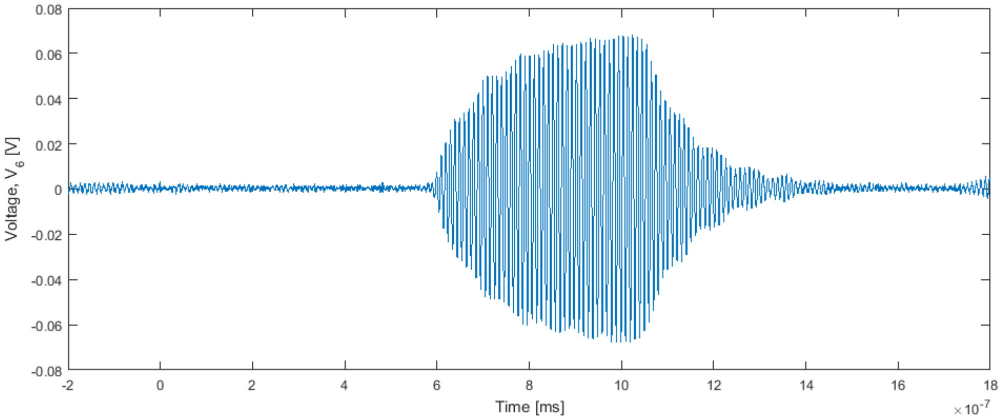

FIGURE D.14: Waveform of received pulse at the first peak associated with R_1 at 98.572 kHz with a separation distance $d = 20$ cm.

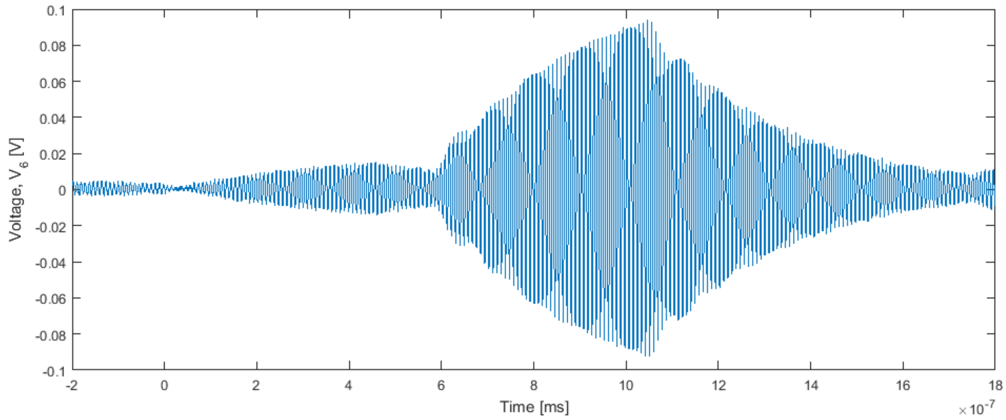

FIGURE D.15: Waveform of received pulse at the second peak associated with R_1 at 112.04 kHz with a separation distance $d = 20$ cm.

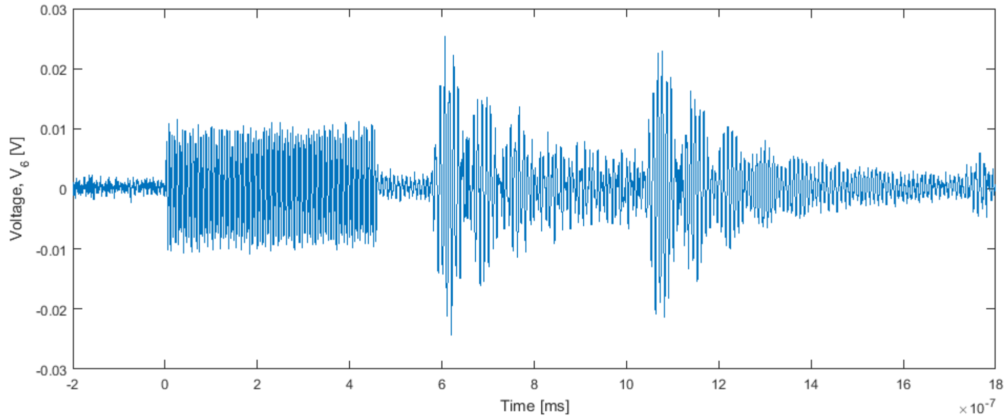

FIGURE D.16: Waveform of received pulse at 175.192 kHz at a separation distance $d = 20$ cm.

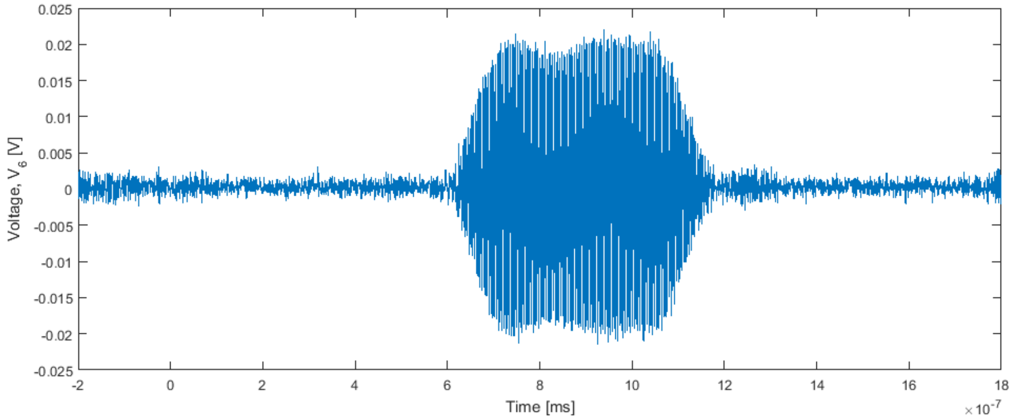

FIGURE D.17: Waveform of received pulse at the first peak associated with R_2 at 251.214 kHz with a separation distance $d = 20$ cm.

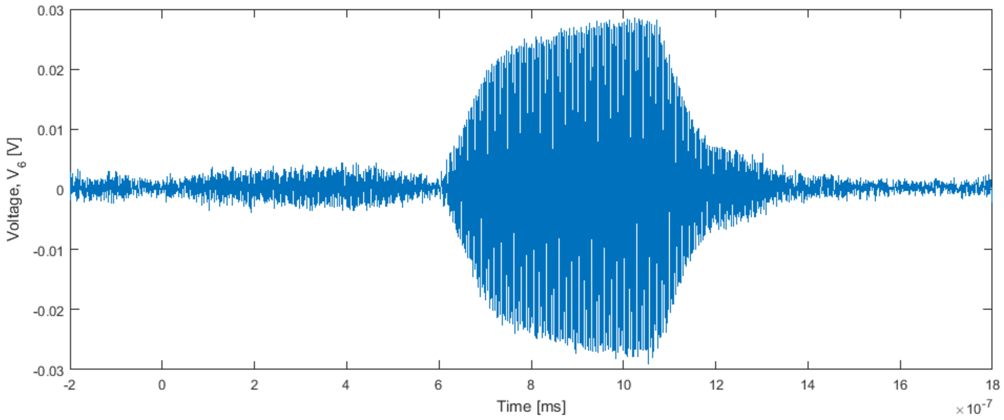

FIGURE D.18: Waveform of received pulse at the second peak associated with R_2 at 255.105 kHz with a separation distance $d = 20$ cm.

D.4 Waveform of pulses at $d = 15$ cm

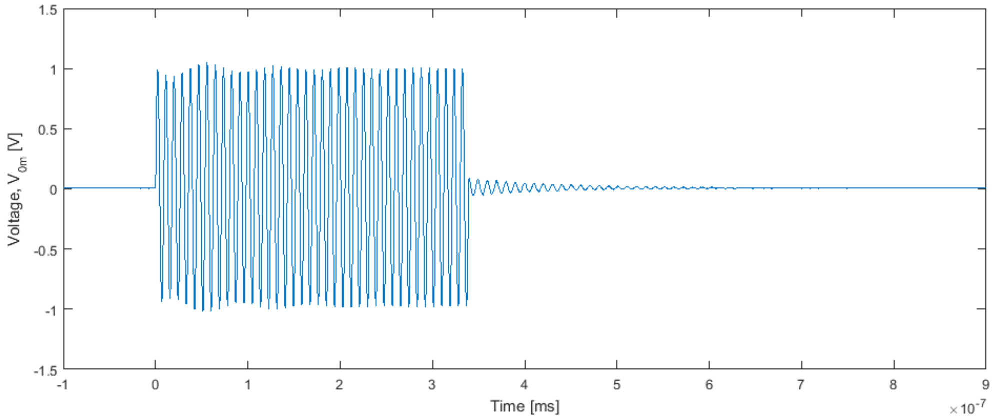

FIGURE D.19: Waveform of sent pulse at 112.04 kHz at a separation distance $d = 15$ cm.

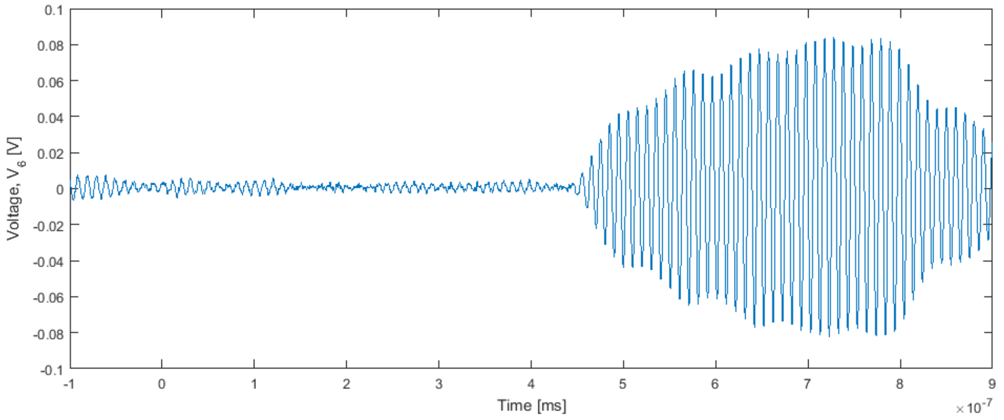

FIGURE D.20: Waveform of received pulse at the first peak associated with R_1 at 98.572 kHz with a separation distance $d = 15$ cm.

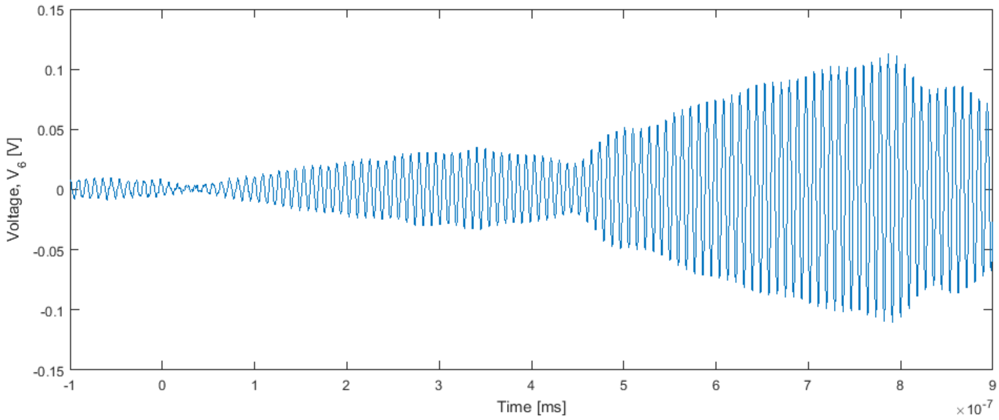

FIGURE D.21: Waveform of received pulse at the second peak associated with R_1 at 112.04 kHz with a separation distance $d = 15$ cm.

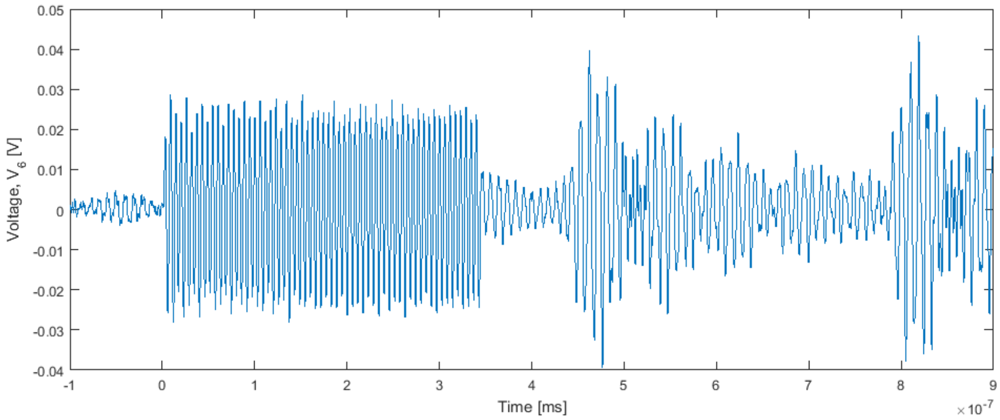

FIGURE D.22: Waveform of received pulse at 175.192 kHz at a separation distance $d = 15$ cm.

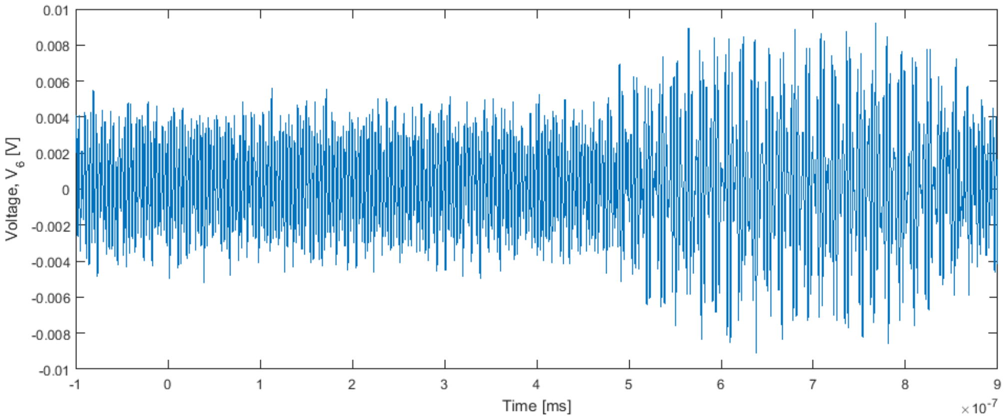

FIGURE D.23: Waveform of received pulse at the first peak associated with R_2 at 251.214 kHz with a separation distance $d = 15$ cm.

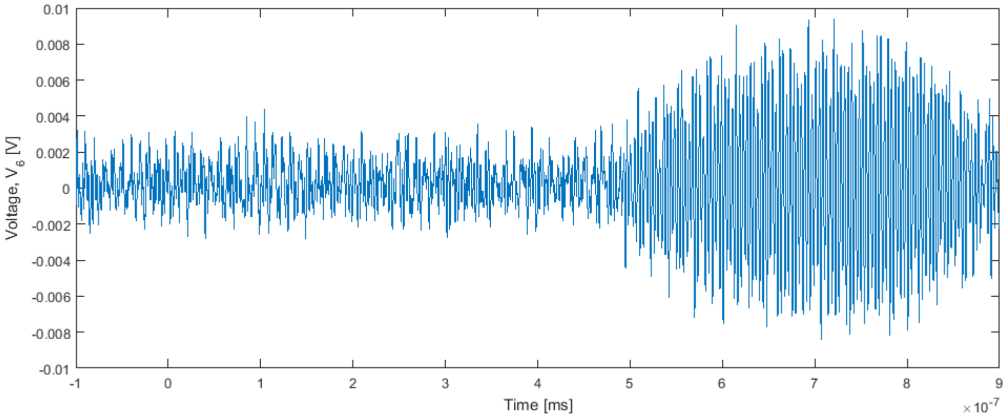

FIGURE D.24: Waveform of received pulse at the second peak associated with R_2 at 255.105 kHz with a separation distance $d = 15$ cm.

Appendix E

Conference proceeding (SSPA)

Conference article in the proceedings of the 42nd Scandinavian Symposium on Physical Acoustic 2019, Geilo, Norway, Jan 27-31, 2019

Proceedings of the 42nd Scandinavian Symposium on Physical Acoustics, Geilo, Norway, Jan. 27–30, 2019

Characterization of ultrasound transmit-receive measurement systems in air

Comparison with prior work on piezoelectric elements in radial mode vibration

Renate Grindheim[1], Per Lunde[1,2], Magne Vestrheim[1]

[1] University of Bergen, Department of Physics and Technology, P.O. Box 7803, NO-5020 Bergen, Norway
[2] NORCE, Norwegian Research Centre AS, P.O. Box 6031, NO-5898 Bergen, Norway
Contact email: renate.grindheim@uib.no

Abstract

Ultrasound transmit-receiver measurement systems are used in numerous applications in the industry and scientific applications. A system model describing the voltage-to-voltage transfer function for a transmit-receiver pair based on simulations using the finite element model for piezoelectric transducers (FEMP) is used. The elements used in this work are ceramic piezoelectric Pz27 disks vibrating radially in air at room temperature and 1 atm in the frequency range of 3 - 300 kHz. Comparisons are made between measurements and simulations. The effect of uncertainties in alignment is examined and comparison with previous works is presented.

1 Introduction

Accurate modelling of ultrasonic measurement systems for characterization of gas is of interest in industrial and scientific applications. Examples include fiscal flow measurement for custody transfer of natural gas [1, 2], energy and quality measurement of gas [2–4], and sound velocity and absorption measurements [5, 6]. In the present work a "system model" of a transmit-receive measurement system refers to "a mathematical / numerical model aiming to describe the chain of electro-acoustic signal propagation through the system, from the electrical signal generator to the electrical recording equipment (e.g., an oscilloscope), via the piezoelectric transmit and receive transducers, the propagation medium, and possible transmit and receive cables/electronics" [7].

Various approaches have been used to describe transmit-receive ultrasonic measurement systems for fluids. This includes methods based on (i) the Mason model [or equivalent one-dimensional (1D) approaches] for thickness-mode transmitting and receiving transducers, combined e.g. with uniform piston [2, 8–14] or plane wave [15–20] type of radiation models; (ii) 1D "electroacoustic measurement (EAM) model" types of description [21–24]; and (iii) purely electrical transmission line system modelling [25]. More rigorous and accurate descriptions based on finite element modelling (FEM) have proven highly useful for ultrasonic system modelling, accounting for e.g. thickness-mode [26–30] and radial mode [5, 7, 31–36] transducers in such measurement setups.

The work presented here builds on prior work described in Refs. [5, 7, 31, 32, 34–36], using finite element modelling of an ultrasonic measurement system for air employing piezoelectric elements vibrating in their lower radial modes. Measurements and simulations of the frequency response of a voltage-to-voltage transmit-receive transfer function are compared, including comparison with some recent work in this area [35, 36]. A second objective is to investigate and quantify measurement deviations due to uncertainties in alignment and positioning of the transmitting and receiving piezoelectric elements in this setup.

2 Theory

The experimental measurement setup used in the present work is described in Section 3.1. A system model based on this setup is presented.

2.1 System model

The system model illustrated in Figure 1 shows the different components included in the measurement setup as linear, time invariant blocks where transfer functions relates the signal going from one block to another in the frequency domain. The system model consists of two piezoelectric disks in radial mode vibration in air, where the transmitting disk, Tx, is coupled to transmitting electronics (signal generator, oscilloscope and cables) and the receiving disk, Rx, is coupled to receiving electronics (amplifier, filter, oscilloscope and cables).

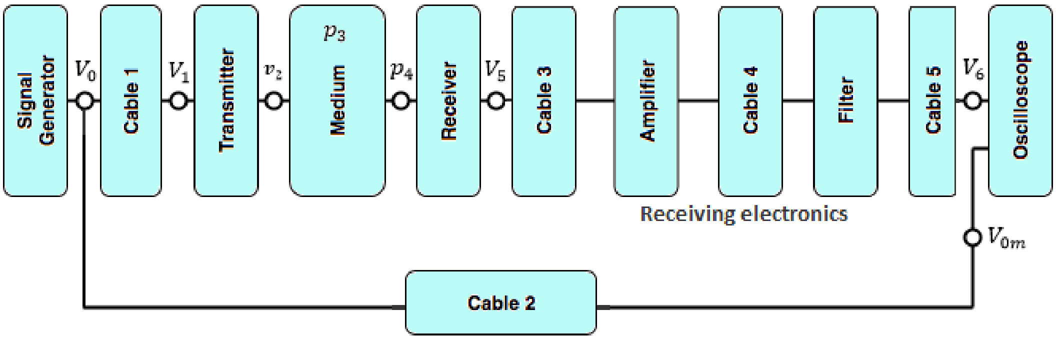

Figure 1: Block diagram representation of the system model used in the present work.

V_0 is the output voltage generated by the signal generator and V_{0m} is the output voltage measured in Channel 1 on the oscilloscope. V_1 is the input voltage to the transmitting disk, T_x. v_2 is the particle displacement at front of T_x. p_3 is the on-axis free-field pressure in the medium and p_4 is the on-axis free-field pressure at the front of the receiving disk, R_x. V_5 is the output voltage from R_x going in to cable 3 and $V_{5'}$ is the output voltage from cable 3 going into the amplifier. V_6 is the input voltage measured and terminated in Channel 2 on the oscilloscope.

2.2 Transfer function representation

The output voltage V_6 measured at the oscilloscope divided by the input voltage V_{0m} measured at the oscilloscope gives the voltage-to-voltage transfer function of the system model

$$H_{0m6}^{VV}(f) = |H_{0m6}^{VV}(f)|e^{i\theta_{0m6}} = \frac{V_6}{V_{0m}} \tag{1}$$

where $|H_{0m6}^{VV}(f)|$ is the magnitude and $e^{i\theta_{0m6}}$ is the phase of the transfer function.

In order to simplify simulation and cut down simulation time only the loss-free element-to-element transfer function is simulated,

$$H_{15open}^{VV}(f) = \frac{V_{5open}}{V_1} \tag{2}$$

where V_1 is the input voltage at the transmitter and V_{5open} is the open-circuit voltage at the receiver. To compare simulations and measurements transfer functions for the transmitting and receiving electronics and cables along with corrections for attenuation and absorption are used to obtain the loss-free element-to-element transfer function $H_{15open}^{VV}(f)$.

The transfer function for cable 1, H_{0m1}^{VV} is given as described by [35]

$$H_{0m1}^{VV}(f) = \frac{V_1}{V_{0m}} \tag{3}$$

The transfer functions H_{5open5}^{VV} describing the cable from the receiver to the amplifier and H_{56}^{VV} describing the receiving electronics including cable 4 and 5 are given as described by [36] yielding

$$H_{5open5}^{VV}(f) = \frac{V_{5open}}{V_5} \tag{4}$$

and

$$H_{56}^{VV}(f) = \frac{V_6}{V_5}. \tag{5}$$

The transfer functions H_{0m1}^{VV} and H_{5open5}^{VV} are estimated using transmission line models as proposed by [34], and the transfer function H_{56}^{VV} is found by measuring the transfer function of only the receiving electronics including cable 4 and 5 by coupling the signal generator to an attenuator and then directly into the receiving electronics, bypassing the transmitter and receiver completely.

Correction for the attenuation in air, C_α, is found by accounting for attenuation due to classical absorption of sound in air, α_{cl}, rotational motion of the air molecules, α_{cl}, vibrations of oxygen moleculer, $\alpha_{vib,O}$ and vibration of nitrogen molecules, $\alpha_{vib,N}$. These are calculated according to [37] and the theory described in [35, 36]. The correction for diffraction effects due to the finite size of the transmitter, C_{dif}, is accounted for by using a baffled piston diffraction correction as in [35, 36], where the diffraction correction is calculated according to Khimunin [38, 39].

The measured loss-free voltage-to-voltage transfer function describing the sound propagation from the transmitting disk to the receiving disk is given as

$$H_{15open}^{VV}(f) = \frac{H_{06}^{VV}(f)}{H_{0m1}^{VV}(f)H_{5open5}^{VV}(f)H_{56}^{VV}(f)}C_\alpha C_{dif} \tag{6}$$

The total phase is composed by a slowly varying phase and a plane wave component. The slowly varying phase is thus given by

$$e^{i\theta_{15open}^{slow}} = e^{i(\theta - kd)} \tag{7}$$

where k is the wave number and d is the separation distance between the transmitter and the receiver.

2.3 Simulated transfer function H^{VV}_{15open}

The simulated transfer function H^{VV}_{15open} is calculated using the simulated far-field pressure $p_{ff} = p_{ax}(z_{ff})$, where $z_{ff} = 1000$ m is used and spherical reciprocity is assumed. This is given as

$$H^{VV}_{15open}(f) = \frac{Z_T p_4^2(z_{ff}) 2 z_{ff}^2}{i\rho d f} e^{ik(2z_{ff}-d)} \tag{8}$$

where Z_T is the impedance of the transmitting disk, p_4 is the simulated pressure at the front of the receiving disk, ρ is the density of the medium, f is the frequency, k is the complex wave number of the medium and d is the separation distance between the front faces of the disks.

3 Methods

The experimental setup has been largely kept as used by [34–36] with only minor changes such as the lengths of cables 4 and 5, and the different instruments have been moved due to a renovation at the lab in 2017. A brief overview of the setup is given in Section 3.1.

3.1 Experimental Setup

The two piezoelectric disks are mounted in air on positioning stages (Physik Instrumente GmbH&Co, Germany). The transmitting disk, T_x is connected to a linear stage (PI M-531.DG [40]) allowing movement in the z-direction and to a rotation stage (PI M-037.PD [41]) for rotation along the x-axis, Figure 3. The receiving disk, R_x i connected to a lateral stage (PI M-535.22 [42]) moving in x-direction. A laser is mounted on a rod which is suspended between the two disks in order to measure aligning and accurately determine the distance, d, between the disks. In this work the distance used is d = 0.50 m.

An Agilent 33220A function generator is used to generate the input signal at desired voltage over the frequency range 3-300 kHz. The signal is then monitored through a Tektronix DPO3012 digital oscilloscope. The receiver is connected to a Bruel&Kjær 2636 amplifier and a Krohn-Hite 3940A digital filter before the signal terminates in the Tektronix DPO3012 digital oscilloscope. The cables used to connect the instruments (cables 2, 4 and 5) are coaxial cables of type RG-58. The cables used to connect the oscilloscope to the transmitter and the receiver to the amplifier (cable 1 and 3 respectively) are coaxial cables of type RG-178 B/U with length $l_1 = 3.045$ m and $l_3 = 0.304$ m respectively. For the current work the piezoelectric elements used are elements 7 and 13, for transmitter and receiver respectively. This is the same as [36], where [35] used elements 4 and 13 in the results presented later from that thesis.

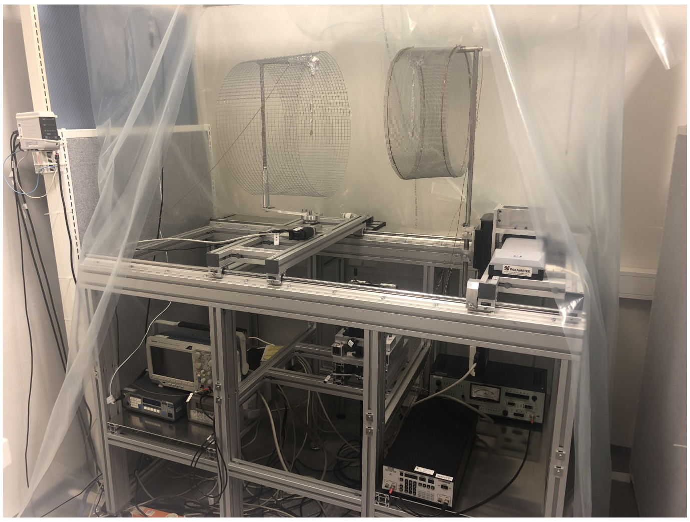

Figure 2: Experimental setup at the acoustics laboratory.

3.2 Aligninment of the transmitter and receiver

The disks are welded onto wires shielded with aluminium foil mounted onto a Faraday cage, Figure 2. The aim is to have the disks center on the z-axis and place them parallel in the xy-planeas shown in Figure 3. This is done using a high precision Keyence laser, installed by [35] and the high precision translation stages from Physik Instrumente from Section 3.1.

Firstly the disks are roughly placed on the z-axis by adjusting R_x in x- and y-direction so that the lasers point to the x marking the center on each of the disks. This mark has a finite size, so the laser is moved to the top, bottom (vertically) and side edges (horizontally) of the disks to see if these are aligned and adjustments are made by moving R_x in x- and y-direction if necessary.

When the disks are both on the z-axis and aligned vertically and horizontally the rotational alignment is investigated. For rotation along the y-axis this is done by moving to the top of either of the disks, choosing it as reference zero on the laser, moving to the bottom of the disk and reading the degree of tilt on the laser display. This is referred to as uncertainty in the alignment caused by rotation along the x-axis. If alignment is not satisfactory the disks, both T_x and R_x are moved by a light touch at the bottom of the disk until desired deviation along the x-axis is acquired.

Then the laser is placed on one of the furthest horizontal sides of the disk, this is chosen as reference zero and the degree of alignment is read at the opposite side of the disk. For T_x corrections are now made by using the rotation stage mentioned in Section 3.1, and a light touch or a screw at the top of the mounting rod allows for the rod and the R_x to be rotated is used to correct its positioning.

The process is repeated several times, to check that corrections in one direction did not affect the deviation or uncertainty in alignment in another direction, until satisfied alignment is achieved. .

Lastly the lateral stage in z-direction is used to position the front of the transmitting disk at the separation distance $z = d$, where d is the desired distance between the disk, and the front face of the receiver is placed at $z = 0$.

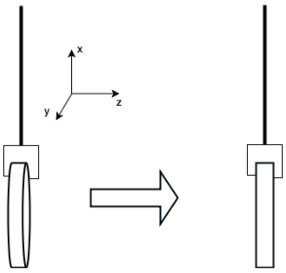

Figure 3: Aligning of a piezoelectric disc.

4 Results

4.1 The effect of accuracy in alignment

A difference in uncertainty of alignment has been shown in previous work. In [35] the uncertainty in alignment that was tolerated was 10 μm or less, where [36] allowed for uncertainties up to 40 μm. Therefore the effect of different alignment uncertainty is investigated by aligning the disks to different degrees of accuracy and observing how this affects the transfer function, H_{06}^{VV} . The accuracies chosen were 500 μm, 50 μm and 10 μm. The result is shown in Figure 4.

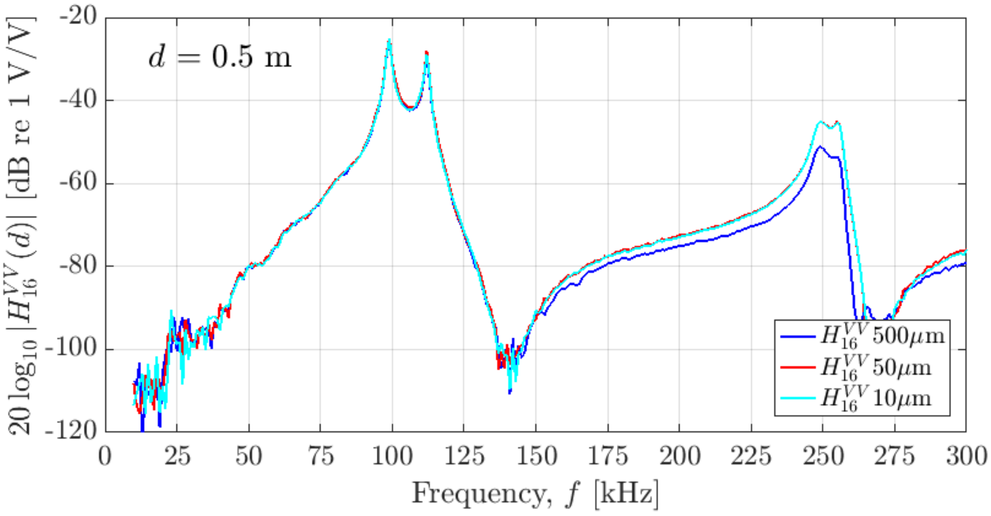

Figure 4: Measurements of transfer function H_{06}^{VV} magnitude with different accuracy in the aligning of the disks.

For the first two peaks associated with radial mode R_1, there is little to no change in the magnitude of the transfer function H_{06}^{VV}. At the second pair of peaks, radial mode R_2, there is no noticeable change in the magnitude for alignment to the degree of 50 μm and 10 μm, however the measurement with an 500 μm error in the alignment shows a decrease in magnitude of almost 5 dB, going from -51.1 dB re 1 V/V for the 50 μm and 10 μm alignment uncertainty measurement to -45.1 dB re 1V/V for the 500 μm alignment uncertainty measurement.

4.2 Comparison with previous work

Measurements of the loss-free transfer function compared to previous works is shown in Figure 5.

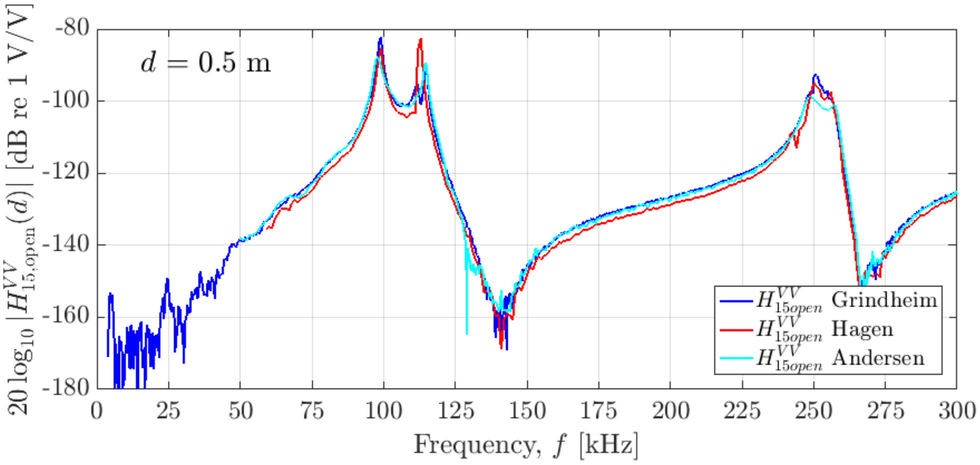

Figure 5: Measurements of transfer function H^{VV}_{15open} magnitude compared with previous work

The measurements done in this work starts at lower frequencies than previous measurements and undulations are observed before R_1, which is not as noticeable in the previous works presented here. It should be noted that the receiving disk used by Hagen [36] and Grindheim were not the same as by Andersen [35] and the calculation of the receiving electronics transfer function differ slightly.

Simulations for both the phase and magnitude of the transfer function H^{VV}_{15open} is done and compared to previous work done in two different finite element software tools; FEMP and COMSOL, Figure 6.

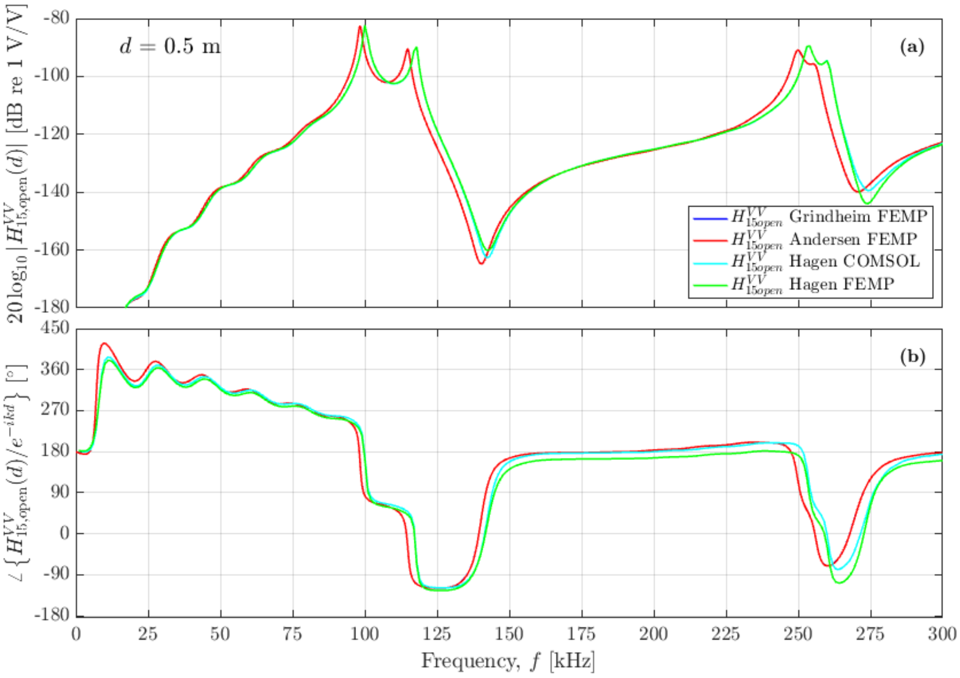

Figure 6: Simulated transferfunction H^{VV}_{15open} for magnitude a) and slowly varying phase b) compared with previous work

Figure 6 b) shows the slowly varying phase $<H^{VV}_{15open}$. The same parameters and software (FEMP) is used for simulations in the current work and by Andersen [35]. Therefore these curves are identical. The simulations done in COMSOL and FEMP by Hagen [36] differ from the current work and Andersen. There is a higher frequency for the resonances both at R_1, where the difference is 2 and 3 kHz for the two peaks, and R_2, where the difference is 4 and 14 kHz. There is a greater magnitude at R_2 of -84.4 dB re 1V/V [36] to -95.68 dB re 1V/V [35, 43] for the first peak and -89.5 dB re 1V/V [36] to -90.91 dB re 1V/V [35, 43] for the second peak. There is a noticeable difference in frequency step between the works causing the two latter to have a higher decimal point in both the frequency and magnitude values.

5 Conclusions and further work

The effect of aligning has proven to affect the magnitude of the transfer function H^{VV}_{16}, in the case of R_2 where the results show a decrease of approximately 5 dB re 1V/V. The measurement setup at the laboratory is however more than capable of obtaining a sufficient accuracy of 10 μm in x, y and z direction if aligned sufficiently by using the method explained in Section 3.2. There is observed some discrepancies in the different works on the measurements of the lossless transfer function, H^{VV}_{15open}. There change in the resonance frequencies at R_1 and R_2 are not as prominent, despite different receiving element [35, 36], and the differences in magnitude can be due to different post processing routine concerning the receiving electronics, H^{VV}_{5open6}. For the simulation Hagen [36] utilized other material constants and there are some differences seen both in FEMP simulation and the COMSOL simulation. The shift in frequency for the radial modes R_1 and R_2 is observed as well as differences in magnitude and further work will investigate if this is caused by the difference in the material data used for the piezoelectric disks and/or other parameters such as the elements used for the finite element description of the system.

6 Acknowledgements

The present work is part of an ongoing masters work on piezoelectric elements vibrating in air at University of Bergen, due in June 2019 [43]. The following persona are acknowledged for guidance and assistance: Espen Storheim, Andreas Hagen, Magnus Rentch Ersdal and Kenneth K. Andersen.

References

[1] ISO 17089-1:2010, “Measurement of fluid flow in closed conduits. ultrasonic meters for gas. part 1: Meters for custody transfer and allocation measurement,” *International Organization for Standardization, Geneva, Switzerland*, 2010.

[2] P. Lunde, K.-E. Frøysa, R. A. Kippersund, and M. Vestrheim, “Transient diffraction effects in ultrasonic meters for volumetric, mass and energy flow measurement of natural gas.” 21st International North Sea Flow Measurement Workshop, Tønsberg, Norway, 28-31 Oct., 2003.

[3] K.-E. Frøysa, P. Lunde, A. Paulsen, and E. Jacobsen, “Density and calorific value measurement of natural gas using ultrasonic flow meters. results from testing on various north sea gas field data.” 24th International North Sea Flow Measurement Workshop, St. Andrews, Scotland, 24-27 Oct., 2006.

[4] M. Farzaneh-Gord, A. Arabkoohsar, and R. N. N. Koury, “Novel natural gas molecular weight calculator equation as a function of only temperature, pressure and sound speed,” *Journal of Natural Gas Science and Engineering*, vol. 30, pp. 195–204, 2016.

[5] P. Norli, *"Sound velocity cell for gas characterizsation"*. PhD thesis, University of Bergen, Department of Physics and Technology, Bergen, Norway, 2007.

[6] P. Lunde, P. Norli, M. Vestrheim, and R. Kippersund, “Precision sound velocity cell as reference for gas quality measurement in ultrasonic flow meters. preliminary results using two candidate methods with argon at low pressure.” Proc. 30th Scand. Symp. Phys. Acoust., Geilo, Norway, Jan. 28-31, 2007.

[7] R. Øyerhamn, E. N. Mosland, E. Storheim, P. Lunde, and M. Vestrheim, “Finite element modeling of ultrasound measurement systems for gas. comparison with experiments in air,” *Acoustical Society of America*, vol. 144(4), pp. 2613–2625, 2018.

[8] P. Stepanishen, “Pulsed transmitt/receiver response of ultrasonic piezoelectric transducers,” *J. Acoust. Soc. Am.*, vol. 69(6), pp. 1815–1827, 1981.

[9] A. Lygre, M. Vestrheim, P. Lunde, and V. Berge, “Numerical simulation of ultrasonic flowmeters,” *Proc. 1987 Ultrasonics International, Butterworth Scientific Ltd., Guildford, UK*, pp. 196–201, 1981.

[10] D. A. L. Collie and M. A. Player, “Extended computer method for predicting the transient response of ultrasound NDT probes,” *Ultrasonics*, vol. 27, pp. 141–149, 1989.

[11] S. Vervik, “Transitt-tidsbestemmelse for ultralyd strømingsmetre. Nullstrømningsforhold [Transit time detection for ultrasonic flow meters at zero flow conditions].” Cand. Scient. thesis, Dept. of Physics, Univ. of Bergen, Norway (in Norwegian), 1995.

[12] M. Willatzen, “Ultrasound transducer modeling - Receieved voltage signals and the use of half-wavelength window layers with acoustic coupling layers,” *IEEE Trans. Ultrason. Ferroelectr. Freq. Control*, vol. 46(5), pp. 1164–1174, 1999.

[13] S. Vervik, *"Methods for characterization of gas-coupled ultrasonic sender-receiver measurement systems"*. PhD thesis, University of Bergen, Department of Physics and Technology, Bergen, Norway, 2000.

[14] M. Willatzen, “Ultrasound transducer modeling - General theory and applications to ultrasound reciprocal systems,” *IEEE Trans. Ultrason. Ferroelectr. Freq. Control*, vol. 48(1), pp. 100–112, 2001.

[15] E. Papadakis, “Ultrasonic transducer evaluation in five "domains": time, space, frequency, surface motion, and theory,” *IEEE Trans. Ultrason. Symp., Phoenix, Arizona, USA, Oct. 26-28*, pp. 104–112, 1977.

[16] G. Low, "A simple computer method for predicting the transient response of ultrasonic NDT probes," *NDT International*, vol. 13(6), pp. 285–290, 1980.

[17] G. Hayward and M. Jackson, "Discrete-time modeling of the thickness mode piezoelectric transducer," *IEEE Trans. Son. Ultras.*, vol. 31(3), pp. 137–150, 1984.

[18] G. Hayward, M. Jackson, and T. Durrani, "A systems model of the thickness mode piezoelectric transducer," *J. Acoust. Soc. Am.*, vol. 76(2), pp. 369–382, 1984.

[19] K. Yamaguchi, H. Yagami, and T. Fuji, "New method of time domain analysis of the performance of multilayered ultrasonic transducers," *IEEE Trans. Ultrason., Ferroelect., Freq. Contr.*, vol. 33(6), pp. 669–678, 1986.

[20] P. Wilcox, R. Monkhouse, P. Cawley, M. Lowe, and B. Auld, "Development of a computer model for an ultrasonic polymer film transducer system," *NDT & E International*, vol. 31(1), pp. 51–64, 1998.

[21] C. Dang, L. W. Schmerr, and A. Sedov, "Modeling and measuring all the elements of an ultrasonic nondestructive evaluation system I: modeling foundations," *Res. Nondestr. Eval.*, vol. 14(3), pp. 141–176, 2002.

[22] C. Dang, L. W. Schmerr, and A. Sedov, "Modeling and measuring all the elements of an ultrasonic nondestructive evaluation system II: model-based measurements," *Res. Nondestr. Eval.*, vol. 14(4), pp. 177–201, 2002.

[23] L. W. Schmerr and S. Song, "Ultrasonic nondestructive evaluation systems: Models and measurements." Springer London, Ltd., 2007.

[24] L. W. Schmerr and A. Sedov, "Ultrasonic measurement models for contact testing with bulk waves, surface waves, and plate waves," *Res. Nondestr. Eval.*, vol. 22, pp. 129–146, 2011.

[25] J. van Deventer, T. Lofqvist, and J. Delsing, "Pspice simulation of ultrasonic systems," *IEEE Trans. Ultrason., Ferroelect., Freq. Contr.*, vol. 47, pp. 1014–1024, 2000.

[26] P. Lunde, R. A. Kippersund, and M. Vestrheim, "Signal modeling using the flosim system model in ultrasonic instrumentation for industrial applications." Proc. Norw. Symp. Signal Proc. (NORSIG 2003), Bergen, Oct. 6, 2003.

[27] M. Bezdêk, H. Landes, A. Rieder, and R. Lerch, "A coupled finite-element, boundary-integral method for simulating ultrasonic flowmeters," *IEEE Trans. Ultrason., Ferroelect., Freq. Contr.*, vol. 54(3), pp. 636–646, 2007.

[28] M. Bezdêk and B. Tittman, "Dispersion analysis of a three-layered waveguide with finite element and matrix methods," *Acta Acustica united with Acustica*, vol. 94, pp. 792–806, 2008.

[29] M. Bezdêk, "Numerical modeling of ultrasonic flowmeters." VDM Verlag Dr. Müller GmbH & Co KG, Saarbrücken, Germany, 2008.

[30] L. Ge, X. Wang, and C. Jin, "Numerical modeling of PZT-induced Lamb wave-based crack detection in plate-like structures," *Wave Motion*, vol. 51, pp. 867–885, 2014.

[31] R. Hauge, “Finite element modeling of ultrasound measurements for gas. Comparison with experiments in air,” Master’s thesis, University of Bergen, Department of Physics and Technology, Bergen, Norway, Norway, 2013.

[32] E. Mosland, “Reciprocity calibration method for ultrasonic piezoelectric transducers in air,” Master’s thesis, University of Bergen, Department of Physics and Technology, Bergen, Norway, Norway, 2013.

[33] E. Storheim, *"Diffraction effects in the ultrasonic field of transmitting and receiving circular piezoseramic disks in radial mode vibration"*. PhD thesis, University of Bergen, Department of Physics and Technology, Bergen, Norway, 2015.

[34] A. A. Søvik, “Ultrasonic measurements systems for gas. Finite element modeling compared with measurements in air,” Master’s thesis, University of Bergen, Department of Physics and Technology, Bergen, Norway, Norway, 2015.

[35] K. K. Andersen, “Reciprocity calibration of ultrasonic piezoelectric disks in air,” Master’s thesis, University of Bergen, Department of Physics and Technology, Bergen, Norway, Norway, 2015.

[36] A. Hagen, “Ultrasonic measurement system with diffraction correction for gas,” Master’s thesis, University of Bergen, Department of Physics and Technology, Bergen, Norway, Norway, 2017.

[37] ANSI S1.26 , “Method for calculation of the absorption of sound by the atmosphere,” *American National Standards Institute, New York*, vol. (R2009), pp. 2613–2625, 1995.

[38] S. Khimunin, “Numerical calculation of the diffraction correction for the precise measurement of ultrasound absorption,” *Acta Acustica united with Acustica*, vol. 27, pp. 173–181, 1972.

[39] S. Khimunin, “Numerical calculation of the diffraction corrections for the precise mea- surement of ultrasound phase velocity,” *Acta Acustica united with Acustica*, vol. 32, pp. 192–200, 1975.

[40] Physik Instrumente (PI) GmbH & Co. KG, Auf der Römerstr. 1, 76228 Karlsruhe, Germany, *Datasheet M-511 • M-521 • M-531, High-Precision Linear Stage*, January 15 2018.

[41] Physik Instrumente (PI) GmbH & Co. KG, Auf der Römerstr. 1, 76228 Karlsruhe, Germany, *User Manual MP 34E Rotation Stages M-038, M-035 Series*, August 29 2002.

[42] Physik Instrumente (PI) GmbH & Co. KG, Auf der Römerstr. 1, 76228 Karlsruhe, Germany, *MP 33E User Manual, M-5x1 Series Linear Positioning Stages*, September 20 2004.

[43] R. Grindheim, “Working title: Modeling and measuring near field sound preassure from piezoelectric elements,” Master’s thesis, University of Bergen, Department of Physics and Technology, Bergen, Norway, Norway, In preparation, 2019.